

# 3D Modelling and Simulation of Reactive Fluidized Beds for Conversion of Biomass with Discrete Element Method

Vom Fachbereich Maschinenbau  
an der Technischen Universität Darmstadt  
zur  
Erlangung des Grades eines Doktor-Ingenieurs (Dr.-Ing.)  
genehmigte

## D i s s e r t a t i o n

vorgelegt von

**M.Sc. Dipl.-Ing. Falah Alobaid**  
aus Damaskus

Berichterstatter: Prof. Dr.-Ing. Bernd Epple  
Mitberichterstatter: Prof. Dr. rer. nat. Amsini Sadiki

Tag der Einreichung: 03. 06. 2013  
Tag der mündlichen Prüfung: 17. 07. 2013

Darmstadt 2013



# Preface

The present Ph.D. thesis “3D Modelling and Simulation of Reactive Fluidized Beds for Conversion of Biomass with Discrete Element Method” is the result of my time as a doctoral candidate at the Department of Energy Systems and Technology at the Technische Universität Darmstadt. I would like to express my gratitude to all those who gave me the possibility to complete this thesis.

I wish to thank:

Prof. Dr.-Ing. Bernd Epple, the supervisor of this Ph.D. thesis, for his valuable guidance and for giving me the golden opportunity to do this wonderful work,

Prof. Dr.-Ing. Amsini Sadiki, the reviewer of this Ph.D. thesis, for numerous words of advice and taking over the co-review of this work,

Dr.-Ing. Thilo Kissel, Dipl.-Ing. Karl Karner, colleagues of mine at the Technische Universität Darmstadt, for interesting discussions,

Dipl.-Ing. Nabil Baraki, M.Sc. Naser Almohammed and M.Sc. Vitali Kez, friends of mine, for the friendship, lots of valuable scientific discussions and many evenings of fun,

Klaus Servaty, Daniel Binzer, for close cooperation with all issues relating to programming and image processing

and all scientific staff and students at EST.

Exceptionally, I wish to express my gratitude to my parents (Zakia and Elias) and my sisters (Maysoun, Rima, Rasha and Ola) for supporting me the long time period of my education and their help I received whenever they could. Special thanks to my first cousin Salam and my uncle Moufid for their continuous support and wonderful charisma days. I wish also to thank my second cousin Nabil for his advices during the long evenings of fun.

# Ehrenwörtliche Erklärung

Ich erkläre hiermit ehrenwörtlich, dass ich die vorliegende Arbeit selbstständig angefertigt habe. Sämtliche aus fremden Quellen direkt oder indirekt übernommenen Gedanken sind als solche kenntlich gemacht.

Die Arbeit wurde bisher keiner anderen Prüfungsbehörde vorgelegt und noch nicht veröffentlicht.

Darmstadt, den 03. Juni 2013

---

(Falah Alobaid)

# TABLE OF CONTENTS

PREFACE.....	III
EHRENWÖRTLICHE ERKLÄRUNG .....	IV
TABLE OF CONTENTS.....	V
NOMENCLATURES.....	VIII
Latin symbols .....	viii
Greek symbols.....	ix
Constants .....	ix
Dimensionless numbers.....	x
Subscripts and indices.....	x
Most used chemical symbols .....	xii
Abbreviations .....	xii
ABSTRACT .....	1
1 INTRODUCTION .....	3
1.1 State of the scientific knowledge .....	4
1.2 Research objectives.....	8
1.3 Computational code .....	8
1.4 Thesis outline .....	9
2 BIOMASS CONVERSION IN FLUIDIZED BED.....	10
2.1 Biomass.....	10
2.2 Fluidization .....	11
2.3 Conclusion.....	15
3 DESCRIPTION OF GAS-SOLID FLOW.....	16

---

<b>3.1 Numerical methods .....</b>	<b>16</b>
3.1.1 Quasi-single-phase method .....	17
3.1.2 Two-fluid method .....	17
3.1.3 Single-particle method .....	19
3.1.4 Representative-particle method .....	21
3.1.5 Hybrid method .....	21
<b>3.2 Conclusion.....</b>	<b>21</b>
<b>4 COLLISION MODELS.....</b>	<b>23</b>
<b>4.1 Collision detection models.....</b>	<b>23</b>
4.1.1 Stochastic collision detection models .....	23
4.1.2 Deterministic collision detection models.....	24
4.1.2.1 Standard method.....	26
4.1.2.2 Neighbourhood method.....	27
4.1.2.3 Bounding-boxes method .....	29
<b>4.2 Collision treatment model .....</b>	<b>30</b>
4.2.1 Hard sphere model.....	30
4.2.2 Soft sphere model .....	33
<b>4.3 Conclusion.....</b>	<b>34</b>
<b>5 DISCRETE ELEMENT METHOD.....</b>	<b>36</b>
<b>5.1 Forces balance.....</b>	<b>36</b>
5.1.1 Volume forces .....	36
5.1.2 Surface forces.....	37
5.1.2.1 Aerodynamic surface forces .....	38
5.1.2.2 Short-range surface forces .....	42
5.1.2.2.1 Contact force.....	43
5.1.2.2.2 Adhesive forces without physical contact.....	50
5.1.2.2.3 Adhesive forces with physical contact .....	54
<b>5.2 Momentum balance .....</b>	<b>65</b>
5.2.1 Moment of force due to the fluid-particle interaction.....	66
5.2.2 Moment of force due to short-range forces between particles.....	67
<b>5.3 Conclusion.....</b>	<b>69</b>
<b>6 NUMERICAL METHODS FOR FLUID MOTION .....</b>	<b>74</b>
<b>6.1 Mesh-free particle methods.....</b>	<b>75</b>
6.1.1 Smoothed particle hydrodynamic method .....	76
6.1.2 Mesh-free Galerkin methods .....	77
6.1.3 Other particle methods.....	77
<b>6.2 Grid-based methods .....</b>	<b>78</b>
6.2.1 Numerical grid.....	79
6.2.2 Discretisation approaches.....	81
6.2.2.1 Finite difference method.....	81
6.2.2.2 Finite element method.....	83
6.2.2.3 Finite volume method .....	84
6.2.2.4 Other discretisation methods.....	88
6.2.3 Time discretisation .....	89

6.2.4 Pressure velocity coupling.....	89
6.2.5 Boundary conditions .....	91
6.2.6 Turbulence .....	92
6.2.7 Solution of equations system.....	93
6.2.8 Extended balance equations.....	95
<b>6.3 Conclusion.....</b>	<b>97</b>
<b>7 FLUID–PARTICLE INTERACTION .....</b>	<b>102</b>
<b>7.1 Inter-phase coupling .....</b>	<b>102</b>
7.1.1 Volumetric void fraction.....	104
7.1.2 Momentum transfer.....	104
7.1.3 Heat transfer .....	106
<b>7.2 Particle time step .....</b>	<b>107</b>
<b>7.3 Conclusions .....</b>	<b>108</b>
<b>8 RESULTS .....</b>	<b>112</b>
<b>8.1 Non-reactive gas–solid flow .....</b>	<b>112</b>
8.1.1 Validation .....	112
8.1.1.1 Test rig and numerical models .....	112
8.1.1.2 DEM model / experiment .....	115
8.1.1.3 DEM / Euler–Euler / stochastic Euler–Lagrange models .....	121
8.1.2 Offset method .....	137
8.1.3 Particle grid method.....	140
8.1.4 Particle search grid method .....	143
8.1.5 Parameter study.....	145
8.1.5.1 Variation of stiffness coefficient.....	146
8.1.5.2 Variation of fluid time step.....	152
8.1.5.3 Variation of processor number .....	158
<b>8.2 Reactive gas–solid flow .....</b>	<b>161</b>
8.2.1 Numerical model.....	162
8.2.2 Combustion with fuel gas.....	163
8.2.3 Combustion with solid fuel .....	166
<b>8.3 Conclusion.....</b>	<b>169</b>
<b>9 CONCLUSION AND FUTURE WORK.....</b>	<b>172</b>
<b>10 APPENDIX.....</b>	<b>178</b>
<b>10.1 Experimental and simulation parameters .....</b>	<b>178</b>
<b>10.2 Spatial distribution of particles in a cold 3D fluidized bed test rig .....</b>	<b>184</b>
<b>BIBLIOGRAPHY .....</b>	<b>185</b>
<b>LEBENSLAUF .....</b>	<b>193</b>

# Nomenclatures

## Latin symbols

<i>A</i>	surface, vessel cross-section area, pre-exponential factor	[m <sup>2</sup> ], [m <sup>2</sup> ], [1/s]
<i>a</i>	translational acceleration	[m/s <sup>2</sup> ]
<i>B</i>	magnetic flux density	[N/A m]
<i>b</i>	angular acceleration	[rad/s <sup>2</sup> ]
<i>C</i>	coefficient, correction factor	[–]
<i>c</i>	concentration	[kmol/m <sup>3</sup> ]
<i>c<sub>p</sub></i>	specific heat capacity	[J/kg K]
<i>D</i>	surface diffusion coefficient, volume diffusion coefficient	[m <sup>2</sup> /s], [m <sup>3</sup> /s]
<i>d</i>	displacement, diameter	[m]
<i>E</i>	Young modulus, electric field intensity, energy	[N/m <sup>2</sup> ], [N/A s], [J]
<i>ER</i>	expansion ratio	[–]
<i>e</i>	restitution coefficient	[–]
<i>F</i>	force	[N]
<i>FI</i>	fluidization index	[–]
<i>FR</i>	fluctuation ratio	[–]
<i>f</i>	force density	[N/m <sup>3</sup> ]
<i>G</i>	shear modulus	[N/m <sup>2</sup> ]
<i>g</i>	standard gravity	[m/s <sup>2</sup> ]
<i>h</i>	enthalpy, height, rotation unit vector	[kJ/kg], [m], [–]
<b>I</b>	unit matrix	[–]
<i>I</i>	moment of inertia	[kg m <sup>2</sup> ]
<i>J</i>	impulse vector	[kg m/s]
<i>k</i>	stiffness coefficient, reaction rate constant	[N/m], [1/s]
<i>k<sub>R</sub></i>	rotational stiffness coefficient	[s]
<i>l</i>	length	[m]
<i>M</i>	moment of force, molar mass	[N m], [kg/kmol]
<i>m</i>	mass	[kg]
<i>ṁ</i>	mass flow rate	[kg/s]
<i>N</i>	number of particle	[–]
<i>n</i>	number of north magnetic poles	[A m]
<i>p</i>	static pressure	[N/m <sup>2</sup> ]
<i>q</i>	charge	[A s]
<b>R</b>	rotation matrix	[–]
<i>R</i>	radius	[m]

$r$	radius, position vector, reaction rate	[m], [m], [kmol/m <sup>3</sup> s]
$S$	source term, saturation level	[different], [-]
$s$	distance, unit vector	[m], [-]
$T$	torque, temperature, computing time	[N m], [K], [s]
$\mathbf{T}$	stress tensor for Newtonian fluids	[N/m <sup>2</sup> ]
$t$	time	[s]
$U$	electric potential	[kg m <sup>2</sup> /A s <sup>3</sup> ]
$u$	translational velocity	[m/s]
$V$	volume	[m <sup>3</sup> ]
$\dot{V}$	volume flow rate	[m <sup>3</sup> /s]
$W$	weight	[kg]
$w$	angular velocity	[rad/s]
$X$	mass fraction	[kg/kg <sub>mix</sub> ]
$x, y, z$	Cartesian coordinates	[m]

### Greek symbols

$\alpha$	heat transfer coefficient, collision angle	[W/K m <sup>2</sup> ], [rad]
$\alpha_{UDS}$	blending factor	[-]
$\beta$	resistance coefficient, restitution coefficient	[kg/s m <sup>3</sup> ], [-]
$\gamma$	surface tension	[N/m]
$\delta$	penetration depth	[m]
$e$	restitution coefficient	[-]
$\varepsilon$	volumetric void fraction (porosity), emissivity	[-], [-]
$\eta$	damping coefficient, rolling damping constant	[N s/m], [kg m <sup>2</sup> /s]
$\theta$	contact angle	[rad]
$\lambda$	thermal conductivity, bulk viscosity	[W/K m], [kg/m s]
$\mu$	dynamic viscosity, friction coefficient, relative permeability	[kg/m s], [-], [-]
$\mu_r$	rolling friction coefficient	[m]
$\xi$	fill angle	[rad]
$\omega$	angular velocity	[rad/s]
$\rho$	density	[kg/m <sup>3</sup> ]
$\sigma$	surface tension	[N/m]
$\tau$	viscous stress	[N/m <sup>2</sup> ]
$\varphi$	angular displacement, rotation angle, surface charge	[rad], [rad], [A s/m <sup>2</sup> ]
$\phi$	physical value	[different]
$\nu$	Poisson's number, stoichiometric coefficient	[-], [-]
$\Omega$	computational domain	[-]
$\partial\Omega$	grid surface	[m <sup>2</sup> ]

### Constants

$A$	Hamaker constant	[kg m <sup>2</sup> /s <sup>2</sup> ]
$a$	lattice constant	[m]
$h$	Planck constant	[kg m <sup>2</sup> /s]

---

$k_B$	Boltzmann constant	[kg m <sup>2</sup> /s <sup>2</sup> K]
$R$	universal gas constant	[N m/kmol K]
$\epsilon_0$	absolute permittivity (electric constant)	[A <sup>2</sup> s <sup>4</sup> /kg m <sup>3</sup> ]
$\epsilon_{rel}$	relative permittivity (dielectric constant)	[−]
$\lambda$	London constant	[kg m <sup>8</sup> /s <sup>2</sup> ]
$\sigma$	Stefan–Boltzmann constant	[kg/s <sup>3</sup> K <sup>4</sup> ]
$hw$	Lifshitz–van der Waals constant	[kg m <sup>2</sup> /s <sup>2</sup> ]

### Dimensionless numbers

Kn	Knudsen number
Pe	Peclet number
Pr	Prandtl number
Re	Reynolds number
Sc	Schmidt number
Stk	Stokes number

### Subscripts and indices

<i>adh</i>	adhesion
<i>bas</i>	Basset
<i>bc</i>	boundary condition
<i>bio</i>	biomass
<i>bub</i>	bubble
<i>buo</i>	buoyancy
<i>CV</i>	control volume
<i>cap</i>	capillary
<i>cav</i>	cavity
<i>cha</i>	char
<i>char</i>	characteristic
<i>col</i>	collision
<i>con</i>	convection, contact
<i>cri</i>	critical
<i>D</i>	dimensional
<i>dam</i>	damping
<i>dis</i>	displaced
<i>dif</i>	diffusion
<i>dra</i>	drag
<i>e</i>	east
<i>ela</i>	elastic
<i>ele</i>	electric
<i>elst</i>	electrostatic
<i>equ</i>	equivalent
<i>ext</i>	external
<i>f</i>	fluid or function

<i>g</i>	gas
<i>gra</i>	gravitation
<i>het</i>	heterogeneous
<i>hom</i>	homogenous
<i>hor</i>	horizontal
<i>i</i>	component, notation, particle index
<i>in</i>	inner
<i>int</i>	internal
<i>j</i>	component, notation, particle index
<i>k</i>	component, notation
<i>kin</i>	kinetic
<i>lea</i>	lean
<i>liq</i>	liquid
<i>loc</i>	located
<i>mag</i>	magnetic
<i>mags</i>	Magnus
<i>max</i>	maximum
<i>min</i>	minimum
<i>n</i>	normal, north
<i>Out</i>	outer
<i>P</i>	particle, cell centre
<i>pre</i>	pressure
<i>pyr</i>	pyrolysis
<i>R</i>	rotation
<i>r</i>	rolling
<i>rad</i>	radiometric, radiation
<i>rel</i>	relative
<i>relax</i>	relaxation
<i>res</i>	resultant
<i>S</i>	shear flow
<i>s</i>	solid, surface, south
<i>saf</i>	Saffman
<i>sg</i>	search grid
<i>sgc</i>	search grid cell
<i>sol</i>	solid
<i>sup</i>	superficial
<i>t</i>	tangentia
<i>tot</i>	total
<i>tra</i>	transition
<i>V</i>	volume
<i>vac</i>	vacuum
<i>van</i>	Van der Waals

<i>ver</i>	vertical
<i>ves</i>	vessel
<i>vir</i>	virtual
<i>volat</i>	volatile
<i>W</i>	wall
<i>w</i>	west
<i>wat</i>	water
<sup>^</sup>	non-dimensional

**Most used chemical symbols**

<i>C</i>	carbon
<i>CH</i> <sub>4</sub>	methane
<i>C</i> <sub>2</sub> <i>H</i> <sub>4</sub>	ethane
<i>C</i> <sub>2</sub> <i>H</i> <sub>6</sub>	ethane
<i>C</i> <sub>3</sub> <i>H</i> <sub>8</sub>	propane
<i>CO</i>	carbon monoxide
<i>CO</i> <sub>2</sub>	carbon dioxide
<i>H</i> <sub>2</sub>	hydrogen
<i>H</i> <sub>2</sub> <i>O</i>	water
<i>HCl</i>	hydrogen chloride
<i>N</i> <sub>2</sub>	nitrogen
<i>NO</i> <sub>x</sub>	nitrogen oxides
<i>O</i> <sub>2</sub>	oxygen
<i>SO</i> <sub>x</sub>	sulphur monoxide/dioxide/trioxide
<i>SO</i> <sub>2</sub>	sulphur dioxide

**Abbreviations**

ANSYS	commercial CFD software
CPFD	commercial CFD software
BDS	backward difference scheme
BTL	biomass to liquid
CDS	central differencing scheme
CFB	circulating fluidized bed
CFD	computational fluid dynamics
CPU	central processing unit
CVFEM	control volume based finite element method
DEM	discrete element method, diffuse element method
DEMEST	in-house CFD/DEM code
DNS	direct numerical simulation
EFG	element free Galerkin method
EST	energy systems and technology department
FD	finite difference method
FDS	forward difference scheme

FE	finite element method
FTT	fast Fourier transform
FV	finite volume method
IGCC	integrated gasification combined cycle
KTDG	kinetic theory of dense gases
KTGF	kinetic theory of granular fluids
LBM	Lattice Boltzmann method
LES	large eddy simulation
MATLAB	commercial mathematical software
MD	molecular dynamics approach
MLPG	Mesh-less Local Petrov–Galerkin method
MPI	message passing interface
MPICH2	software for message passing interface
ODE	ordinary differential equation
PDE	partial differential equation
PIC	particle-in-cell method
PISO	pressure-implicit with splitting of operators
PSIC	particle source in cell method
PUM	partition of unity method
QUICK	quadratic upwind interpolation for convective kinematic
RANS	Reynolds averaged Navier–Stokes method
RKPM	reproducing kernel particle method
RMS	root mean square
SC	steam cycle
SIMPLE	semi-implicit method for pressure-linked equations
SIMPLEC	semi-implicit method for pressure-linked equation consistent
SFB	stationary fluidized bed
SM	spectral method
SPH	smoothed particle hydrodynamic method
TCP/IP	transmission control protocol / internet protocol
UDS	upwind differencing scheme
VM	vortex method



# Abstract

The use of biomass as a CO<sub>2</sub>-neutral renewable energy source gains more importance due to the decreasing resources of fossil fuels and their impact on the global warming. The thermochemical conversion of biomass in fluidized beds offers an economic and sustainable contribution to the global energy supply. Although the fluidized bed has reached a commercial status since many decades ago, its hydrodynamic behaviour is not completely understood. The availability of detail experimental information from real facilities is extremely difficult because the lack of accessibility, the measurement costs and the associated inevitable reduction in production. The numerical simulation provides an effective complement to the costly measurements. This requires besides the calculation of a gas-solid flow, an accurate description of particle-particle/wall collisions. Furthermore, kinetic models for pyrolysis, homogenous reactions, heterogeneous reactions and the related heat and mass transfer processes should be considered. Basically, there are two different methods for the representation of the gas-solid flow, viz. Euler-Euler and Euler-Lagrange models. The solid phase is treated as a continuum in the Euler-Euler model, while each particle trajectory is determined in the Euler-Lagrange model. In the Euler-Euler approach, the single particle-particle or particle-wall collision can be considered using additional assumptions. In the Euler-Lagrange approach, the particle-particle/wall collisions can be stochastically modeled or deterministically detected.

The aim of this study is to develop a 3D program for the numerical simulation of biomass conversion in fluidized beds. The particle-particle/wall and gas-solid interactions are modeled by tracking all individual particles. For this purpose, the deterministic Euler-Lagrange/discrete element method (DEM) is applied and further developed. The fluid-particle interaction is studied using a new procedure, known as the offset method. The proposed method is highly precise in determining the interaction values, thus improving the simulation accuracy up to an order of magnitude. In this work, an additional grid, so-called particle grid, in which the physical values of solid phase is computed, is introduced. The suggested procedure allows the variation of the fluid grid resolution independent of the particle size and consequently improves the calculation accuracy. The collision detection between particle-particle/wall is performed with the aid of the particle search grid method. The use of the particle search grid method enhances the efficiency of collision detection between collision partners. The improved Euler-Lagrange/DEM model is validated towards the measurements obtained from a cold quasi-2D fluidized bed. The results suggest that the extended Euler-Lagrange/DEM model can predict accurately the motion of particles and the gas bubble expansion in the bed. The received results from the DEM model are also compared with other numerical approaches, namely the Euler-Euler and stochastic Euler-Lagrange models. Compared to measurements, the results show that the Euler-Euler model underestimates the bubble sizes and the bed expansions, while the stochastic Euler-Lagrange model reaches faster the maximum bed expansions.

The efficiency and accuracy of the Euler-Lagrange/DEM model is investigated in detail. Parameter studies are carried out, in which stiffness coefficient, fluid time step and processor number are varied for different particle numbers and diameters. The obtained results are compared with the measurements in order to derive the optimum parameters for Euler-

Lagrange/DEM simulations. The results suggest that the application of higher stiffness coefficients (more than  $10^5$  N/m) improves the simulation accuracy slightly, however, the average computing time increases exponentially. For time intervals larger than five milliseconds, the results show that the average computation time is independent of applied fluid time step, while the simulation accuracy decreases extremely by increasing the size of fluid time step. The use of fluid time steps smaller than five milliseconds leads to negligible improvements in the simulation accuracy, but to exponential rise in the average computing time. The parallel calculation accelerates the Euler–Lagrange/DEM simulation if the critical number of domain decomposition is not reached. Exceeding this number, the performance is not anymore proportional to the number of processors and the computational time increases again. The critical number of domain decomposition depends on particle numbers. An increase in solid contents results in a shift of critical decomposition number to higher numbers of CPUs.

The local concentrations of solid and gaseous species, the local gas and particle temperatures, the local heat release and heat transfer rates can also be calculated with the developed program. In combination with the simulation of the gas–solid flow, it is possible to model the biomass conversion in the fluidized bed. Three series of warm simulations in a quasi-2D fluidized bed model are performed, viz. combustion with fuel gas without and with inert sand particles as well as combustion with solid fuel (a mixture of inert sand and pine wood particles). The received results realise the coupling of the Euler–Lagrange/DEM model with chemical reaction mechanism. The extended Euler–Lagrange/DEM model under the consideration of thermochemical reaction model is able to simulate, by the same token, the conversion of other solid fuels such as coal in fluidized beds.

# 1 Introduction

The rapid worldwide increase in the consumption of fossil fuels in the last few decades to meet the energy demand suggests that the turning point for depletion of petroleum, natural gas and coal reserves has already been reached. However, the economic and social development of each country is highly depended on the energy security so that the energy supply is a strategic interest of any nation. The optimisation of existent as well as in planning stage thermal power plants that play an important role in energy production offers for the short time an efficient solution (Flynn 2003, Rukes and Taud 2004, AlObaid et al. 2008, AlObaid et al. 2009, AlObaid et al. 2012b). On the other hand, the rise employment of renewable energy as a complement to conventional energy sources gains in importance. Biomass provides a clean energy source that could basically improve the economy, the independence and the self-sufficiency in energy supply. Compared to fossil as well as other renewable energy sources, the biomass is globally widespread. The use of biomass reduces the amount of burned fossil fuels and consequently the greenhouse emissions. Carbon dioxide is one of primary products of fossil fuel combustion that is widely believed to be associated with the global warming.

The thermochemical conversion of biomass by combustion or gasification is an advanced technology. The released energy can be used in different processes such as the integrated gasification combined cycle (IGCC), the biomass to liquid (BTL) and the steam cycle (SC). Due to its high heat and mass transfer rates in addition to very low NO<sub>x</sub> and SO<sub>2</sub> emissions, the fluidized bed presents an efficient system for the biomass conversion. The fluidized bed is a bulk of solid particles through which gas or liquid flows. The emerging forces of the fluid carry the particles and cause a fluidization condition. Depending on the fluidization velocity, a distinction is made between stationary fluidized beds (SFB) and circulating fluidized beds (CFB).

In the fluidized bed for the biomass conversion, multifaceted physical and chemical processes are gathered. Here, the thermochemical reactions and the multi-phase flow play a significant role. In this flow exist at least two phases that are characterised by different material properties and are separated by a sharp boundary called the phase boundary. Diverse materials lead to different two-phase flows. In practice, they are classified as gas-fluid, fluid-solid and gas-solid flows. While in the gas-fluid flow one of the phases is existent in a dispersible form, the solid remains always in dispersed phase in the fluid-solid and gas-solid flows.

The description of single-phase flow has been extensively investigated for a long time as opposed to the multi-phase flows, which the industrial and academic researchers have been substantially interested. Here, the reactive gas-solid flow in terms of gasification and combustion of solid fuels in energy sector is especially the focus of research. The modeling, the characterisation and the advanced understanding of this flow present now a major challenge, since this behaviour is still unknown and difficult to predict in many applications. Nowadays, the design and optimisation of equipment including reactive gas-solid flow are mostly based on experimental studies. Due to the combination of increased computer efficiency and the possibility to parallelise the numerical solutions, the numerical simulations offer an alternative complement to the costly experiments. These simulation programs are relevant for modelling the energy systems in order to consider various aspects of the investigated process.

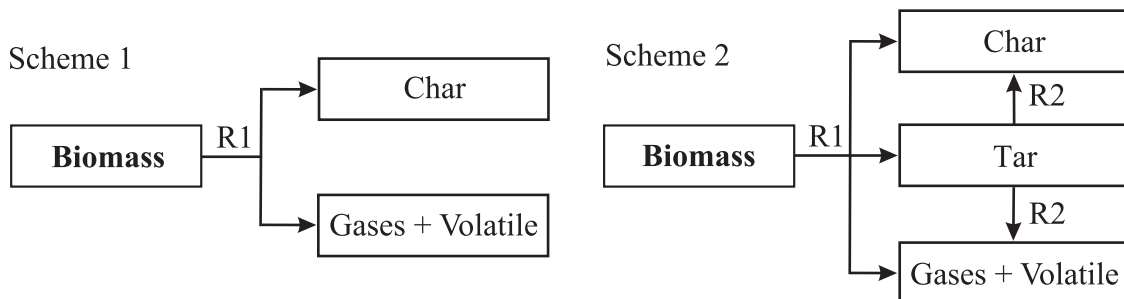
In this study, the Euler–Lagrange/DEM model is coupled with the thermochemical reaction mechanism to describe the biomass conversion in fluidized beds.

### 1.1 State of the scientific knowledge

Many scientific and industrial efforts have been achieved on making the thermochemical conversion of biomass more efficient and economically admissible. An essential part of these works has concentrated over the past two decades on the development of numerical simulation models for the thermochemical reactors (such as: gasifiers, boilers and combustors) that can help in the design and analysis of associated processes. Different kinetic models have been suggested, various numerical methods were investigated and a set of parameters were introduced. The complexity of the process has many reasons such as the large number of chemical components that appear as intermediates or end products and the dependence on several parameters (for example: thermodynamic and transport properties, particle shape and size as well as material composition). All these factors motivate the necessity of research for enhancing the modelling and simulation of biomass conversion.

The biomass conversion comprises different chemical and physical processes such as drying, pyrolysis and combustion of solid fuel. Throughout the drying process, the steam leaves the biomass particles once the temperature exceeds 100°C. The pyrolysis as a key element of biomass gasification has a complex nature and can influence the effectiveness of the whole process intensely. The pyrolysis is a process, where the thermal degradation of organic substances takes place with absence of oxygen. During the biomass pyrolysis, the products of char, tar, gases (such as: carbon monoxide, carbon dioxide and nitrogen) and volatile organic compounds are basically formed, which are released in different proportions. The tar composes of various species including heavy hydrocarbons, organic acids, aldehydes, alcohols and phenols. In subsequent reaction, the tar splits in char as well as in volatile components and gases. The char is the remaining solid that almost consists of pure carbon. The proportion of the major components is determined depending on biomass properties, oxidiser (nitrogen, air or steam), heating rate and residence time. (Mohan, Pittman and Steele 2006) have prepared an overview of various operating conditions during the pyrolysis process and consequently the proportions of obtained components.

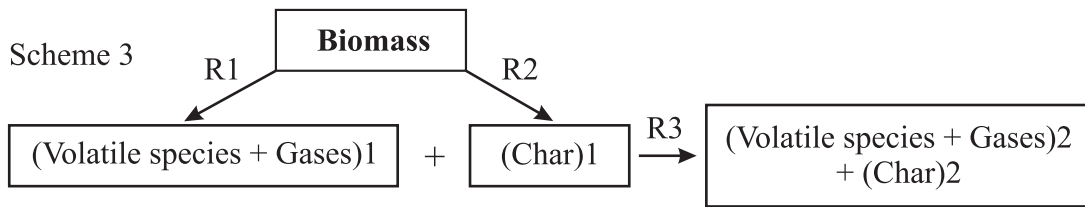
For the pyrolysis modelling of biomass, (Prakash and Karunanithi 2008) distinguish between three kinetic mechanisms. While the single-step global model (scheme 1) considers the pyrolysis as one reaction of first-order, the single-step multi-reaction mechanism (scheme 2) consists of a primary and a secondary reaction.



During the secondary kinetic mechanism for the tar-cracking (Scheme 3), the biomass decomposes into volatile compounds, gases and char. The primary pyrolysis products participate in secondary interactions (R3), resulting in different compositions of volatile substances, gases and char.

The first two categories of kinetic models (single-step global and single-step multi-reactions mechanism) are relative simple, since the ratio between the char and gases is assumed to be constant. On the other hand, the tar-cracking model has a superior flexibility

because it describes the degradation of the biomass in different ratios and offers the possibility of primary pyrolysis products to interact with each other. Therefore, this model is suitable for the pyrolysis of biomass with comparative large particles.



The modelling of biomass conversion requires as well detailed information about the char-oxidation process. During combustion, the fed oxygen from the surrounding flow reacts with the carbon in char-particles in heterogeneous elementary reaction into CO and CO<sub>2</sub>. The steam gasification, the Boudouard-reaction and the hydrogenating gasification lead to an additional production of H<sub>2</sub>, CO and CH<sub>4</sub>. For the char-conversion, several kinetic approaches have already been developed and applied. A comprehensive model for the char-combustion of biomass in a circulating fluidized bed was presented among others by (Kaushal, Pröll and Hofbauer 2008). The model based on the particle-shrinkage theory and is assumed that the char-particle diameter decreases at constant density.

The gases and volatile compounds that are set free by the pyrolysis process react with each other and with the available oxidant. The generated heat by the exothermic reactions plays an important role for releasing further volatile components and the ignition of char-particles. (Fletcher et al. 2000, Wang and Yan 2008) and other authors, who have applied simplified homogeneous reactions in their models, have only considered the gaseous species CH<sub>4</sub>, H<sub>2</sub>, CO, H<sub>2</sub>O and CO<sub>2</sub>. Others as (Khan et al. 2007, Oevermann, Gerber and Behrendt 2009b) extended their homogeneous reaction mechanisms by additional species such as ethane, ethene and propane. Detailed reaction mechanisms for the gas phase, in which radicals or gas species such as sulphur oxides, hydrochloric acid etc. are also modeled, is not considered in the scope of this work.

The numerical simulation of energy systems has become an effective tool for the development of new technologies. The combination of increased computer performance and advanced numerical methods such as computational fluid dynamics (CFD) has led to realisable simulations for thermochemical conversion systems (for instance: fluidized beds, pulverised coal firings and combustion chambers). Compared to experimental data, the CFD results are capable of predicting qualitative and in many cases quantitative information. Accurate simulation results can be very useful in the design as well as in understanding the dynamic operation of reactors. The relevant applications of CFD models are mainly related to the coal power plants and boilers (among others: (Belosevic et al. 2006, Asotani et al. 2008)). Several numerical investigations of coal combustion have been modified to make them available for the combustion and co-firing of biomass. A list of commercial CFD programs is on hand, but the selection of a suitable program depends basically on the partial model for the biomass combustion. (Abbas, Awais and Lockwood 2003) developed a pyrolysis model for coal, coal blends and biomass, which was implemented into a 3D CFD simulation model and validated by using various fuel mixtures. (Backreedy et al. 2005) carried out a CFD study to analyse the coal and wood co-combustion regarding the burning behaviour of large biomass particles and the effects of wood particle shape on the burning characteristics. Further CFD works concerning the biomass co-firing were published among others by (Syred et al. 2007, Ghenai and Janajreh 2010, AlObaid et al. 2012a). For the biomass combustion, (Kær 2004, Kær, Rosendahl and Baxter 2006) have developed a model with the aid of a commercial CFD program to simulate a 33 MW<sub>th</sub> straw fired system. Other studies on the biomass combustion are carried out for example by (Ma et al. 2007, Collazo et al. 2012). On CFD applications for biomass gasification,

(Fletcher et al. 2000) improved a detailed 3D CFD model, which describes flow turbulence, heat transfer, mass transfer, pyrolysis, combustion of particles and gas phase reactions. Further contributions in reference to the biomass gasification are carried out by (Yuen et al. 2007, Gerun et al. 2008, Gómez-Barea and Leckner 2010). An overview on the recent and relevant CFD studies of thermochemical biomass conversion in the fluidised beds including biomass gasification, combustion and co-firing is prepared by (Wang and Yan 2008, Basu and Kaushal 2009).

However, the modelling of biomass is complicated due to the inhomogeneous composition of raw material as well as the complex thermochemical processes (Moghtaderi 2006). The biomass consists of hemicellulose, cellulose, lignin, inorganic ash and small amounts of other organic substances. The heterogeneous structure of biomass and its anisotropic physical properties have the consequence that different reaction rates and diverse reaction mechanisms take place during the pyrolysis process and the char-combustion. Furthermore, the heat and mass transfer rates are highly depended on the particle geometry (Blasi 1998). Relative big particles correspond to large temperature gradients and own longer fluid residence times. The particle shape has also certain effects on the pyrolysis process. Compared to the spherical particles, the ellipsoidal particles with the same volume need more time for completing the pyrolysis. While the released volatile components and gases outweigh for spherical particles during the pyrolysis process, the particles with an ellipsoid shape are dominated by the rest of pyrolysis products (Gera et al. 2002, Babu and Chaurasia 2004). In addition, the correct consideration of particle-particle/wall collisions has an influence on the flow, the gasification and combustion models and consequently qualitative on the accuracy of obtained results.

For a precise description of solid phase, the classical application of CFD to solve the conservation equations is not sufficient. Basically, there are two different approaches for the representation of gas-solid flow. In the Euler-Euler method, also known as two-fluid method, each phase is regarded as a continuum and is mathematically calculated by solving the balance equations. On the other hand, the Euler-Lagrange approach (single-particle method) combines the continuum descriptions of fluid phase with the Lagrange representation of dispersed phase on the basis of Newton's transport equations. This combined method for the modelling of granular flows provides detailed information regarding the behaviour of particle phase. The single particle-particle/wall collision in the Euler-Euler method is merely considered with the aid of additional model assumptions. In contrast, the collision detection between the particle-particle/wall in the Euler-Lagrange approach can be stochastically modeled or deterministically detected.

The stochastic collision detection models present today the most efficient method to handle the practical gas-solid flows numerically by means of the single-particle approach. In dense gas-solid flow, the stochastic collision models produce, however, unrealistic results such as solid volume fractions (porosity) greater than unity in the control volume (Götz 2006). Therefore, these models are mainly appropriated for the simulation of dilute gas-solid flows. For the discrete particle simulations with deterministic collision detections, two models are widely used, namely the hard sphere model and the soft sphere model. In the hard sphere model, single binary collisions are modeled as instantaneous processes, which restrict the application of this model to dilute systems. The properties of particles after the collision are related to the properties of particles before the collision through momentum and energy balances (Hoomans et al. 1996). In the so-called soft sphere model, also known as discrete element method (DEM), force, velocity and displacement are determined during the collision (Cundall and Strack 1979). The particles in the DEM model can overlap each other or penetrate into the wall. Depending on the penetration depth, a resulting contact force can be modeled using a spring-damper-slider system.

Since the Euler–Lagrange/DEM model has been successfully employed by (Tsuji, Tanaka and Ishida 1992, Tsuji, Kawaguchi and Tanaka 1993) to simulate the hydrodynamic behaviour of non-reactive dense gas–solid flow in a laboratory scale fluidized bed, significant advances have been accomplished in this field. From 1995, Kuipers and his team engage in the numerical simulations of cold flow fluidized bed using the discrete particle model, where relevant contributions were published by (Hoomans, Kuipers and Van Swaaij 2000, Link et al. 2005, Deen, Annaland and Kuipers 2006, Van Buijtenen et al. 2011, Sutkar, Deen and Kuipers 2012). (Chiesa et al. 2005) compared the numerical results of both Euler–Euler and Euler–Lagrange/DEM approaches with a 2D lab-scale bubbling fluidized bed. In contrast to the Euler–Euler model, the received results from DEM show much better agreement towards the experiments. However, the simulation based on DEM is computationally very expensive. (Götz 2006) introduced the parallel DEM simulation on multi–CPUs, in which the computational domain is divided into several decompositions and each sub–block is allocated one processor. (Alobaid and Epple 2013) extended the DEM model to describe the hydrodynamic behaviour of gas–solid flow in a non-reactive quasi–2D fluidized bed. Here, the particle–particle/wall collisions as well as the fluid–particle interactions are considered and the simulation is performed on multiple processors. A validation study has performed to assess the results obtained from the DEM model and a fluidized bed of Plexiglas®. The five second long comparison shows a good qualitative correlation regarding the particle distribution in the bed and an acceptable quantitative agreement regarding the pressure gradient on different positions of the bed. (Tsuji, Yabumoto and Tanaka 2008) have presented a 3D numerical study of a laboratory scale fluidized bed by means of DEM model. The particles trajectories are determined by solving Newton's equations of motion and the physical quantities of continuum phase are calculated with Navier–Stokes equations. Here, the simulation was parallelised on 16 processors and more than 4.5 million particles have been tracked. Due to the extreme computing time, few milliseconds are simulated and thus a complete fluidization state could not be achieved. On the other hand, (Alobaid et al. 2010a) have reached in a later DEM work the fluidization state of 1.5 million particles, wherein the calculation is performed on 21 processors.

Although the Euler–Lagrange/DEM model has been frequently applied to simulate the cold flow fluidized bed in different dimensions (2D and 3D), the consideration of thermochemical reaction mechanism is still in the early stages. However, the challenges for the energy systems simulations as actual state of research are to combine the gas flow and the homogenous reactions with the particles motions and the heterogeneous reactions. (Zhou, Flamant and Gauthier 2004b) have published one of the first works in this filed. In their study, a DEM code was extended by a coal combustion model to study the behaviour of reactive gas–solid flow in a 2D bubbling fluidized bed. The effects of bed temperature and inlet gas velocity on the flow structure of gas–solid system and its properties were investigated. (Simsek et al. 2009) included a DEM model in a commercial CFD–code “ANSYS–CFX” for the numerical simulation of waste with a grate firing system. The numerical results indicate a satisfactory correlation with the measurements even though the model had a few restrictions such as the assumption of spherical particles as well as the constant temperature distribution inside the particles. Recently, (Oevermann, Gerber and Behrendt 2009a) combined the DEM model with a chemical reaction mechanism to simulate the gasification process of wood in a 2D fluidized bed. (Alobaid, Ströhle and Epple 2010b) presented at a workshop in Leipzig the procedure for the 3D numerical simulation of reactive fluidized bed for the combustion of biomass with the aid of the Euler–Lagrange/DEM model. According to the author's knowledge, to the title “3D Modelling and Simulation of Reactive Fluidized beds for Conversion of Biomass with Discrete Element Method” neither new studies nor the extension of previous works were found in the DEM literature. At this point, the proposed Ph.D. thesis starts.

The coupling of the Euler–Lagrange/DEM model with the thermochemical reaction mechanism enables the modelling and simulation of reactive dense gas–solid flow. The modelling of multiple energy systems can be covered by this concept for example the reactive fluidized bed, the ash deposition on boiler walls, the gasification or combustion of solid fuel as well as the CO<sub>2</sub> capture in the thermal power plants by chemical or carbonate looping process. The simulation of cyclone for particle separation and the milling process as found in coal pulveriser, in which thermal gradients existent, could be realized in the course of time.

All in all, the Euler–Lagrange/DEM model in combination with the reaction and heat transfer models could become a standard tool to design the fluidized bed for the biomass conversion. Nevertheless, significant research efforts are required for making DEM as competitive as the present stand of CFD. Here, the presented Ph.D. thesis contributes to the field of basic DEM research.

## 1.2 Research objectives

The aim of this study is to develop a 3D program for the numerical simulation of biomass conversion in the fluidized bed. To achieve this, both dense gas–solid flow and thermochemical reaction model must be modeled with high accuracy. The work deals essentially with the following points:

First, the program should calculate the trajectories of particles and the gas flow in the fluidized bed. The particle–particle/wall and gas–solid interactions should be considered by tracking all individual particles. For this purpose, the discrete element method is applied and further developed. Main attention is given to the determination of interaction values such as volumetric void fraction, momentum and energy transfers, the collision detection using the particle search grid method and the introduction of particle grid method. Furthermore, the efficiency and accuracy of the Euler–Lagrange/DEM model are investigated in detail. Parameter studies, in which the stiffness coefficient, the fluid time step and the processor number are varied for different particle numbers and diameters, are carried out. The enhanced Euler–Lagrange/DEM model will be validated towards the experiments delivered from a cold fluidized bed test rig. The obtained results are also compared with the Euler–Euler and stochastic Euler–Lagrange models.

Second, the biomass conversion in the fluidized bed involves chemical and physical processes that should be accurately modeled. This includes kinetic models for drying, pyrolysis, char–oxidation and gas phase reactions as well as the associated heat and mass transfer processes. In combination with the simulation of the gas–solid flow, it is possible to calculate the local concentrations of solid and gaseous substances, the local gas and particle temperatures, the local heat release and the heat transfer rates. In this context, the coupling of CFD, DEM and the chemical reaction mechanism is achieved.

Finally, the improved code should be able to simulate the biomass as well as other solid fuels conversion in a 3D fluidized bed with acceptable computing time. Therefore, efficient and modern programming techniques and numerical approaches such as the parallelisation, the multi-grid, the particle search grid and the offset method etc. are investigated in this PhD thesis.

## 1.3 Computational code

As a basis for the modelling served the DEM code that was developed by Götz and his predecessors (Götz 2006). At present, the DEM program “DEMEST”, which combines the classical computational fluid dynamics to calculate the fluid phase in the Eulerian coordinates with the discrete particle method to describe the solid phase in the Lagrange coordinate, has been further extended by (Alobaid, Ströhle and Epple 2011, Alobaid and Epple 2013, Alobaid,

Ströhle and Epple 2013b). The DEMEST code bases on the operating system Windows® for 32 or 64-bit architectures and as an integrated development environment serves the Microsoft Visual C++®. The parallel simulation can be performed by special computer clusters as well as by commercial computers with multi-core processors. With the aid of a 10-gigabit network, the workstation clusters are distributed and communicated with one another via the TCP/IP protocol. The data exchange between the processors is settled through the message passing interface (MPI). The visualisation of calculated results is achieved by separate codes that are programmed by means of MATLAB® functions and libraries. Since the DEMEST code is based on widespread hardware and software components, the executable program can be utilized by other universities or research institutions. Currently, the program has the following features:

- Euler–Lagrange/DEM model (4-way coupling) and thermochemical reaction mechanism
- Mono and polydisperse spherical particles
- Fine fluid grid in combination with multi-grid method for fluid phase calculation
- Particle grid for solid phase calculation
- Particle search grid (advanced algorithms for collision detection)
- Offset method for calculation of volumetric void fraction, momentum and heat transfers
- Tool and software (Microsoft Visual C++®, MPICH2 and MATLAB®)

Besides the DEMEST program, the commercial CFD package ANSYS–FLUENT®, based on the Euler–Euler formulation, and the commercial program CFD–BARRACUDA®, based on the stochastic Euler–Lagrange formulation, are employed to model the complex hydrodynamic behaviour of the gas–solid flow in a cold fluidized bed.

#### 1.4 Thesis outline

The presented thesis “3D Modelling and Simulation of Reactive Fluidized Beds for Conversion of Biomass with Discrete Element Method” is structured as follows:

- Chapter 2 provides the basic information of biomass conversion in the fluidized bed. Here, a short description of biomass and its characteristic as well as the fluidized bed classification is introduced.
- Chapter 3 presents the numerical simulation methods for the gas–solid flow including the quasi-single-phase model, the Euler–Euler approach and the single-particle method. The advantages and disadvantages of these models are discussed in detail.
- Chapter 4 will concentrate on the deterministic and stochastic collision detection models.
- Chapter 5 explains the discrete element method and the acting forces on particles. The determination of aerodynamic forces, contact force as well as the adhesive forces is discussed. Furthermore, the moments of force acting on particles are explained.
- Chapter 6 deals with the numerical methods used to calculate the fluid phase in a gas–solid flow.
- Chapter 7 describes the gas–solid flow interaction as well as the determination of the particle time step.
- Chapter 8 presents the cold and warm fluidized bed simulations as well as the comparisons with measurements.
- The last chapter provides the conclusion from the preceding chapters and prospects future investigations.

## 2 Biomass conversion in fluidized bed

The growth of world population and the steady developing of newly industrialised countries urge the international community to adopt environmentally conscious behaviour. In this context, the reduction of the carbon dioxide emissions is in the focus of politics and societies, since CO<sub>2</sub> is regarded as the main cause of impending climate change. To achieve this aim, the share of renewable energies in the electricity and heat supply besides the conventional energy resources should be increased. This specifically means not only for energy industries, but also for households, to reduce the pollutant emissions by more use of renewable energy sources. The conversion of biomass in fluidized bed in addition to the expansion of wind and solar farms and the increasing number of geothermal plants can meet the mandatory target.

### 2.1 Biomass

Biomass is a mixture of organic molecules including hydrogen, oxygen, nitrogen and small amount of other inorganic compounds such as alkaline, alkali and heavy metals. Under the term biomass for energy, one can understand all energy sources from phyto and zoo masses. This includes a wide range of materials such as wood, agriculture activities, by-products of plant and animal origin, food and industrial wastes. The main difference between the biomass and the fossil fuels is that the biomass absorbs carbon dioxide from atmosphere during the growing, but it returns CO<sub>2</sub> back while burning. As opposite to fossil fuels combustion, this maintains a carbon cycle without increasing the concentration of carbon dioxide in the atmosphere. The latent heat and density of biomass is lower compared with coal. The biomass is also characterised with high moisture and volatile content. The carbonisation of biomass, also known as torrefaction process, increases the energy density. Here, the released water and low calorific volatile components reduce the mass by approximately 30%, while the heating value of torrefied biomass decreases by about 10%. Compared to raw biomass, the torrefied biomass shows much better grindability and has a high energy density similar to coal (Alobaïd et al. 2012a).

The biomass can be converted into a mixture of gases (synthesis gas), liquid (bio-oil) and/or solid (char). The overall amount of these components depends on the conversion mechanism used. Here, it can be distinguished between thermochemical, physico-chemical and bio-chemical processes. The pyrolysis, also known as devolatilisation, is the first step in thermochemical conversion. When the biomass is devolatilised, its structure is altered, resulting in formation of gaseous substances, tar and char. The thermochemical conversion can end either with complete oxidation, where the gaseous substances are burned or without oxidation with unburned gaseous substances. The physico-chemical processes involve changes in the physical properties and the chemical structure of biomass, e.g. the energy supply based on vegetable oil. In the bio-chemical process, the conversion of biomass into a secondary energy carrier is performed with the aid of biological processes.

The thermochemical process of biomass by combustion or gasification using fluidized bed systems represents the most effective technology to convert the biomass into useful energy. The released energy can be applied to different processes such as the integrated gasification combined cycle and steam cycle.

## 2.2 Fluidization

Depending on the volumetric loading of the dispersed phase in the gas–solid flow, it can be distinguished between dilute flows ( $d_p \ll r$ ) and dense flows ( $d_p \gg r$ ). Here,  $d_p$  is the characteristic length of a particle, e.g. diameter and  $r$  represents the inter–particle distance. Dense gas–solid flow with solid volume fraction greater than 10% is important in many facilities such as fluidized beds. A fluidized bed is a bulk of solid particles, through which gas flows. The emerging forces from gas to particles cause a fluidization condition and offer an effective way for gas–solid interaction.

The fluidized bed is characterised by several advantages. 1) The continuous operation with the possibility of solid transport in and out of system. 2) High heat and mass transfer rates from gas to solid, resulting in uniform temperature gradients in the bed even with highly exothermic or endothermic reaction rates. 3) Very low NO<sub>x</sub> and SO<sub>2</sub> emissions in addition to simple CO<sub>2</sub> capture. 4) The possible operation over a wide range of geometrical and mechanical properties of particles. 5) High solid mixing rate for polydisperse particles. 6) Simple construction and the suitability for large–scale operation. 7) The possibility of using different solid fuels such as coal, biomass or a mixture of both fuels. 8) The continuous ability of adding or withdrawing of catalysts. As a result of their competitive advantages, the fluidized beds can be found in various industrial applications such as the mineral processes, the coating processes, the CO<sub>2</sub> capture in the thermal power plants by chemical or carbonate looping process as well as the solid fuels conversion including gasification and combustion.

Different variables can influence the fluidization behaviour such as fluidization volume flow rate, particle size, static bed height and vessel geometry. The fluidization volume flow rate is an extensive variable due to the fact that it depends on the vessel cross–section area. By dividing the volume fluidization flow rate by the cross–section area of vessel, the fluidization volume flow rate per unit of cross–section area of vessel is obtained, which is also known as superficial fluidization velocity (intensive variable):

$$\left| \overset{\rightarrow}{u}_f^{sup} \right| = \frac{\dot{V}_f}{A_{ves}}. \quad (2.1)$$

In a fluidized bed with defined particle size, static bed height and vessel geometry, the fluidization regimes depend on the superficial fluidization velocity (see **Figure 2.1**) as:

**Fixed bed:** At lower superficial fluidization velocities below the minimum fluidization velocity  $\overset{\rightarrow}{u}_f^{min}$ , the particles remain stationary packed since the gas flows through the interstitial space of particles. In this case, the bed behaves like a porous medium.

**Particulate fluidization:** If the superficial fluidization velocity increases, the force exerted by fluid on particles increases accordingly. At the point, where the gas velocity is between the minimum fluidization velocity and the minimum bubbling velocity, the drag force compensates the bed weight. In the particulate fluidization, the inter–particle distances between the particles become bigger and thus the bed expands, but bubbles are not formed. Here, the suspended particles in the gas characterize the bed behaviour.

**Bubbling fluidization:** If the superficial fluidization velocity exceeds the minimum bubbling velocity  $\overset{\rightarrow}{u}_f^{bub}$ , the bed becomes inhomogeneous and bubbles can be clearly distinguished. In this regime, the coalescence and breakup of bubbles may occur.

**Slugging bed:** A further increase in the superficial fluidization velocity enhances the rate of bubbles coalescence. As a result, cavities as large as the cross–sectional area of vessel

can be formed. The slugging flow regime takes place, when the vessel diameter is small and/or the ratio of the vessel height to the vessel diameter is large.

**Turbulent fluidization:** If the superficial fluidization velocity exceeds the solid terminal velocity, the particles start moving faster and form streamers and clusters. The solid terminal velocity is the velocity that the particle reaches in free fall due to gravity. Compared to the slugging bed, the rate of bubbles breakup is enhanced, reducing the presence of large bubbles. Here, the overall structure of the bed transforms to be more homogeneous.

**Spouting bed:** The gas flows through a small jet nozzle at higher superficial fluidization velocities. The particles used in this system are generally of group D (see **Figure 2.2**). Here, the gas penetrates the entire bed, dividing the bed into two regions, namely dilute flow region and the annular flow region. In the dilute flow region, the particles move upward, while in the annular flow region the particles move downward to the core region.

**Pneumatic transport:** At higher superficial fluidization velocity, the particles are completely entrained. The entire bed becomes as lean gas–solid suspension.

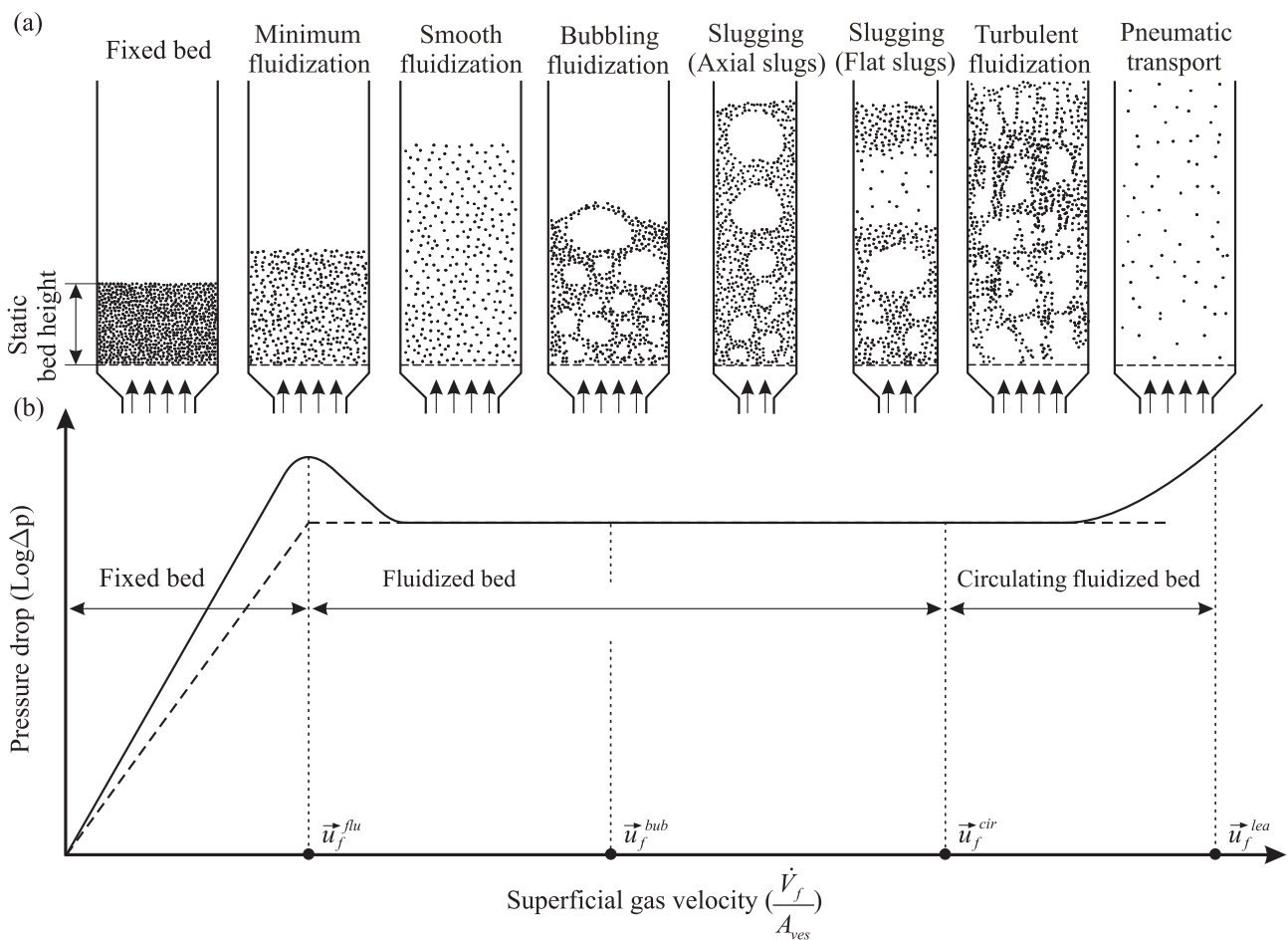


**Figure 2.1:** Fluidization: (a) schematic representation of different flow regimes for gas–solid flow and (b) pressure drop versus superficial fluidization velocity (solid line: a real bed; dashed line: an ideal bed) (Kunii and Levenspiel 1991)

Besides the superficial fluidization velocity, boundary and operating conditions, the fluidization behaviour of the gas–solid flow depends also on the mechanical and physical properties of particles. (Geldart 1973) classified the particles into four groups based on their fluidization behaviour. Geldart identified the particles in terms of mean particle diameter and the difference between solid and fluid densities (see **Figure 2.2**). The map was obtained

empirically for air at ambient temperature and has been widely used in the research of the gas–solid flow.

**Group C:** The particles are cohesive and have very small diameter ( $d_p \leq 20 \mu\text{m}$ ). In fluidization for particles of group C, the short-range forces between the particles that result from interactions between particles (contact, van der Waals, electrostatic and capillary forces) dominate the aerodynamic forces. The particles tend to stick together and thus are difficult to fluidize. In case of fluidization, the bed expansion for particles of group C can be very high.

**Group A:** The particles are aeratable and have a typical diameter between ( $30 \leq d_p \leq 100 \mu\text{m}$ ). In fluidization of particles in group A, the aerodynamic surface forces that result from the interactions between fluid and solid (drag, Basset, pressure, Saffman and Magnus forces) affect the fluidization behaviour more than the short-range forces. However, the short-range contact force may also play a significant role in dense systems. The minimum fluidization velocity is smaller than the minimum bubbling velocity. The bed expands homogeneously at fluid velocities between both minimum fluidization and bubbling velocities. In case of bubbling fluidization, a maximum stable bubble size can be reached.

**Group B:** The particles have a typical size range of ( $30 \leq d_p \leq 1000 \mu\text{m}$ ). The minimum fluidization velocity and the minimum bubbling velocity have the same value. The bubble size increases with the bed height, but no maximum stable bubble size can be reached. In case of fluidization, the bed expansion for particles of group B is moderate.

**Group D:** The particles are coarse ( $d_p > 1 \text{ mm}$ ) and spoutable. In case of fluidization, the bed expansion is low. Compared to groups A, B and C, the mixing process for particles of group D is not effective.

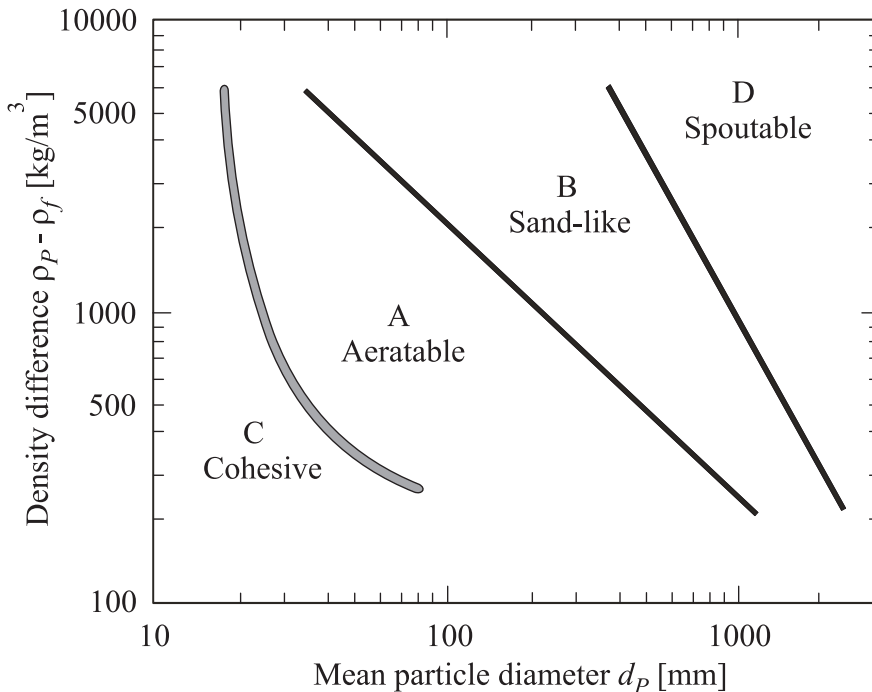


Figure 2.2: Particle classifications after (Geldart 1973)

To evaluate the bed behaviour during the fluidization quantitatively, there are a lot of identification numbers available such as absolute bed height, bed expansion ratio, bed fluctuation ratio and fluidization index. These identification numbers can be applied to any superficial fluidization velocity and thus they are suitable for all fluidization regimes.

The absolute bed height can directly be defined by measuring the highest point in the bed, while the bed expands. The bed expansion ratio  $ER$  is determined as the ratio of average expanded bed height to the initial static bed height:

$$ER = \frac{h_{bed}^{hyd}}{h_{bed}^{sta}}. \quad (2.2)$$

The bed fluctuation ratio  $FR$  is calculated as the ratio of maximum expanded bed height to minimum bed height within the bed fluctuates:

$$FR = \frac{h_{bed}^{max}}{h_{bed}^{min}}. \quad (2.3)$$

The fluidization index is a measure of the fluidization uniformity and can be determined as the ratio of bed pressure drop to bed material weight per unit area of cross-section of vessel:

$$FI = \frac{\Delta p_{bed}}{\left( \frac{W_{bed}}{A_{ves}} \right)}. \quad (2.4)$$

Here, it should be mentioned that the identification numbers depend on the superficial fluidization velocity, the particle size and shape, the static bed height and the density ratio between both phases.

For bubbling and slugging regimes, the equivalent bubble diameter can also be evaluated as an additional quantitative measurement of fluidization behaviour. Here, two approaches can be used to assess the equivalent bubble diameter  $d_{bub}^{equ}$  (Kuijpers, Prins and Van Swaaij 1991). In the first procedure, the equivalent bubble diameter is calculated based on the assumption that the bubble has an elliptical shape. The resulted equivalent bubble diameter is then defined as:

$$d_{bub}^{equ} = \sqrt{d_{bub}^{ver} d_{bub}^{hor}}, \quad (2.5)$$

where  $d_{bub}^{ver}$  and  $d_{bub}^{hor}$  represent the vertical and horizontal bubble diameters, respectively. In the second procedure, the equivalent bubble diameter is calculated from the measured bubble area as:

$$d_{bub}^{equ} = \sqrt{\frac{4}{\pi} A_{bub}}. \quad (2.6)$$

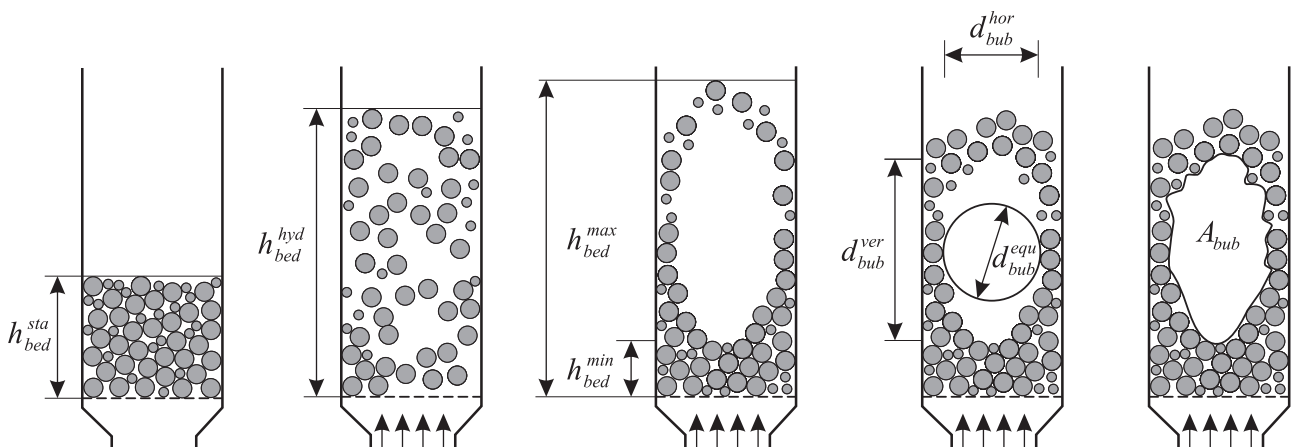


**Figure 2.3:** Evaluation the bed behaviour during fluidization

Using the previous identification numbers as well as the equivalent bubble diameter, the simulated bed behaviour can quantitatively be compared with measurements. Besides these parameters, the visual observation of solid distribution in the bed is used to evaluate quantitatively the bed behaviour during the fluidization.

### 2.3 Conclusion

Due to the continuous growth of population and industrial activities, the worldwide electricity and heat consumptions have been increased. In order to avoid a further jump in carbon dioxide emissions, the use of renewable energies for the electricity and heat supply besides the conventional energy resources is assigned duty. The biomass consists mainly of carbon, hydrogen, oxygen and nitrogen and provides a clean energy source. Compared to coal, the biomass contains higher moisture and volatile contents, while it has lower density and latent heat. The thermochemical conversion of biomass in a fluidized bed is an advanced technology, where the obtained energy can be used in different processes.

A fluidized bed is a vertical vessel, in which the particles are located and the gas streams form the bottom via a porous plate or nozzles. The fluidized bed is characterised with several advantages such as the high heat and mass transfer rates as well as the low  $\text{NO}_x$  and  $\text{SO}_2$  emissions. Depending on the superficial fluidization velocity, it can basically be distinguished between fixed bed, stationary fluidized bed and circulation fluidized bed. In the fixed bed, the particles remain motionless due to the fact that the superficial fluidization velocity is smaller than the minimum fluidization velocity. When the superficial fluidization velocity becomes bigger than the minimum fluidization velocity, the bed enters a fluidization state and the flow regime is called the bubbling flow. Here, the drag force overcomes the effective weight of particles. If the superficial fluidization velocity exceeds the solid terminal velocity, the particles start moving faster, resulting in circulation fluidized bed. The fluidization behaviour can also be influenced by the mechanical and physical properties of particles. Based on their fluidization behaviour, (Geldart 1973) classified the particles into four groups, viz. group C, group A, group B and group D.

Besides the visual observation of solid distribution, the bed behaviour during the fluidization can be quantitatively assessed using various identification numbers such as the absolute bed height, the bed expansion ratio, the bed fluctuation ratio and the fluidization index. The absolute bed height is determined by measuring the highest point in the bed during its expansion. The bed expansion ratio is defined as the ratio of actual bed height to the initial static bed height. The ratio of maximum bed height to minimum bed height, in which the bed fluctuates, is known as the bed fluctuation ratio. The fluidization index is calculated as the ratio of bed pressure drop to bed material weight per unit area of cross-section of fluidized bed geometry. For bubbling and spouting beds, the equivalent bubble diameter can also be used to evaluate the fluidization behaviour.

This study engages in developing a numerical simulation program for the thermochemical conversion of biomass in a fluidized bed. The work is basically divided in two parts. In the first phase of this PhD thesis, the developed Euler–Lagrange/DEM model should simulate the cold behaviour of the gas–solid flow in a fluidized bed. In the second phase, the biomass conversion in a fluidized bed should be modeled. For the cold fluidized bed simulations, the spouted flow regime with particles of group D is selected, while for the warm fluidized bed simulations the bubbling flow regime with particles of group B is considered. The validation of the developed Euler–Lagrange/DEM model is carried out with the aid of visual observation of solid distribution, the absolute bed height and the equivalent bubble diameter.

### 3 Description of gas–solid flow

Different numerical models at diverse levels of accuracy have been applied to simulate the hydrodynamic behaviour of dense gas–solid flow. While the solid phase can be generally calculated by two different levels of detail: a quasi–continuum or discrete phase, the fluid phase is presented in each case as a continuum. In **Figure 3.1**, the numerical methods for gas–solid flow computation and their variants are depicted.

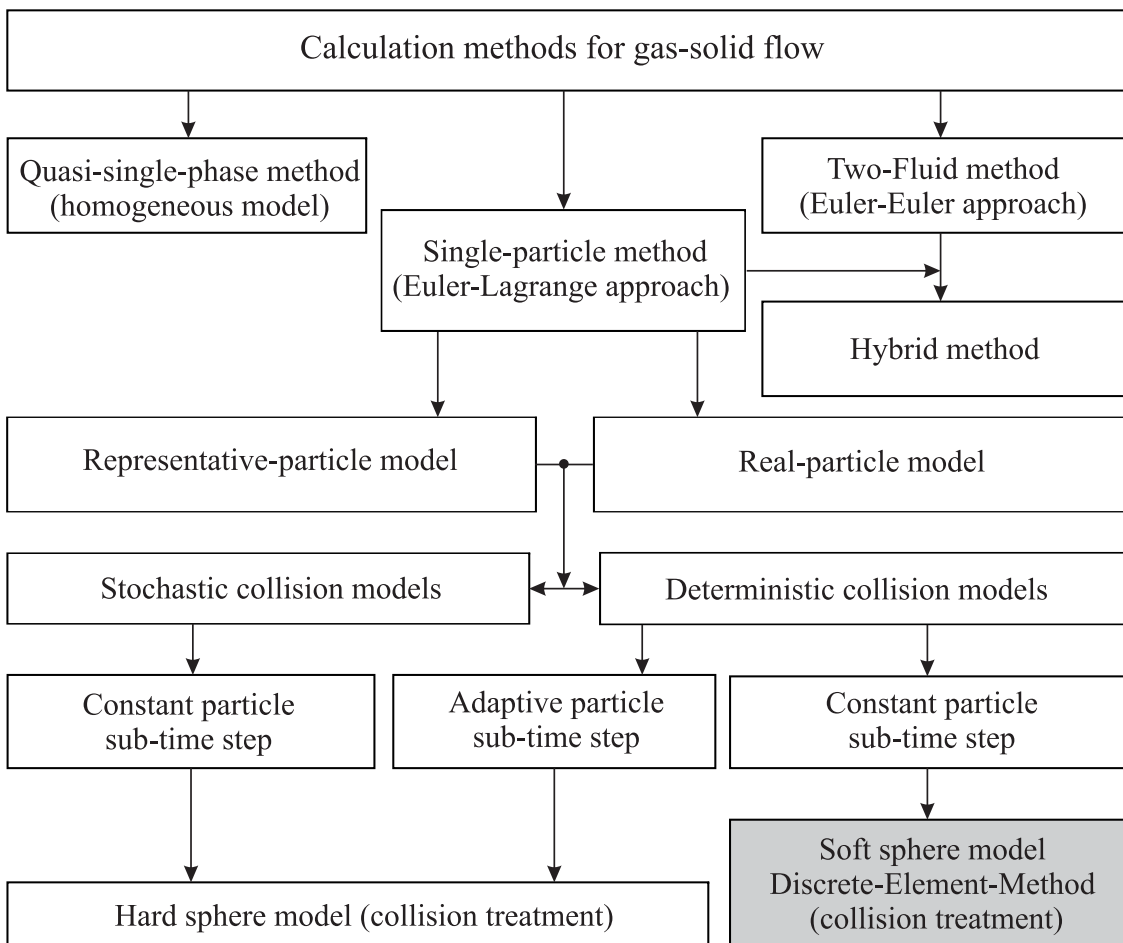


**Figure 3.1:** Computation methods for gas–solid flow (Epple et al. 2012), extended

#### 3.1 Numerical methods

The simplest approach for the computation of a gas–solid flow is feasible with the assumption of homogeneity. Hence, the physical values of dispersed and fluid phase can be described as volume average values by solving the balance equations for the single–phase flow. A particulate flow can be regarded as homogeneous if the volume distribution of particles in the fluid phase is uniform and the velocity differences between the two phases are negligible small. In many practical flows, these requirements are not fulfilled, so that the homogeneous model cannot be used. An alternative method is the Euler–Euler approach that distinguishes itself from the homogeneous model with higher accuracy and a wide range of applications. In

principle, the gas phase in the fluid–solid flow is modeled with the balance equations of single–phase. For the disperse phase, the conservation equations for momentum, mass and energy are solved, too. The impact of solid phase on the fluid phase is considered by additional terms in the fluid balance equations. A bridge between the Euler–Euler approach on the one hand and the discrete modelling of each individual particle on the other hand is the representative particle model that offers an efficient and accurate compromise. This model assumes that one representative particle owns the same characteristic of a few real particles. In the third group of models, each particle of the solid phase is followed employing the Newtonian equations of motions, while the gas phase is described in the Eulerian framework.

In the following sections, the quasi–single–phase, the two–fluid and single–particle, the representative particle as well as the hybrid method will be briefly explained.

### 3.1.1 Quasi-single-phase method

The quasi–single–phase model assumes that the gas–solid flow is homogeneous and no difference in velocities between both phases. Under these conditions, the gas–solid flow can be treated as a quasi–single–phase flow. The conservation equations for momentum, mass and energy of single–phase flow is applied to model the mixture physical values. The density in the balance equations should be replaced by the average density of two–phase mixture:

$$\bar{\rho} = \frac{\rho_s}{1 + \varepsilon_f \left( \frac{\rho_s}{\rho_f} - 1 \right)}, \quad (3.1)$$

where  $\varepsilon_f$  is the fluid volumetric void fraction (porosity) that describes the ratio of fluid volume to entire control volume. Although the quasi–single–phase method shows relevant distinguishing advantages such as relative simple programming effort, high computing stability and low computing cost, the obtained results are associated with high inaccuracy. Furthermore, the configurations of practical gas–solid systems do not fulfil the method criterions in most cases. The quasi–single–phase model is, therefore, not employed anymore for the simulation of the gas–solid flow by the reason of the mentioned limitations.

### 3.1.2 Two-fluid method

In the two–fluid method, also known as Euler–Euler approach or multiphase–Euler method, the fluid and solid phases are modeled with the balance equations of the single–phase flow, where the solid phase is considered as a second heavy gas phase. Here, the continuity, the Navier–Stokes and the energy equations of both phases should be extended through major modifications. The modified equations contain transport values of dispersed phase such as granular viscosity, granular pressure and granular stress. The modelling of these values is based on the concept of kinetic theory of granular fluids (KTGF) that allows for a given solid to own all physical gas properties. The KTGF theory is described in detail by (Gidaspow 1994), which is related to the kinetic theory of dense gases (KTDG) (Chapman and Cowling 1970).

The basic idea behind the KTGF is: the particles are in continuous and chaotic motion due to the interaction within the fluid phase for dilute system and with particles/walls or both for dense flows. Similar to gas, a temperature, so–called the granular temperature, is defined that is a measure of particles velocities fluctuations. The granular viscosity, the granular pressure and the granular stress are a function of granular temperature that varies in time and position within the entire computational domain. For the calculation of the granular temperature, an additional balance equation similar to the energy equation of the fluid phase has to be solved.

The valid application of the two–fluid method to the gas–solid flow is associated with the satisfaction of continuum hypothesis, i.e. the number of particles and fluid molecules in each control volume is sufficiently large. If this criterion fulfils, the physical variables of each phase (gas or solid) can then be assessed in every control volume as statistical average values. With the aid of Knudsen number  $Kn$ , which is defined as the ratio of mean free path  $\bar{l}$  to characteristic length  $l_{char}$ , the continuum hypothesis is checked for its validity:

$$Kn = \frac{\bar{l}}{l_{char}}. \quad (3.2)$$

The mean free path represents the average distance that can cover by a moving particle or gas molecular till the next collision with other object occurs, leading to modify the physical properties of particles such as position, velocity and temperature. The characteristic length is a function of grid cell volume:

$$l_{char} = (V^{CV})^{\frac{1}{3}}. \quad (3.3)$$

According to the definition of Knudsen number, the Knudsen domain ( $0 < Kn < \infty$ ) is often divided into four regimes, namely continuum flow, slip flow, transient flow and free molecular flow (see Figure 3.2).

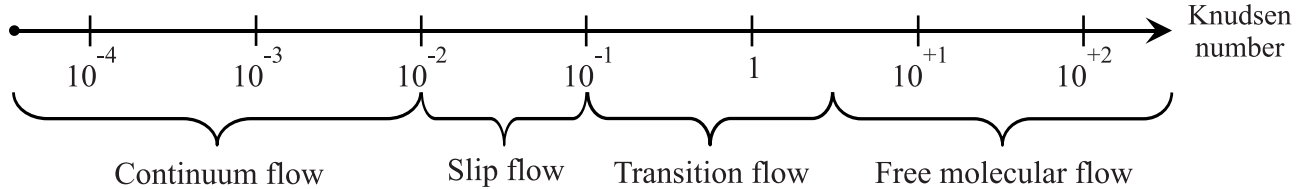


**Figure 3.2:** Gas–solid flow regimes as a function of Knudsen number

Flows with smaller Knudsen numbers  $kn \leq 10^{-2}$  is considered to be continuum, while flows with higher Knudsen numbers  $kn \geq 3$  is seen as free molecular flows. For slip and transient regimes ( $0.01 < kn < 3$ ), the gas–solid flow can be characterised as continuum as well as free molecular flows.

It is clear that flows with high solid content have smaller average free paths and thus result in Knudsen numbers less than 0.01. As a consequence of this, the two–fluid method is suitable for the simulation of dense gas–solid flow. However, the solid distribution in the fluid phase shows for example in stationary and circulating fluidized beds high measure of inhomogeneity. For strands and gas bubbles, in which the solid mass fraction is very low or the solid does not exist, the continuum assumption by inadequate spatial resolution is not fulfilled. Reducing the grid resolution in order to meet the continuum hypothesis leads on the one hand to inaccurate resolution of local inhomogeneities and on the other hand to imprecise numerical resolving of both phases. Other restriction of the two–fluid method application to the simulation of dense gas–solid flow is related to the kinetic theory of granular fluids. The KTGF can only consider a certain range of solid velocity fluctuations as a function of granular temperature. (Götz 2006) and (Kanther 2003) investigated the Maxwell–Boltzmann distribution of particles velocities in order to draw conclusions about the suitability of the two–fluid method for the dense fluid–solid flow simulation (e.g. fluidized bed). Employing a coupled CFD/DEM program, Götz carried out a fluidized bed simulation, in which the distribution of particles velocities can be determined numerically. The resulted distributions show in large areas high deviations from Maxwell–Boltzmann distribution. The maximum deviations are noticed at the interface between gas bubbles and fluidized dispersed particles. In these boundary layers might be raised bimodal distribution functions that are not summarised

under the KTGF theory. How the impact of these distribution functions on the quality of numerical simulations is still not clear and further examinations are required.

### 3.1.3 Single-particle method

The single-particle method provides in contrast to the two-fluid method a growing alternative approach for the numerical representation of the gas–solid flow, particularly with increasing the solid loading. Here, the solid phase is considered as dispersed phase, i.e. for each particle a set of transport equations is solved.

By means of so-called splitting-technique, which was proposed by (Bird 1976), the simulation of particles can be divided in two sequential steps. In the first step (the free flight phase), the simultaneous calculation of particle position and angular displacement changes for a particle-time step is taken place, which it is usually based on the explicit Euler method:

$$\vec{x}_P(t + \Delta t_P) = \vec{x}_P(t) + \int_t^{t + \Delta t_P} \vec{u}_P(t) dt, \quad (3.4)$$

$$\vec{\varphi}_P(t + \Delta t_P) = \vec{\varphi}_P(t) + \int_t^{t + \Delta t_P} \vec{w}_P(t) dt. \quad (3.5)$$

The changes of particle translational velocity  $\vec{u}_P$  and angular velocity  $\vec{w}_P$  for a particle time step  $\Delta t_P$  are calculated with the aid of forces  $\sum_k \vec{F}_{P,k}(t)$  and moments of force  $\sum_k \vec{M}_{P,k}(t)$ :

$$\vec{u}_P(t + \Delta t_P) = \vec{u}_P(t) + \int_t^{t + \Delta t_P} \vec{b}_P(t) dt, \quad (3.6)$$

$$\vec{w}_P(t + \Delta t_P) = \vec{w}_P(t) + \int_t^{t + \Delta t_P} \vec{a}_P(t) dt, \quad (3.7)$$

with the translation and angular accelerations  $\vec{b}_P$  and  $\vec{a}_P$ :

$$\vec{b}_P(t) = \frac{1}{m_p} \sum_k \vec{F}_{P,k}(t), \quad (3.8)$$

$$\vec{a}_P(t) = \frac{1}{I_p} \sum_k \vec{M}_{P,k}(t). \quad (3.9)$$

The symbol  $k$  represents the number of acting forces or moments of force on the investigated particle. The values  $m_p$  and  $I_p$  denote the particle mass and the moment of inertia, respectively.

In the second step of splitting-technique, the unconsidered contact forces in the first step (free flight phase) can now be calculated. The contact forces result from the particle-particle/wall collisions. The collision process is divided into collision detection and collision treatment, where the collision detection plays a special role for the efficiency of the entire algorithm. Generally, the collision detection between particle-particle/wall can be stochastically modeled or deterministically detected. In view of their high efficiency, the stochastic collision models are to date the only possibility to examine numerically the practise relevant gas–solid flow in large-scale facilities. Although the deterministic collision models

show much better agreement with the experimental data compared to the stochastic collision models, they stand today due to the challenges of computational effort helpless to simulate industrial systems. In principle, the treatment of real facilities is possible. It raises, however, the question when the required high-performance computers are available.

For the discrete particle simulations with collision detection models, two approaches are widely used: the hard sphere model and the soft sphere model. In the first model, single binary collisions are considered as instantaneous processes (Hoomans et al. 1996). The properties of particles after the collision are related to the properties of particles before the collision through momentum and energy balances. In the so-called soft sphere model, also known as discrete element method (DEM), the particles can overlap each other or penetrate into the wall (Cundall and Strack 1979). Depending on the penetration depth, a contact force is determined, resulting in changing the motions of particles.

While the collision treatment in the stochastic method is only carried out with the hard sphere model, the collision in the deterministic collision models can be treated with both hard and soft sphere models. Which model is more appropriate to describe particle–particle/wall collisions, it depends on the average particle velocity and the solid loading in the gas–solid flow. At low particles velocities, as for example in bubbling or circulating fluidized beds, the hard sphere model causes significant difficulties in considering multiple simultaneous collisions of a particle with other collision partners. As opposed to the hard sphere model, the soft sphere model has the disadvantage that at high particle velocities relatively small particle time steps should be applied and thus the computational time further increases. Flows with high solid content require an accurate description of multiple simultaneous particle–particle/wall collisions and therefore the soft sphere model is preferred. The hard sphere model, by contrast, is more suitable for dilute gas–solid flows, where the simultaneous collisions occur rarely.

In the literature, the distinction between dense and dilute gas–solid flows may follow different criteria. A distinguishing feature can be the mass flow ratio of solid to fluid, where flows with values greater than 15 (Marcus et al. 1990), 20 (Leva 1959) or 80 (Kunii and Levenspiel 1991) are regarded as dense. Another criterion is the volumetric void fraction, which describes the ratio of fluid volume to entire control volume. In this context, dense fluid–solid flows have fluid volumetric void fraction values less than 0.9 (Epple et al. 2012). (Crowe 1982) classified whether the fluid–solid flow is dense or dilute by the influence of particle–particle/wall collisions on the particle trajectories. Similar to Knudsen number, the Stokes number  $Stk$  is introduced, which is a measure of particles abilities to follow the surrounding flow streamlines. It is formed from the ratio of particle relaxation time  $t_{relax}$  to characteristic time of fluid flow  $t_{char}$ :

$$Stk = \frac{t_{relax}}{t_{char}}. \quad (3.10)$$

The relaxation time is defined as:

$$t_{relax} = \frac{l_{stop}}{\left| \vec{u}_P \right|}. \quad (3.11)$$

The stopping distance  $l_{stop}$  is obtained when a particle with initial velocity  $\left| \vec{u}_P \right|$  is released in a quiescent fluid and comes to rest after a certain time  $t_{relax}$ . Generally, the stopping distance is calculated under the assumption of laminar flow. The characteristic time is defined as:

$$t_{char} = \frac{l_{char}}{\left| \bar{\vec{u}_f} \right|}. \quad (3.12)$$

The parameters  $l_{char}$  and  $\left| \bar{\vec{u}_f} \right|$  are the characteristic length of flow apparatus and mean fluid velocity, respectively. Stokes numbers bigger than unity represent dense gas–solid flows, i.e. the particles trajectories deviate from the flow streamlines, while Stokes number smaller than unity denotes to dilute flows, i.e. the particles trajectories are strongly oriented to flow lines.

### 3.1.4 Representative–particle method

The representative particle method offers an efficient and accurate compromise between the single–particle and two–fluid methods. Representative in this sense means that all particles within the volume element are assumed to own the same characteristics of one representative particle. In this approach, the fluid phase is modeled with the Euler framework, while the representative particles are calculated using the Lagrange representation. A detailed derivation of governing differential balance equations can be found for example in (Zobel 2007). The most important advantage of representative particle method compared to the single–particle method is the significantly lower computational effort. Therefore, this method has been applied to large industrial facilities more frequently than the single–particle model, but is not as widely employed as the two–fluid model. However, the representative particle method is used only for the simulation of the fixed bed and has difficulties in describing the heat transfer between the particles in contact via thermal convection and conduction. Furthermore, the resulting effects due to the change in representative particles size during the combustion process on the bed properties (such as the reduction of bed height) are still an open issue, which needs to be clarified. These difficulties are related to the representative particle method that cannot represent the microstructure of individual particles.

### 3.1.5 Hybrid method

In form of a so–called hybrid method, the two–fluid and single–particle methods are coupled. Here, the computational domain is basically divided in two sub–domains, namely the continuum and the free molecular domains. While the two–fluid method is used for the sub–domain, in which the continuum hypothesis is satisfied, the single–particle method in combination with the stochastic or deterministic collision detection models is applied to the free molecular sub–domain including walls. Although the idea behind the hybrid method is simple, it shows the advantages of both methods (two–fluid and single–particle). This procedure was successfully tested for the simulation of dilute fluid–solid flows by (Grüner 2004). Here, the two–fluid method and single–particle in combination with a stochastic collision model was coupled. Grüner developed a criterion with the help of the equilibrium index proposed by (Kanther 2003) that divided the whole computational domain adaptive into continuum and free molecular sub–regions. Since that time, several authors have been employed this approach to simulate the hydrodynamic behaviours of gas–solid flows. However, the hybrid method is not suitable for the simulation of dense flow in the fluidized beds due to the high inhomogeneity of solid distribution during the operation.

## 3.2 Conclusion

For the simulation of the gas–solid flow, several approaches with different levels of detail are available, namely the quasi–single–phase, the two–fluid, the single–particle, the representative–particle and the hybrid methods.

If the continuum hypothesis is fulfilled, the particle phase can then be described as a fluid. The single-phase model presents in this context the simplest approach to simulate the behaviour of a gas–solid flow. Hence, the physical values of dispersed and gas phases can be represented as volume average values by solving the balance equations of the single-phase flow. The quasi-single-phase assumes that the solid is evenly distributed in the fluid phase and the velocities differences between both phases are negligible small. In many cases, the configurations of practical gas–solid flows do not meet the method criterions. Therefore, the more sophisticated continuum approach i.e. two-fluid method, which is related to a better accuracy and wide application range, has been most frequently employed. The basic idea of two-fluid method is that the fluid and solid phases are regarded as coexisting continua. Both phases are modeled with the balance equations of single-phase flow, where the solid phase is considered as second dense fluid phase. Due to the continuous increase in the computer performance, the solid phase can be treated as a disperse phase (single-particle-method), e.g. the trajectory of a single particle is followed. Compared to continuum methods, the single-particle model shows much better agreement towards the measurement. However, the numerical simulation performed with the single-particle method is computationally expensive, especially when the number of particles exceeds one million. The use of representative particle model can lead to a significant reduction in computation time. Here, instead of modelling each single particle in the computational domain, only a certain number of representative particles are considered. In so-called hybrid method, the two-fluid method and the single-particle-method are coupled. In the domain, where the continuum hypothesis is satisfied, the two-fluid method is employed, while the single-particle method is applied to the free molecular domain and walls. Although the last both approaches offer a compromise between the efficiency and accuracy, some open questions still need to be answered; such as the description of reactive particles in the representative particle model and the inhomogeneity of solid distribution for the possible application of hybrid method.

Which approach is more appropriate to describe the behaviour of the gas–solid flow, it can completely not be stated. Generally, it depends on the flow configurations, the mechanical properties of particles, the solid content in the flow and the level of accuracy that has to be accomplished. The continuum approach will likely remain the predominant choice for the fixed bed simulation and for granular flow with particle size less than 1 mm (Zobel 2007). The use of continuum approach is, however, limited to monodisperse gas–solid flow, but the calculation of polydisperse systems is possible. In this case, each particle size class should be seen as a distinct phase. The consideration of different particle sizes leads to an increase in computing time up to the level, at which the single-particle method offers a competitive approach.

This study engages in developing a numerical simulation program for the simulation of reactive gas–solid flow in a bubbling fluidized bed. This system is characterised by high solid loading, high inhomogeneity in solid distribution and high velocities differences between the gas and solid phases. Furthermore, the particle diameters will be continuously changed during the combustion process, which lead to polydisperse flow with a broad range of particle sizes. For this system, although the continuum hypothesis is not met, the two-fluid method is still utilized by the reason of the efficiency advantage and the numerical stability (among others: (Yurong et al. 2004, Hartge et al. 2009, Gryczka et al. 2009, Herzog et al. 2012)). In contrast to the continuum approach, the single-particle method is more suitable, especially if detailed information on physical and chemical properties of solid phase is required. Besides the physical and chemical values, also microscopic characteristics such as the burnout behaviour of each particle during the combustion should be assessed in this work. Therefore, the single-particle method is applied, since it fulfils the standards of this PhD thesis. In order to test the validity of single-particle and Euler–Euler methods application to fluidized bed, a complete comparison between two approaches is carried out.

# 4 Collision models

For gas–solid flows with Stokes numbers bigger than unity, the short–range forces that rise between the particle–particle/wall such as the contact force have a relevant influence on the obtained results. The considering of short–range forces is required a specific description of collision process, which is divided in collision detection and collision treatment. The collision detection between the particle–particle/wall can be stochastically modeled or deterministically detected. Compared to the stochastic collision models, the deterministic collision models show much better agreement with experimental data. Nevertheless, the deterministic collision models are computationally very expensive.

If the collision is detected with a stochastic collision model, the collision treatment is only performed with the hard sphere model. In this model, single binary collision is considered, where the properties of particles after the collision are related to the properties of particles before the collision. In case of deterministic collision models, the subsequent collision treatment can be achieved either with hard sphere model or soft sphere model. In the soft sphere model, the velocity and the displacement of each particle are determined during the collision.

## 4.1 Collision detection models

Basically, the stochastic or deterministic collision model can be applied in a frame of the single–particle method to detect the particle–particle/wall collisions.

### 4.1.1 Stochastic collision detection models

The stochastic collision models offer today due to their high efficiency, the only way to handle numerically the practical gas–solid flows by means of the single–particle method. As a result of the stochastic nature of the collision detection, these models are often grouped under the so–called Monte Carlo methods.

The earliest research in this field is ascribed to O'Rourke (O'Rourke 1981), who developed a collision detection model based on a stochastic method. In this model, the collision probability is determined for each pair of particles in the grid cell using a Poisson distribution. The computation effort of O'Rourke model is proportional to the square of particle number. A linear dependence between the computation effort and the particle number has been reached by (Oesterlé and Petitjean 1993). The idea behind Oesterlé model is: the trajectories of particles are sequentially determined. In this context, sequentially means that the motion of each particle remains uninfluenced by the presence of remaining particles. Nevertheless, information on other particles should be available, which enables the calculation of collision between the observed particle and their partners. For this purpose, mean values as well as standard deviations of certain variables such as particles velocities and particles positions are determined in each grid cell. The local statistical data serves as a basis for generating virtual collision partners whose properties are given by the local average values of neighbouring particles of the investigated particle. The probability of a collision between the real particle and the virtual particles can be met by means of random numbers. If the collision event occurs, the subsequent collision treatment is then performed by the hard sphere model. The physical properties of real particle after the collision are calculated using the properties of real and

virtually particle before the collision. While the obtained velocity of the investigated particle is stored in the memory, the virtual particle is eliminated. If the collision event doesn't take place, the velocity of the real particle remains then unaltered.

The major disadvantage of Oesterlé collision model is that the kinetic energy conservation cannot be guaranteed even during completely elastic collisions. The extension of Oesterlé model by Sommerfeld (Sommerfeld 1996), in which the local velocity fluctuations of the neighbouring particles are considered with additional partial correlations, cannot eliminate the model weakness, too (Hußmann 2009). In contrast to Oesterlé model, the modified Babovsky–Nanbu model (Nanbu 1980, Babovsky 1989) ensures on the one hand the conservation of the kinetic energy and on the other hand has a linear computational effort to the number of particles. Therefore, it considers as one of the most efficient and accurate stochastic collision detection models.

The application of the stochastic collision models, although they show considerable efficiency advantage, is related to low simulation accuracy. Furthermore, the number of existent particles in the balance volume cannot be limited in these models. This might lead in dense gas–solid flows to solid volume fraction bigger than unity in the control volume (Götz 2006). The reason of this non–physical effect hearkens back to the stochastic nature of the collision detection. In worst cases, several particles after the collisions with the virtual particles can be located in the same control volume, which lead to unrealistic volume fraction of solid. Accordingly, the stochastic methods are more suitable for the collision detection in granular flows with a low solid loading.

#### 4.1.2 Deterministic collision detection models

While the detection of collision partners in stochastic collision models is taken place with the aid of random numbers, the deterministic methods detect each single particle for possible collision with remaining particles or walls. In deterministic collision models, the particle time step can be selected constant or adaptive in opposite to the stochastic collision models, where the particle time step is assumed to be constant (see **Figure 3.1**).

For the adaptive deterministic collision model, the particle time step is varied during the simulation. In the period of time between  $t$  and  $(t + \Delta t_p)$ , no collision will occur, but only at the time  $(t + \Delta t_p)$  one particle collides with other particle or wall. The size of the particle time step is determined by fixing the intersection points between the particles trajectories and the wall (Epple et al. 2012). This event–oriented method was presented for the first time by Hoomans (Hoomans et al. 1996). It is characterised mainly by high accuracy, since the collision partner and the collision time must be exactly specified. If the collision partner moves away from each other as it will not collide, the scalar product of relative velocity  $\vec{u}_{ij} = \vec{u}_i - \vec{u}_j$  and position vector  $\vec{r}_{ij} = \vec{r}_i - \vec{r}_j$  has then a positive value (see **Figure 4.1-a**). A collision takes place only when the collision partners move towards each other, i.e. the scalar product of relative velocity and the position vector has a negative value (see **Figure 4.1-b** and c). The computation effort of the deterministic collision detection model with a variable particle time step behaves quadratic to number of particles.

The particle properties after the collision is subsequently determined with the hard sphere model (see section 4.2.1). Employing the single–particle method, the particle position and the angular displacement can be calculated (see Eq. (3.4) and Eq. (3.5)). The use of variable particle time step improves the simulation accuracy of granular flow, since the collision detection between the particles partners are described in more detail. However, the event–oriented method can be efficiently applied to dilute fluid–solid flows, in which the mean free path of particles is relatively large, resulting in coarser particle time steps. In dense fluid–solid

flows, by contrast, the efficiency advantage cannot be achieved due to smaller mean free paths and thus more frequent collision events occur per time unit. In case of parallel computing, the event-oriented method results in efficiency loss due to the asynchronous parallel load between the computer nodes (Götz 2006).

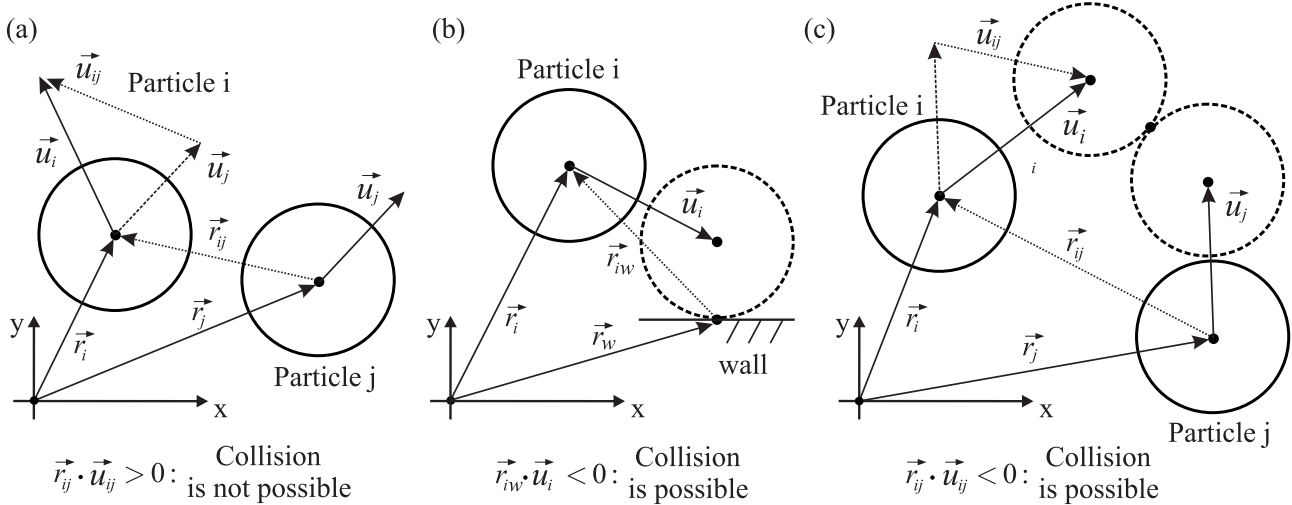


**Figure 4.1:** Probability of collision occurrence in event-oriented method: (a) collision is not possible and (b) particle–wall collision is possible and (c) particle–particle collision is possible

In deterministic collision detection model with constant particle time step, the particles can overlap each other or penetrate into the wall (see Figure 4.2-a and b). Depending on the penetration depth  $\delta$ , a contact force is modeled using a spring-damper-slider system. This approach has been introduced first by Cundall and Strack (Cundall and Strack 1979) and in the literature is often referred to as discrete element method (DEM). Due to the penetrating behaviour both collision partner, this model is also known as soft sphere model. Although DEM dated back originally to Cundall and Strack, (Tsuiji et al. 1992, Tsuiji et al. 1993) are often cited, since they have been successfully employed the DEM model to simulate the hydrodynamic behaviour of dense gas–solid flow in a fluidized bed.

The collision detection in the DEM model is based on a simple principle: each particle is tested for possible collision events with other particles or walls. Similar to the deterministic detection model with variable particle time step, the computational effort of the DEM model is a quadratic function to number of particles. Therefore, optimisations on collision detection algorithm are required, especially for the simulation of granular flows with high solid content.

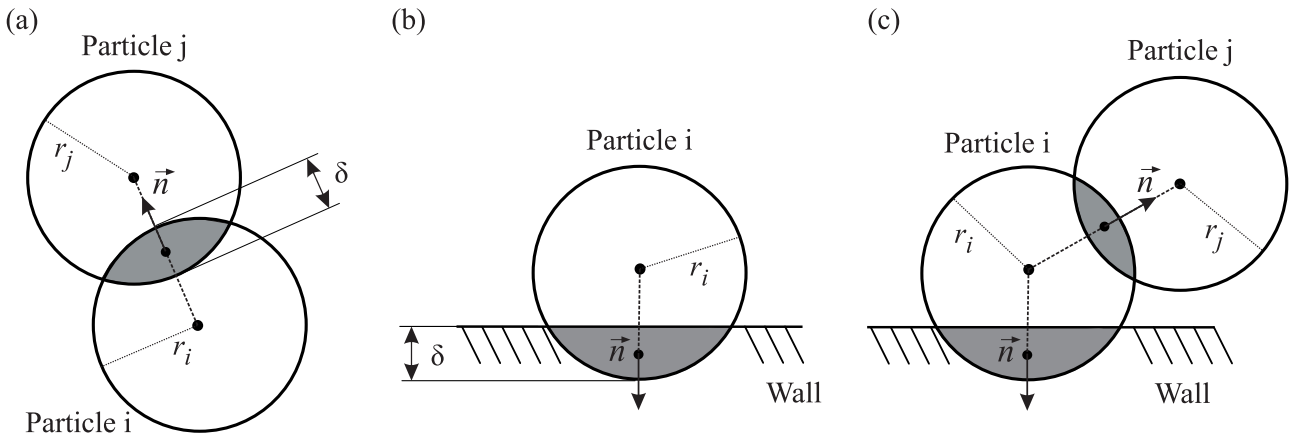


**Figure 4.2:** Occurrence of collision in DEM model: (a) particle–particle collision, (b) particle–wall collision and (c) particle–particle/wall collisions

An important advantage of the DEM model is the possibility to consider simultaneously the multiple collisions between particles–particles/walls (see **Figure 4.2–c**). This is due to the fact that the description of multiple contact forces is of major relevance, particularly in dense gas–solid flow. Besides the contact force, other short–range forces such as adhesive forces can also be determined in frame of the DEM model. However, it is necessary first to detect the collision using a specific criterion. For the contact criterion as an example, the distance between the centres points of two particles or the distance between the particle centre point and the wall surface should be smaller than the sum of both radii or smaller than the particle radius, respectively (see **Figure 4.2**). Another example for the short–range forces is the criterion of liquid bridge formation, where the distance between the centres points of two particles has to be smaller than the critical distance (see section 5.1.2.2.3).

The computational effort represents the great disadvantage of the DEM model. The collision detection between particle–particle/wall in DEM causes the most part of the computational time, where there is a substantial difference between one–dimensional, two–dimensional and three–dimensional cases. In 1D case, only the particles on left and right of the investigated particle are eligible as collision candidates. Furthermore, the neighbouring particles remain unchanged during the calculation. In 2D and 3D cases, by contrast, the number of possible collision partners is significantly higher and the continuous changing of neighbouring particles leads to extra computation time.

Different algorithms to determine the collision between particle–particle/wall in granular flows can be found in the literature. A review article about them has been published for example by (Vemuri et al. 1998, Jiménez, Thomas and Torras 2001). In the following sections, the most applied deterministic collision algorithms, namely the standard, the neighbourhood and the bounding–boxes methods will be explained in detail including their applications, efficiency, programming and implementation effort.

#### 4.1.2.1 Standard method

The standard method presents the simplest algorithms to examine each particle for possible collisions with other partners, e.g. all particles and walls in the computational domain. The collision detection of spherical particles runs relatively trivial in this method. Here, the investigated particle is tested for possible collisions with all remained particles and walls according to a predefined criterion. The collision probabilities between particles are indirectly given by the corresponding particle spacing. In concrete term, this means that the algorithm computes the collision probabilities between the tested particle and all other particles regardless of their relative positions. Distant particles, even their contact probabilities are clearly impossible, are examined for possible contact with the investigated particle (see **Figure 4.3**). Since the collision detections between the particles are computed independent of the corresponding particles positions, the computational effort behaves approximately quadruple to the number of particles:

$$T_{\text{tot}} = T_{\text{col}} (N - 1) N \approx T_{\text{col}} N^2. \quad (4.1)$$

The symbol  $T_{\text{col}}$  denotes the computing time that is required for single collision detection. Although the programming and the implementation complexity of the standard method is comparatively low, the computational time for the collisions detections is enormous. Even at dilute solid content in the fluid phase, the standard method leads to potential loss of the calculation efficiency and thus cannot be practically applied to gas–solid flow simulation.

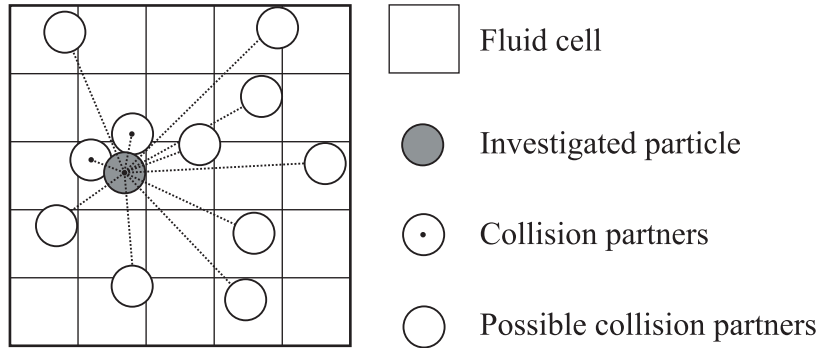


Figure 4.3: Collision detection process in standard algorithm

#### 4.1.2.2 Neighbourhood method

In contrast to the standard method, the neighbourhood algorithm shows a significant improvement regarding the collision detection efficiency. Here, the collision detection consists of two consecutive steps. While the first phase involves in searching for possible collision partners, the second step detects the accurate collisions between the investigated particle and their potential candidates. The well-known and frequently applied neighbourhood methods are the Verlet algorithm and the search grid method.

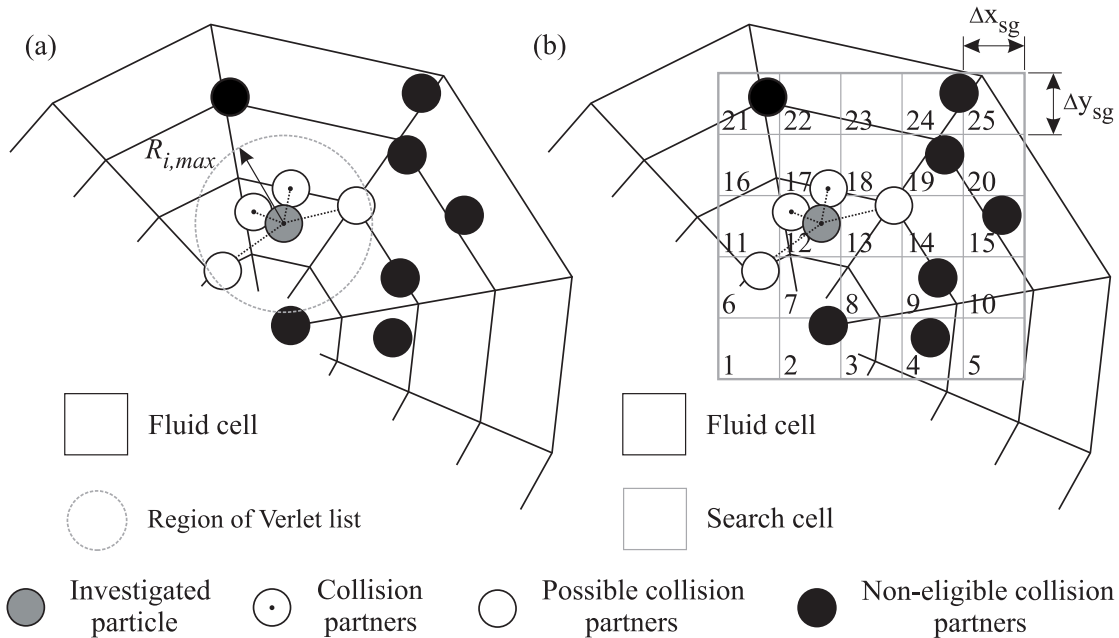


Figure 4.4: The relationship between particles in neighbourhood methods: (a) Verlet algorithm and (b) search grid method

The Verlet algorithm (Allen and Tildesley 1989) defines for each particle a circular (2D) or spherical (3D) collision region that includes the possible collision partners (see Figure 4.4-a). The radius of the collision region  $R_{i,\max}$  depends on the selected fluid time step as well as on the properties of the observed particle and their adjacent particles. According to (Hoomans et al. 1996, Deen et al. 2007), the collision region radius  $R_{i,\max}$  can be determined with the following equations:

$$R_{i,\max} = r_i + r_{P,\max} + 2|\vec{u}_{P,\max}| \Delta t_f, \quad (4.2)$$

with:

$$\begin{aligned} r_{P,\max} &= \max(r_i) \quad \forall i \in A, \\ |\vec{u}_{P,\max}| &= \max(|\vec{u}_i|) \quad \forall i \in A. \end{aligned} \quad (4.3)$$

where  $A = \{0, 1, \dots, N\}$  is a list that contains all particles and walls of computational domain. The distances between the investigated particle  $i$  and all collision partners are computed and compared with the radius  $R_{i,\max}$ . The particles including walls that are within the collision area of the particle  $i$  will be stored in its neighbour list (Verlet list). The exact collision detection can then be performed after building all neighbour lists, where each considered particle is only tested with its potential collision partners in the Verlet list.

Similar to the standard method, the computation effort of the Verlet algorithm is a quadratic function to the number of particles. This is due to the fact that the building of the particle neighbour lists is numerically very expensive. In practice, the neighbour lists should not be updated for each time step. The actualisation of the particle  $i$  neighbour list is performed only when a particle leaves its collision area. This requires that the distance between the particle  $i$  and the particles in its neighbour list to be again computed and compared with the radius  $R_{i,\max}$  in every time step. If one or more particles left the particle  $i$  Verlet list, then a new list should be rebuilt. In dilute gas–solid flows, in which the neighbour lists can be updated once in a while, the Verlet algorithm can be employed. As opposed to dilute systems, the efficiency advantage of the Verlet method for dense gas–solid flows is no longer valid. This is because the neighbour lists must be actualised for each time step.

In the search grid method after (Hockney and Eastwood 1988), the computational domain is divided into finite cells, which contain indexed particles. A particle may come in contact only with particles of its own cell or with those of its direct neighbouring cells. By neglecting any further collisions with particles that are located in far cells, the computational time is reduced. In **Figure 4.4-b**, a particle in cell 12 (gray), its potential collision partners in cells 12, 6, 7, 8, 11, 13, 16, 17, 18 (white) and its non-eligible collision partners in remaining cells (black) are illustrated. In contrast to the Verlet algorithm, the search grid method can be applied to dilute as well as dense gas–solid flows without efficiency loss. On the other hand, this method necessitates a virtual orthogonal grid, which is placed over the entire computational domain. The applied virtual grid is independent of computational grid and thus an allocation with fluid and particle grids is not required. The computational complexity of the search grid method depends on the total number of particles  $N$  in the computational domain as well as on the particle numbers in the search grid cell  $N_{sgc}$ . It consists of two parts: the computing time  $T_{loc}$  that is needed for the allocation of each individual particle in the search cells and the computing time  $T_{col}$  that is required for the collision detection between the investigated particle and its potential collision partners:

$$T_{tot} = N(T_{loc} + D \cdot N_{sgc} T_{col}). \quad (4.4)$$

The constant  $D$  relates to the demission of the computational domain. For 1D case, it has the value 3, while it corresponds to values 9 and 27 for 2D and 3D cases, respectively. The computing time  $T_{loc}$  for allocating the particles in the orthogonal cells is much smaller than the required time for the collision detection  $T_{col}$  (Götz 2006). For a monodisperse system with a homogeneous particle distribution, it can reach in ideal case to a computational effort almost proportional to the number of particles. This can occur if the size of the search grid is chosen equal to the particle diameter and in each search cell one particle is allocated. The Equation (4.4) can then be reduced to:

$$T_{tot} = N \left( \underbrace{T_{loc}}_{\text{very small} \approx 0} + D \cdot \underbrace{\sum_{i=1}^{N_{sgc}} T_{col}}_{\text{Constant}} \right) \approx N \left( D \cdot \underbrace{T_{col}}_{\text{Constant}} \right) \approx N. \quad (4.5)$$

Since the computing time is a function of the search cell size ( $\Delta x_{sg}, \Delta y_{sg}$ ), the correct selection of the grid size is of crucial importance. The computing time dependence on the size of the search cell and accordingly on the particle diameter represents the weakness of this procedure. For a polydisperse system with a broad range of particle sizes, the determination of the search grid size is correlated to the largest particle (see **Figure 4.5**). As a consequence, the average particle number per search cell increases and thus the computational effort rises. If the size of the search cell corresponds in worst cases to the geometry size, then the computing time is a quadratic function to the particle number as similar to that of the standard method.

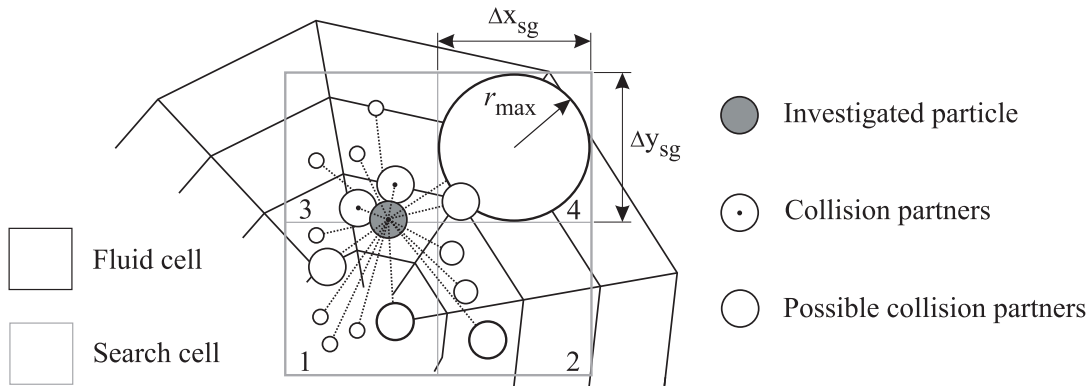


**Figure 4.5:** The determination of search cell size in polydisperse system

#### 4.1.2.3 Bounding-boxes method

In the bounding-boxes algorithm (Baraff 1995, Cohen et al. 1995), each particle is enclosed with a cuboid whose edges are aligned parallel to the coordinate axes. The enveloping cuboid is identified by the positions of its projected four vertices in 2D or six vertices in 3D cases on the correspond axes, respectively. For each axis, a particle list is generated, in which the vertices of all cuboids and thus the geometrical properties of particles are stored. A possible collision between two particles will then be occurred, once their cuboids vertices overlap in the x-, y-and z-directions. If this happens, an addition condition should be verified in order to specify, which surfaces of the colliding partners have come into contact (see **Figure 4.6**: particles 4 and 5). Here, it should be mentioned that a collision can be detected between the cuboids, but on the other hand no collision takes place on particles level (see **Figure 4.6**: particles 6 and 7). The bounding-boxes algorithm, although is associated with high programming cost during the implementation phase, is characterised by two relevant advantages. The non-spherical particles can be treated in this method with a similar computational effort as spherical particles. Furthermore, the particle size distribution has no impact on the efficiency of procedure. This is due to the fact that each particle is enclosed with a suitable cuboid independent of its shape or geometry.

The computational complexity of the bounding-boxes method behaves quadratic to particle number. However, the computational effort can significantly be reduced by a special sort and insertion methods, so-called incremental sort and update algorithm (Schinner 1999). Here, the cuboids vertices are sorted in the particle lists (x-, y-and z-directions) in ascending order for each time step. The sorting process permutes the elements within a list based on simple mathematical methods. According to (Sedgewick 1992), the required time for sorting process has the order of  $O(N \log N)$  per coordinate list. The computational effort of the bounding-boxes algorithm under the consideration of the sorting method behaves

approximately linear to the particle number, which is more or less as the neighbourhood method.

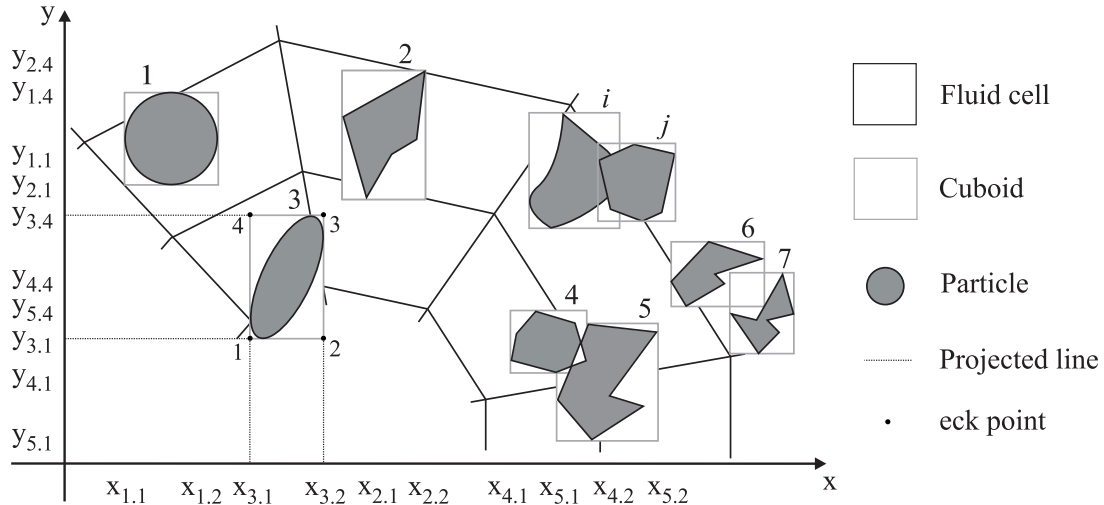


**Figure 4.6:** The bounding–boxes algorithm under the consideration of sorting method

In dilute gas–solid flows, where the cuboids vertices are far apart from each other, the bounding–boxes algorithm can be applied satisfactory. In dense granular flows, by contrast, a significant increase in the computational effort arises. This efficiency loss is caused due to the extreme small distances between the sorted vertices. Here, the order of the vertices between two time steps in worst case may completely reverse, which results in a computational effort for the sorting process of the second–order of particle number (see **Figure 4.7**). It should be acknowledged that even under the assumption of low particle velocities and smaller particle time steps, the sorted lists within two successive time steps can be quite different. As results of this, the computational complexity of the bounding–boxes algorithm can highly fluctuate from time step to other time step.

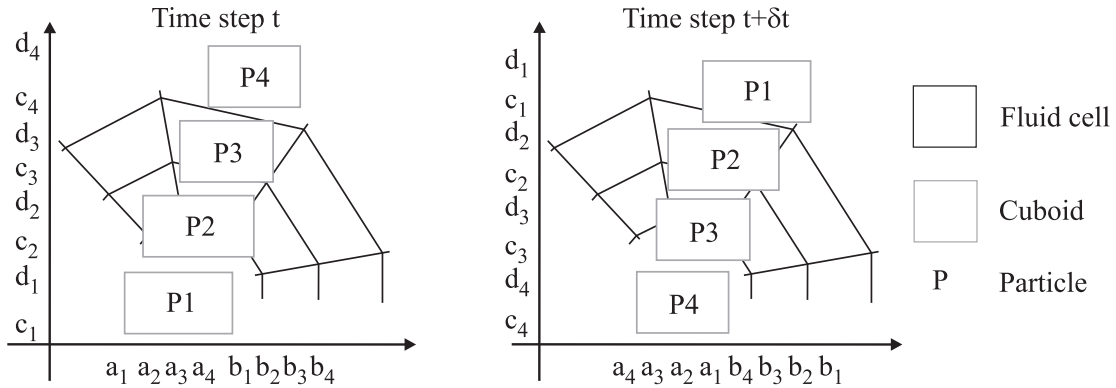


**Figure 4.7:** The order of sorted vertices between successive time steps

## 4.2 Collision treatment model

Depending on whether a stochastic or a deterministic detection model is applied, the subsequent collision treatment is performed either with the hard sphere model or the soft sphere model. In the following sections, the hard and soft sphere models will be explained in detail.

### 4.2.1 Hard sphere model

If the collisions between the particle–particle/wall are stochastically modeled or deterministically detected with adaptive particle time step, the collision treatment is then carried out with the hard sphere model. Here, the properties of particles after the collision are

correlated to the properties of particles before the collision through momentum and energy balances. In the hard sphere model, single binary collisions are modeled as instantaneous processes, where the contact between the collision partners occurs at a point. This model assumes that the particles are perfect spherical as well as all other finite forces that act on the collided particles during the collision are neglected. The first hard sphere model was developed by (Campbell and Brennan 1985), and since that time has been successfully employed to study a variety of complex granular systems.

The hard sphere model of (Hoomans et al. 1996) and (Sommerfeld 1996) will be briefly described here. **Figure 4.8** shows two colliding particles  $i$  and  $j$  with position vectors ( $\vec{r}_i$ ,  $\vec{r}_j$ ), radii ( $r_i$ ,  $r_j$ ) and masses ( $m_i$ ,  $m_j$ ).

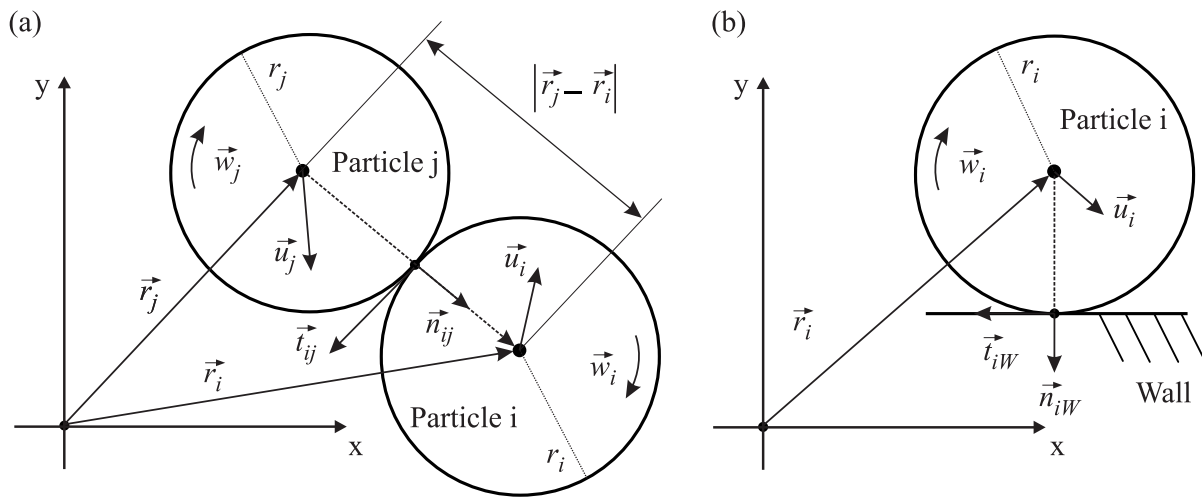


**Figure 4.8:** Hard sphere model: (a) particle–particle collision and (b) particle–wall collision (Epple et al. 2012)

The relative velocity at the contact point can be calculated using the translational as well as the angular velocities of collision partners as follows:

$$\vec{u}_{ij}^{(0)} = \left( \vec{u}_i^{(0)} - \vec{u}_j^{(0)} \right) + \left( \vec{r}_i \vec{w}_i^{(0)} + \vec{r}_j \vec{w}_j^{(0)} \right) \times \vec{n}_{ij}, \quad (4.6)$$

where the superscript (index 0) identifies the situation before the collision. The normal unit vector  $\vec{n}_{ij}$  that is directed from the centre of the particle  $j$  to centre of the particle  $i$  is defined as:

$$\vec{n}_{ij} = \frac{\vec{r}_i - \vec{r}_j}{|\vec{r}_i - \vec{r}_j|}. \quad (4.7)$$

The tangential unit vector can be calculated with the aid of the relative velocity before the collision and the normal unit vector:

$$\vec{t}_{ij} = \frac{\vec{u}_{ij}^{(0)} - \vec{n}_{ij} (\vec{u}_{ij}^{(0)} \cdot \vec{n}_{ij})}{\left| \vec{u}_{ij}^{(0)} - \vec{n}_{ij} (\vec{u}_{ij}^{(0)} \cdot \vec{n}_{ij}) \right|}. \quad (4.8)$$

By applying Newton's second and third laws, the translational and the angular velocities of particles after the collision, which result directly from the properties of collided particles before the collision, can be determined for the particle  $i$ :

$$\begin{aligned}\vec{u}_i &= \vec{u}_i^{(0)} + \frac{\vec{J}_{ij}}{m_i}, \\ \vec{w}_i &= \vec{w}_i^{(0)} + \frac{\vec{r}_i \vec{n} \times \vec{J}_{ij}}{I_i},\end{aligned}\tag{4.9}$$

and for the particle  $j$ :

$$\begin{aligned}\vec{u}_j &= \vec{u}_j^{(0)} - \frac{\vec{J}_{ji}}{m_j}, \\ \vec{w}_j &= \vec{w}_j^{(0)} + \frac{\vec{r}_j \vec{n} \times \vec{J}_{ji}}{I_j}.\end{aligned}\tag{4.10}$$

The symbols  $\vec{J}_{ij}$  and  $I_p$  represent the impulse vector and the moment of inertia for a particle, respectively. Rearranging equations ((4.9) and (4.10)) under the consideration of equation (4.7) and the mathematical relationship  $(\vec{n} \times \vec{J}) \times \vec{n} = \vec{J} - \vec{n}(\vec{J} \cdot \vec{n})$ , the following equations can be obtained:

$$\begin{aligned}\vec{u}_{ij} - \vec{u}_{ij}^{(0)} &= \frac{7\vec{J}_{ij} - 5\vec{n}_{ij}(\vec{J}_{ij} \cdot \vec{n}_{ij})}{2m_{ij}}, \\ \vec{w}_{ij} - \vec{w}_{ij}^{(0)} &= \frac{5(\vec{J}_{ij} \times \vec{n}_{ij})}{2m_{ij}},\end{aligned}\tag{4.11}$$

with the moment of inertia for spherical particles:

$$I_p = \frac{2}{5}m_p r_p^2.\tag{4.12}$$

The quantity  $m_{ij}$  denotes the reduced mass or the effective mass that allows treating two collided particles as a one particle:

$$m_{ij} = \frac{m_i m_j}{m_i + m_j} = \left(1/m_i + 1/m_j\right)^{-1}.\tag{4.13}$$

For particle–wall collision, the mass of the particle  $j$  (i.e. the wall) is infinitely large and therefore the reduced mass is equal to particle  $j$  mass ( $m_{ij} = m_i$ ). In order to determine the translational and the angular velocities of collided particles after the collision using equation (4.11), the impulse vector should be known. This requires, however, an exact physical description of binary collisions. For the fluidized bed simulation employing the hard sphere model, a large number of collisions should be considered, which is typically between  $10^6$  and  $10^9$  collisions per time step (Link 2006). In order to increase the calculation efficiency for processing the collisions, together with maintaining the simulation accuracy, the physical description of collisions should be simplified to some extent. In this context, three constitutive relations (parameters) are introduced to the model to close the set of equations as follows:

The restitution coefficient in normal direction:

$$e^n = -\frac{\vec{u}_{ij}^{(0)} \cdot \vec{n}_{ij}}{\vec{u}_{ij} \cdot \vec{n}_{ij}} \quad 0 \leq e^n \leq 1,\tag{4.14}$$

the restitution coefficient in tangential direction:

$$\beta^t = -\frac{\vec{u}_{ij}^{(0)} \cdot \vec{t}_{ij}}{\vec{u}_{ij} \cdot \vec{t}_{ij}} \quad 0 \leq \beta^t \leq 1, \quad (4.15)$$

and the dynamic coefficient of friction:

$$\mu_{dyn} = -\frac{\vec{n}_{ij} \cdot \vec{J}_{ij}}{|\vec{n}_{ij} \times \vec{J}_{ij}|} \quad \mu_{dyn} \geq 0. \quad (4.16)$$

The impulse vector results from a vector addition of normal and tangential contributions:

$$\vec{J}_{ij} = J_{ij}^n \cdot \vec{n}_{ij} + J_{ij}^t \cdot \vec{t}_{ij}, \quad (4.17)$$

where the normal component of the impulse vector is obtained by combining equations ((4.11) and (4.14)).

$$J_{ij}^n = -(1 + e^n) m_{ij} \left( \vec{u}_{ij}^{(0)} \cdot \vec{n}_{ij} \right). \quad (4.18)$$

For the tangential component of the impulse vector, two types of collisions have to be distinguished, viz. sticking and sliding collisions. The collision is sliding if gross sliding takes place throughout the duration of contact. On the other hand, sticking collision occurs when the restitution coefficient in tangential direction has the value zero (Link 2006). The distinction between static and sliding collisions is verified with the aid of Coulomb's law of friction. By inserting equations ((4.15) and (4.16)) in equation (4.11), the magnitude of the tangential impulse vector is obtained:

$$J_{ij}^t = \begin{cases} \underbrace{-\frac{2}{7}(1 + \beta^t) m_{ij} \left( \vec{u}_{ij}^{(0)} \cdot \vec{t}_{ij} \right)}_{\text{Sticking collision}} & \text{case } \mu_{dyn} J_{ij}^n \geq \frac{2}{7}(1 + \beta^t) m_{ij} \left( \vec{u}_{ij}^{(0)} \cdot \vec{t}_{ij} \right) \\ \underbrace{-\mu_{dyn} J_{ij}^n}_{\text{Sliding collision}} & \text{case } \mu_{dyn} J_{ij}^n < \frac{2}{7}(1 + \beta^t) m_{ij} \left( \vec{u}_{ij}^{(0)} \cdot \vec{t}_{ij} \right) \end{cases}. \quad (4.19)$$

The impulse vector is calculated with equation (4.17) employing the relative velocity between the collision partners before collision as well as the known collision parameters that consider the dissipation of kinetic energy during the collision. The post-collision velocities of colliding objects after the collision are then defined, applying equations ((4.9) and (4.10)). For determination the new position and the angular displacement of collided particles, equations ((3.4) and (3.5)) are used, where the particle time step must be known.

#### 4.2.2 Soft sphere model

The soft sphere model is applied to the collision treatment if the collisions between the particle-particle/wall are detected deterministically with constant particle time step. In soft sphere model, also known as discrete element method, the force, the velocity and the displacement are determined during the collision. It is assumed in this approach that the particles undergo deformation during their contact. Here, the particles can overlap each other or penetrate into the wall. Depending on the penetration depth, the resulting contact force can be modeled using a simple mechanical analogue system involving spring, damper and slider. Here, the damper and slider components enable the consideration of energy dissipation during the collision. The contact force is obtained by summing up all normal and tangential contact forces that act simultaneously between the particle and other particles and walls. Besides the

resulting contact force, aerodynamic surface forces and volume forces are considered in the Newton's equation of motion and the angular momentum equation ((3.6) and (3.7)). Typical volume forces are the gravitational force and the buoyancy force, which acts against the weight. The aerodynamic surface forces result from the interactions between the fluid and the particles (e.g. drag force, pressure force, Saffman force and Magnus force). Finally, the particle position and the angular displacement can be determined applying equations (3.4) and (3.5). Detailed explanation regarding the DEM model can be found in the next section.

### 4.3 Conclusion

In the single-particle method, the detection of particle–particle/wall collisions is crucially important with respect to both computational effort and simulation accuracy. Basically, the collisions between particle–particle/wall can be stochastically modeled or deterministically detected. The idea behind the stochastic collision models is: the motion of each particle is calculated independent of remaining particles. However, information on other particles should be available in order to generate virtual collision partners whose properties are derived by the local average values of these particles. The occurrence probability of a collision between the investigated particle and the virtual particle can then be met by means of random numbers, where the particle time step is assumed to be constant. While the collision partners are chosen coincidence in the stochastic collision models, each particle is tested for a possible collision with other partners (particle, wall or both) in the deterministic methods. In contrast to the stochastic collision models, the particle time step in deterministic collision models can be selected constant or adaptive. For adaptive deterministic collision model, also known as event-oriented method, no collision during successive time steps will occur, but only at the time ( $t + \Delta t_p$ ) one particle collides with other particle or wall. In deterministic collision models with constant particle time step, also known as discrete element method, a particle–particle collision takes place when the distance between the centres points of two particles is smaller than the sum of both radii. By the same token, a particle–wall collision will occur if the distance between the particle centre point and the wall surface is smaller than the particle radius.

Which model is preferred to detect the particle–particle/wall collisions, it depends on solid loading, computational effort and level of accuracy that has to be achieved. The stochastic collision models, although are related to relative lower simulation accuracy, present today the most efficient approach for considering the particle–particle/wall collision. In dense gas–solid flow, the stochastic collision models produce, however, unrealistic results such as solid volume fractions greater than unity in the control volume (Götz 2006). Moreover, the conservation of the kinetic energy in these models cannot be guaranteed even during completely elastic collisions (Hußmann 2009). Therefore, these models are mainly applied to dilute gas–solid flows. These limitations, on the other hand, do not exist in deterministic collision models that are more appreciated for dense flow simulations. The deterministic collision model with variable particle time step allows more detailed information and correct physical description of collisions compared to the deterministic collision model with constant particle time step. Although the use of variable particle time step improves the simulation accuracy, it results in dense gas–solid flows in high number of collision events per unit of time and thus in efficiency loss. Furthermore, single binary collisions can only be modeled in this approach, which restricts the application to dilute systems. By contrast, the deterministic collision model with constant particle time step has the possibility to consider the multiple collisions between particles–particles/walls simultaneously. This is of major relevance, particularly for the simulation of the gas fluidized bed. The entire contact force results finally by summing all binary contributions.

To determine the collision between particle–particle/wall in dense granular flows, different algorithms are available, namely standard, neighbourhood and bounding–boxes methods. In the standard algorithm, all probabilities for possible collision between the

investigated particle and other partners are considered, leading to total computational cost scales as  $O(N^2)$ . Compared to the standard method, the neighbourhood methods provide a starting point to enhance the efficiency. Here, a collision list is generated for each particle, in which potential collision partners are only saved. This means, a particle can only come in contact with particles in its direct neighbourhood. By neglecting any further collisions probabilities with particles that are far away from the investigated particle, the computational effort is reduced. For particles with wide size distributions and/or complex geometries, the efficiency of the neighbourhood method decreases. In this context, the bounding-boxes algorithm offers a competitive procedure. Here, each particle is enclosed with a cuboid its edges are projected on the coordinate axes. A particle list, in which the vertices of all cuboids are saved, is generated for each axis. A possible collision between two objects will occur if their cuboids vertices overlap in the x-, y-and z-directions. The computational effort of the bounding-boxes method is more or less equated to the neighbourhood methods, by skilful use, approximately linear to the particle number. However, the bounding-boxes method allows the collision detection between particles with complex polygonal shapes. Furthermore, the particle size distributions have no influence on the method efficiency.

If the collision is detected with stochastic collision models, the collision treatment is only performed with the hard sphere model. In this model, single binary collision is modeled, where the properties of particles after the collision are related to the properties of particles before the collision. In case of deterministic collision models, the subsequent collision treatment can be achieved either with the hard sphere model or the soft sphere model. In soft sphere model, the force, velocity and displacement variances are determined simultaneously during the collision. Here, the particles can overlap each other and/or penetrate into the wall. Depending on the penetration depth, a contact force is modeled using a spring-damper-slider system, which leads to a change in the motion of particles.

The aim of this work is to develop a numerical simulation program for the simulation of reactive, dense gas-solid flow in a fluidized bed. For this system, the single particle method with stochastic collision models cannot be applied. This is due to the fact that these models can cause non-physical result, such as solid volume fraction more than unity in the control volumes. In contrast to the stochastic collision models, the deterministic methods would fulfil the necessary standards of this PhD thesis. The event-oriented method combined with the hard sphere model has been employed in many cases. Besides (Hoomans et al. 1996, Goldschmidt, Beetstra and Kuipers 2004, Link 2006, Kosinski, Kosinska and Hoffmann 2009) and other co-workers have made outstanding contributions to this field. In dense gas-solid flows, the event-oriented method has, however, low advantages regarding the computational time. Furthermore, the parallelisation of algorithm leads to asynchronous load between the computers, thus to efficiency loss. Consequently, the soft sphere model, also known as discrete element method, is used in this work to describe the solid phase. Since the DEM model was first successfully employed by (Tsuiji et al. 1992, Tsuiji et al. 1993) to simulate the hydrodynamic behaviour of dense gas-solid flow in a laboratory scale fluidized bed, significant advances have been accomplished in this field (summarised by (Deen et al. 2007) and (Zhu et al. 2007)). The collision detection between particle-particle/wall is carried out in this study with the neighbourhood method by the reason of its high efficiency and its low implementation complexity. Indeed, the bounding-boxes algorithm outweighs the neighbourhood method in case of collision detection for particles with a wide size distributions and complex geometries, but this method is not considered here as well as in other on-going DEM codes. This is because the bounding-boxes algorithm involves considerable implementation effort and, for the time being, the simulations of non-spherical, polydisperse particles are of lesser interest.

# 5 Discrete element method

The DEM model offers detailed information on the hydrodynamic behaviour of granular flows. Here, the determination of a single particle trajectory and the angular displacement is achieved by establishing balances of forces and moments of force on each particle with the aid of Newtonian equations of motion.

## 5.1 Forces balance

The translational velocity of a single particle is calculated through the integrating of Newton's second law of motion:

$$m_p \frac{d\vec{u}_p}{dt_p} = \sum \vec{F}_i = \underbrace{\vec{F}_{gra} + \vec{F}_{buo} + \vec{F}_{ele} + \vec{F}_{mag}}_{\text{Volume forces}} + \underbrace{\underbrace{\underbrace{\vec{F}_{dra} + \vec{F}_{vir} + \vec{F}_{bas} + \vec{F}_{pre} + \vec{F}_{saf} + \vec{F}_{rad} + \vec{F}_{mags}}_{\text{Aerodynamic forces}} + \underbrace{\vec{F}_{con}^n + \vec{F}_{con}^t}_{\text{Contact forces}} + \underbrace{\underbrace{\vec{F}_{van} + \vec{F}_{elst}}_{\text{Without physical contact}} + \underbrace{\vec{F}_{liq} + \vec{F}_{sol}}_{\text{With physical contact}}}_{\text{Adhesive forces}}}_{\text{Short-range forces between the particles}}}_{\text{Surface forces}}. \quad (5.1)$$

Here,  $\vec{u}_p$  is the particle translational velocity,  $t_p$  represents the particle time step,  $m_p$  is the particle mass and  $\vec{F}_i$  denotes the forces acting on the particle. These forces are classified as volume and surface forces. The particle volume forces are gravitational, buoyancy, electric and magnetic forces. The surface forces can be divided into two categories: the aerodynamic surface forces that result from the interactions between the fluid and the particles (drag, virtual mass, Basset, pressure, Saffman, radiometric and Magnus forces) and the short-range surface forces that result from interactions between particles (contact and adhesive forces). The adhesive force is divided into adhesive forces associated either with or without physical contact. While the adhesive forces without physical contact include van der Waals and electrostatic forces, the adhesive forces with physical contact are liquid bridge and sintering forces. It is common practice here to neglect definite forces because of their subordinate importance. However, the neglecting of these forces because of their additional computational effort in the single-particle method or due to the limited capability of approach used like in the two-fluid method can significantly influence the entire simulation accuracy.

In the following sections, the acting forces on particles including the volume, aerodynamic surface and the short-range surface forces will be explained in detail. Further information can be found in (Schubert 1979), (Paschedag 2004), (Fan and Zhu 2005), (Götz 2006) and (Epple et al. 2012).

### 5.1.1 Volume forces

Volume forces, also known as body or field forces, imposed by external fields outside the flow system such as gravity, magnetic or electric field. The volume forces act throughout the

volume of object regardless of flow configuration. They have a quadratic dependence on distance between two bodies. Typical volume forces in the gas–solid flow are gravitational force, buoyancy force, electric and magnetic forces.

**Gravitational force:** For spherical particles, the gravitational force is determined from the product of particle mass  $m_p$  and acceleration of gravity  $\vec{g}$  as follows:

$$\vec{F}_{gra} = m_p \vec{g} = \frac{\pi}{6} \rho_p d_p^3 \vec{g}, \quad (5.2)$$

where  $d_p$  and  $\rho_p$  represent the diameter and the density of particle, respectively.

**Buoyancy force:** According to Archimedes' buoyancy principle, the static buoyancy force acting on a floating particle is equal to the fluid weight  $m_{dis}$  that is displaced by this object. The static buoyancy force occurs in liquids and gases and counteracts the gravitational force. For spherical particles, it is expressed by:

$$\vec{F}_{bau} = -m_{rep} \vec{g} = -\frac{\pi}{6} \rho_k d_p^3 \vec{g}. \quad (5.3)$$

Here, the subscript  $k$  is either  $g$  (gas) or  $liq$  (liquid).

**Electric force:** If an electric field is applied to charged particles in a gas–solid flow, the particles are subjected to an electric force that is calculated by the product of the particle charge  $q$  and the electric field intensity  $\vec{E}$ :

$$\vec{F}_{ele} = q \vec{E}. \quad (5.4)$$

While positivity charged particles move to cathodic side, the negative charged particles tend to move to anodic side. In case of static charged particles, the electric force is also known as Coulomb force.

**Magnetic force:** When the particles in a gas–solid flow are magnetized, a magnetic force is then exerted once the particles are exposed to a magnetic field. It can be calculated as follows:

$$\vec{F}_{mag} = n \varepsilon_{rel} \vec{B}_{vac}, \quad (5.5)$$

where  $n$  represents the number of north magnetic poles,  $\varepsilon_{rel}$  is the relative permeability of the material and  $\vec{B}_{vac}$  denotes the magnetic flux density in vacuum. In an electromagnetic field, the forces acting on charging particles consist of three parts: the force due to the net charge, the force due to the electric dipole in electric field and force due to the magnetic dipole in magnetic field. The resulted Lorentz force on a charged particle that moves with velocity  $\vec{u}_p$  through an electromagnetic field can be determined by neglecting the effect of the magnetic dipole as follows:

$$\vec{F}_{mag,ele} = q (\vec{E} + \vec{u}_p \times \vec{B}). \quad (5.6)$$

### 5.1.2 Surface forces

While the volume forces act on the entire body of particles, the surface forces exert on the surface of particles. These forces can lead to abrupt changes in the particle trajectories and their angular displacements. It can be distinguished between the aerodynamic surface forces and the short-range surface forces. Compared to other numerical methods, the aerodynamic

surface forces as well as the short-range surface forces can be calculated in frame of the DEM model in more detail, since the solid is treated as disperse phase.

### 5.1.2.1 Aerodynamic surface forces

The aerodynamic surface forces, resulting from the interactions between fluid and solid, depend highly on the relative velocity of both phases. By the reason of complex nature of gas-particle interaction, the aerodynamic surface forces can be identified through analytical methods with extreme effort. The most common way to describe this complex behaviour is: the particle movement may be perceived as a superposition of four simple motions of sphere with the assumption that they are non-interactive (see **Figure 5.1**). First: particle moving in an isotropic flow field (uniform) with constant velocity (i.e. drag force); second: particle accelerating or decelerating in an isotropic flow field (i.e. virtual mass and basset forces); third: particle moving in an anisotropic flow field (non-uniform) with constant velocity (i.e. pressure, Saffman and radiometric forces); fourth: particle rotating in an isotropic flow field with constant angular velocity (i.e. Magnus force).

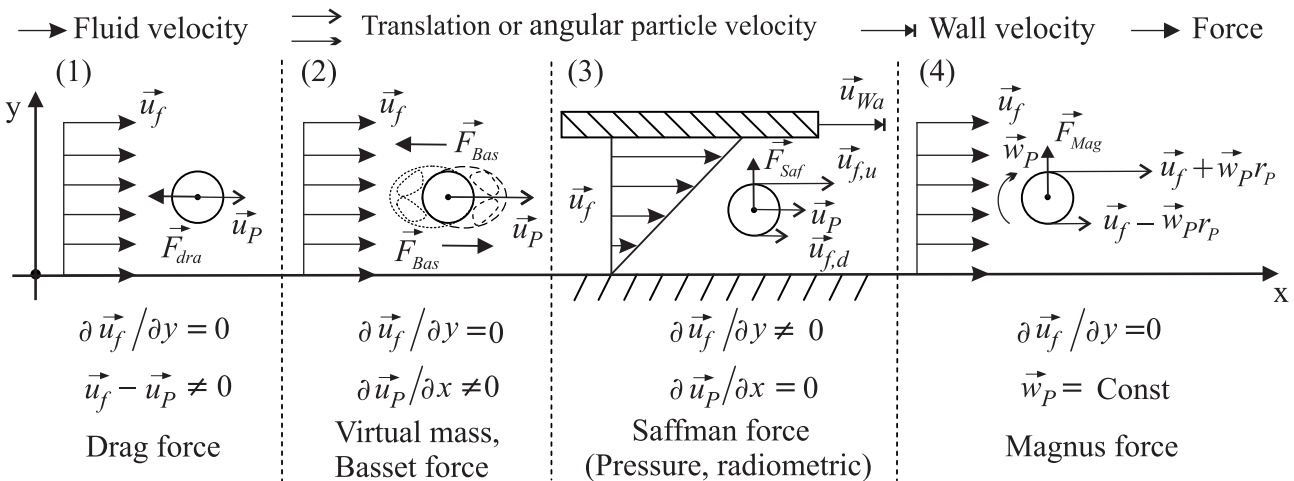


**Figure 5.1:** Description of gas-solid interaction as superposition of four simple motions of sphere (Epple et al. 2012), extended

(1) When a particle moves in an uniform flow filed, where the particle velocity is constant, a force is resulted that resists the particle motion:

**Drag force:** In practical gas-solid flow, the particle velocity  $u_p$  differs, generally, from the gas velocity  $\vec{u}_f$ . The relative velocity (slip velocity) causes a viscous stress and an unbalanced pressure distribution on the particle surface, which yields a force, known as the drag force. In an isotropic flow field, the drag force of a moving particle with a constant velocity acts opposite to the direction of particle velocity. It can be determines as follows:

$$\vec{F}_{dra} = \frac{1}{2} C_{dra} A_p \rho_f (\vec{u}_f - \vec{u}_P) |\vec{u}_f - \vec{u}_P|. \quad (5.7)$$

Here,  $A_p$  represents the cross-section area of particle (the exposed area to the incoming flow),  $\rho_f$  is the gas density and  $C_{dra}$  denotes the drag coefficient that is a function of particle Reynolds number:

$$Re_p = \frac{\rho_f d_p |\vec{u}_f - \vec{u}_P|}{\mu_f}, \quad (5.8)$$

where  $\mu_f$  is the dynamic viscosity of fluid. For creeping flow regime ( $Re_p \ll 1$ ), where the viscous effect dominates the flow and the inertia is negligible, the drag coefficient is determined by Stocks as:

$$C_{dra} = \frac{24}{Re_p}. \quad (5.9)$$

In the transition flow regime ( $1 \leq Re_p \geq 10^3$ ), there are a lot of approximations with sufficient accuracy available, for example, the relationship of (Schiller and Naumann 1933):

$$C_{dra} = \frac{24}{Re_p} \left( 1 + 0.15 Re_p^{0.687} \right). \quad (5.10)$$

In the creeping flow and the transition regimes, the drag force decreases with increasing the particle Reynolds number. For flow regime ( $10^3 \leq Re_p \geq 3 \cdot 10^5$ ), where the inertia is predominant, the drag coefficient is defined from Newton's experiments ( $C_{dra} = 0.44$  independent of  $Re_p$ ). For higher particle Reynolds numbers, the drag coefficient drops to about 0.07 for a spherical particle in incompressible flow and then rises again to about 0.3.

In the literature, there are a lot of experimental works and analytical studies on the drag coefficient for a single sphere at various particles Reynolds numbers. These data have been collected into a drag coefficient curve for a fixed sphere particle (see **Figure 5.2**) by (Schlichting and Gersten 2000).

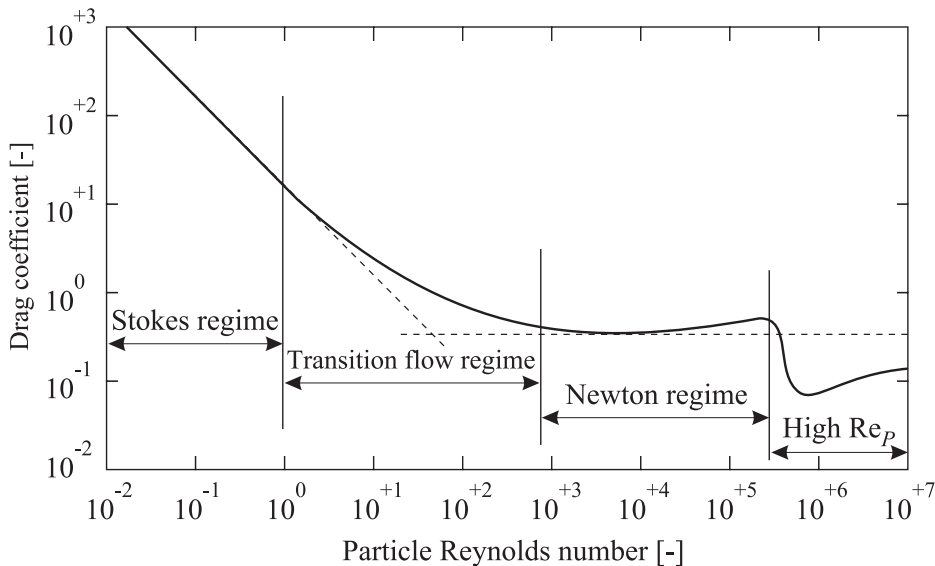


**Figure 5.2:** Drag coefficient curve for fixed sphere particle (Schlichting and Gersten 2000)

(2) When a particle moves in an uniform flow filed, where a particle velocity changes, additional forces related to particle acceleration or decelerating can arise:

**Virtual mass force:** During the acceleration or the deceleration of a particle in a fluid, the surrounding fluid (boundary layer) due to the adhesion to the particle surface must be accelerated or decelerated, too. Here, a wake vortex is generated, which its vorticity depends highly on particle Reynolds number. Consequently, an additional form of resistance referred to as virtual mass, also called as carried mass or added mass, is induced. The virtual mass force that is directed opposite to the gradient of the particle velocity is proportional to the relative acceleration or deceleration and to the density ratio between fluid and solid phases. It can be generally expressed by:

$$\vec{F}_{ver} = C_{ver} \frac{\rho_f}{\rho_p} m_p \left( \frac{D\vec{u}_f}{dt} - \frac{d\vec{u}_p}{dt} \right), \quad (5.11)$$

where  $C_{ver}$  is a correction factor that considers the disproportionate increase in the virtual mass force by the reason of generated wake vortex. At lower particle Reynolds numbers, this factor has the value of unity, while it rises significantly at higher relative velocities (Sommerfeld 1996):

$$C_{ver} = 1.05 - \frac{0.066}{A^2 + 0.12}, \quad (5.12)$$

with:

$$A = \frac{\left| \vec{u}_f - \vec{u}_p \right|^2}{d_p \left| \frac{d}{dt} (\vec{u}_f - \vec{u}_p) \right|}. \quad (5.13)$$

**Basset force:** The Basset force, also known as history force, is caused due to relative acceleration or deceleration of particle to fluid. During the acceleration or the deceleration process, the shape and volume of boundary layer is subjected to continuous changes. The Basset force occurs during the unsteady processes as well as by fluctuations of particle movement in quasi-steady state flow. It describes the temporal delay in boundary layer development when the relative velocity changes. The resulting force depends highly on the density ratio between fluid and particle as well as on the relative acceleration or deceleration. The Basset force is directed opposite to the gradient of the relative velocity and can be calculated as follows:

$$\vec{F}_{bas} = 9 \sqrt{\frac{\rho_f \mu_f}{\pi}} \frac{m_p}{\rho_p d_p} C_{bas} \int_{t_0}^t \frac{\frac{D\vec{u}_f}{dt} - \frac{d\vec{u}_p}{dt}}{\sqrt{t - t_{relax}}} dt_{relax}, \quad (5.14)$$

where  $t_{relax}$  denotes the Stokes relaxation time (see equation (3.11)) and  $C_{bas}$  is a correction factor that describes the dependence of this force on the particle Reynolds number.

$$C_{bas} = 2.88 + \frac{3.12}{(1+A)^3}. \quad (5.15)$$

The Basset force is of relevance if the relative acceleration or deceleration rate is high, the time change is much greater than the Stokes relaxation time and/or the density difference between fluid and solid has considerable value.

(3) When a particle moves at constant velocity in an anisotropic flow field, where velocity, pressure or temperature gradients are existent, additional forces correlated to these gradients can arise:

**Pressure gradient force:** The dynamic buoyancy force acts on the particle surface due to the existence of pressure gradient in fluid. The resulting force is in the opposite direction of pressure gradient (i.e. from higher pressure region to lower pressure region). The force due to the pressure gradient can be expressed by the following equation:

$$\vec{F}_{pre} = -\frac{\pi}{6} d_p^3 \nabla p. \quad (5.16)$$

**Saffman force:** When a particle moves at a constant velocity in a flow field, where a velocity gradient exists (e.g. near the wall or in a shear flow), the opposite sides of particle undergo different velocities. Subsequently, a pressure gradient on the particle surface is formed due to the velocity distribution. While a positive pressure arises at side with lower velocity, a negative pressure forms at the faster side. This leads to a lift force perpendicular to the relative velocity and in opposite direction to the pressure gradient. The resulted force was determined analytically by (Saffman 1965):

$$|\vec{F}_{saf}| = 6.46 \frac{d_p^2}{4} \sqrt{\rho_f \mu_f} \left| \frac{\partial \vec{u}_f}{\partial y} \right| |\vec{u}_f - \vec{u}_P|. \quad (5.17)$$

The Saffman force depends on the particle diameter, the velocity gradient and the relative velocity of both phases. For three-dimensional flows, the Saffman force can be expressed as follows:

$$\vec{F}_{saf} = 6.46 \frac{\pi d_p^2}{4} \sqrt{\frac{\rho_f \mu_f}{|w_f|}} (\vec{u}_f - \vec{u}_P) \times \vec{w}_f f(\text{Re}_p, \text{Re}_s), \quad (5.18)$$

with the angular velocity vector of fluid phase:

$$\vec{w}_f = \frac{\nabla \vec{u}_f}{2}, \quad (5.19)$$

where  $\text{Re}_s$  represents the Reynolds number of shear flow. It is calculated on the basis of relative angular velocity of fluid and solid phases:

$$\text{Re}_s = \frac{\rho_g d_p^2 |\vec{w}_P - \vec{w}_f|}{\mu_f}. \quad (5.20)$$

The correction factor  $f(\text{Re}_p, \text{Re}_s)$  that ensures the dependence of Saffman force on particle Reynolds number is calculated with the aid of threshold function (Mei 1992):

$$f(\text{Re}_p, \text{Re}_s) = \begin{cases} \left(1 - 0.3314 \sqrt{\frac{\text{Re}_s}{2\text{Re}_p}}\right) \exp\left(\frac{\text{Re}_p}{10}\right) + 0.3314 \sqrt{\frac{\text{Re}_s}{2\text{Re}_p}}, & \text{case } \text{Re}_p \leq 40 \\ 0.0524 \sqrt{\frac{\text{Re}_s}{2}}, & \text{case } \text{Re}_p > 40 \end{cases}. \quad (5.21)$$

**Radiometric force:** In a region, where a fluid temperature gradient or non-uniform radiation field exists, a particle is subjected to radiometric force caused by the temperature. It is directed towards the region of lower temperature (i.e. opposite to the temperature gradient). If the mean free path of fluid is much smaller than the particle diameter, the radiometer force can be calculated as:

$$\vec{F}_{rad} = -\frac{3\pi}{2} \eta_f^2 d_p \frac{R}{p} \nabla T_p, \quad (5.22)$$

with  $\nabla T_p$  the temperature gradient on the particle, which is proportional to the temperature gradient of fluid  $\nabla T_f$ :

$$\nabla T_p = \frac{3\lambda_f}{2\lambda_f + \lambda_p} \nabla T_f. \quad (5.23)$$

The mean free path of fluid represents the average distance that can cover by a moving gas molecular till the next collision with other object occurs. It can be estimated from the kinetic theory of gases (Chapman and Cowling 1970). The constant  $R$  is the ideal gas constant, the parameters  $\lambda_f$  and  $\lambda_p$  denote to the thermal conductivities of fluid and solid phases, which are material properties. For flow with low temperature gradient, the radiometer force should only be considered for particles of submicron size. At higher temperature gradients, the radiometer force is, however, relevant for larger particles.

**Concentration gradient force:** If the particle is found in flow, where a concentration gradient, so the particle will accelerate in the direction of negative concentration gradient.

(4) When a particle rotates with a constant angular velocity in an uniform flow filed, an addition lift force related to this rotation can arise:

**Magnus forces:** A similar effect as in the shear flow can be obtained when the particle rotates by itself. The particle rotation leads also to an irregular pressure distribution on the particle surface as a result of relative velocity difference between the particle surface and the incoming flow. The resulting shear/lift force is called Magnus force and was measured by (Tsuji, Morikawa and Mizuno 1985) as:

$$\vec{F}_{mag} = \frac{\pi}{8} d_p^2 c_{mag} \rho_g \frac{|\vec{u}_f - \vec{u}_P|}{|\vec{w}_P - \vec{w}_f|} [(\vec{u}_f - \vec{u}_P) \times (\vec{w}_f - \vec{w}_P)]. \quad (5.24)$$

For the lift coefficient  $c_{mag}$ , the following relation is applied:

$$c_{mag} = \begin{cases} 0.4G, & \text{if } G \leq 1 \\ 0.4, & \text{if } G > 1 \end{cases}, \quad (5.25)$$

with:

$$G = \frac{d_p}{2} \frac{|\vec{w}_P - \vec{w}_f|}{|\vec{u}_f - \vec{u}_P|}. \quad (5.26)$$

The Magnus force depends on the particle diameter, the relative translational and angular velocities both phases. The main reason for particle rotation is the particle–wall collisions. Therefore, the Magnus force is of relevance for granular flows, in particularly when the wall has a significant effect on the particle movements (e.g. particle flow in a pipe). However, the influence of particle rotation on the drag can be neglected at lower particle Reynolds number. At high particle Reynolds numbers, this force becomes important and should be considered. In this context, (Sommerfeld 1996) compared the Magnus and Saffman forces with the drag force. A margin of particle sizes is defined, at which these forces should not be disregarded anymore.

### 5.1.2.2 Short-range surface forces

The position and the angular displacement of particles are also influenced by the short-range forces that act between the particle–particle/wall. These forces can be classified as adhesive and contact forces.

The contact force is of particular relevance in dense gas–solid flows. The contact force is determined using the Voigt–Kelvin model, which describes the viscoelastic and time–dependent behaviour of collision. The Voigt–Kelvin model is composed of a Hooke’s spring and a Newton’s damper, which are connected in parallel. The spring is used for modelling the reversible deformation, while the damper for time–dependent and irreversible deformation. Since the Voigt–Kelvin model can only describe the normal interaction, a sliding element is introduced to determine the tangential interaction.

The adhesive force depends heavily on the particle diameter, the particle density, and the mechanical properties of contacting objects. On the basis of adhesion formation, the adhesive forces can be divided into two categories, viz. the adhesive forces associated either with or without physical contact. The adhesive forces without physical contact include van der Waals and electrostatic forces. The adhesive forces with physical contact are based on the formation of a physical bond between particles and/or particles and wall. This connection can occur as solid bridges (sintering, melting or bonding) or by wetting the particle surface (adsorption or movable liquid bridges).

Here, it should be mentioned that the short-range forces cannot be calculated, before the collision partners are identified. This can be achieved employing a detection collision model with a specific criterion. One example is the contact criterion, where the distance between the centres points of two particles should be smaller than the sum of both radii (see section 5.1.2.2.1). Another example is the criterion of liquid bridge formation. A liquid bridge will build when the distance between the centres points of two particles falls below the bridge critical length (see section 5.1.2.2.3).

### 5.1.2.2.1 Contact force

In the discrete element method, it is assumed that the particles can overlap each other or penetrate into the wall. The contact point is seen as a line in 2D or as a surface in 3D cases. Depending on the penetration depth, the resulting contact force can be determined and will be calculated here as an example for particle–particle collision. Similar procedures are used to calculate the contact force due to the particle–wall collision with the assumptions that the wall has an infinite radius and its values of translational and angular velocities are zero. The contact between two spherical particles  $i$  and  $j$  with the position vectors  $\vec{r}_i$  and  $\vec{r}_j$ , the radii  $r_i$  and  $r_j$ , the masses  $m_i$  and  $m_j$ , the translational and angular velocities  $\vec{u}_i$ ,  $\vec{u}_j$ ,  $\vec{w}_i$ ,  $\vec{w}_j$ , is shown in **Figure 5.3**.

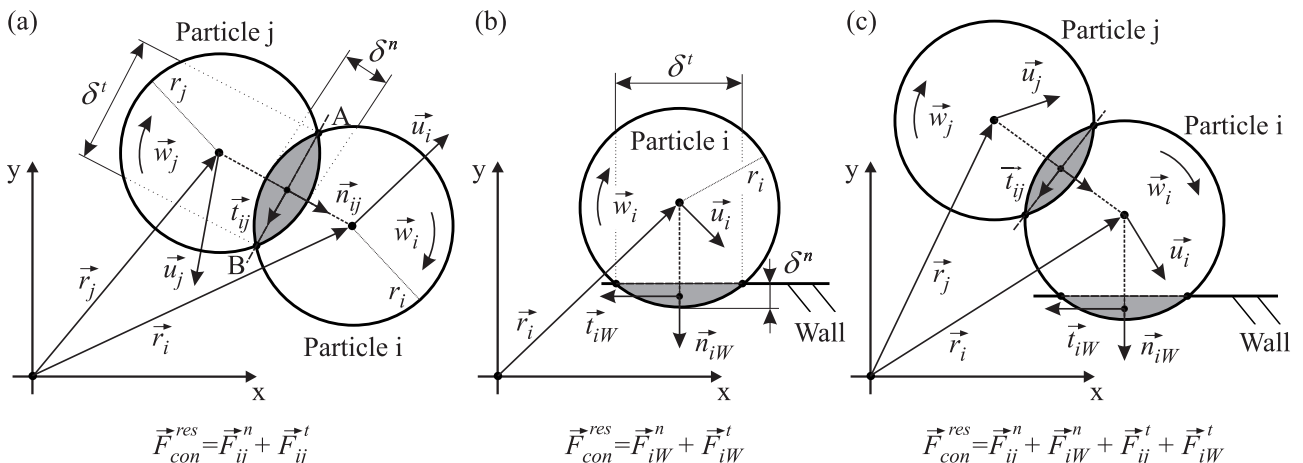


**Figure 5.3:** Contact force (a) particle–particle collision, (b) particle–wall collision and (c) particle–particle/wall collisions

The relative velocity at the contact point is obtained by summation of normal and tangential components under the consideration of translational and angular velocities of collided particles:

$$\vec{u}_{ij} = \vec{u}_{ij}^n + \vec{u}_{ij}^t, \quad (5.27)$$

with:

$$\begin{aligned} \vec{u}_{ij}^n &= \left( (\vec{u}_i - \vec{u}_j) \cdot \vec{n}_{ij} \right) \cdot \vec{n}_{ij} = \left| \vec{u}_{ij}^n \right| \vec{n}_{ij}, \\ \vec{u}_{ij}^t &= (\vec{u}_i - \vec{u}_j) + (r_i \vec{w}_i + r_j \vec{w}_j) \times \vec{n}_{ij} - \vec{u}_{ij}^n = \left| \vec{u}_{ij}^t \right| \vec{t}_{ij}. \end{aligned} \quad (5.28)$$

While the normal unit vector is calculated using the radii and the position vectors of collision partners, the tangential unit vector is determined using the tangential relative velocity:

$$\begin{aligned} \vec{n}_{ij} &= \frac{\vec{r}_i - \vec{r}_j}{\left| \vec{r}_i - \vec{r}_j \right|}, \\ \vec{t}_{ij} &= \frac{\vec{u}_{ij}^t}{\left| \vec{u}_{ij}^t \right|}. \end{aligned} \quad (5.29)$$

The overlap area between two particles or particle–wall is characterised by the normal and tangential penetration depths. The penetration depth in normal direction  $\delta^n$  is defined as follows:

$$\delta^n = r_i + r_j - \left| \vec{r}_i - \vec{r}_j \right|. \quad (5.30)$$

The tangential penetration depth cannot be explicitly determined from the particle positions, but can be calculated through time integration of relative tangential velocity at the contact point:

$$\delta^t = \int_{t_0}^t \left| \vec{u}_{ij}^t \right| dt_P \quad (5.31)$$

By knowing the distribution of force on the contact point, it is possible to calculate the resultant contact force. The determination of contact force distribution needs, however, exact physical description of collision, which is a complex process. This is due to the dependence on various geometrical and physical factors, in particular the mechanical properties and the motion state of particles in contact. For this reason, the description of collision process should be simplified to some extent. In this context, the distribution of force over the contact area can be modeled employing a mechanical analogue system. Based on the well-known viscoelastic Voigt–Kelvin model that describes the time-dependent behaviour of collision, the physical effects of particles interaction during the collision can be described. The Voigt–Kelvin model consists of a Hookean spring (with stiffness  $k$ ) and a Newtonian dashpot (with viscosity  $\eta$ ), connected in parallel. While the spring describes the purely elastic collisions (i.e. the reversible deformation), the damper represents the time-dependent irreversible deformation. According to Voigt–Kelvin model, a collision can occur elastically or inelastically. If the resulted deformation during the collision is stored as potential energy and is completely transformed back into kinetic energy, the collision considers then as elastic. In elastic collisions, the sum of kinetic energies of colliding particles before and after the collision is the same (i.e. neither damping nor friction forces are regarded). Consequently, the damping element has to be

omitted in these cases. In inelastic collisions, by contrast, a part of the stored potential energy is dissipated in other energy forms, like for example inner energy.

The resulted contact force is calculated as the sum of both tangential and normal components. The tangential contact force is assumed to be either a static or sliding force. The static friction is modeled using the damper element, while the sliding friction that occurs due to the relative velocity between the collision partners is modeled employing the sliding element. The Voigt–Kelvin model can describe the normal contact force (see **Figure 5.4–(a)**), but the model should be extended by integration a sliding component in order to determine the tangential contact force (see **Figure 5.4–(b)**).

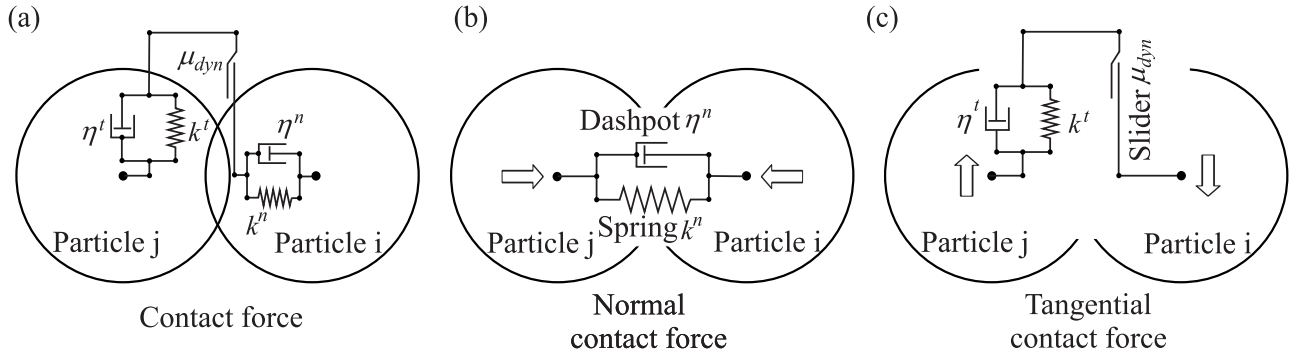


**Figure 5.4:** Mechanical analogue according to Voigt–Kelvin model (a) the resultant contact force, (b) the normal contact force and (c) the tangential contact force

The resulting contact force on the particle  $i$  is obtained by summing up all normal and tangential contact forces that act simultaneously between the particle  $i$  and other particles and walls:

$$\vec{F}_{con}^{res} = \sum_{\substack{k=1 \\ k \neq i}}^{k=N} \left( \vec{F}_{con,ik}^n + \vec{F}_{con,ik}^t \right). \quad (5.32)$$

The index  $N$  represents the number of contacts for the particle  $i$ . Based on the Voigt–Kelvin model, the normal contact force, resulting from the sum of the elastic force  $\vec{F}_{ela}^n$  and the damping force  $\vec{F}_{dam}^n$ , is described by the differential equation of the spring–damper system:

$$\vec{F}_{con,ij}^n = m_{ij} \frac{d\vec{u}_{ij}^n}{dt_P} = \underbrace{-k^n (\delta^n)^a \vec{n}_{ij}}_{\vec{F}_{ela}^n} - \underbrace{\eta^n \vec{u}_{ij}^n}_{\vec{F}_{dam}^n}, \quad (5.33)$$

where  $k^n$  is the normal stiffness constant,  $\eta^n$  is the normal coefficient of damping,  $m_{ij}$  is the reduced mass (effective mass; see equation (4.13)),  $\delta^n$  and  $\vec{u}_{ij}^n$  represent the displacement and the relative velocity in the normal direction. Specifying the exponent  $a$  in equation (5.33) allows one of several spring contact models to be selected. The linear approach ( $a=1$ ) proposed by Hooke and also used by (Cundall and Strack 1979) shows a satisfactory accuracy in most applications. Non-linear approaches proposed by (Hertz 1882), (Maw, Barber and Fawcett 1976) ( $a \neq 1$ ) improve the accuracy of the force calculation, but lead to increase in the computational costs. This is due to the consideration of the changes in the geometrical and physical properties of the colliding particles. A detailed comparison of different contact force models was reviewed by (Di Renzo and Di Maio 2004, Kruggel-Emden et al. 2007).

To calculate the normal contact force, the stiffness coefficient and the damping parameter in the normal direction must be determined. For the approach of Hooke with a

linear dependence between the spring force and the penetration depth, the stiffness coefficient is calculated from the ratio of maximum normal contact force to maximum penetration depth:

$$k^n = \frac{|\vec{F}_{con,max}^n|}{\delta_{max}^n}. \quad (5.34)$$

Depending on the maximum relative velocity between the colliding objects, the maximum normal contact force and the maximum penetration depth can analytically be determined using a complex non-linear model developed by Di Renzo (Di Renzo and Di Maio 2004). The normal stiffness coefficient can also be defined depending on the properties of collision partners as:

$$k^n = \sqrt[3/2]{\frac{1}{\gamma_{ij}}}, \quad (5.35)$$

with:

$$\gamma_{ij} = \sqrt[3]{\frac{9}{64} \frac{r_i + r_j}{r_i r_j} \left( \frac{1 - v_i}{G_i} + \frac{1 - v_j}{G_j} \right)^2}. \quad (5.36)$$

The shear modulus  $G$ , which describes the linear elastic deformation of a body due to a shear stress, and Poisson's ratio  $\nu$  that enables the calculation of the transverse contraction of the body, are material properties and can be defined experimentally. Typical values of shear modulus and Poisson's ratio for different materials are listed in **Table 5.1**.

**Table 5.1:** Shear modulus and Poisson's numbers of different materials

Material	Shear modulus [GPa]	Poisson's ratio [-]
Aluminium	26	0.34
Copper	45	0.33
Glass	31	0.17
Rubber	0.0006	0.5
Steel	80	0.29

The resulting stiffness coefficient is in the range of  $(10^4 - 10^9 \text{ N/m})$  and depends to a large extent on the material properties of the contacting partners.

The dissipation of energy during an inelastic collision can be defined through the coefficient of restitution in the normal direction  $e^n$ , which is also known as the collision coefficient. The coefficient of restitution is defined as the ratio of the normal relative velocity at the contact point after the contact to that before the contact (index: 0):

$$e^n = \frac{|\vec{u}_{ij}^n|}{|\vec{u}_{ij}^{(0)}|} = \sqrt{\frac{h}{h^{(0)}}}. \quad (5.37)$$

The coefficient of restitution can be experimentally measured. Here, the particle is dropped from the height  $h^{(0)}$  to a large plate that has the same material properties as the contacting objects, and then the height of the rebound is measured. The coefficient of

restitution depends on several parameters, e.g. material paring, collision velocity and/or particle shape.

In **Table 5.2**, the coefficient of restitution is listed for different material pairings under the consideration of spherical particles and low relative velocities. At higher relative velocities, additional part of kinetic energy is irreversibly dissipated in form of deformation energy, which results in decreasing the restitution coefficient.

**Table 5.2:** Restitution coefficient of different material parings at low relative velocities

Material pairing	Coefficient of restitution [-]
Glass–Glass	0.96
Iron–Iron	0.67
Lead–Lead	0.16
Rubber–Rubber	0.75
Steel–Steel	0.90
Wood–Wood	0.48

The determination of damping parameter in normal direction, which describes the energy dissipation during the collision, is expressed by:

$$\eta^n = \begin{cases} \alpha_{Dam}(e^n) \sqrt{m_j k^n} (\delta^n)^b & \text{for } e^n \neq 0 \\ 2\sqrt{m_j k^n} (\delta^n)^b & \text{for } e^n = 0 \end{cases}. \quad (5.38)$$

The empirical constant  $\alpha_{Dam}(e^n)$  can be calculated with the aid of following equation:

$$\alpha_{Dam}(e^n) = -\frac{2 \ln e^n}{\sqrt{\pi^2 + \ln^2 e^n}} \quad \text{for } e^n \neq 0. \quad (5.39)$$

The empirical constant  $\alpha_{Dam}(e^n)$  is a function of restitution coefficient in normal direction  $e^n$ . This correlation is valid for particle–particle as well as particle–wall collisions. The influence of dissipation on the normal contact force can be adjusted with the exponent  $b$ . By combining the linear spring model ( $a=1$ ) with a linear visco–elastic damping element ( $b=0$ ), a complete linear model can be obtained. A partial non–linear visco–elastic contact model that combines a non–linear spring approach by Hertz ( $a \neq 1$ ) with a linear visco–elastic damping element ( $b=0$ ) shows by lower relative velocities a reduction in coefficient of restitution. A fully non–linear visco–elastic model tends, by the contrast, to increase the coefficient of restitution at lower relative velocities. A detailed comparison of different contact force models is reviewed by (Di Renzo and Di Maio 2004) and (Zhu et al. 2007).

If the stiffness coefficient value in normal direction is underestimated or the relative collision velocities are very high, great penetration depths raise between the collision partners. As a result of this, the elastic force becomes much bigger than the damping force, which can lead to unrealistic contact forces and consequently an erroneous in the energy balance. On the other hand, traction forces between the collision partners can take place when the elastic force becomes smaller than the damping force by the reason of high damping coefficient used. Due to the fact that rigid objects can only transmit the compressive forces, the influence of the traction forces on the determination of contact force can be disregarded. (Lungfiel 2002) introduced in

his work for determining the contact forces in the gas–solid flow a maximum function that neglects the effect of traction forces as:

$$\vec{F}_{con,ij}^n = \max(0; -k^n (\delta^n)^a \vec{n}_{ij} - \eta^n \vec{u}_{ij}^n). \quad (5.40)$$

The modelling of resulting tangential contact force is based on the spring–damper–slider system, where the tangential contact force is assumed to be either a static or sliding force. The selection of friction force is given by following differential equation:

$$\vec{F}_{con,ij}^t = m_{ij} \frac{d\vec{u}_{ij}^t}{dt_p} = \begin{cases} \underbrace{-k^t (\delta^t)^a - \eta^t \vec{u}_{ij}^t}_{\vec{F}_{ela}^t}, & \text{for } |\vec{F}_{static}^t| \leq |\vec{F}_{slide}^t| \\ \underbrace{\vec{F}_{static}^t}_{\vec{F}_{static}} & \\ \underbrace{-\mu_{dyn} |\vec{F}_{con,ij}^n| \vec{t}_{ij}^t}_{\vec{F}_{slide}^t}, & \text{for } |\vec{F}_{static}^t| > |\vec{F}_{slide}^t| \end{cases}. \quad (5.41)$$

The static force is modeled by a spring–damper system similar to the treatment of normal contact force. The dynamic friction force is proportional to the amount of normal contact force. The constant of proportionality is called the dynamic friction coefficient  $\mu_{dyn}$ . To determine the tangential contact force the tangential stiffness coefficient  $k^t$ , the tangential damping parameter  $\eta^t$  and the dynamic friction coefficient  $\mu_{dyn}$  have to be known. The tangential stiffness coefficient is calculated using the normal stiffness coefficient and the mechanical properties of colliding objects:

$$k^t = k^n \frac{(1-\nu_i)/G_i + (1-\nu_j)/G_j}{(1-0.5\nu_i)/G_i + (1-0.5\nu_j)/G_j}. \quad (5.42)$$

The shear modulus  $G$  and Poisson's ratio  $\nu$  denote material properties (see **Table 5.1**). The damping parameter in the tangential direction is given by:

$$\eta^t = \begin{cases} \alpha_{Dam}(\beta^t) \sqrt{\frac{2}{7} m_{ij} k^t (\delta^t)^b}, & \text{for } \beta^t \neq 0 \\ 2 \sqrt{\frac{2}{7} m_{ij} k^t (\delta^t)^b}, & \text{for } \beta^t = 0 \end{cases}. \quad (5.43)$$

The empirical constant  $\alpha_{Dam}(\beta^t)$  is a function of the coefficient of restitution in the tangential direction  $\beta^t$ :

$$\beta^t = \frac{|\vec{u}_{ij}^t|}{\left| \vec{u}_{ij}^{t(0)} \right|}, \quad (5.44)$$

where  $\vec{u}_{ij}^{t(0)}$  and  $\vec{u}_{ij}^t$  represent the relative velocity in tangential direction before and after the contact, respectively. The dynamic friction coefficient  $\mu_{dyn}$  can be obtained from such experiments as that are carried out by (Kharaz, Gorham and Salman 1999). The tangential contact force can be linear or non-linear modeled depending on the required accuracy of the contact force curve. Non-linear approaches of varying complexity are published and tested by

several authors. In general, non-linear models tend to higher computational complexities as well as to higher costs regarding the implementation phase. In the literature, detailed comparison studies of different contact force models can be found (summarised by (Di Renzo and Di Maio 2004) and (Zhu et al. 2007)).

The tangential penetration depth is determined with the aid of the following threshold function:

$$\vec{\delta}' = \delta' \vec{t}_{ij} = \begin{cases} \vec{\delta}^{t(0)} R + \int_{\tau_0}^{\tau} \vec{u}_{ij} dt_p, & \text{if } |\vec{F}_{static}^t| \leq |\vec{F}_{slide}^t| \\ \frac{\mu_{dyn}}{k'} |\vec{F}_{con,ij}^n| \vec{t}_{ij}, & \text{if } |\vec{F}_{static}^t| > |\vec{F}_{slide}^t| \end{cases}. \quad (5.45)$$

The rotation matrix that is applied to perform a rotation in three-dimensional space of Euclidean geometry can be defined as:

$$R = \begin{bmatrix} (1 - \cos \varphi) h_x^2 + \cos \varphi & (1 - \cos \varphi) h_x h_y - h_z \sin \varphi & (1 - \cos \varphi) h_x h_z + h_y \sin \varphi \\ (1 - \cos \varphi) h_x h_y + h_z \sin \varphi & (1 - \cos \varphi) h_y^2 + \cos \varphi & (1 - \cos \varphi) h_y h_z - h_x \sin \varphi \\ (1 - \cos \varphi) h_x h_z - h_y \sin \varphi & (1 - \cos \varphi) h_y h_z + h_x \sin \varphi & (1 - \cos \varphi) h_z^2 + \cos \varphi \end{bmatrix}, \quad (5.46)$$

with the rotation unit vector:

$$\vec{h} = \frac{\vec{n}_{ij} \times \vec{n}_{ij}^{(0)}}{\left| \vec{n}_{ij} \times \vec{n}_{ij}^{(0)} \right|}, \quad (5.47)$$

and the rotation angle:

$$\varphi = \arcsin \left( \left| \vec{n}_{ij} \times \vec{n}_{ij}^{(0)} \right| \right). \quad (5.48)$$

The calculation of the static force necessitates the tangential penetration depth to be known (see equation (5.41)). However, the tangential penetration depth cannot be explicitly determined, but through time integration of the relative tangential velocity at the contact point (see equation (5.45)). This requires the application of complex numerical algorithm, leading to additional computational effort. Therefore, explicit approaches for calculating the static force should be introduced, e.g. the proposed equation by (Lungfiel 2002):

$$\vec{F}_{static}^t = \mu_{dyn} \frac{\left| \vec{u}_{ij}^t \right|}{\left| \vec{u}_f \right|} \left| \vec{F}_{con,ij}^n \right|, \quad (5.49)$$

where  $\vec{u}_f$  is the gas velocity. The simplification of procedures for calculating the static force and accordingly the tangential contact force is analysed by Götz (2006) with respect to the absolute values after the collision. Here, the calculated tangential restitution coefficient and the angular velocities after the collision are compared with the experimental data at different collision angles  $\alpha$ . The tangential restitution coefficient is defined using the ratio of tangential velocities before and after the collision. The contact force is determined employing a linear model after Hooke and a non-linear model based on Hertz theory, where the damping force is disregarded. The applied particle diameter and density are ( $d_p = 5$  mm) and ( $\rho_p = 4000$  kg/m<sup>3</sup>), respectively. Furthermore, the relative collision velocity is (3.9 m/s) that equates to particle velocity before the collision due to the zero values of wall translational and angular velocities.

The comparison shows a very good agreement with the experimental data over a large range of collision angles (see **Figure 5.5**). The coefficient of restitution in tangential direction is, however, overestimated at lower collision angles, where the particle collides almost vertically in direction to wall. As previously mentioned, the influence of selected contact model is insignificant on the macroscopic physical values after the collision. Compared to complex, non-linear model, the efficient linear approach provides better accuracy, especially at lower collision angles. Similar results are also obtained by Di Renzo. Finally, it should be noted that these results are only valid to completely elastic collision models. For partial or fully non-linear visco-elastic models, this matter stills an open issue which needs to be clarified through further investigations.

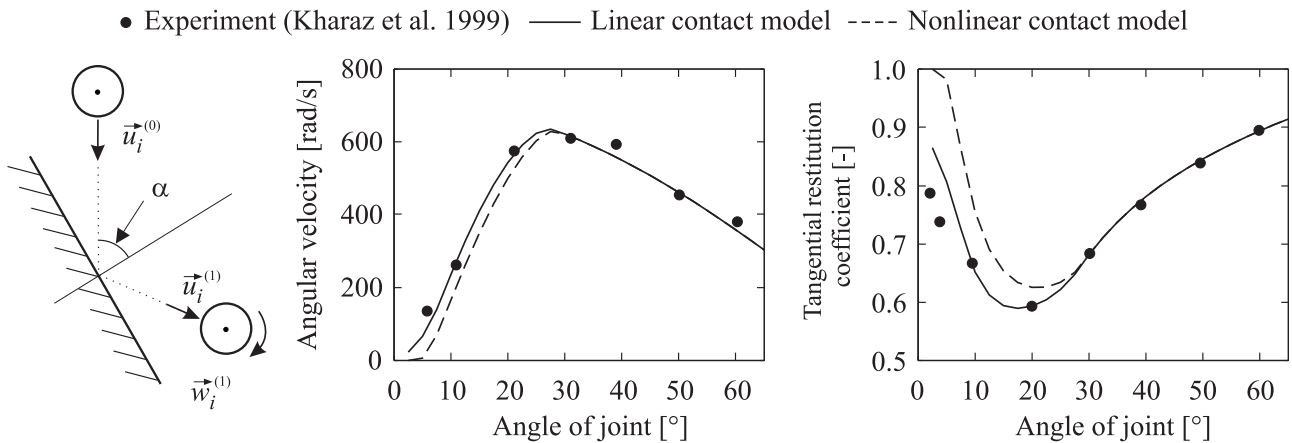


**Figure 5.5:** Angular velocity after the collision and tangential restitution coefficient (Götz, 2006); comparison between simulation (considered equation (5.49)) and experiment

All in all, the resulting contact force can be determined with the sum of normal and tangential components by means of restitution coefficient, the spring constant and the dynamic coefficient of friction. These constants that have a decisive influence on the accuracy and efficiency of simulations are functions of mechanical properties of collision partners. The restitution coefficient in normal and tangential directions can be defined by the shear modulus and the Poisson's ratio. The damping parameter in normal and tangential directions depends on the coefficient of restitution. The dynamic friction coefficient can be obtained from experiments.

### 5.1.2.2 Adhesive forces without physical contact

If the size of particle decreases, the inter-particle adhesive forces without physical contact between particles or particle and wall will then increase up to the level that should not be disregarded anymore. This is due to the fact that they can significantly influence the particles trajectories. The van der Waals force and the electrostatic force are the main sources of short-range adhesive forces without physical contact (see **Figure 5.6**).

**Van der Waals force:** Van der Waals referred in 1873 to the existence of electromagnetic force between real gas molecules or atoms, resulting from the dipoles interactions. The van der Waals force consists of three types of attractive intermolecular forces: the force caused by the interactions between two permanent dipoles, the force caused by two instantaneously induced dipoles and the force caused by dipole-induced dipole. The interactions of permanent dipoles of molecules lead to electrostatic force such as a dipole-dipole interaction in hydrogen chloride HCl, where the polar molecule end with positive charge will attract the negative end of other molecules. The instantaneous dipole-induced dipole force, also known as London force, results from the interacting molecules, where the movements of electrons of both molecules influence each other. The induced dipole force caused by the very

fast changing in atom dipole. This dipole fluctuations results in an electric field that affects the neighbouring atoms polarisability. Here, the polarisability is the measure of changing electron cloud distribution of molecule by an external electric field. The induced dipole of neighbouring atom tends to move in phase with original state, which leads to an attractive atomic force (Fan and Zhu 2005).

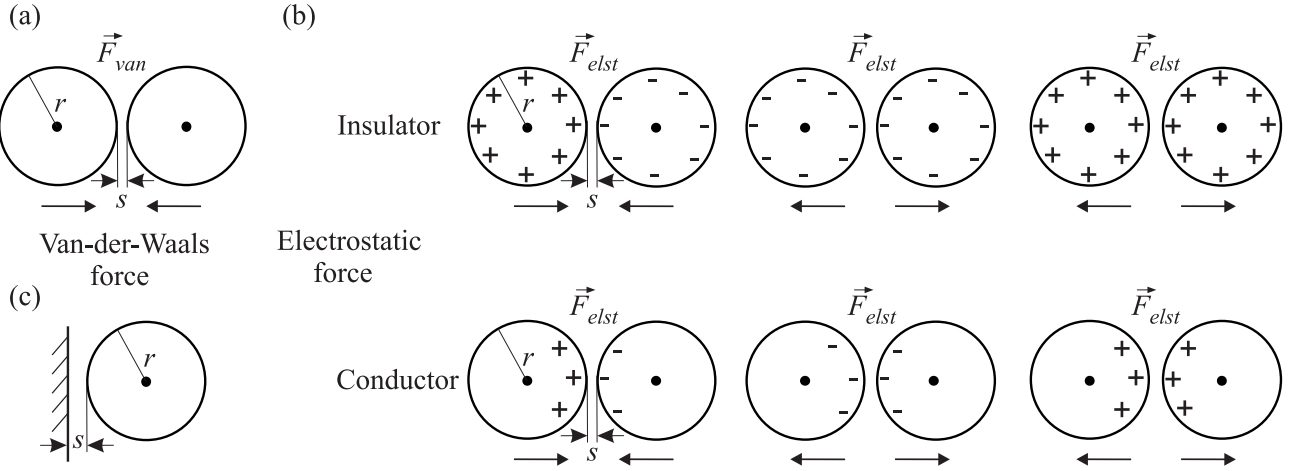


**Figure 5.6:** The short-range adhesive forces without physical contact: (a) van der Waals force (particle–particle), (b) electrostatic force (particle–particle: insulator or conductor) and (c) van der Waals or electrostatic force (particle–wall)

In general, the van der Waals force describes the dipole–dipole interactions between atoms, molecules and surface and can occur between two microscopic molecules or between two macroscopic bodies (e.g. particle–particle or particle–wall). Here, different approaches can be utilized to determine the van der Waals force. While the theory of London and van der Waals is used for microscopic bodies, the theory of Lifshitz and van der Waals is applied to macroscopic bodies.

The van der Waals force between two atoms or molecules ( $i$  and  $j$ ) separated by a distance  $s$  can be expressed by:

$$\vec{F}_{van} = \frac{\partial E}{\partial s} \vec{s}, \quad (5.50)$$

where  $\vec{s}$  represents the unit vector and  $E$  denotes to the potential energy of interaction that can be calculated employing the theory of London and van der Waals as:

$$E = -\frac{\lambda_{ij}}{s_{ij}^6}. \quad (5.51)$$

The constant  $\lambda_{ij}$ , which is generally referred to as London constant, depends on the characteristic of interacting molecules or atoms. For microscopic bodies, the energy of interaction between two objects  $i$  and  $j$  can be obtained according to Hamaker by the use of additively concept. This means by integration all interactions energies of molecules that exist in the objects:

$$E = - \int_{V_i} \int_{V_j} \frac{\lambda_{ij}}{s_{ij}^6} n_i n_j dV_i dV_j, \quad (5.52)$$

where  $V_i$  and  $V_j$  are the volume of the objects ( $i$  and  $j$ ),  $n_i$  and  $n_j$  represent the atom densities, also known as number density (i.e. number of atoms per unit volume in body). For

two spherical bodies of radii  $r_i$  and  $r_j$ , the van der Waals force can be calculated by inserting equation (5.52) in equation (5.50):

$$\vec{F}_{van,ij} = \frac{A_{ij}}{6s_{ij}^2} \vec{r}_{ij}, \quad (5.53)$$

with the position vector  $\vec{r}_{ij}$  and the relative radius (reduced radius) that allows treating two bodies as a one object:

$$s_{ij} = \frac{r_i r_j}{r_i + r_j} = \left( \frac{1}{r_i} + \frac{1}{r_j} \right)^{-1}, \quad (5.54)$$

and Hamaker constant:

$$A_{ij} = \pi^2 n_i n_j \lambda_{ij}. \quad (5.55)$$

Similar procedures are followed to calculate the van der Waals force between a spherical body with a radius  $r_j$  and a wall. With the assumption that the wall has an infinite radius, the equation (5.54) is reduced. The van der Waals force can then be determined as:

$$\vec{F}_{van,iw} = \frac{A_{ij} r_i}{12 s_{iw}^2} \vec{r}_{iw} = \frac{\pi^2 n_i n_j \lambda_{ij} r_i}{6 s_{iw}^2} \vec{r}_{iw}. \quad (5.56)$$

The Hamaker constant between two different materials in air can be calculated with the aid of Hamaker constants for each material:

$$A_{ij} = \left( A_{ii} A_{jj} \right)^{\frac{1}{2}}. \quad (5.57)$$

If the materials  $i$  and  $j$  interact thorough a third material  $k$ , the Hamaker constant is expressed by:

$$A_{ijk} = (A_{ii} - A_{kk})(A_{jj} - A_{kk}). \quad (5.58)$$

In case of macroscopic rigid bodies, where atoms are closely packed, the concept of additively is insufficient to calculate the van der Waals force. The additively problem can be eliminated by using the macroscopic theory of Lifshitz and van der Waals. This can be realised by regarding the solids as a continuum, where the van der Waals force can be determined in term of bulk properties, e.g. the dielectric constants and the refractive indices of the substances. The modified Hamaker constant is then defined as:

$$A = \frac{3}{4\pi} h \varpi. \quad (5.59)$$

The Lifshitz–van der Waals constant  $h \varpi$  depends on the substances properties; but is independent of material geometry. For two bodies of materials  $i$  and  $j$  separated by a medium  $k$ , the Lifshitz–van der Waals constant is given by:

$$h \varpi = h \int_0^\infty \left( \frac{\varepsilon_{rel,i} - \varepsilon_{rel,k}}{\varepsilon_{rel,i} + \varepsilon_{rel,k}} \right) \left( \frac{\varepsilon_{rel,j} - \varepsilon_{rel,k}}{\varepsilon_{rel,j} + \varepsilon_{rel,k}} \right) d\zeta, \quad (5.60)$$

where  $h$  denotes to Planck constant. The dielectric constant  $\varepsilon_{rel,i}$  describes the relative permittivity of the dielectric substance  $i$  along the imaginary frequency axis  $\zeta$ . Many

approximations have been suggested to enable the calculation of Lifshitz–van der Waals constant due to the fact that the solving of equation (5.60) is non-trivial (summarised by (Fan and Zhu 2005)). By knowing the Lifshitz–van der Waals constant, the modified Hamaker constant and thus the resulted van der Waals force can be calculated.

**Electrostatic force:** The electrostatic effect arises due to different reasons. 1) Particle–particle/wall collisions: during the contact, the interaction between the collided objects can lead to charge the particles surfaces. 2) Corona charging and scattering (electrostatic contact potential difference): if a current flows from an electrode with a high potential into a neutral fluid, the fluid will be ionized and generates an areas of plasma around the electrode. This plasma field enables accordingly charge to be passed from high potential electrode to lower potential region. 3) Thermionic emission in high temperature environment. 4) Other charging mechanisms e.g. colloidal propulsion for dielectric substances in intense electric field (Soo and Deyan 1990), also known as image–charge effect. Coulomb reports in 1785 that “the force of attraction or repulsion between two point charges is directly proportional to the product of magnitude of each charge and indirectly proportional to the square of distance between them”. While particles with opposite charges attract each other, particles with identical polarity are repulsive. In the gas–solid flow, the electrostatic force resulted from the charged particles can highly influences the particles motions and accordingly is of major relevance. The electrostatic force between two charged bodies, although the basic mechanism of electrostatic effect has not fully understood, is given by Coulomb’s law:

$$\vec{F}_{elst,ij} = \frac{1}{4\pi\epsilon_0} \frac{q_i q_j}{s_{ij}^2} \vec{r}_{ij}, \quad (5.61)$$

where  $q_i$  represents the charge carried by the object  $i$ ,  $s_{ij}$  is the distance between centres of both bodies,  $\epsilon_0$  denotes to the electric constant (vacuum permittivity) of the surrounding medium. With the aid of Coulomb’s law, the electrostatic force can be determined for two charged particles with radii  $r_i$  and  $r_j$  made of electrical insulating materials as:

$$\vec{F}_{elst,ij} = \frac{\pi}{\epsilon_0 \epsilon_{rel}} \frac{\varphi_i \varphi_j r_{ij}^2}{\left(1 + \frac{s_{ij}}{r_i + r_j}\right)^2} \vec{r}_{ij}, \quad (5.62)$$

and for charged particles made of electrical conduction materials as:

$$\vec{F}_{elst,ij} = \frac{\pi}{2} \epsilon_0 \epsilon_{rel} U_{ij}^2 \frac{r_{ij}}{s_{ij}} \vec{r}_{ij}. \quad (5.63)$$

In the previous equations,  $\epsilon_{rel}$  represents the relative permittivity that is equal to unity in vacuum,  $\varphi_i$  is the surface charge of object  $i$  and  $U_{ij}$  denotes to contact potential of two particles. The electrostatic force between a charged particle with radius  $r_i$  and a wall, both of them made of electrical insulation materials, is expressed by:

$$\vec{F}_{elst,iw} = \frac{2\pi}{\epsilon_0 \epsilon_{rel}} \varphi_i \varphi_j r_{iw}^2 \vec{r}_{iw}. \quad (5.64)$$

For a charged particle and wall made of electrical conducting materials, the electrostatic force can be given as follows:

$$\vec{F}_{elst,iw} = \pi \varepsilon_0 \varepsilon_{rel} U_{iw}^2 \frac{r_{iw}}{s_{iw}} \vec{r}_{iw}. \quad (5.65)$$

### 5.1.2.2.3 Adhesive forces with physical contact

The adhesive forces with physical contact are characterised by a material connection between particle–particle/wall, resulting in strong adhesion compared to adhesive forces without physical contact (see **Figure 5.7**). Depending on the material properties of the physical bond, these forces can be classified into two categories, Viz. solid or liquid bridge. While the adhesive forces with solid connection occur due to sintering, melt adhesion, thermochemical reaction or crystallisation, the adhesive forces with liquid connection form high viscosity binding mechanism and/or capillary binding force by the reason of water existence in the granular flow.

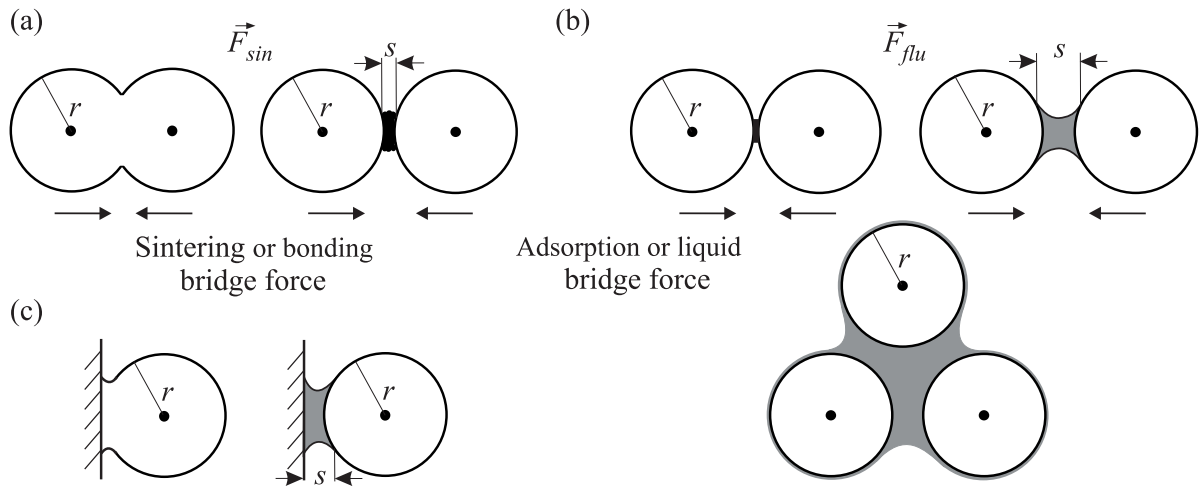


**Figure 5.7:** The short-range adhesive forces with physical contact: (a) solid bridge (particle–particle), (b) liquid bridge (particle–particle) and (c) solid bridge or liquid bridge (particle–wall)

**Adhesive force due to liquid bridge:** In gas–solid flows with certain moisture content in gas phase, adsorption process that acts at the interface area can be occurred, i.e. the addition of a liquid at particle surfaces. If the distance between two particles, whose surfaces are wetted with liquid films due to adsorption process, falls below a critical distance, a liquid bridge is then formed, resulting in adhesive and cohesive forces. The adhesive force denotes to attractive force between two objects of different materials. On the other hand, the cohesive force represents the attractive forces between molecules of same substance. In **Figure 5.8**, the liquid bridges between particle–particle and particle–wall are shown at low moisture content.

For particles with diameters less than 1 mm, the gravity and buoyancy forces acting on the liquid bridge can be neglected. Based on this assumption, the resultant adhesive force between two spherical particles with radius  $r_p$  can be determined by summing up the contributions of contact and capillary actions. The contact force is caused by the surface tension effect of liquid at the contact line of three phases. It occurs by the reason of intermolecular force between the gas, liquid and solid surfaces. The capillary effect arises due to the pressure difference between surrounding fluid  $p_{sur}$  and the phase boundary between the liquid bridge and the particle  $p_{liq}$ . The capillary force results then by multiple the pressure difference with the cross-section area  $A_{liq}$ :

$$\vec{F}_{cap,ij} = A_{liq} (p_{sur} - p_{liq}) \vec{n}_{ij}. \quad (5.66)$$

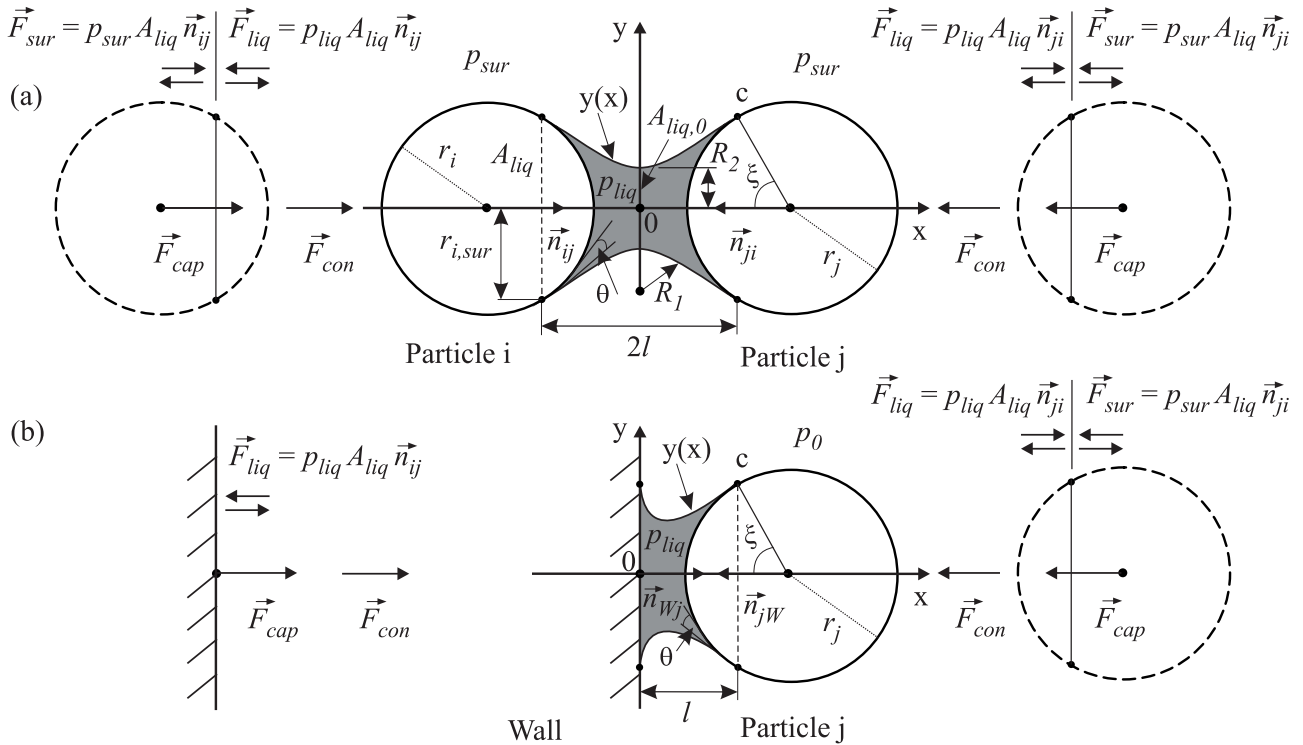


**Figure 5.8:** Adhesive force due to liquid bridge (same contact and fill angles): (a) particle–particle collision and (b) particle–wall collision

If the liquid bridge has biconcave shape as is often the case in water bridges, a capillary negative pressure  $p_{liq}$  is existent inside the liquid of bridge relative to gas phase  $p_{sur}$ . Here, the resultant adhesive force between two particles, which acts in the direction of collision normal vector  $\vec{n}$ , can be calculated according to the equation proposed by (Lian, Thornton and Adams 1993):

$$\vec{F}_{liq} = \left( \underbrace{2\pi r_p \sigma \sin(\xi) \sin(\theta + \xi)}_{\vec{F}_{con}} + \underbrace{\pi r_p^2 \Delta p \sin^2(\xi)}_{\vec{F}_{cap}} \right) \vec{n}, \quad (5.67)$$

where  $\sigma$  denotes to the surface tension of liquid,  $r_p$  is the particle radius,  $\xi$  and  $\theta$  are the fill and contact angles,  $l, R_1$  and  $R_2$  represent the length and the radii of bridge, respectively. For the particle  $i$ , the adhesive force due to the liquid bridge is in the direction of collision normal vector  $\vec{n}_{ij}$  and for the particle  $j$  is in the direction of  $\vec{n}_{ji}$ .

A liquid bridge can only be formed when the distance between two particles falls below the critical bridge length. If it occurs, the calculation of the adhesive force requires then the knowledge of the liquid bridge geometry. One possibility to determine the geometry of the bridge and thus the adhesive force due to the liquid bridge is based on the assumption of so-called toroidal shape. Here, the meridian profile of phase boundary is considered as a circular between the liquid and the surrounding fluid and as a circular segment among the liquid, the surrounding fluid and the solid surface of particle. Under this assumption, the resulted adhesive force can be calculated using three different approaches, namely boundary pressure method, boundary method or Gorge method, also known as neck method. In the boundary pressure and boundary methods, the adhesive force is estimated at the solid–liquid phase interface, while in Gorge method is determined at the smallest cross-section area of liquid bridge  $A_{liq,0} = \pi R_2^2$ . (Lian et al. 1993) compared the obtained adhesive force due to the liquid bridge with the aid of

toroidal shape assumption with experimental data, showing a good agreement. Furthermore, he found a relative error between the analytical solution taking into account the exact geometry of the liquid bridge (e.g. hyperboloid or nodoid) and the toroidal shape assumption less than 10%. However, the approximation that a liquid bridge is toroid results in a liquid bridge surface with a non-constant mean curvature. This leads to inconsistent with the Laplace–Young equation that is applied to determining the contribution of the capillary force. Other disadvantages by using the toroidal shape assumption are on the one hand that the critical length of the bridge cannot be estimated. On the other hand the adhesive force cannot be expressed as an explicit function of the liquid bridge volume and the separated distance between two collided particles.

An alternative approach to the toroidal shape assumption is to calculate the capillary force by reducing the Laplace–Young equation to non-dimensional form. The Laplace–Young equation is a non-linear partial differential equation that describes the relationship between mean curvature of phase boundary (i.e. liquid bridge) and the capillary pressure difference. (Mikami, Kamiya and Horio 1998) developed a simulation program based on the DEM model, which considers the adhesive force due to liquid bridges. The numerical code was applied to understand the agglomeration processes of wet particles in a fluidized bed. The results of numerical simulations are presented in **Figure 5.9** for particle–particle and particle–wall collisions.

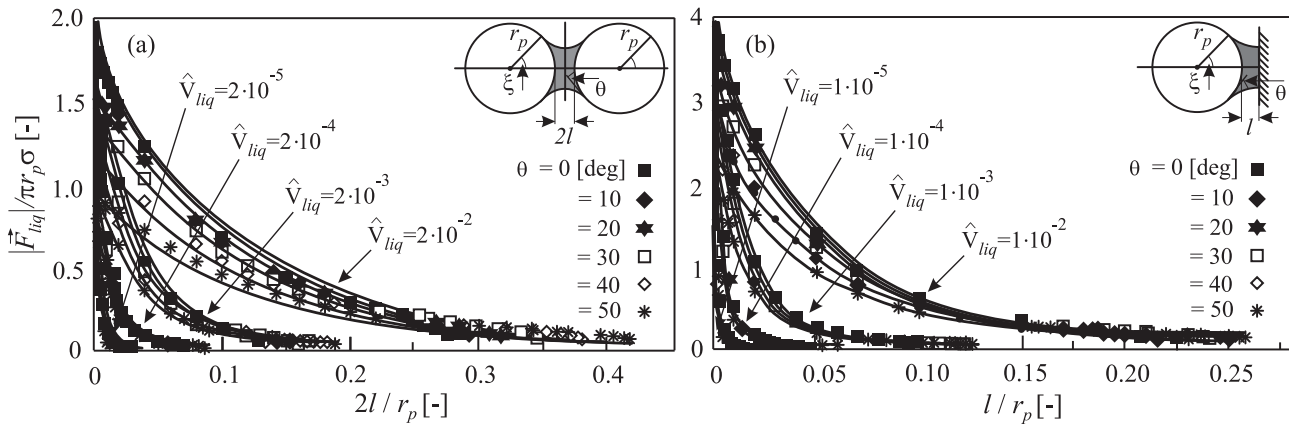


**Figure 5.9:** Dimensionless liquid bridge force against dimensionless distance as a function of contact angle: (a) particle–particle with same radius and (b) particle–wall (Mikami et al. 1998)

An explicit correlation between the absolute value of the non-dimensional adhesive force and the non-dimensional distance are proposed by Mikami with the aid of regression analysis:

$$\frac{|\vec{F}_{liq}|}{\pi r_p \sigma} = \exp\left(A \frac{l}{r_p} + B\right) + C. \quad (5.68)$$

The parameters  $A$ ,  $B$  and  $C$  is highly depended on the fluid moisture in the gas phase and thus on the non-dimensional volume of liquid bridge:

$$\hat{V}_{liq} = \frac{V_{liq}}{r_p^3}. \quad (5.69)$$

The following correlations are used to determine these parameters in case of particle–particle collisions:

$$\begin{aligned} A_{PP} &= -1.1 \hat{V}_{liq}^{-0.53}, \\ B_{PP} &= (-0.34 \ln \hat{V}_{liq} - 0.96) \theta^2 - 0.019 \ln \hat{V}_{liq} + 0.48, \\ C_{PP} &= 0.0042 \ln \hat{V}_{liq} + 0.078, \end{aligned} \quad (5.70)$$

and for particle–wall collisions:

$$\begin{aligned} A_{Pw} &= -1.9 \hat{V}_{liq}^{-0.51}, \\ B_{Pw} &= (-0.016 \ln \hat{V}_{liq} - 0.76) \theta^2 - 0.12 \ln \hat{V}_{liq} + 1.2, \\ C_{Pw} &= 0.0013 \ln \hat{V}_{liq} + 0.18. \end{aligned} \quad (5.71)$$

Another important parameter for determination the adhesive force is the non-dimensional critical bridge length  $\hat{l}_{cri}$ :

$$\hat{l}_{cri} = \frac{l_{cri}}{r_p}, \quad (5.72)$$

where  $l_{cri}$  specifies the maximum distance between two particles or particle and wall, at which a stable liquid bridge is still existing. If the critical distance is transcended, the liquid bridge will be destroyed as a result of instabilities and accordingly the related adhesive force will be vanished. By contrast, a liquid bridge will be reformed again when the distance between collision partners falls short of the critical distance (see Figure 5.10). For the non-dimensional critical bridge length, the following equations between two particles:

$$\hat{l}_{cri,PP} = (0.62\theta + 0.99)\hat{V}_{liq}^{0.34}, \quad (5.73)$$

as well as between a particle and a wall:

$$\hat{l}_{cri,P,Wa} = (0.22\theta + 0.95)\hat{V}_{liq}^{0.32}, \quad (5.74)$$

are valid.

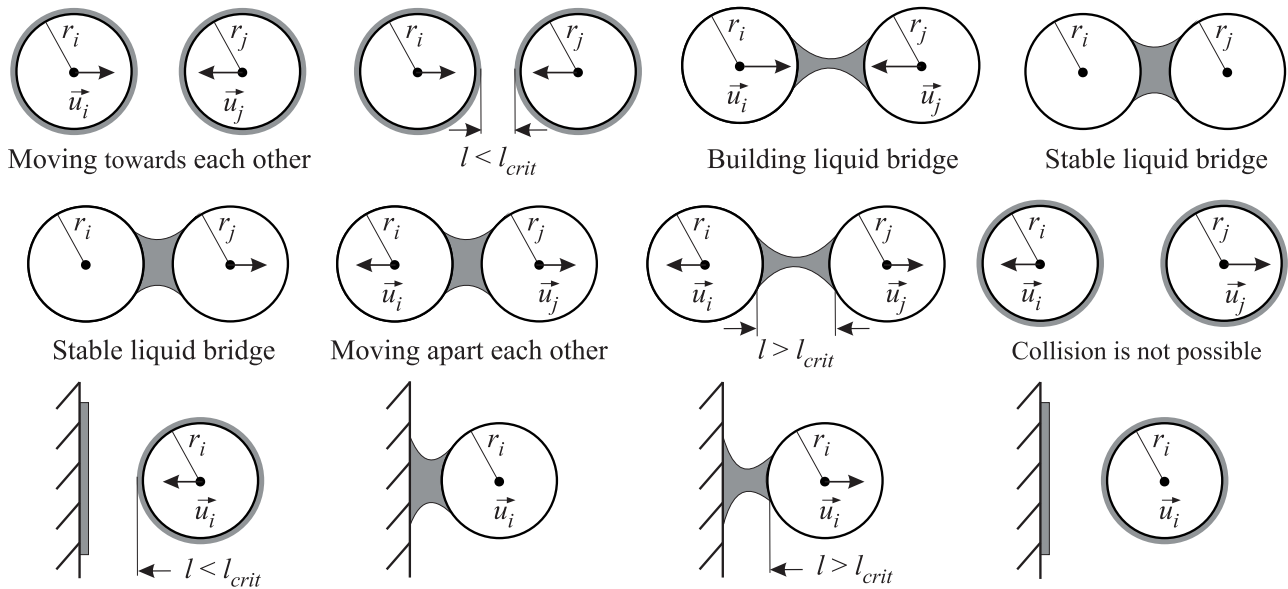


**Figure 5.10:** Formation and destroying mechanisms of liquid bridge

For modelling the adhesive force due to liquid bridge with the aid of previous equations, the following assumptions should be considered (Mikami et al. 1998): 1) The fluid is evenly

dispersed in the packed bed among all particles. 2) The particles are spherical in shape, uniform in diameter and have the same material properties (i.e. monodisperse system and homogeneous material). 3) The dynamic force due to viscosity in comparison to the static adhesive force by the reason of surface tension is negligibly small. 4) The maximum number of liquid bridges that can be formed by each particle is related to the number of coordinate axes. This means, two liquid bridges in 2D cases and three liquid bridges in 3D simulations. 5) All particles are wetted with a liquid film with constant thickness. However, the liquid volume should be sufficient for building three liquid bridges in case of 3D problem. 6) A stable bridge will be formed, once the separation distance between particles falls below the critical length. The required fluid of the bridge is equally taken from both collision partners. 7) When the critical length of the bridge is exceeded, it comes to the separation of the liquid bridge between the collision partners. Here, the liquid is distributed in equal parts to each collision partner. 8) For particle–wall liquid bridge, the assumption points 3, 6 and 7 are taken into account.

At low volume fraction of water in the gas phase, Mikami model employing the above mentioned correlations represents a compromise between the physically results obtained and acceptable computational effort. By increasing the fluid proportion in the gas flow, transition regions are built, which are filled with liquid. Isolated liquid bridges are not possible in this case due to the fact that several particles are agglomerated to each other. Further increasing in volume fraction of liquid can finally lead to unifying some of transition regions. In these regions, the particles can be completely surrounded with fluid and accordingly no movable liquid bridges are existent. Here, the resulted adhesive force on particles in the transition regions cannot be determined by Mikami model. In this context, a saturation level  $S_{liq}$ , which is defined as the ratio of the liquid volume  $V_{tra}$  in the transition regions to the cavity volume  $V_{cav}$ , is defined to check Mikami model for its validity:

$$S_{liq} = \frac{V_{tra}}{V_{cav}}. \quad (5.75)$$

According to (Schubert 1979), the transition region starts forming at ( $S_{liq} \geq 0.2$ ). This means, if the criterion ( $S_{liq} < 0.2$ ) is fulfilled, then the adhesive force due to liquid bridge can be determined using Mikami model. At ( $S_{liq} > 0.4$ ), the single transition region becomes more closely each other, which results in building bigger transition regions as can be observed in Figure 5.11.

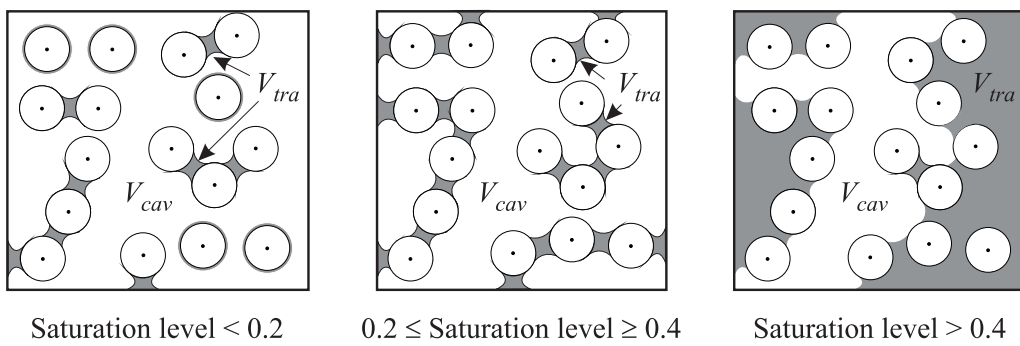


**Figure 5.11: Saturation level**

During the formation of stable liquid bridge, each partner should contribute a certain amount of the bridge liquid. If the bridge is, however, broken by the reason of exceeding the critical length, the liquid should redistribute again between the collision partners. The redistribution of the liquid in the bridge is currently based on three different principles. (Mikami et al. 1998) presupposes that the particles are wetted with constant liquid film and the

formed bridge is axially symmetrical in direction of  $x$  coordinate and rotationally symmetrical with respect to  $x - y$  plane. In case of separation, the liquid of bridge will be evenly distributed over the collided objects. (Muguruma, Tanaka and Tsuji 2000) assumes that the particles can be wetted with different amounts of liquid. Here, the collision partners contribute to different amounts of liquid for building the bridge. During the destroying of the bridge, each partner receive, however, the same amount of liquid, which is already participated in its. In the above two approaches, the meridian profile of phase boundary between the liquid of the bridge and the surrounding fluid is considered as to have parabolic geometry. This is the case in granular flows at low moisture content, where the particles have spherical geometry, constant diameter and from the same material properties. Here, each collision partner has the same contact and fill angels. The separation of the liquid bridge due to its symmetrical form occurs exactly in the middle. The redistribution of the bridge liquid is taken place equally to each collision partner (no liquid transport is considered).

Diverse contact and fill angles can arise during the formation of liquid bridges between monodisperse particles two different material properties or between two polydisperse particles of identical or different material properties. Here, the bridge neck is not anymore in the centre between the collision partners, but closer to the particle with larger contact angle. In case of separation, the particle with smaller contact angle holds more proportion of liquid back, while the particle with larger contact angle receives the reaming liquid (see **Figure 5.12**).

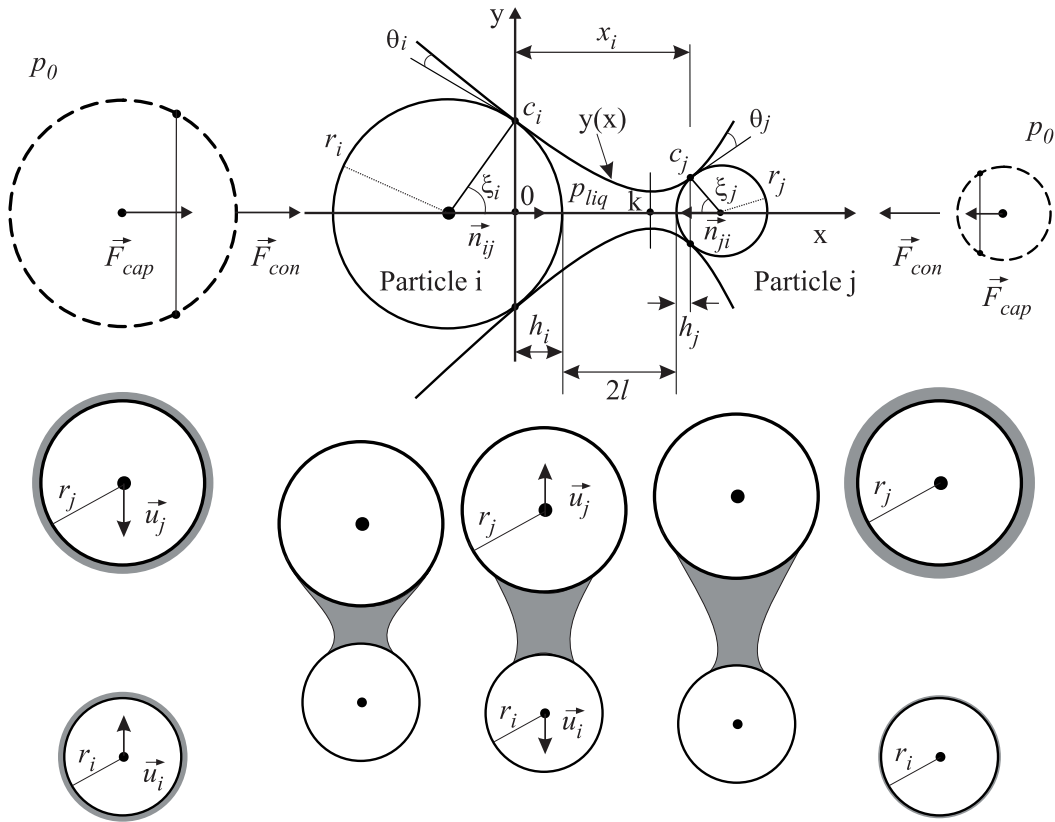


**Figure 5.12:** Adhesive force due to liquid bridge (diverse contact and fill angles)

(Shi and McCarthy 2008) calculated the adhesive force due liquid bridge under the consideration of polydisperse particles and unequal moisture distribution. In their study, the single particle surfaces can be wetted with different amounts of liquid (i.e. liquid film with diverse thickness). For each collision, the volume of liquid bridge should be determined separately, which is relatively time consuming. The entire liquid volume of exiting bridge is analytically calculated by summing up the liquid contributions of collision partners:

$$V_{liq,i} = \pi \int_{x_k}^{x_{c,i}} y^2(x) dx - \frac{1}{3} \pi (1 - \cos \xi_i)^2 (2 + \cos \xi_i), \quad (5.76)$$

$$V_{liq,j} = \pi \int_{x_k}^{x_{c,j}} y^2(x) dx - \frac{1}{3} \pi (1 - \cos \xi_j)^2 (2 + \cos \xi_j). \quad (5.77)$$

Simpler expression to determine the entire liquid volume of the bridge can be achieved using the spherical cap that is a portion of a particle cut off by a plane:

$$V_{liq} = \pi \int_{x_{c,i}}^{x_{c,j}} y^2(x) dx - \frac{\pi}{6} (3y_{c,i}^2 h_i + h_i^3 + 3y_{c,j}^2 h_j + h_j^3). \quad (5.78)$$

By exceeding the critical length of the bridge, the bridge is broken and the liquid will not distributed over the collided objects as uniform, but according to the following equations:

$$V'_{liq,i} = \pi \int_{x_{\min}}^{x_{c,i}} y^2(x) dx - \frac{\pi}{6} (3y_{c,i}^2 h_i + h_i^3), \quad (5.79)$$

$$V'_{liq,j} = \pi \int_{x_{\min}}^{x_{c,j}} y^2(x) dx - \frac{\pi}{6} (3y_{c,j}^2 h_j + h_j^3), \quad (5.80)$$

with the mass conservation of liquid bridge:

$$V_{liq} = V_{liq,i} + V_{liq,j} = V'_{liq,i} + V'_{liq,j}. \quad (5.81)$$

The heights of the cap are a function of colliding particles radii:

$$h_i = r_i - \sqrt{r_i^2 - \left( \frac{r_i r_j}{r_i + r_j} \right)^2}, \quad (5.82)$$

$$h_j = r_j - \sqrt{r_j^2 - \left( \frac{r_i r_j}{r_i + r_j} \right)^2}. \quad (5.83)$$

The bridge length is expressed by:

$$2l = x_{c,i} + x_{c,j} - h_i - h_j. \quad (5.84)$$

In order to determine the new distribution of liquid between the particles, the thinnest point of liquid bridge shortly before the separation should be known:

$$x_{\min} = x_{k,sep}. \quad (5.85)$$

It can be numerically solved with the aid of following boundary conditions:

$$y(x_{c,i}) = \sqrt{r_i^2 - (r_i - h_i)^2}, \quad (5.86)$$

$$y(x_{c,j}) = \sqrt{r_j^2 - (r_j - h_j)^2}, \quad (5.87)$$

$$y(x_{\min}) = 0, \quad (5.88)$$

$$\frac{dy(x_{\min})}{dx} = 0, \quad (5.89)$$

where the meridian profile of the phase boundary between the liquid bridge and the surrounding fluid is described as a polynomial of degree two (quadratic polynomial).

If the volume ratio  $V'_i/V_i$  is greater than unity, the liquid transport occurs during the bridge separation in direction of the particle  $i$ , while the liquid transport takes place towards the particle  $j$  when the volume ratio is less than unity. If the volume ratio is equal unity, each collision particle holds the same amount of the liquid back, which contributes already with its.

**Adhesive force due to solid bridge:** The adhesive force due to solid bridge results in a strong and a permanent bond between the collision partners. On the one hand, this effect can be the desired procedure in industrial applications such as briquette or powder coating. In briquetting process, the materials are compressed, allowing the particle to agglomerate each other. The powder coating is a coating process that uses dry particles. Compared to the conventional liquid paint, the powder coating does not need a solvent to maintain the liquid suspension form of binder and filler parts. On the other hand, the adhesive force due to solid bridge can also have negative consequences for most combustion systems by the reason of ash deposition on boiler walls and resulted worse heat transfer between flue gas and water–steam side.

At a sufficiently high temperature and a long contact time sintered bridges can arise between particles. A stable solid bridge can be formed when the collided particles temperature exceeds 60% of absolute melting temperature. The more the temperature falls below this limit the slower the sintering neck will grow, till finally the resulting adhesive force can be neglected. The building of sinter neck is depending on the surrounding pressure and the interfacial energies. While in case of low pressure and small particles, the interfacial tension is the main mechanism in building the solid bridge, the pressure sintering is crucial at higher pressure level ( $p > 1$  bar) and relatively big particle ( $r_p \geq 10^{-3}$  mm) (Schubert 1979).

The agglomeration between the particles due to solid bridge can be described in the frame of the DEM model. As an example, a solid bridge of two colliding objects i.e. particle–particle or particle–wall is illustrated in **Figure 5.13**.

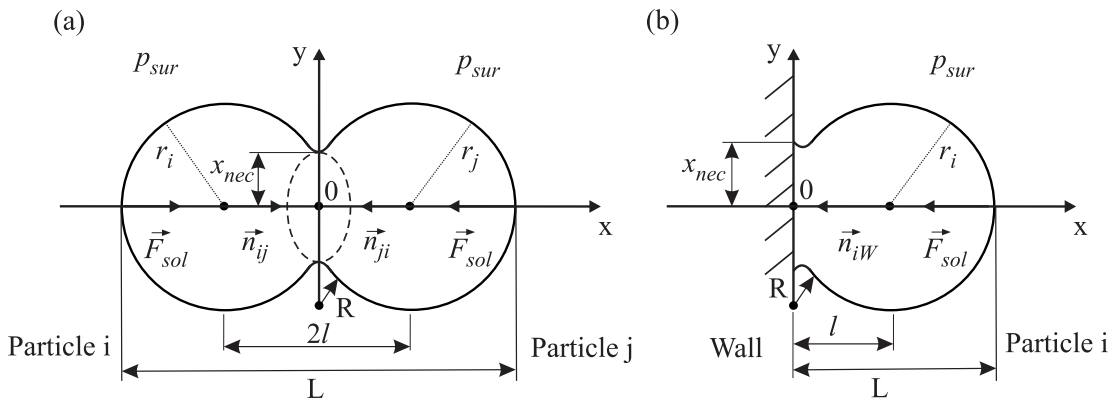


**Figure 5.13:** Adhesive force due to solid bridge: (a) particle–particle collision and (b) particle–wall collision

As a reference study for metallic bridging, (Kuwagi, Mikami and Horio 2000) investigated the sintering process of iron particles at atmospheric pressure. Here, the pressure sintering effect can be neglected, while the sintering due to the interfacial tension is the main mechanism. The neck growth of solid bridge between collision partners is based on Kuczynski sintering model (Kuczynski 1949). This model assumes that the surface diffusion including the

effect of surface roughness and the volume diffusion mechanisms have a relevant influence on the metal powders sintering. The neck growth, i.e. the neck radius  $x_{nec}$  is a function of neck growth time  $t_{nec}$  for surface diffusion cases as:

$$x_{nec} = \left( \frac{56\sigma a^4}{k_B T_p} D_s R^3 t_{nec} \right)^{\frac{1}{7}}, \quad (5.90)$$

and for volume diffusion cases as:

$$x_{nec} = \left( \frac{10\sigma a^3}{k_B T_p} D_V R^2 t_{nec} \right)^{\frac{1}{5}}, \quad (5.91)$$

where  $R$  denotes to the neck curvature radius,  $k_B$  is the Boltzmann constant,  $T_p$  refers to the particle temperature,  $\sigma$  is the surface tension,  $a$  is the lattice constant,  $D_s$  and  $D_V$  represent the surface and volume diffusion coefficients. The neck growth time  $t_{nec}$  that corresponds to each neck is reset to zero when the neck is broken during collisions. The diffusion coefficients can be calculated with the aid of Arrhenius equation as:

$$D_k = A_{0,k} \exp(-E_k / RT_p), \quad (5.92)$$

where  $A_{0,k}$  is the pre-exponential factor or frequency factor,  $R$  denotes to the universal gas constant and  $E_k$  is the activation energy. The subscript  $k$  is either surface ( $s$ ) or volume ( $V$ ). The pre-exponential factor as well as the activation energy can be experimentally measured. According to Kuczynski sintering model, the selection between the diffusion mechanisms depends on the temperature of particles. While the surface diffusion is the main factor that plays an important role in sintering of iron particles at relative lower temperature ( $T_p < 1050^\circ\text{C}$ ), the volume diffusion is the dominant mechanism at higher temperature. The resulted adhesive force due to solid bridge is related to the neck radius and the surface or volume energy of the neck  $\sigma_{nec,k}$ . It can be expressed between two spherical particles as follows:

$$\vec{F}_{sol} = \begin{cases} \pi x_{nec}^2 \sigma_{nec,s} \vec{n} = \pi \sigma_{nec,s} \left( \frac{56\sigma a^4}{k_B T_p} D_s R^3 t_{nec} \right)^{\frac{2}{7}} \vec{n} & \text{case } T_p < 1050^\circ\text{C} \\ \pi x_{nec}^2 \sigma_{nec,V} \vec{n} = \pi \sigma_{nec,V} \left( \frac{10\sigma a^3}{k_B T_p} D_V R^2 t_{nec} \right)^{\frac{2}{5}} \vec{n} & \text{case } T_p \geq 1050^\circ\text{C} \end{cases}. \quad (5.93)$$

Here, the adhesive force for the particle  $i$  is in the direction of collision normal vector  $\vec{n}_{ij}$  and for the particle  $j$  is in the direction of  $\vec{n}_{ji}$ . The surface roughness is an important parameter for estimating the neck radius and thus the sintering behaviour. (Kuwagi et al. 2000) investigated the roughness effect by introducing spherical sub-grains into the particle surface. For smooth surface, the contact area has one grain. A grain can be broken down to multiple micro-contact points. As a result, the number of the sub-grains between particles with a surface roughness can be changed then to three or nine micro-contact points (see **Figure 5.14**). The resulted adhesive force due to solid bridge between two spherical particles at lower temperature under the consideration of surface roughness is determined for a smooth surface (one grain):

$$\vec{F}_{sol,1} = \pi \sigma_{nec} \left( \frac{56\sigma a^4}{k_B T} D_s R^3 t_{nec} \right)^{\frac{2}{7}} \vec{n}, \quad (5.94)$$

for three sub-grains:

$$\vec{F}_{sol,3} = 3\pi \sigma_{nec} \left( \frac{56\sigma a^4}{k_B T} D_s \left( \frac{R}{10} \right)^3 t_{nec} \right)^{\frac{2}{7}} \vec{n}, \quad (5.95)$$

and for nine sub-grains:

$$\vec{F}_{sol,9} = 9\pi \sigma_{nec} \left( \frac{56\sigma a^4}{k_B T} D_s \left( \frac{R}{10} \right)^3 t_{nec} \right)^{\frac{2}{7}} \vec{n}. \quad (5.96)$$

From the previous equations, it can be concluded that the surface roughness leads to an increase in the solid bond strength between the collided particles.

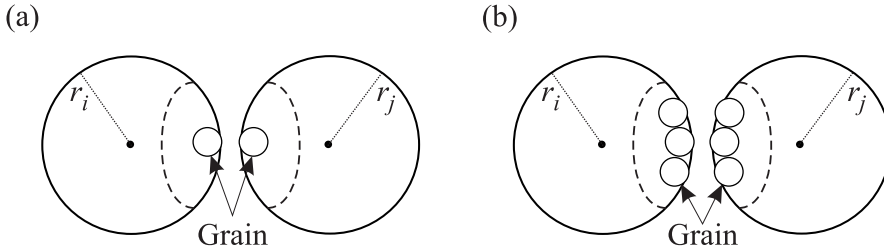


**Figure 5.14:** Surface roughness: (a) smooth surface and (b) rough surface (Kuwagi et al. 2000)

The neck is assumed to continue growing, i.e. the neck radius and neck growth time will be further accumulated. This will occur when the absolute value of contact force in normal or tangential direction is smaller than the sum of neck cross-sectional areas of all micro-contact points  $A_{nec,k}$ . The neck is, however, broken if one of following conditions is met:

$$\begin{aligned} \left| \vec{F}_{con}^n \right| &\geq \sigma_{nec} \sum_{k=1}^{k=n} A_{nec,k}, \\ \left| \vec{F}_{con}^t \right| &\geq t_{nec}^{acc} \sum_{k=1}^{k=n} A_{nec,k}, \end{aligned} \quad (5.97)$$

where  $n$  represents the number of micro-contact points.

For modelling the adhesive force due to solid bridge with the aid of Kuwagi model, the following assumptions should be considered: 1) The stiffness constant of solid bridge has the same value as collision partners. 2) A neck can be formed between any particles in contact. 3) The neck radius will only be increased during the period of contact. 4) For each contact, the neck between the collision partners can be developed or separated. The neck will be broken when the absolute value of normal or tangential contact force transcends the sum of neck cross-sectional areas of all micro-contact points. 5) In case of neck breakage, the neck growth time and thus the neck radius is reset to zero. 6) The dynamic friction coefficient  $\mu_{dyn}$  is set equal to infinity so that the resulting tangential contact force is supposed to be a static force, i.e. no sliding is allowed between the collision partners (see equation (5.41)). 6) The calculation of the contact force requires the stiffness constant to be known (see section 5.1.2.2.1). As a rule, the stiffness constant  $k$  is adopted to smaller values in order to reduce the computation effort. The use of smaller stiffness coefficients increases the value of particle time step compared to the real particle time step (see section 8.1.5.1). Sequentially, the

period of collision (contact time) using the modified stiffness coefficients will be smaller than the collision period of non-modified stiffness constants. In the case of determining the adhesive force due to solid bridge, the neck radius at the end of collision should be calculated based on the real time of the collision, i.e., without modifying the stiffness coefficient. Other important point is the spring contact models that are applied to calculate the contact force. The linear approach proposed by Hooke that shows a satisfactory accuracy is frequently used. However, the neck radius at the end of a linear Hookean collision should have the same value as that at the end of a non-linear Hertzian collision. This is very important to have the correct judgement whether the neck is broken after collision or not. The judgement should not be influenced with the modification of stiffness coefficients by the reason of computation time as well as the using of a linear collision model. For this reason, an additional factor is considered that corrects the neck growth rate for the real contact time. Accordingly, the neck radius with the modified stiffness constant has the same value like the non-modified one. The correct neck radius can be determined by the following equation:

$$x_{nec} = x_{nec}^0 \left( \frac{t_{nec}}{t_{nec}^0} \right)^{\frac{1}{7}}, \quad (5.98)$$

with:

$$t_{nec} = t_{nec}^0 + t_{nec}^+, \quad (5.99)$$

where  $t_{nec}^0$  represents the neck growth time based on the modified collision period,  $x_{nec}^0$  is the neck radius resulted from  $t_{nec}^0$  and  $t_{nec}^+$  is the time correction factor. This correction factor is an increment of the modified neck growth time, which considers the difference between the real collision time  $t_{col}^{Hertz}$  and the adopted collision time  $t_{col}^{Hooke}$ . It can be expressed with the aid of applied collision time  $t_{col}$  as follows:

$$t_{nec}^+ = t_{col} \frac{t_{col}^{Hertz}}{t_{col}^{Hooke}}. \quad (5.100)$$

The duration of the collision estimated by Hertz and Hooke theories can be calculated as:

$$t_{col}^{Hertz} = 2.44 \left( \frac{m_{ij}^2}{\xi^2 u_{ij}} \right)^{\frac{1}{5}}, \quad (5.101)$$

$$t_{col}^{Hooke} = \pi \sqrt{\frac{m_{ij}}{k}}, \quad (5.102)$$

where  $m_{ij}$  and  $u_{ij}$  represent the reduced mass and the relative velocity of the collision partner ( $i$  and  $j$ ), respectively. The constant  $\xi$  is a function of material properties, viz. Young's modulus  $E$  and Poisson's ratio  $\nu$ :

$$\xi = E \frac{\sqrt{d_p}}{3(1-\nu^2)}. \quad (5.103)$$

The Young's modulus, also known as elastic modulus, describes the stiffness of an elastic material. Typical values of Young's modulus and Poisson's ratio for different materials are listed in **Table 5.1** and **Table 5.3**.

Based on the above model, the adhesive force due to solid bridge for monodisperse and homogenous materials can be numerically determined. However, the simulation of adhesive force due to solid bridge requires significantly more computational time than other adhesive forces such as liquid bridge or van der Waals. In real system, the numerical calculation of adhesive force due to solid bridge is more complicated by the reason of particle size distribution as well as the inhomogeneity in the material composition. Generally, the particles consist of different materials, which lead to diverse surface and volume diffusion coefficients. At high temperature, these materials may react to each other, resulting in particles with different species compositions. For polydisperse and inhomogeneous particles, the calculation of adhesive force due to solid bridge is still an open issue, which needs to be clarified via additional theoretical and numerical works.

**Table 5.3:** Young's modulus of different materials

Material	Young's modulus [GPa]
Aluminium	69
Copper	117
Glass	50–90
iron	195
Rubber	0.01–0.1
Steel	200

## 5.2 Momentum balance

The rotation of particles can result from a velocity gradient in an anisotropic flow field (e.g. near the wall or in a shear flow) or from the particle–particle/wall collisions. The resulted moment of force acting on a particle  $i$  is calculated as a sum of two contributions, namely the moment of force due to the fluid–particle interaction and the moment of force due to short-range forces between particles (see **Figure 5.15**).

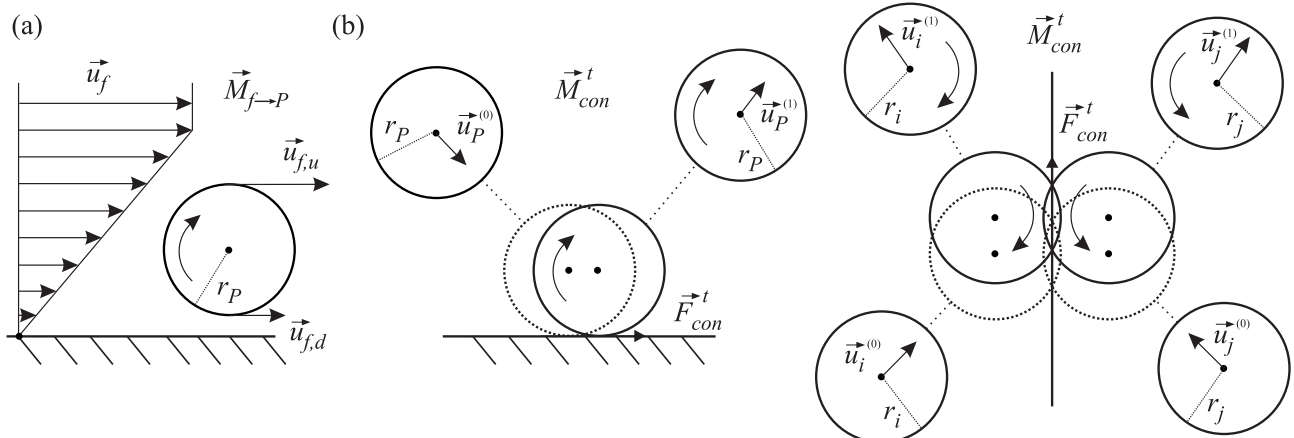


**Figure 5.15:** The resulted moment of force acting on a particle: (a) moment of force due to fluid–solid interaction and (b) moment of force due to short–range forces

$$I_P \frac{d\vec{w}_P}{dt_P} = \sum \vec{T}_i = \underbrace{\vec{M}_{f \rightarrow P}}_{\text{Fluid-Particle interaction}} + \underbrace{\vec{M}_{con}^t}_{\substack{\text{Moment of tangential contact force} \\ \text{Moment of short-range forces}}} + \underbrace{\vec{M}_{con}^r}_{\substack{\text{Moment of friction force} \\ \text{Moment of short-range forces}}}. \quad (5.104)$$

Here,  $\vec{w}_P$  is the angular velocity,  $I_p$  denotes to the moment of inertia,  $t_p$  represents the particle time step and  $\vec{T}_i$  denotes moments of force acting on the particle.

### 5.2.1 Moment of force due to the fluid–particle interaction

The resulting moment of force due to the fluid–particle interaction can be determined for lower particle Reynolds numbers with the relation of (Rubinow and Keller 1961). For higher particle Reynolds numbers, it can be caudated with the equation proposed by (Sommerfeld 1996) based on the theoretical and numerical results of (Dennis, Singh and Ingham 1980):

$$\vec{M}_{f \rightarrow P} = \begin{cases} \pi \mu_f d_p^3 \vec{w}_{rel} & \text{case } \text{Re}_p \leq 1 \\ \frac{1}{64} \rho C_R d_p^5 |\vec{w}_{rel}| \vec{w}_{rel} & \text{case } \text{Re}_p > 1 \end{cases}, \quad (5.105)$$

with the particle Reynolds number:

$$\text{Re}_p = \frac{\rho_f d_p |\vec{u}_{rel}|}{\mu_f}, \quad (5.106)$$

where  $C_R$  is a rotation coefficient,  $\vec{u}_{rel}$  and  $\vec{w}_{rel}$  represent the relative translation and the angular velocities between solid and fluid phases, respectively. The rotation coefficient is dependent on the rotating Reynolds number  $\text{Re}_R$  and can be defined using a step function as follows:

$$C_R = \begin{cases} \frac{16\pi}{\text{Re}_R} & \text{case } 0 \leq \text{Re}_R < 10^1 \\ \frac{6.45}{\sqrt{\text{Re}_R}} + \frac{32.1}{\text{Re}_R} & \text{case } 10^1 \leq \text{Re}_R < 10^3 \\ \frac{6.8}{\sqrt[20]{\text{Re}_R}} & \text{case } 10^3 \leq \text{Re}_R < 4 \cdot 10^4 \\ \frac{0.058}{\sqrt[20]{\text{Re}_R}} & \text{case } 4 \cdot 10^4 \leq \text{Re}_R < 4 \cdot 10^5 \\ \frac{0.397}{\sqrt[5]{\text{Re}_R}} & \text{case } 4 \cdot 10^5 \leq \text{Re}_R < 10^7 \end{cases}, \quad (5.107)$$

with:

$$\text{Re}_R = \frac{0.25 \rho_f d_p^2 |\vec{w}_{rel}|}{\mu_f}. \quad (5.108)$$

The dependence of the rotation coefficient on the rotating Reynolds number is shown graphically in **Figure 5.16**. It is clear that the rotation coefficient increases with decreasing the rotating Reynolds number. Consequently, the moment of force due to the fluid–particle interaction should not be neglected even at lower relative angular velocities.

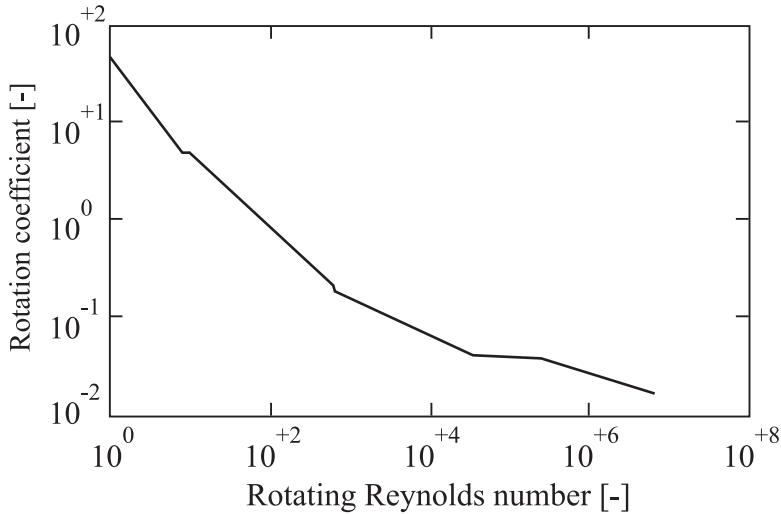


**Figure 5.16:** The relationship between the rotation coefficient and the rotating Reynolds number

### 5.2.2 Moment of force due to short-range forces between particles

The moment of force due to short-range forces between particles results from the forces acting at the contact point. The moment of force due to short-range forces consists of two components, viz. the tangential contact force and the asymmetrical normal traction distribution.

The resulting tangential moment of force on the particle  $i$  is explicitly calculated by multiplying the particle radius with the tangential contact forces that act simultaneously between the particle  $i$  and other collision partners:

$$\bar{M}_{con,i}^t = \sum_{\substack{k=1 \\ k \neq i}}^{k=N} r_i \bar{F}_{Con,ik}^t \times \vec{n}_{ik}, \quad (5.109)$$

where the index  $N$  represents the number of collision partners, i.e. particles and walls, which are in contact with the particle  $i$ .

The moment of force due to the asymmetrical normal traction distribution, also known as rolling friction torque, results from the rolling resistance between two particles or a particle and a wall in contact due to the relative rotation. The normal traction distribution is symmetrical and thus this additional torque is neglected when the particles are rigid and the contact occurs only at a point or a relative small penetration depth between the collision partners. For inelastic particles, the normal traction distribution is asymmetrical. This produces a higher traction on the front half of the contact area than the rear (see **Figure 5.17**).

Generally, the torque due to the asymmetrical normal traction distributions can be neglected for rigid as well as viscoelastic particles. It plays, however, a significant role in some cases, where the transition between static and dynamic states is existent, such as the formations of shear band, the heaping and the movement of a single particle on a plane (Zhu et al. 2007). By contrast to the tangential moment of force, the determination of rolling friction torque is very difficult and still remains an open issue. Different approaches are proposed to calculate the moment of force due to asymmetrical normal traction distribution acting on the particle  $i$ , which are listed below:

$$\vec{M}_{Con,i}^r = \begin{cases} \sum_{\substack{k=1 \\ k \neq i}}^{k=N} \mu_r \left| \vec{F}_{con,ik} \right| \vec{w}_{ik}^n & (\text{Beer, 1976}) \\ \sum_{\substack{k=1 \\ k \neq i}}^{k=N} \left( -k_r \vec{\varphi}_{ik,rel} - \eta_r \frac{d\vec{\varphi}_{ik,rel}}{dt_p} \right) & (\text{Iwashita et al., 1998}/(\text{Iwashita et al., 2000})) \\ \sum_{\substack{k=1 \\ k \neq i}}^{k=N} k_R \left| \vec{F}_{Con,ik} \right| \left| \vec{w}_{ik}^n \right| \hat{\vec{w}}_{ik}^n & (\text{Brilliantov et al., 1998}) \\ \sum_{\substack{k=1 \\ k \neq i}}^{k=N} -\min \left[ \frac{\mu_r \left| \vec{F}_{Con,ik} \right|}{k_R \left| \vec{F}_{Con,ik} \right| \left| \vec{w}_{ik}^n \right|}, \left| \vec{w}_{ik}^n \right| \right] \hat{\vec{w}}_{ik}^n & (\text{Zhou et al., 1999}/(\text{Zhu et al., 2002})) \end{cases}, \quad (5.110)$$

where  $\vec{\varphi}_{ik,rel}$  represents the relative angular displacement and  $\vec{w}_{ij}^n$  is the unit vector of the component of relative angular velocity in contact plane:

$$\vec{w}_{ik}^n = \frac{\vec{w}_{ik}}{\left| \vec{w}_{ik} \right|}, \quad (5.111)$$

and  $\left| \vec{w}_{ik} \right|$  the magnitude of the component of the relative angular velocity between the particles ( $i$  and  $k$ ):

$$\left| \vec{w}_{ik} \right| = \left| (r_i \vec{w}_i + r_k \vec{w}_k) \times \vec{n}_{ik} \right|. \quad (5.112)$$

The rolling friction coefficient  $\mu_r$ , the rotational stiffness coefficient  $k_R$ , the rolling stiffness constant  $k_r$  and the rolling damping constant  $\eta_r$  are material properties and can be defined experimentally.

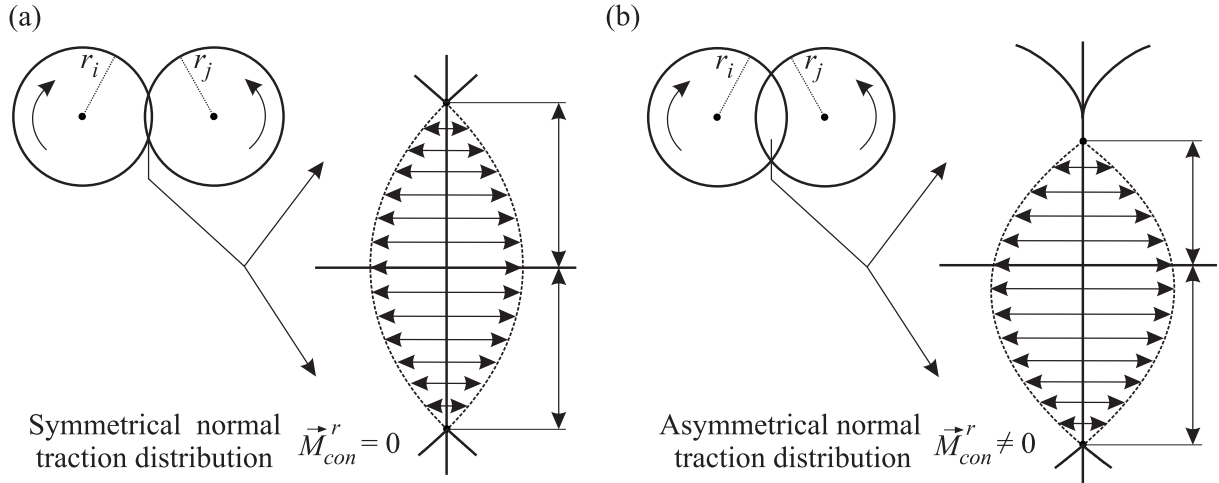


**Figure 5.17:** Moment of force due to short-range forces: (a) symmetrical normal traction distribution and (b) asymmetrical normal traction distribution

The main difference among these models is by considering the relative angular velocity for determination the rolling friction torque. While the model of (Beer and Johnston 1967) is independent of the relative angular velocity, the approaches by (Iwashita and Oda 1998,

Iwashita and Oda 2000) and (Brilliantov and Pöschel 1998) are function of relative angular velocity. (Zhou et al. 1999) and (Zhu and Yu 2002) combined the approaches of Beer and Brilliantov into a dynamic model by means of a minimum function. Due the complexity of describing the asymmetrical normal traction distribution, there is no universal model that can be applied to calculate the rolling friction torque. Which approach is suitable for a specific problem, further numerical and experimental studies should be carried out.

### 5.3 Conclusion

In the DEM model, the change of the translational and angular velocities is determined by forces and momentums balances on each particle. The single particle trajectory and the angular displacement can then be calculated through integration the Newtonian equations of motion.

The forces acting on particles are divided into two categories, namely: volume and surface forces. The surface forces can be classified as aerodynamic surface forces and short-range surface forces that can also be decomposed into contact force, adhesive forces associated either with or without physical contact.

The volume forces result from external fields and act throughout the volume of object regardless of flow configuration. They show quadratic dependence on the distance between two bodies. Typical volume forces are gravitational force, buoyancy force, electric and magnetic forces.

The aerodynamic surface forces that exert on the surface of particles result from the interactions between fluid and solid. They depend highly on the densities as well as the translational and angular velocities of both phases. In the gas–solid flow, the aerodynamic surface forces are drag force, virtual mass force, Basset force, force due to velocity gradient (Saffman), force due to pressure gradient, force due to temperature gradient, force due to concentration gradient and Magnus force. The drag force that hinders the movement of a particle represents, in most cases, the dominant force on the particle in the granular flow. It is composed of two forces: the drag form force and the frictional resistance force that depends on the surface structure of particle. With the acceleration or deceleration of a particle in a fluid, the surrounding fluid must be accelerated or decelerated, too. The unsteady effect due to the acceleration or the deceleration of particle with respect to fluid can be divided into two forces: the virtual mass force as an additional form of resistance and the Basset force due to the viscous effects when the relative velocity of both phases changes. The Basset force describes the temporal delay in boundary layer development during the acceleration or deceleration of particles. For anisotropic flow (i.e. flow with non-uniform characters), additional forces can arise by the reason of existing flow gradients such as velocity, pressure, temperature or concentration gradient. In a shear flow, the particle surface undergoes an unsteady pressure distribution that results in a force perpendicular to the relative velocity. This force was determined analytically by Saffman (1965) and denoted as Saffman force. The pressure gradient in the flow induces an additional force that acts in the opposite direction of the pressure gradient. If the particle locates in a flow with temperature or concentration gradients, an irregular pressure distribution will arise on the particle surface, leading to a force that acts in the opposite direction of this gradient. In isotropic flow (i.e. flow with uniform characters), the particle rotation leads also to an irregular pressure distribution on the particle surface. The resulting force on the particle is called Magnus force.

The contact and adhesive forces that are known as short–range surface forces or inter-particle forces result from the interactions between particle–particle/wall. In the DEM model, the collision partners are allowed to overlap slightly. As a sequence, the contact between two rigid particles is not represented as a single point like in the hard sphere model but as an

infinite area in 3D and as a line in 2D cases. This deformation is equivalently considered to be the contact between the collision partners. Depending on the penetration depth, the resulting contact force can be modeled using a mechanical analogous model. It consists of a Hookean spring and a Newtonian damper, which are connected in parallel. Using this model, the collision can be modeled as either elastic or inelastic. In an elastic collision, the sum of kinetic energies of contact particles before and after the collision are equal (neither damping nor frictional forces is allowed). During an inelastic collision, by contrast, a part of kinetic energies of collided particles is converted into internal energy. The energy dissipation at inelastic collisions can be expressed by the collision coefficients. The well-known Kelvin–Voigt model (spring–damper–slider system) is generally applied to determine the contact force. The linear contact model by Hooke shows an adequate accuracy in most applications. The non-linear contact models based on Hertz theory improve the calculation accuracy, but lead on the other hand to an additional computing time. This is due to the fact that these models should consider the changes of geometric and physical properties of partners during the collision. The resulted contact force is determined as the sum of two components: the normal and the tangential contact forces. By the calculation of the tangential contact force, it has to be differed between static and sliding frictions, which can be achieved with the aid of Coulomb's friction law. The distinction between the static and sliding forces improves the realistic representation of the collision.

The hydrodynamic behaviour of solid phase is also influenced by the formation of adhesive forces between particles or rather particles and walls. The adhesive forces depend highly on the material pairings such as diameter, density and surface roughness. Based on the adhesive forces formation, it can be distinguished between two mechanisms. The first adhesive mechanism is formed without material connection (i.e. without physical connect) between the collision partners such as Van der Waals and electrostatic forces. The van der Waals force describes the dipole–dipole interactions between particle–particle and particle–wall. The electrostatic force that arises between two charged particles is directly proportional to the product of magnitude of each charge and indirectly proportional to the square of distance. The second mechanism is characterised by material connection (i.e. with physical connect) between the collision partners. This connection can be formed as solid or liquid bridges. The moisture content in the gas–solid flow leads to adhesive force between the collision partners. The adhesive force due to liquid bridge can be obtained as the sum of capillary force and force caused by the surface tension. While the capillary force results from the pressure difference between the bridge liquid and the surrounding fluid, the surface tension force results from the axial component of surface tension of bridge liquid. The definition of the liquid bridge geometry is crucial to enable the calculation of this adhesive force. (Mikami et al. 1998) assumed that the bridge geometry has toroidal shape. He derived explicit correlations between the absolute value of non-dimensional adhesive force due to liquid bridge and the non-dimensional distance between both collision partners. In case of bridge separation, the liquid of bridge is evenly distributed over the collided particles due to identical contact angles. Unequal contact angles appear, however, during the building of liquid bridges between monodisperse particles two different materials or between two polydisperse particles of identical or different materials. In this case, the neck of liquid bridges shifts to the particle with a large contact angle. During the bridge separation, the particle with a large contact angle holds less proportion of the liquid back compared to the particle with a small contact angle. At high temperature, adhesive force due to solid bridge becomes more important, which leads to a strong and a permanent bond between the collision partners. The building of the sinter neck is a function of the surrounding pressure and the interfacial energies of contact particles. Generally, the neck growth due to the pressure sintering can be neglected at atmospheric pressure. The neck growth due to the interfacial energies is based on Kuczynski sintering model. The model

assumed that the surface diffusion including the effect of the surface roughness and the volume diffusion mechanisms have a relevant influence on the metal powders sintering (Kuwagi et al. 2000, Wakai and Brakke 2011).

Finally, it should be mentioned here that the determination of the short-range surface forces requires the identifying of the collision partners. This can be achieved employing a detection collision model with a specific criterion. For example, a contact between two particles will occur, if the distance between particles centres is smaller than the sum of their radii. Other example is the criterion of the liquid bridge formation. A collision is registered when the distance between particles centres falls below the bridge critical length.

The resulted moment of force acting on the particles is classified as the moment of force due to fluid-particle interaction and the moment of force due to short-range forces that can also be divided into two parts, viz, the tangential contact force and the force due to asymmetrical normal traction distribution. In an anisotropic flow, e.g. with a velocity gradient, the moment of force due to fluid-particle interaction leads to particles rotations. The moment of force due to the tangential contact forces is calculated by multiplying the particle radius with the tangential component of the contact force. The moment of force due to the asymmetrical normal traction distribution is caused by the rolling resistance of particles. Generally, the normal traction distribution is symmetrical for rigid particles with small penetration depth. Asymmetrical normal traction distribution can occur when the penetration depth of rigid particles is relative large or for inelastic particles independent of their penetration depths. By contrast to the DEM model, the moment of force due to the tangential contact force and the asymmetrical normal traction distribution cannot be considered in the hard sphere model. This is due to the fact that the inter-particle forces (e.g. contact force) are calculated as impulsive actions. However, the moment of force due to the fluid-particle interaction can be taken into the hard sphere model account.

Based on the above models, equations and correlations, the volume, the aerodynamic surface forces and the short-range surface forces including the contact forces and the adhesive forces associated either with or without physical contact as well as the resulted moment of force acting on particles can be determined with the DEM model. However, the applied models are restricted to circular particles in 2D or spherical particles in 3D cases. The consideration of particles with complex geometries is hindered not only by the modelling of mechanical behaviour of these particles, but also by the related additional computation time. According to (Zhu et al. 2007), two approximation methods for the non-spherical particles are of relevance. In the first approach, the particle with complex geometry can be built as cluster of circles or spheres. In the second approach, the predefined particle geometry is described by polynomial functions. The advantage of approximation the complex geometry of particle using circles or spheres is that the mechanical behaviour of spherical particles has been actively investigated. By contrast, the second method requires mathematical functions to describe the particle geometries. Furthermore, the models that are used to calculate the volume and surface forces should be extended based on the particle shapes. Since the computational complexity increased sharply with raising the order of polynomial function, the second approach is generally limited to simple geometries such as cylindrical or ellipsoidal particles.

The aim of this work is to develop a numerical simulation program for the simulation of reactive, dense gas-solid flow in a fluidized bed. For this system, the volume forces play an important role, especially for particles with high density and relative big diameters. While the gravity force is always considered, the buoyancy force is neglected in most DEM simulations due to the low density of gas (among others: (Tsuji et al. 1993, Link et al. 2005, Van Buijtenen et al. 2011). The electric and magnetic forces are also omitted by the reason of absence the extern electric and magnetic fields in fluidization systems. In the DEMEST program, besides the

gravitational force, the bouncy force is also included since the impact of considering this force on the entire computation time is extremely small.

In the DEM simulations, definite aerodynamic forces are commonly neglected because of their subordinate importance. While the drag force is always taken into account, the remaining aerodynamic forces are partly neglected (among others: (Mikami et al. 1998, Deen et al. 2007, Van Buijtenen et al. 2011). The practical reasons of this simplification are: 1) In a fluidized bed, the relative acceleration or deceleration rate is low, the time change is much smaller than the Stokes relaxation time and the density differences between fluid and solid is small. The virtual mass and the Basset force can be omitted consequently. 2) The DEM model is applied, in most cases, to simulate the cold flow fluidized bed. Therefore, the aerodynamic forces due to the temperature and concentration gradients are neglected, too. 3) The aerodynamic forces due to non-uniform distributions of the velocity and the pressure (Saffman and pressure gradient forces) are not considered by the reason of the additional computational effort. 4) The Magnus force is also omitted since the momentum balance on particles is not solved and thus the particles do not rotate. However, these simplifications can influence the simulation accuracy. Furthermore, the behaviour of the dense gas-solid flow in the fluidized bed is characterised with higher pressure and velocity gradients compared to the dilute granular flow or the single-phase flow. Therefore, the Saffman force and the force due pressure gradient should not be disregarded. They increase significantly by decreasing the solid density and increasing the particles diameters. Moreover, the Magnus force should be considered by the reason of velocity gradient existence. In the DEMEST program, the drag force, the Saffman force, the force due pressure gradient, the force due temperature gradient and the Magnus force are included. The considering of these aerodynamic forces, although causes an additional computation time, leads to improvement in the simulation accuracy.

The contact force is of particular relevance in fluidisation systems and thus it was taken into account of all DEM simulations. The contact force is calculated using the Voigt–Kelvin model, which describes the viscoelastic and time-dependent behaviour of collision. The part of kinetic energy that is irreversibly dissipated in form of deformation energy can be defined with the aid of restitution coefficients. At higher collision velocities or for particle with non-spherical shapes, the restitution coefficients decrease and thus cannot be considered constant (Sommerfeld 2002). In the fluidized bed, the particles velocities are relatively low. Furthermore, the DEM simulations are limited, for the time being to spherical particles. For this reason, the restitution coefficients are assumed to be constant in the previous DEM studies as well as in this work. Although the non-linear contact models show an accurate distribution of contact force curve, the linear contact model that consists of a linear spring model and a linear visco-elastic damping element has been frequently applied (among others: (Tsuji et al. 1993, Mikami et al. 1998, Link 2006). This is due to the fact that on the one hand the calculation of macroscopic parameters of collision is fundamental while the defining of specific distribution curve of contact force is irrelevant in most applications. On the other hand, the non-linear contact models are related to an additional computational effort. In the DEMEST program, the linear contact model is used due to its higher efficiency. Furthermore, a distinction between the static and sliding tangential contact forces is considered.

If the particles size decreases, then the adhesive forces either with or without physical contact increase (see **Figure 5.18**). The fine particles are characterised with strong inter-particle forces without material connection such as the van der Waals force and the electrostatic force, making these particles difficult to fluidize compared to larger size particles. The electrostatic force that occurs between the oppositely charged surfaces plays an important role in the fluidized bed. During the fluidization, the particle–particle/wall collisions lead to charge the particle surfaces, exhibiting in different fluidization regimes. Here, the particles tend to agglomerate each other and/or with walls. In the DEM literature, the effect of the adhesive

forces without material connection on the fluidized bed is not investigated. This is due to the fact that these forces are of relevance for micro-size particles. Accordingly, the number of fine particles per a volume unit is enormous and the DEM simulation of the fluidized bed with finer particles is extremely expensive. In this work, the van der Waals force and the electrostatic force are neglected due to relative large particles used (in the range between 0.5–3.5 mm).

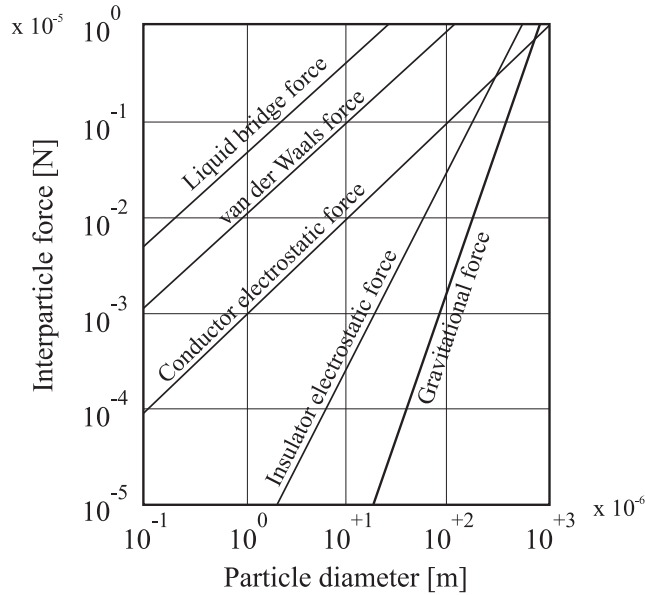


**Figure 5.18:** Magnitude comparison of adhesive forces either with or without physical contact  
Schubert (1979)

At high moisture level, the adhesive force due to liquid bridge can particularly have a major influence on the behaviours of the gas–solid flow in the fluidized bed. The modelling of this adhesive force has been discussed widely in the DEM literature (among others: (Mikami et al. 1998, Shi and McCarthy 2008, Anand et al. 2009)). In this work, the hydrodynamic behaviour of the reactive gas–solid flow in the fluidized bed is investigated. During the pyrolysis process, the water is released, resulting in these areas to particles agglomerations. Therefore, the adhesive force due to the liquid bridge is implemented in the DEMEST program based on the Mikami model. This model shows a satisfactory result and a relatively low computational effort. However, the water transport process due to the liquid bridge separation can be neglected since the water on the particle surfaces will be evaporated. This will occur apart from pyrolysis regions, where the temperature is very high by the reason of the homogenous and heterogeneous reactions. Here, the adhesive force due to solid bridge becomes more important. The DEM simulation of the fluidized bed under the consideration of the solid bridge requires significantly more computational time compared to the adhesive force due to liquid bridge and thus received less attention in the DEM literature. In the DEMEST program, the solid bridge force is disregarded as well. Nevertheless, important works on the adhesive force due to solid bridge in the fluidized bed can be found in the literature (among others: (Mikami, Kamiya and Horio 1996, Kuwagi et al. 2000, Knight et al. 2000)). In the DEM simulations for the fluidized bed, the moments of force acting on particles are limited to one contribution, namely the tangential contact force (among others: (Deen et al. 2007, Van Buijtenen et al. 2011)). The moment of force due to fluid–particle interaction and the moment of force due to asymmetrical normal traction distribution are generally neglected. In the DEMEST program, the moment of force due to the fluid–particle interaction and moment of force due to the tangential contact force are considered. This is very important since the resulted moment of force can significantly influence the translational velocities of particles and thus the simulation accuracy. This is due to the fact that the considered Magnus force in the forces balance is a function of the particle angular velocity.

# 6 Numerical methods for fluid motion

A better understanding of mechanical and thermal behaviour of complex granular flow can be obtained with numerical methods in addition to experimental studies. The modelling of the gas–solid flow can be achieved at different levels of detail. Generally, the solid phase is represented as continuum or discrete phase. The particle phase can be described as a fluid when the continuum hypothesis is satisfied. Hence, the physical values of the solid phase are modeled with the balance equations of the single-phase flow. By the reason of continuous increase in the computer performance, the solid can be treated as disperse phase by solving Newton's equations of motion, e.g. the trajectory of each particle is followed. In the previous sections 3 and 5, the calculation of the solid phase is discussed in detail. The physical values of the fluid phase such as velocity, pressure, temperature, density can be determined with two different approaches, namely grid-based methods and mesh-free particle methods (see **Figure 6.1**). In the grid-based method, the computational domain is discretised in finite objects, so-called numerical grid. The conservation equations are solved numerically based on different numerical methods, e.g. finite element method, finite volume method or spectral method. The physical values of the fluid phase can also be calculated based on the mesh-free particle methods such as determined particle hydrodynamic method or mesh-free Galerkin methods. Here, the computational domain is divided into a finite number of nodes (mass particles), where the variations of physical values around each mass particle along its trajectory are described.

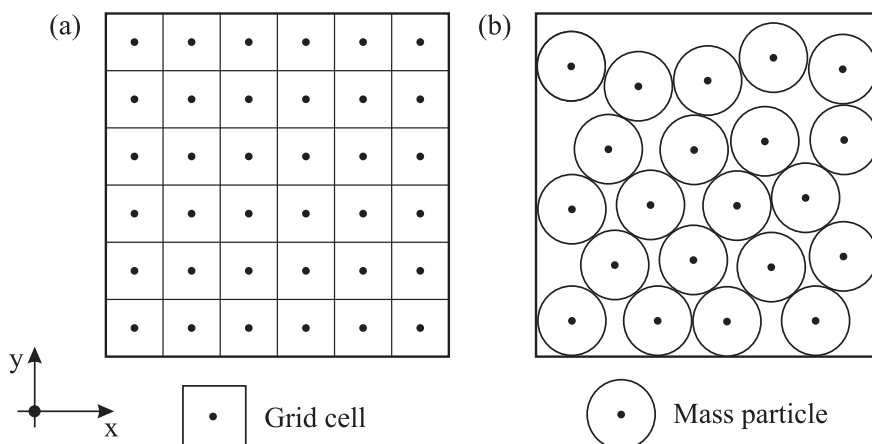


**Figure 6.1:** Numerical approaches for modelling the fluid phase: (a) grid-based methods and (b) mesh-free particle methods

In the grid-based methods, the fluid motion can be modeled in two different approaches: Eulerian and Lagrangian representations. In the Eulerian description or the spatial description, a certain fixed location in the flow field is selected, where the change in its physical properties is followed as different fluid materials move through that location. This means, the mesh cells and their grid points remain spatially fixed in space and don't change with time, while the material flows across the grid cell. In the Lagrangian description, also known as the material description, the fluid materials are tracked as they move in the computational domain while their physical properties changes are monitored. Here, the grid is attached to the fluid

material and it moves with the material motion. Similar to the grid-based methods, the fluid motion in the mesh-free particle methods can be described based on Eulerian or Lagrangian representation. In the literature, the Lagrangian particle methods are, however, almost employed.

## 6.1 Mesh-free particle methods

The calculation of the fluid motion with the particle methods offers complementary tools to the conventional grid-based approaches. These methods are known as mesh-free particle methods due to the absence of the numerical grid. It should be mentioned here that some particle methods are associated with a grid like in Lattice Boltzmann method. Therefore, the particle methods cannot be completely considered as mesh-free methods. The majority of the particle methods are pure Lagrangian, but there are a few works on mesh-free particle methods based on the Eulerian formulation as well as on the arbitrary Lagrangian Eulerian formulations. Generally, the following steps are necessary to obtain the solution. 1) The continuum should be decomposed into a finite number of particles. 2) At each particle, the functions, the derivatives and the integrals are approximated with the aid of all neighbour particles that exert on the investigated particle. 3) The resulting ordinary differential equations with respect to time are solved using numerical technique methods. The mesh-free particle methods are characterised by several advantages such as: the possible dealing with very large deformations, the accurate representation of geometry due to the mesh-free, the possible used of higher-order continuous shape functions and the simple control of simulation accuracy since in the computational sub-domains, where higher accuracy is required, additional nodes (particles) can be added. The most important disadvantage is the high computational effort. Furthermore, certain mesh-free methods are related to numerical instability.

By replacing the numerical grid with particles, the conservation equations can significantly be simplified. For example, the particle equivalent of momentum equation for isothermal and incompressible single-phase flow is expressed by:

$$\rho_i \frac{d\vec{u}_i}{dt} = \underbrace{\mu_f \nabla^2 u_i - \nabla p}_{\vec{f}_{int} + \vec{f}_{ext}} + \vec{f}, \quad (6.1)$$

where  $\vec{u}_i$  is the velocity of the particle  $i$ ,  $\rho_i$  denotes the density evaluated at the position of particle  $i$ ,  $\vec{f}_{int}$  and  $\vec{f}_{ext}$  represent the internal and external forces densities (force per volume) that acting on the particle, respectively. Typical forces densities are pressure, viscosity, gravitational, buoyancy and contact.

In the literature, there are a lot of particle methods available, which are difficult to classify in separated groups. According to (Li and Liu 2002), the particle methods can, however, be divided based on the computational formulation into three different categories: the particle methods with a strong form approximation of partial differential equations (PDEs), particle methods with a weak form approximation of the PDEs and particle methods with strong and weak forms approximations of the PDEs. While the partial differential equations in the strong formulation are satisfied exactly at each point, the PDEs in the weak formulation are only satisfied in an averaged, integral sense over the computational domain. In the first approach, the PDEs are discretised with the aid of specific collocation technique such as the smoothed particle hydrodynamic, the vortex methods and the generalized finite difference method. In the second group of particle methods that are generally summarised under mesh-free Galerkin methods, the Galerkin weak formulations are used. Examples of the mesh-free Galerkin methods are diffuse element method, element free Galerkin, h-p cloud method and

many others. The last class of the particle methods is used strong and weak approximations of the PDEs, like particle-in-cell method and reproducing kernel particle method.

The particle methods can also be classified depending on the applied collision detection models in two different categories, viz. stochastic or deterministic particle methods. In this context, the majority of the particle methods are based on stochastic collision detection model such as molecular dynamics methods, direct simulation Monte Carlo methods and Lattice Boltzmann method. The deterministic particle methods e.g. smoothed particle hydrodynamic and vortex methods are not employed as frequently as the stochastic particle methods by the reason of higher computational effort.

In the following sections, the numerical simulation of fluid motion based on particle methods including the smoothed particle hydrodynamic method and the mesh-free Galerkin methods is explained briefly. Further information for these methods can be found in (Belytschko et al. 1996, Li and Liu 2002, Liu and Liu 2003, Li and Liu 2004).

### 6.1.1 Smoothed particle hydrodynamic method

The smoothed particle hydrodynamic method (SPH) is an interpolation numerical method to approximate the values and derivatives of continuous fluid by main of discrete sample particles. The SPH method is based on a strong form approximation of partial differential equations. Originally, the SPH method dated back to (Lucy 1977) and was applied to the simulation of astrophysical problems. In 1992, (Monaghan 1992) modified this to deterministic mesh-free particle method and applied to solid and fluid mechanics simulation. The SPH method for the determination of fluid motion is based on Navier–Stokes equations using particles instead of the numerical grid.

The basic idea behind the SPH method is: the continuum has to be divided into discrete mass packets that are arbitrarily distributed in the computational domain and move according to the flow. The discrete objects, which are identified as smoothed SPH particles, represent the fluid entities such as mass, velocity, pressure and density. The spatial distance between the SPH objects is considered as the smoothing length. In the SPH model, the system of partial differential equations (PDE) is transformed into a system of time-dependent ordinary differential equations (ODE). The solution of ODE system can be then preformed employing standard time integration methods. To achieve this transformation, the hydrodynamics equations (i.e. Navier–Stokes equations) should be approximated in two successive steps. In first phase, the continuum physical quantities and their derivatives are averaged by main of kernel function that can serve as a smoothing interpolation field. In the next step, the obtained kernel integrals of each SPH object can be determined by a summation of the physical properties of all SPH particles that are existent within the range of the smoothing length. The physical meaning of the kernel function, often called window or weighting function, denotes to the particle position probability, but is here just a smoothing technique. The main point of the SPH method is the selecting of a smooth kernel for the localisation of the strong form of the PDE using a convoluted integration.

Similar to the DEM model, the SPH method uses a deterministic collision model to detect the contact between the SPH particles. Here, a contact is registered when a penetration between the collision partners occurs. The distance that the SPH particle has travelled inside its collision partner is defined as the penetration depth.

The SPH method can be applied to different numerical problems such as compressible flow, incompressible flow, multiple phase flow, heat conduction, surface tension and many others. Recently, a lot of improvements have been achieved, for example the method efficiency, the correct selection of the interpolation kernel and the possibility of the parallel calculation (summarised by (Li and Liu 2002, Liu and Liu 2003)).

### 6.1.2 Mesh-free Galerkin methods

Compared to the SPH method, the mesh-free Galerkin methods are newly developed. Based on Galerkin weak formulations of partial differential equations, different approaches are proposed. In the mesh-free Galerkin methods, the approximations (interpolants) are constructed among a set of particles that don't have any topological connections and are randomly distributed in the computational domain. The most applied mesh-free approximations are formulated by a data fitting algorithm. This can be achieved using an inverse distance weighted principle that is deterministic multivariate interpolation for a set of scattered particles. Based on this principle, diverse mesh-free Galerkin methods can be found in the literature, for example diffuse element method, element free Galerkin method, reproducing kernel particle method, partition of unity methods, mesh-less local Petrov–Galerkin method and many others.

In 1992, the diffuse element method (DEM) is proposed. The basic idea behind the diffuse element method is to approximate the continuous function from a given set of points. The partial differential equations can then be solved employing this approximation method. In fact, the essence of this method is based on the moving least squares approximation that enables the reconstructing of continuous function from sample of unorganized points. The element free Galerkin method (EFG) that is devolved in 1994 is based on the moving least square approximation. It avoids, however, the inconsistencies inherent of some smoothed particle hydrodynamic method formulations. Meanwhile, a similar approach, so-called the reproducing kernel particle method (RKPM) is developed in 1995. The only difference between EFG and RKPM is that the reproducing kernel particle method originates from the wavelets instead of the curve-fitting. The partition of unity methods (PUM) can be considered as a generalisation of classic finite element method. The basic difference among all partition of unity methods such as hp-cloud method, particle partition of unity method and extended finite element method is by the selection of partition of unity functions and/or the enrichment functions. One of well-known mesh-free Galerkin methods is the Mesh-less Local Petrov–Galerkin method (MLPG). This method differs from other methods since the local weak forms are generated over overlapping sub-domains instead using the global Galerkin weak formulations. In the literature, there are many other relevant mesh-free Galerkin methods (summarised by (Li and Liu 2002, Li and Liu 2004)).

### 6.1.3 Other particle methods

Since 1990, many particle methods have been developed. Furthermore, the research is still active on proposing new theories and computational formulations for the particle methods. However, each method owns its properties and thus it is difficult to find a suitable method for all cases. In this context, there are important contributions that are worth to mentioned here.

The molecular dynamics approaches (MD) are one of the most important particle methods. It is widely applied to simulate several scientific and engineering problems. In principle, the molecular dynamics methods can be classified in two categories, namely ab initio molecular dynamics and semi-empirical molecular dynamics. Another important particle method, especially for fluid mechanics applications is the vortex method (VM). In the conventional grid-based methods, the numerical solution of the Navier–Stokes equations is achieved with a velocity–pressure coupling. The vortex method presents an alternative method based on the vorticity–velocity formulation. Similar to vortex method, the particle-in-cell method (PIC) is a dual Lagrangian and Eulerian descriptions. The basic idea behind the dual descriptions is to follow the motions of material particles that include information of physical values in a Lagrangian representation. The spatial discretisation (displacement interpolation) is carried out with respect to fixed spatial coordinate disregarded from the material particles in Eulerian representation. Other particle method that has been successful used for complex fluid

calculation is the Lattice Boltzmann method (LBM). Here, the discrete Boltzmann equation is solved instead of the Navier–Stokes equations. Further detailed information regarding the particle methods can be found in (Belytschko et al. 1996, Li and Liu 2002).

## 6.2 Grid-based methods

The analytical solution of Navier–Stokes equations is only possible under extreme simplifications and assumptions. Therefore, the partial differential equations must be numerically solved. In this context, the exact solution is approximated by a finite number of values that can be determined through solving several algebraic equations instead of partial differential equations. To achieve this, the following steps are, however, necessary. First, the computational domain should be divided into sub-domains, also known as control volumes or grid cells. Second, the partial differential equations should be converted into a system of algebraic equations employing one of discretisation approaches such as finite element method, finite volume method or spectral method. Third, numerical techniques are used to solve the obtained algebraic equations system. Here, the solution of algebraic equations system is an approximation of the exact solution.

The fluid motion in grid-based methods can be described in the Eulerian or Lagrangian representation. The Lagrangian grid-based methods are characterised with several advantages such as: 1) The complex geometries can easily treated using an unstructured mesh. 2) The program is simpler due to the fact that there are no convective terms in the associated partial differential equations. 3) The numerical grid is only needed within the problem domain and thus these methods are numerically very efficient. By the reason of these advantages, the Lagrangian grid-based methods are widely applied to solid mechanics problems. By the contrast, the Eulerian grid-based methods are almost employed exclusively in fluid mechanics, because the partial differential equations are mathematically simple to handle. A complete comparison between the Lagrangian and Eulerian grid-based methods can be found for example in (Epple et al. 2012).

The basic mathematical formulations of the single-phase flow are the balance equations (conservation equations) of momentum, mass, energy and species concentration as well as the constitutive relations and the thermodynamic equation of state. In the Eulerian representation, the continuity equation and the momentum equations that usually known as Navier–Stokes equations, are expressed by:

$$\frac{\partial \rho_f}{\partial t_f} + \nabla \cdot (\rho_f \vec{u}_f) = 0, \quad (6.2)$$

$$\frac{\partial(\rho_f \vec{u}_f)}{\partial t_f} + \nabla \cdot (\rho_f \vec{u}_f \vec{u}_f) = -\nabla \cdot (\mathbf{T}_f) - \nabla p + \rho_f \vec{g}, \quad (6.3)$$

with the stress tensor for Newtonian fluids (Bird 1976):

$$\mathbf{T}_f = -\left[ \left( \lambda_f - \frac{2}{3} \mu_f \right) (\nabla \cdot \vec{u}_f) \mathbf{I} + \mu_f \left( (\nabla \vec{u}_f) + (\nabla \vec{u}_f)^T \right) \right], \quad (6.4)$$

where  $\vec{u}_f$  represents the fluid velocity,  $\mu_f$  is the fluid dynamic viscosity,  $\mathbf{I}$  is the unit matrix,  $p$  and  $\vec{g}$  denote to the static pressure and the gravity acceleration, respectively. The bulk viscosity  $\lambda_f$ , also known as second or volume viscosity, can be neglected for incompressible fluid. The gas density  $\rho_f$  is calculated with the aid of the ideal gas law as:

$$\rho_f = \frac{M_f}{RT_f} p. \quad (6.5)$$

Here,  $M_f$  is the molar mass and  $T_f$  represents the fluid temperature. The energy and species transport equations can be written as:

$$\frac{\partial(\rho_f h_f)}{\partial t_f} + \nabla \cdot (\rho_f \vec{u}_f h_f) = -\nabla \cdot \left( \frac{\mu_f}{\text{Pr}} \nabla h_f \right) + S_h, \quad (6.6)$$

$$\frac{\partial(\rho_f c_{f,i})}{\partial t_f} + \nabla \cdot (\rho_f \vec{u}_f c_{f,i}) = -\nabla \cdot \left( \frac{\mu_f}{\text{Sc}} \nabla c_{f,i} \right) + S_{c,i}, \quad (6.7)$$

where  $h_f$  is the enthalpy,  $c_{f,i}$  denotes to the concentration of species  $i$ , Pr and Sc represent the Prandtl and Schmidt numbers, respectively. The heat source term  $S_h$  is composed of two parts: the heat source term due to the chemical reactions and the radiation source term. The concentration source term takes into account the formation or reduction of the species  $i$  by the reason of chemical reactions.

With the aid of previous coupled, non-linear partial differential equations, the spatial and temporal changes of single-phase flow variables such as velocity, pressure, temperature, species concentration and density can then be determined. This requires the division of the problem domain into grid cells, the discretisation of the partial differential equations using a discretisation approach and solving finally the generated system of the algebraic equations employing an iterative method. In the following sections, the numerical approaches for the solution of the balance equations of the single-phase flow will be explained. Further information can be found in (Ferziger and Perić 2002, Schäfer 2006, Epple et al. 2012).

### 6.2.1 Numerical grid

The decomposition of the domain into finite control volumes, i.e. numerical grid is the first step in obtaining a numerical solution. The numerical grid represents the discrete locations in the computational domain  $\Omega$ , where the physical values of fluid phase are determined. In 2D cases, the grid is formed with grid lines, while in 3D cases it is formed by grid surfaces (grid curves)  $\partial\Omega$  that consist of grid lines. The grid points identify the intersections of the grid lines (see Figure 6.2).

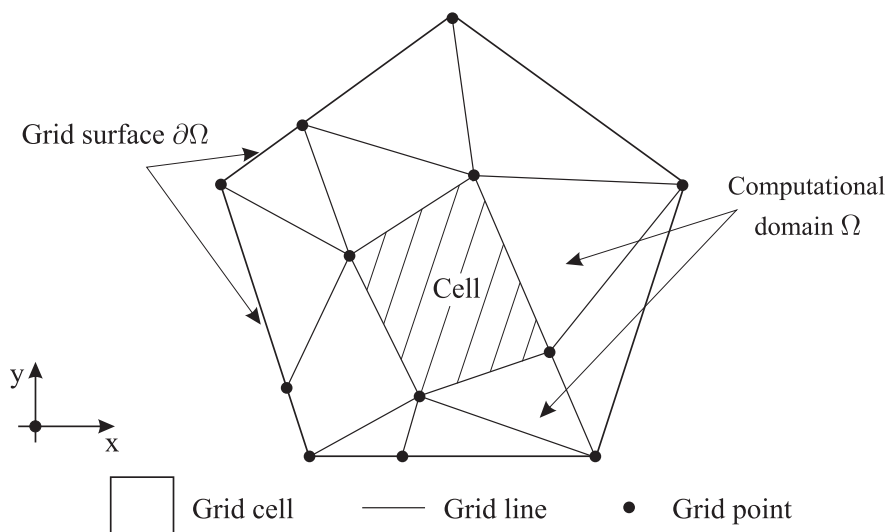


Figure 6.2: Numerical grid

Generally, the numerical grid can be classified regarding the logical arrangement of the grid cells as structured grids and unstructured grids. In the structured grids, the arrangement of the grid cells and thus the grid points is regular. However, the structured grids can be warped, but basically they are rectangles in 2D or cuboids in 3D cases. Due to the regular arrangement of the grid cells, certain fixed relations can be derived between the neighbouring cells, which show important opportunities for a simple discretisation and solution scheme. For the unstructured grids, by contrast, the arrangement of the grid points is irregular. The irregularity by distributing the grid cells over the computational domain offers higher flexibility for an accurate representation of the geometry. Furthermore, the unstructured grids can be easily fitted to computational domains with complex boundaries. However, the locations of the grid points as well as the relations between the neighbouring cells should be stored, which lead to additional data structure in comparison to the structured grids. It should be mentioned here that the combination between the structured and unstructured grids such as block-structured grids and hierarchically structured grids can result in obtaining the advantages of both grids. The block-structured grids, although consist of different sub-blocks that all have structured grids, have irregular blocks arrangement. In the hierarchically structured grids, the grids in the sub-blocks are structured. In certain regions in the computational domain, the mesh is locally refined in a structured grid. In this context, these methods can be considered as a compromise between the structured grids with their inflexibility in the geometry representation and the unstructured grids with their high computational effort.

The numerical grid can also be classified regarding the gird type as Cartesian grid, boundary-fitted grid and overlapping grid. In the Cartesian grids, the problem domain is discretised by a structured numerical grid. At the boundary, unstructured cells may be required, which need a special treatment. By contrast, all boundary parts are approximated with grid lines in the boundary-fitted grids, also known as body-fitted grids. In the overlapping grids, different regions of the computational domain can be covered with independently grids. Here, the use of the structured grids can lead at the interfaces to overlapping areas, which require again a special treatment. Compared to the Cartesian and overlapping grids that are applied only to special applications, the boundary-fitted grids are frequently used. A complete comparison between different grids types and their generation methods can be found for example in (Ferziger and Perić 2002).

The linear equation systems that result from the discretisation of partial differential equations can be solved using iterative solution methods such as Jacobi or Gaus-Seidel methods. For the convergence, the following criterion is valid: the finer is the grid the slower solution is converged. Increasing the number of the grid points leads in these methods to increase the number of iterations needed to reach the same accuracy. In other words, the number of the iterations to obtain a converged solution is linearly proportional to the number of nodes in one coordinate direction. Almost all iterative solution methods converge on finer grids with a higher accuracy, but require considerably more computing time. Therefore, it is advisable first to use a coarse grid to produce a starting solution for the fine grid in order to reduce the computational cost and to maintain the higher accuracy of the fine grid. This approach, which is known in the literature as the multi-grid method, has received a lot of attention in the past decade as it can solve the transport equations very efficiently. Compared to classical methods, the required number of iterations can mostly be unaltered independent of grid spacing in the multi-grid method. As a result, the computational effort is proportional to the numbers of grid nodes  $O(N \log N)$  (Schäfer 2006).

The basic idea behind the multi-grid methods is based on elimination of wavelength error components. In this context, the iterative algorithms eliminate efficiently the error components of an approximate solution if the wavelength error components correspond to the

grid spacing. The errors with larger wavelengths can also decrease but relatively slowly. This is due to the fact that for each grid point only local neighbouring relations are arranged through the discretisation scheme. Sequentially in the iteration methods, the boundary values propagations in the direction of the solution domain interior occur very slowly. The selection of grid levels and thus the coarsest grid depends generally on the geometry that has to be accurately represented. According to (Schäfer 2006), 4 to 5 grid levels for 2D and 3 to 4 grid levels for 3D cases. In the literature, there are a lot of approaches for cycling through the different grid levels, where the well-known of them are V-cycles and W-cycles. The computational effort per cycle in W-cycles is higher than V-cycles. However, the number of required cycles to reach a certain convergence criterion is lower. Detailed information can be found in (Schäfer 2006).

### 6.2.2 Discretisation approaches

Since the analytical solution of partial differential equations is only possible in a few cases, the physical values of the single-phase flow are approximated at each grid cell as a function of time and position. In this context, the second step in obtaining a numerical solution is to approximate the partial differential equations into a system of algebraic equations using discretisation methods. In the following sections, the well-known discretisation approaches including finite difference method, finite element method and finite volume method are discussed.

#### 6.2.2.1 Finite difference method

The finite difference method (FD) is the oldest discretisation approaches for the numerical solutions of partial differential equations. Generally, the numerical grid used in FD method is structured grid, where the solution of differential equations is approximated on the grid points (see **Figure 6.3**). Here, the conservation equations are in differential forms and the derivatives are approximated at each grid point using finite difference equations. The differential form of the generic conservation equation in Cartesian coordinate and tensor notation is given as:

$$\underbrace{\frac{\partial(\rho_f \phi_f)}{\partial t_f}}_{\text{Instationary term}} + \underbrace{\frac{\partial(\rho_f u_j \phi_{f,i})}{\partial x_j}}_{\text{Convective term}} = \underbrace{\frac{\partial}{\partial x_j} \left( \Gamma_\phi \frac{\partial \phi_f}{\partial x_j} \right)}_{\text{Diffusive term}} + \underbrace{S_\phi}_{\text{Source term}}, \quad (6.8)$$

where  $\Gamma_\phi$  and  $S_\phi$  represents the diffusion coefficient and the source term of dependent variable  $\phi_f$ , respectively. Here,  $\phi_f$  can be one of fluid physical values, namely the velocity, the enthalpy or the species concentration.

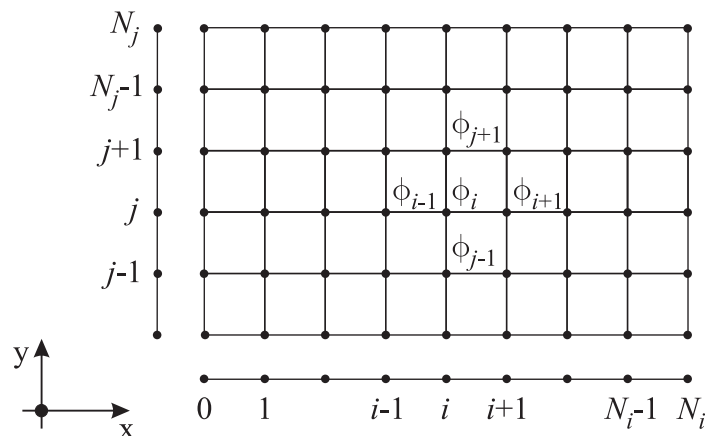


**Figure 6.3:** Typical 2D mesh used in FD method

The iterative solution schemes assumed that  $\phi_f$  is unknown and should be determined, while other variables are already defined from the previous iteration. The number of differential equations and thus the algebraic equations are equal to the number of the grid points. The first and second derivatives of the generic conservation equation can be approximated by mean of different systematic approaches such as Taylor series expansion or polynomial fitting.

Any continuous differentiable function  $\phi(x)$  can be expressed by Taylor series as an infinite sum of function derivatives at a single point  $i$ :

$$\phi(x) = \phi(x_i) + (x - x_i) \left( \frac{\partial \phi}{\partial x} \right)_i + \frac{(x - x_i)^2}{2!} \left( \frac{\partial^2 \phi}{\partial x^2} \right)_i + \dots + \frac{(x - x_i)^n}{n!} \left( \frac{\partial^n \phi}{\partial x^n} \right)_i. \quad (6.9)$$

By neglecting the second and higher-order derivatives and replacing  $x$  with  $x_{i+1}$  or with  $x_{i-1}$ , the following forward and backward schemes for the first derivative in the convective term can be obtained:

$$\left( \frac{\partial \phi}{\partial x} \right)_i \approx \frac{\phi_{i+1} - \phi_i}{x_{i+1} - x_i}, \quad (6.10)$$

$$\left( \frac{\partial \phi}{\partial x} \right)_i \approx \frac{\phi_i - \phi_{i-1}}{x_i - x_{i-1}}. \quad (6.11)$$

Another approximation for the first derivative, so-called central difference scheme, can be obtained by replacing  $x$  with  $x_{i+1}$  and  $x_{i-1}$ :

$$\left( \frac{\partial \phi}{\partial x} \right)_i \approx \frac{\phi_{i+1} - \phi_{i-1}}{x_{i+1} - x_{i-1}}. \quad (6.12)$$

The second derivative in the diffusive term can be determined by using the first derivative approximation twice. The forward scheme for the second derivative (outer derivative) is expressed as:

$$\left( \frac{\partial^2 \phi}{\partial x^2} \right)_i \approx \begin{cases} \frac{\left( \frac{\partial \phi}{\partial x} \right)_{i+1} - \left( \frac{\partial \phi}{\partial x} \right)_i}{x_{i+1} - x_i} & \text{Forward difference scheme (FDS)} \\ \frac{\left( \frac{\partial \phi}{\partial x} \right)_i - \left( \frac{\partial \phi}{\partial x} \right)_{i-1}}{x_i - x_{i-1}} & \text{Backward difference scheme (BDS)} \\ \frac{\left( \frac{\partial \phi}{\partial x} \right)_{i+1} - \left( \frac{\partial \phi}{\partial x} \right)_{i-1}}{x_{i+1} - x_{i-1}} & \text{Central difference scheme (CDS)} \end{cases} \quad (6.13)$$

Here, the inner derivative can also be estimated employing diverse approximations, namely the forward, the backward or the central difference schemes. Furthermore, the Taylor series expansion can be used to approximate the second derivative. By replacing  $x$  with  $x_{i+1}$  and  $x_{i-1}$  in the Equation (6.9), in addition to neglecting the third and higher-order derivatives, the following expressing can be obtained:

$$\left( \frac{\partial^2 \phi}{\partial x^2} \right)_i \approx 2 \frac{\phi_{i+1}(x_i - x_{i-1}) + \phi_{i-1}(x_{i+1} - x_i) - \phi_i(x_{i+1} - x_{i-1})}{(x_i - x_{i-1})(x_{i+1} - x_i)(x_{i+1} - x_{i-1})}. \quad (6.14)$$

The neglecting of higher-order derivatives by the calculation of the first and second derivatives leads to second and third-order truncation errors that measure the accuracy of approximations.

Besides the Taylor series expansion, the polynomial fitting represents an alternative method to approximate the derivatives. Generally, the polynomial fitting, also known as curve fitting, is a method of constructing a mathematical function (curve) that fits a set of data points. It can be achieved either with interpolation approaches, where new data points are generated within the range of a given discrete points or with smoothing methods, in which a smooth function that fits the data points is built. The derivatives can be estimated by fitting the function to an interpolation curve and differentiating the resulting curve. For example, the linear interpolation to approximate the function value at the point  $x$  can be expressed with the aid of  $x_{i+1}$  and  $x_i$  as:

$$\phi(x) = \frac{x - x_i}{x_{i+1} - x_i} \phi_{i+1} - \frac{x - x_{i+1}}{x_{i+1} - x_i} \phi_i. \quad (6.15)$$

The derivative of this function leads to the forward difference scheme (see Eq. (6.10)). Similarly, the backward difference scheme can be obtained if a linear interpolation is applied to interpolate the function between  $x_{i-1}$  and  $x_i$ . The use of quadratic interpolation to fit the function value at the points  $x_{i-1}$ ,  $x_i$  and  $x_{i+1}$  results in the central difference scheme.

The Taylor series expansion and the polynomial fitting are not the only methods to approximate the derivatives. In the literature, there are many special schemes. Further information can be found for example in (Ferziger and Perić 2002). For simple geometries, the FD method is easy to apply and produces on structured grid very effective results due to the possibility to use higher-order schemes. However, the conservation cannot be guaranteed in the FD method unless the consideration of additional assumptions. Furthermore, the limitation of using structured grids and thus the limitation to simple geometries represents the main disadvantages of the FD method.

### 6.2.2.2 Finite element method

The finite element method (FE) is a numerical discretisation approach to approximate the solution of partial differential equations. In the finite element method (FE), the computational domain is divided into a set of finite elements that are generally unstructured. The basic idea behind the FE method is that the partial differential equations are multiplied by a weight function before they integrated over the whole computational domain. Here, the solution of the differential equations is estimated by a linear combination of parameters, which are at the beginning unknown and approximation functions that is defined on the entire computational domain.

The required solution can be approximated using Lagrange interpolation as:

$$\phi(x, y, z) \approx \phi^e(x, y, z) = \sum_{p=1}^{N_K^e} \phi_p^e \psi_p, \quad (6.16)$$

where  $\phi_p^e$  is the unknown variable in the cell grid points and  $\psi_p$  is the local shape functions. If this approximation functions are inserted in the partial differential equations, the

PDEs are no longer satisfied, resulting in residuals  $R$ . In the method of weighted residues, the integrated residual over each element should be disappeared.

$$\int_{CV} R_\phi^e \psi_w dx dy dz = 0. \quad (6.17)$$

Finally, a system of algebraic equations for the determination of variable  $\phi$  can be obtained. The weighting function  $\psi_w$  that is used for the interpolation is identical to the local shape function in Bubnow–Galerkin method. By Petrov–Galerkin method, the weighting function and the local shape function are different. The solution in the FE method is estimated in the grid points. With the aid of weighting function and/or local shape function, the solutions between the grid points can be calculated, too. One of the important advantages of the finite element methods is the possible dealing with complex geometries. On the other hand, the main disadvantage of the FE method is that the matrices of the linearized equations system are unstructured compared to those of the structured grids, leading to difficulty by finding the efficient approach to obtain the solution. This drawback is also found in all discretisation methods that use unstructured grids. Detail information on the finite element method and their application can be found for example in (Zienkiewicz, Taylor and Nithiarasu 2005, Schäfer 2006). It should be mentioned here that FE method is a special case of discontinuous–Galerkin Finite element method that is employed polynomial approximation functions instead of the linear shape function.

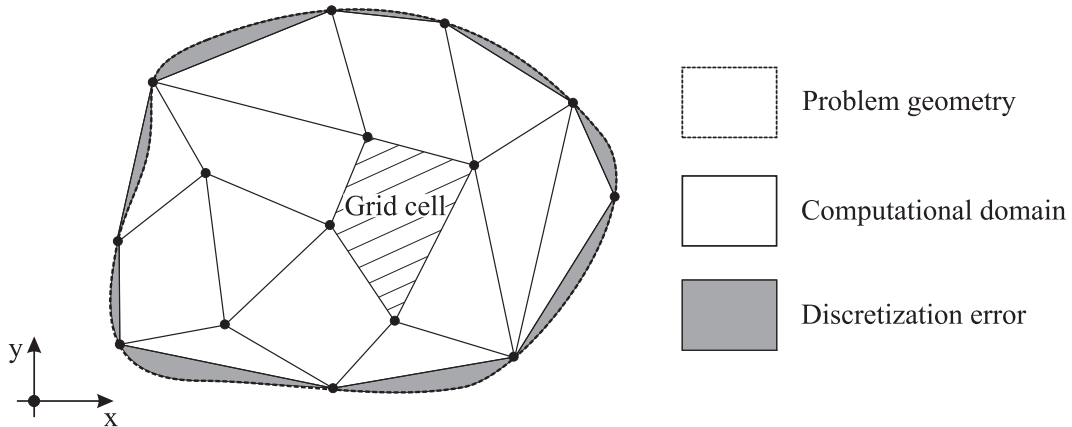


**Figure 6.4:** Typical 2D mesh used in FE method

### 6.2.2.3 Finite volume method

Similar to the finite element method, the finite volume method (FV) approximate the differential equations at discrete volumes. The FV method starts from the integral form of conservation laws. The differential equations of conservation equations are applied to each control volume, where they are approximated in the centre of grid cells. By using the divergence theorem, also known as Gauss's theorem, the volume integrals in a partial differential equation are converted to surface integrals. The variable at the control volume surface can be determined using interpolation techniques with the aid of nodal values of neighbour cells. The surface and volume integrals can then be estimated by main of mathematical formulae. For each control volume, an algebraic equation that contains the nodal values of the control volume and the neighbour cells is obtained. The number of algebraic equations is equal the number of grid cells and thus the number of unknown values. These values can finally be calculated using iterative methods. Due to the fact that the flux entering a certain control volume is equal to that leaving the adjacent volume, the finite volume method is conservative. One of the important advantages of the FV method is the possible application to each grid type (structured or unstructured grid). Accordingly, the finite element method can be

applied to complex geometries. On the other hand, the restriction of using and developing higher-order schemes in particularly in 3D cases represents the major disadvantages of the FV approach. The reason of this is that the FV method needs three level of approximation: interpolation, differentiation and integration. For unstructured grids, the use of higher-order schemes can result in numerical instabilities (Ferziger and Perić 2002).

As a start point for the FV method is the integral form of the generic conservation equation:

$$\underbrace{\frac{\partial}{\partial t} \iiint_{CV} \rho_f \phi_f dV}_{\text{Instationary term}} + \underbrace{\iint_S \rho_f \vec{u}_f \phi_f \cdot \vec{n} dS}_{\text{Convective term}} = \underbrace{\iint_S \Gamma_\phi \nabla \phi_f \cdot \vec{n} dS}_{\text{Diffusive term}} + \underbrace{\iiint_{CV} S_\phi dV}_{\text{Source term}}. \quad (6.18)$$

The finite volume method requires a decomposition of the computational domain into a finite number of non-overlapping grid cells. In 3D cases, each grid cell has six neighbours, unless it is located on the boundary of the computational region. The closed surface of a grid cell consists of sub-areas  $S_i$ . Each sub-surface has a normal vector  $\vec{n}_i$  that is directed outwards of this area (see **Figure 6.5**). In the FV method, the integral form of the generic conservation equation is applied to each control volume. The surface and the volume integrals of the partial differential equations should be approximated in order to obtain a system of the algebraic equations.

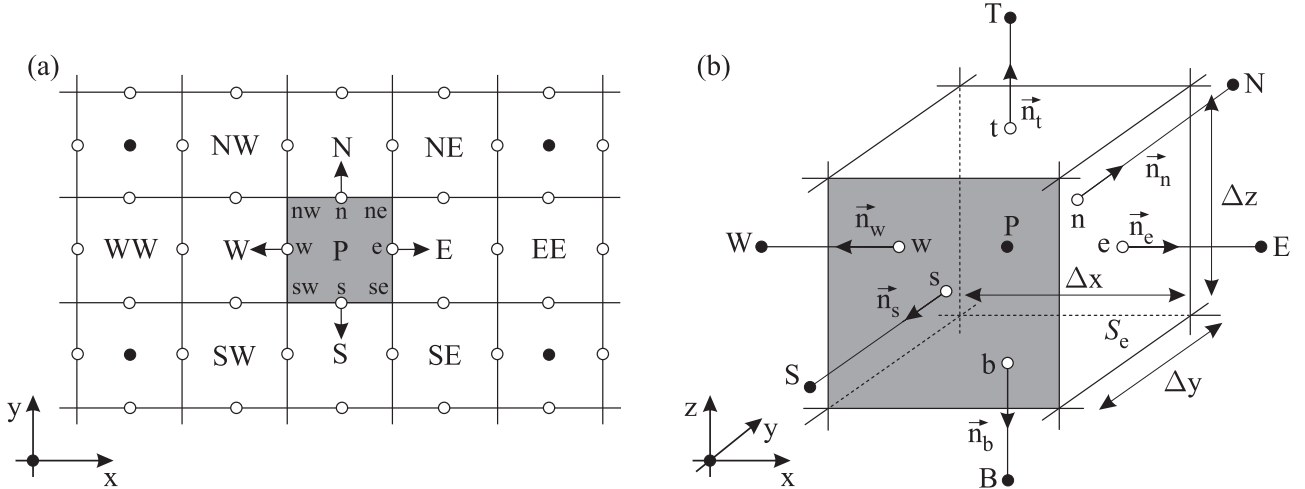


**Figure 6.5:** Cartesian grid used in FV method: (a) 2D mesh and (b) 3D mesh

The approximation of the total flux surface integral can be formed by the sum of fluxes integrals over all sub-surfaces:

$$\iint_S f dS = \sum_{i=1}^k \iint_{S_k} f_k dS_k, \quad (6.19)$$

where  $k$  denotes the number of the control volume sub-surfaces ( $k=4$  for 2D and  $k=6$  for 3D cases). The term  $f$  represents the component of convective or diffusive flux vector in the normal direction to the control volume surface  $k$ :

$$f_k = \begin{cases} \left( \rho_f \vec{u}_f \phi_f \cdot \vec{n} \right)_k & \text{Component of convective flux} \\ \left( \Gamma_\phi \nabla \phi_f \cdot \vec{n} \right)_k & \text{Component of diffusive flux} \end{cases}. \quad (6.20)$$

The exact determination of the surface integral requires the knowledge of the integrand  $f_k$  on the surface  $S_k$ . This cannot be achieved since the only available information is the values of  $\phi_f$  in the centre of the control volumes. Therefore, the flux over a sub-area must be approximated using these nodal values, i.e. the values in the centre of the control volumes. The simplest approximation is the application of the centre rule method. In this context, the surface integral is estimated as a product of the mean value over the surface and the area of the control volume:

$$\iint_{S_k} f_k dS_k = \bar{f}_k S_k \approx f_k S_k. \quad (6.21)$$

Now, the flux  $f_k$  at the centre of the surface  $S_k$  is required. This value is not known and thus it has to be interpolated from the nodal value of the cell and the values of its neighbouring cells. The convective momentum flux can finally be obtained as:

$$\iint_{S_k} (\rho_f \vec{u}_f \phi_f \cdot \vec{n} dS) \approx (\rho_f \vec{u}_f \phi_f \cdot \vec{n})_k S_k = \dot{m}_f^k \phi_f^k. \quad (6.22)$$

The mass flow rate  $\dot{m}_f^k$  that passes through the surface  $S_k$  is again determined by an interpolation. The non-linearity can be dissolved by using a Picard-iteration. It is assumed that the velocity field, the fluid properties and the diffusion coefficient  $\Gamma_\phi$  are known at all control volumes centres. The values of the last iteration are generally used. To calculate the convective and diffusive fluxes, the value  $\phi_f^k$  and its gradient normal to the cell surface should be determined. They can be expressed employing different interpolation methods such as upwind interpolation, linear interpolation, quadratic upwind interpolation and high-order schemes (Ferziger and Perić 2002). This means that the velocity and other fluid properties at the centre of the surface  $S_k$  are calculated by mean of the nodal values.

In the upwind differencing scheme (UDS), the value  $\phi_f^k$  at the control volume face is approximated depending on the flow direction using a backward or forward difference for the first derivative:

$$\phi_f^e = \begin{cases} \phi_f^P & \text{case } (\rho_f \vec{u}_f \cdot \vec{n})_e > 0 \\ \phi_f^E & \text{case } (\rho_f \vec{u}_f \cdot \vec{n})_e < 0 \end{cases}. \quad (6.23)$$

The UDS is a first-order interpolation method and distinguishes itself by its high stability. If the second-order linear interpolation (CDS) is used, the value  $\phi_f^k$  is estimated between the two nearest cells as:

$$\phi_f^e = \phi_f^E \lambda_e + \phi_f^P (1 - \lambda_e), \quad (6.24)$$

with the linear interpolation factor:

$$\lambda_e = \frac{x_e - x_p}{x_E - x_p}. \quad (6.25)$$

The CDS approximation is of second-order accuracy and the error term is proportional to the grid spacing  $\Delta x$  for structured grid and proportional to the product of the grid spacing  $\Delta x$  and the grid expansion factor minus unity for the unstructured grid. The CDS, although characterises with high accuracy, leads to numerical oscillations in the solution at high local Peclet numbers:

$$\text{Pe} = \frac{\rho_f u_f \Delta x}{\mu_f}. \quad (6.26)$$

A blending method that combines the CDS and the UDS can also be applied to approximate the value  $\phi_f^k$  at the control volume face. Here, the advantages of both interpolation methods, i.e. the high numerical stability and the accuracy can be maintained.

$$\phi_f^e = (1 - \alpha_{UDS}) \nabla \phi_f^P (\vec{r}_e - \vec{r}_p) + \alpha_{UDS} \begin{cases} \phi_f^P & \text{case } (\rho_f \vec{u}_f \cdot \vec{n})_e > 0 \\ \phi_f^E & \text{case } (\rho_f \vec{u}_f \cdot \vec{n})_e < 0 \end{cases}, \quad (6.27)$$

where  $\alpha_{UDS}$  denotes the blending factor,  $\vec{r}_e$  and  $\vec{r}_p$  are the position vectors of the subsurface  $k = e$  and the centre of the grid cell, respectively. With the aid of the blending factor, the CDS and UDS can be superimposed.

The next logical improvement to estimate the value  $\phi_f^k$  between the nodal cells ( $P$  and  $E$ ) is to construct a parabola instead of straight line. For this purpose, more nodal values are required for the approximation:

$$\phi_f^e = \begin{cases} \phi_f^P + \lambda_1 (\phi_f^E - \phi_f^P) + \lambda_2 (\phi_f^P - \phi_f^W) & \text{case } (\rho_f \vec{u}_f \cdot \vec{n})_e > 0 \\ \phi_f^E + \lambda_1 (\phi_f^P - \phi_f^E) + \lambda_2 (\phi_f^E - \phi_f^{EE}) & \text{case } (\rho_f \vec{u}_f \cdot \vec{n})_e < 0 \end{cases}. \quad (6.28)$$

The coefficient  $\lambda_1$  can be determined in term of control volumes coordinates as:

$$\lambda_1 = \begin{cases} \frac{(x_e - x_P)(x_e - x_W)}{(x_E - x_P)(x_E - x_W)} & \text{case } (\rho_f \vec{u}_f \cdot \vec{n})_e > 0 \\ \frac{(x_e - x_E)(x_e - x_{EE})}{(x_P - x_E)(x_P - x_{EE})} & \text{case } (\rho_f \vec{u}_f \cdot \vec{n})_e < 0 \end{cases}, \quad (6.29)$$

and for the coefficient  $\lambda_2$  as:

$$\lambda_2 = \begin{cases} \frac{(x_e - x_P)(x_E - x_e)}{(x_P - x_W)(x_E - x_W)} & \text{case } (\rho_f \vec{u}_f \cdot \vec{n})_e > 0 \\ \frac{(x_e - x_E)(x_P - x_e)}{(x_E - x_{EE})(x_P - x_{EE})} & \text{case } (\rho_f \vec{u}_f \cdot \vec{n})_e < 0 \end{cases}. \quad (6.30)$$

The determination of the weighting coefficients on the non-orthogonal and/or unstructured grids, by contrast to the structured grids, is not simple. This scheme is known in literature as quadratic upwind interpolation for convective kinematics (QUICK). The QUICK interpolation is of third-order accuracy. Interpolation of higher-order accuracy than third can be reached employing higher-order mathematical formulae e.g. the use of the fitting polynomial with at least degree three that leads to fourth-order truncation error. According to (Ferziger and Perić 2002), the higher-order interpolations may not result in more accurate solution. High accuracy can only be reached if the grid is fine enough to get all details of the solution.

Besides the determination of the surface integral, some terms in the partial differential equations require integration over the volume. The exact calculation of the volume integral

needs the knowledge of the integrand  $Q_f$  over the grid cell volume. This cannot be analytically achieved. Numerical approximation of the volume integral should, therefore, be carried out. The simplest approximation is to estimate the volume integral by the product of the mean value of the integrand and the control volume as follows:

$$\iiint_{CV} Q_f dV = \bar{Q}_f \Delta V \approx Q_f^p \Delta V. \quad (6.31)$$

Here,  $Q_f^p$  represents the value of the variable at the control volume centre. This approximation is of second-order and doesn't require any interpolation since the variable  $Q_f^p$  is available at each grid cell. Higher-order approximations need the nodal values of the variables at different locations.

#### 6.2.2.4 Other discretisation methods

In the literature, there are a lot of discretisation schemes that can be applied to solve numerically the partial differential equations, i.e. to approximate the surface and the volume integrals of PDEs, such as hybrid method, spectral methods and boundary element method.

In form of a so-called hybrid discretisation approach, the finite volume method and finite element method are combined. The hybrid discretisation approach, also known control volume based finite element method (CVFEM), has the advantage of both FE and FV methods. Similar to the FV method, the conservation equations are in integral form and are applied to each control volume. The flux thorough the boundaries of control volumes are then determined in similar way like the FE method.

The spectral methods (SM) are a class of discretisation approaches. They are used to solve numerically certain classes of the partial differential equations. Compared to the FE and FV schemes, the spectral methods are less suitable for general numerical purposes. However, they can be applied to important applications e.g. turbulence simulations. The basic idea behind the SM is to approximate the spatial derivatives by main of Fourier series or one of their generalisations such as fast Fourier transform (FTT). The solution of the partial differential equations is evaluated as a sum of certain basic functions as in the FTT, where the signal is decomposed into sum of sinusoids (sine and cosine) of various frequencies. The functions coefficients are then calculated in order to satisfy the differential equations. The spectral methods and the finite element methods are based on the same idea. The major difference between both methods is that the SM uses non-zero basis functions over the entire computational domain, while the FE scheme uses these functions only in small sub-areas of the computational domain. As a result, the spectral methods have a very good convergence rate making it's the fastest possible methods for the problems, which they are applicable (Ferziger and Perić 2002).

The boundary element method (BEM), also known as boundary integral equation method, is one of the discretisation approaches for solving the partial differential equations. The boundary element method, although it can be used to solve different engineering problems, is rarely applied to fluid dynamics. The basic idea behind BEM is to reformulate the partial differential equations into integral equations. Here, the given boundary conditions are used to fit values into the integral equations. Similar to the spectral methods, the main disadvantage of the boundary element method is that the integral equations reformulation can only be carried out for certain partial differential equations. For this reason, the BEM is not employed as frequently as the FD or FE methods. On the other hand, the BEM, where it is suited, is computationally more efficient compared to other competitive discretisation methods.

### 6.2.3 Time discretisation

In many engineering applications, the investigated problems are unsteady. In other words this means that the physical values of the fluid phase are spatial and time dependence. For the numerical solution of unsteady flows, the time should be discretised besides the space discretisation. To obtain the time-dependent solution, initial conditions and boundary conditions that can also depend on time should be defined. Let the variable  $\phi_f$  is depending on the time, for example in a first-order differential equation:

$$\frac{d\phi_f(t_f)}{dt_f} = f(t_f, \phi_f(t_f)), \quad (6.32)$$

with the initial condition:

$$\phi_f(t_f^0) = \phi_f^{t_0}. \quad (6.33)$$

Now, the problem is to calculate the solution  $\phi_f^{t_f^0 + \Delta t_f}$  after a short time  $\Delta t_f$  from the start point  $t_f^0$ . By the same token, the solution  $\phi_f^{t_f^0 + \Delta t_f} = \phi_f^{t_f^1}$  can be considered as an initial condition for the new solution  $\phi_f^{t_f^1 + \Delta t_f} = \phi_f^{t_f^2}$  after a time step  $\Delta t_f$ . This problem can be solved by integrating the equation (6.32) from  $t_f^n$  to  $t_f^{n+\Delta t_f}$  as:

$$\int_{t_f^n}^{t_f^{n+1}} \frac{d\phi_f(t_f)}{dt_f} = \int_{t_f^n}^{t_f^{n+1}} f(t_f, \phi(t_f)) dt_f. \quad (6.34)$$

The equation (6.34), although represents the exact solution, cannot be estimated without knowing the integral on the right hand side. For this reason, approximation should be introduced. The explicit method, also known the forward Euler method, is obtained when the integral is evaluated using the value of the integrand at the initial point:

$$\phi_f^{n+1} = \phi_f^n + f(t_f^n, \phi_f^n) \Delta t_f. \quad (6.35)$$

Here, the shorthand notation for  $\phi_f^n = \phi_f^{t_f^n}$  and  $\phi_f^{n+1} = \phi_f^{t_f^{n+1}}$  is used. If however the final point is used to approximate the integral, the implicit or backward Euler method is extracted:

$$\phi_f^{n+1} = \phi_f^n + f(t_f^{n+1}, \phi_f^{n+1}) \Delta t_f. \quad (6.36)$$

When the straight line interpolation between the initial and final points is applied to estimate the integral, the trapezoid rule can be obtained:

$$\phi_f^{n+1} = \phi_f^n + \frac{1}{2} [f(t_f^n, \phi_f^n) + f(t_f^{n+1}, \phi_f^{n+1})] \Delta t_f. \quad (6.37)$$

This approximation is of the second-order accuracy and gives the basic formula for the frequently used Crank–Nicolson method. Higher-order temporal discretisation schemes such as third or fourth-order Runge–kutta as well as Adams methods can be used when the higher-order spatial discretisation schemes are also applied (Ferziger and Perić 2002).

### 6.2.4 Pressure velocity coupling

The direct solution of the Navier–Stokes equations is not possible due to the unknown pressure, whose gradient contributes to all momentum equations. In compressible flow, the

density is appeared as second variable, where the use of an additional equation (equation of state) is necessary. There is no explicit equation for the pressure that enables the pressure gradient to be linked with the momentum equations. However, the pressure can be indirectly defined through the continuity equation. This means, if the correct pressure field is inserted into the momentum equations, the obtained velocity field should also satisfy the continuity equation.

One way to handle this indirect coupling is to eliminate the pressure using a penalty–function formulation. For an incompressible flow, this procedure has many drawbacks. Other approaches eliminate the pressure from the entire formulation making the extension of these methods for compressible flows is not possible, in particularly when the boundary conditions are depending on the pressure. Other possibility is to combine the continuity and momentum equations. In this context, the continuity equation can be used to simplify the divergence of the momentum equation, resulting in the Poisson equation for the pressure. In the Cartesian coordinate and tensor notation, the Poisson equation is expressed as:

$$\frac{\partial}{\partial x_i} \left( \frac{\partial p}{\partial x_i} \right) = - \frac{\partial}{\partial x_i} \left[ \frac{\partial}{\partial x_j} \left( \rho_f u_{f,i} u_{f,j} - \underbrace{\tau_{ij}}_A \right) \right] + \underbrace{\frac{\partial (\rho_f b_i)}{\partial x_i}}_B + \frac{\partial^2 \rho_f}{\partial t_f^2}, \quad (6.38)$$

where  $\tau_{ij}$  is the viscous stress tensor and  $b_i$  the body force per unit mass. The terms ( $A$  and  $B$ ) are zero in case of fluid with constant density and viscosity. The pressure equation can be solved using one of the discretisation methods such as the FE or FV.

The staggered grid arrangement was first proposed to avoid some of convergence problems and oscillations in the pressure and velocity fields. This is due to the fact that the major advantage of this arrangement is the strong coupling between the pressure and the velocities. In the staggered agreement, the scalar variables such as pressure, density, total enthalpy, chemical species and turbulence characteristic values are stored in the cell centres, while the vector variable (velocity) are located at the cell faces of control volumes. For the structured grids, the staggered grid can be applied to simulate compressible or incompressible flows using different discretisation schemes such as FE and FV. The extension of the staggered arrangement to unstructured grids results, however, in higher computational time by the reason of handling with different control volumes for different variables. Therefore, the colocated grid arrangement has become more popular, where all variables share the same nodal point, i.e. all variables are stored in same position. The colocated arrangement, although has significant advantage in complex geometries, was rarely applied to incompressible flows due the difficulty in the pressure–velocity coupling. The increased use of the unstructured grids for the problems with complex geometries makes the colocated arrangement the standard method in the most modern codes.

The Poisson equation is applied to determine the pressure in explicit and implicit solution methods. It is, however, advisable that to derive the equation of the pressure from the discretised momentum and continuity equations rather than the discretisation of the Poisson equation in order to maintain consistency. In the literature, this procedure is known as implicit pressure–correction methods or projecting methods. For incompressible flows, the velocity field is constructed based on predefined pressure field. The obtained velocity field doesn't fulfil the continuity equation. It should then be corrected by subtracting the pressure gradient. The most popular projecting methods such as SIMPLE, SIMPLEC and PISO algorithms can be found for example in (Ferziger and Perić 2002, Epple et al. 2012). Here, they are briefly explained.

The semi-implicit method for pressure-linked equations (SIMPLE) is a two-step algorithm. In the first step, a velocity field, which fulfils the Navier–Stokes equation, is

determined. The pressure gradient is assumed to be known in this step; the values of the last iteration are used. Generally, the calculated values of the velocity field do not stratify the continuity equation. In the second step, the mass defect is defined by using the continuity equation for each control volume. The pressure-correction equation is calculated in order to compensate this mass defect. From the pressure correction, the velocity correction can be estimated. Finally the pressure as well as the velocity is corrected. Both steps are executed in an inner iteration loop until the L2-space of the mass defect  $m^*$  falls below a fixed limited value:

$$|m^*| = \sqrt{\sum_{i=1}^{N^{CV}} m_i^{*2}} < \text{Fixed value.} \quad (6.39)$$

The semi-implicit method for pressure-linked equations consistent SIMPLEC is a similar algorithm to the SIMPLE method. The crucial difference between the two methods is in the formulation of the correction-equation for the velocity field. In the SIMPLE algorithm, the term in the pressure-correction equation that considers velocity correction of neighbour cells is neglected, while in the SIMPLEC algorithm is approximated. The pressure implicit with splitting of operators PISO calculates this term with aid of another correction step. In contrast to previous methods, the PISO algorithm uses besides the implicit also explicit correction steps in order to obtain the solution of the mass and momentum equations.

In principle, there are two approaches for the calculation of the consistent pressure and velocity fields, namely density-based and pressure-based methods. The density-based method assumes that the velocity field is known. The local density is then determined from the continuity equation by the given velocity field. The determination of the pressure is carried out by the use of the thermal state equation for the ideal gas as:

$$p = \frac{\rho_f R T_f}{M_f}. \quad (6.40)$$

The symbol  $R$  denotes the ideal gas constant and  $M_f$  is the molar mass. Generally, the pressure and density fields don't fulfil the momentum equations, so the velocity field is corrected. The density-based method requires an explicit relationship between the pressure and the density. If however this method is applied to incompressible flows, a weak coupling between the pressure and the density should be formulated.

In the pressure-based method for determining the velocity and pressure fields, the local pressure is assumed to be known. For incompressible flows, the velocity field is then calculated from the momentum equations. The obtained velocity field doesn't satisfy the continuity equation, so it should be corrected by subtracting the pressure gradient. Considering compressible flows, the density is calculated at a given pressure from the equation of the state followed then by solving the momentum equations to obtain the velocity field. The pressure-based method has the advantage that can basically be applied to compressible or incompressible flows without the need for the weak coupling between the pressure and the density.

### 6.2.5 Boundary conditions

The continuity, the momentum, the species concentrations and the energy equations describe the behaviour of the fluid inside the computational domain. However, these partial differential equations can only be solved if the boundary conditions and initial values are given. The boundary conditions specify the exchange of the mass, the momentum and the heat between fluid and ambiance. Basically, there are three types of the boundary conditions for the

steady state and unsteady problems, namely Dirichlet, Neumann or Cauchy boundary conditions.

In the Dirichlet boundary condition, the value of the computation quantity  $\phi_f$  such as velocity or total enthalpy is given on the surface of the computational domain  $\partial\Omega$ . Here, the computation quantity can be constant or variable depending on time and space. For example, the velocity value is constant in case of fixed walls ( $|\vec{u}_f| = 0$ ) or time depending in case of moving walls:

$$\phi_f = \phi_f^{bc}(\vec{x}, t_f) \quad \vec{x} \in \partial\Omega. \quad (6.41)$$

By the Neumann boundary condition, the gradient value of the computation quantity in normal direction to the surface of the computational domain is given. In this type of boundary conditions, the derivative of the computation quantity is often defined at the outlet of the flow region, where the quantity doesn't change, for example ( $\nabla(\vec{u}_f \cdot \vec{n}) \cdot \vec{n} = 0$ ):

$$\frac{\partial \phi_f}{\partial \vec{n}} = \phi_f^{bc}(\vec{x}, t_f) \quad \vec{x} \in \partial\Omega. \quad (6.42)$$

The Neumann boundary condition can be used as a symmetry boundary condition. The symmetry in the geometry and the boundary conditions reduce the measure of the computational domain, resulting in a computational time saving.

In the Cauchy boundary condition, also known as Robbins or mixed boundary condition, the value of the computation quantity  $\phi_f$  and its derivative in the normal direction to the surface of the computational domain is given:

$$a \cdot \phi_f + \frac{\partial \phi_f}{\partial \vec{n}} = \phi_f^{bc}(\vec{x}, t_f) \quad \vec{x} \in \partial\Omega \quad a > 0. \quad (6.43)$$

In unsteady problems, the solution at the start time should also be known in the entire computational domain.

### 6.2.6 Turbulence

The turbulent flow is a flow regime that characterised by high properties fluctuations in time and length. The turbulent flow can be found in most of practical engineering applications. The modelling of this flow needs, however, a special treatment. In the literature, the numerical approaches for modelling the turbulent single-phase flow are adequately described (among others: (Pope 2000, Peters 2000, Oberlack et al. 2007)). Here, they are briefly described:

The direct numerical simulation (DNS), although represents the simplest methods regarding content and concept, is the most exact approach for computation the turbulent fluid flow. The length and time scales (turbulence structures) are completely captured by the DNS. To achieve this, a very fine grid and adequate fluid time step should be employed. The required grid resolution and time step, which are necessary for resolving all turbulence structures, lead to an extreme computational effort. The computational time of the DNS behaves almost proportional to the number of the grid cells. The real computational cost is, however, equal to  $O(N_f)^{1.1}$  by the reason of the overheads in the numerical algorithm. According to (Lumley 1990), the required number of the grid cells  $N_f$  for the numerical simulation of a turbulent channel flow depends on the fluid Reynolds number and can be expressed by:

$$N_f \approx 10^{-4} \cdot \text{Re}_f^{2.7}. \quad (6.44)$$

The large eddy simulation (LES) is particularly suited to flows with high Reynolds numbers and/or for computational domain with complex geometries. The computational effort of the LES is significant less than the DNS. The largest scale motions (eddy elements) of the flow are solved by the computational grid, while the small scale motions are approximated. Like the DNS also the LES is a numerical approach for unsteady flow simulations, i.e. all physical values of the flow are spatially and temporally resolved. The earliest and the most known LES model dated back to (Smagorinsky 1963). Since that time, the LES have been further improved, e.g. the dynamic model of Germano (Germano et al. 1991) that doesn't require any model parameters.

The Reynolds averaged Navier–Stokes simulation (RANS) is another possibility to determine the turbulent values of a flow. Here, the equations of motions are averaged over the time, i.e. each fluid variable is written as the sum of a time-average value and fluctuation part. By inserting this in the continuity and the Navier–Stokes equations, the time averaged continuity and Navier–Stokes equations are obtained. To close the equation system, there are different levels of approximations available as algebraic, one-equation, two-equation and Reynolds stress models. Generally, the RANS models are distinguish by their numerical stability and high efficiency and are used in industry large-scale applications since many years ago.

The modelling of the turbulent gas–solid flow is more complicated compared to the single-phase flow. This is due to the fact that the turbulence structures are changed by the reason of solid existence. In the gas–solid flow, strong interactions are taken place between the turbulence structures and the solid particles besides the interactions between the turbulence structures themselves. The influence of the disperse phase on the turbulence of the continuum phase can be summarised as: 1) The particles movements in the flow lead to an additional disturbance (boundary layer separation and vortex formation around a particle). 2) Particles may mechanically influence the turbulence structures. The particles motions result in destroying the large-scale turbulence structures to smaller-scale ones (accelerating the dissipation of turbulent kinetic energy), especially when the size of particles and fluid turbulence elements are approximately the same. 3) Disturbance in the flow field may arise due to the particle–particle interaction.

In the gas–solid flow, the turbulence depends on the density difference between solid and fluid, the particle size and the volume fraction of the dispersed phase. While the turbulence is damped by small particles and strengthened by large particles, the density difference between the interaction phases has a low influence. The increase of the solid loading results in reduction of the turbulence. According to (Elghobashi 1994, Elghobashi 2006), the influence of the turbulence on the fluid velocity field in the gas–solid flows with a solid content higher than 0.001 in each control volume had a low priority and can therefore be neglected. However, this assumption for practical applications such as circulating fluidized beds is not valid due to the high fluid velocities and/or the existence of areas (control volumes), in worst case, with a zero solid loading.

On the other hand, it should be mention that the influence of the turbulence on the solid phase should be also analysed. The fluctuations of the fluid variables in time and length should be considered during the calculation of particle forces and moments of force through additional models. The turbulent dispersed flow including the turbulence–particle interactions are actual state of research and further experimental and theoretical investigations are required.

### 6.2.7 Solution of equations system

The discretisation methods results in an algebraic equation for each fluid variable  $\phi_f$  at every grid cell. This equation contains the value at that cell as well as the nodal values of neighbouring cells. Depending on the nature of partial differential equation, the discretised

equation can be linear or non-linear. In case of a non-linear algebraic equation, the numerical solution approach requires linearisation. The obtained algebraic equation of each control volume has the following form:

$$\underbrace{A^P \phi_f^P}_{\text{Considered cell}} + \underbrace{\sum_{k=1}^l A^k \phi_f^k}_{\text{Neighbouring cells}} = \underbrace{Q^P}_{\text{Source term}}, \quad (6.45)$$

where the index  $P$  represents the node at which the differential equation is discretised and the subscript  $l$  donates to all neighbour cells that involved in the approximation scheme. The coefficients  $A^{P,k}$  depend on the variable values, the geometrical data and the fluid properties. The variables  $\phi_f^{P,k}$  are unknown, while the symbol  $Q^P$  includes all the terms that are known.

The matrix system of the entire computational domain with a finite number of the grid cells  $N_f$  for the fluid variable  $\phi_f$  is then constructed as:

$$A\phi_f = Q. \quad (6.46)$$

Here,  $A$  is the coefficient matrix,  $\phi_f$  is the column matrix that includes the unknown nodal variables and  $Q$  contains the known terms. Each vector in this matrix ( $A$ ,  $\phi_f$  and  $Q$ ) have the length of  $N_f^{CV}$ . In this algebraic equations system, the number of equations and the unknown are equal. The number of the algebraic equations is generally very large, so it cannot be calculated analytically. Instead of that, it can be numerically solved employing one of the iterative methods.

Most elements in the matrix system are zero, i.e. the matrix is spares, which simplifies the task to obtain the solution. For solving a linear system of algebraic equations, the direct methods that deliver an exact solution are preferred. In this context, the Gauss elimination represents the basic direct algorithm. The idea behind the Gauss elimination is the systematic reduction of large systems of linear equations to smaller ones through a sequence of operations performed on the matrix. Based on the Gauss elimination algorithm, different methods have been developed such as LU decomposition and cyclic reduction. The previous algorithms can be applied efficiently to solve any matrix of linear equations. However, the computational effort of the direct methods is very high, in practically, when the triangular factors of sparse matrices are not sparse.

The iterative methods are generally used for solving non-linear system of algebraic equations, but they can also be applied to linear systems. In the iterative methods, the solution is first suggested and then the equation is used to improve the solution. This includes guessing a solution, linearisation the equations, improving the solution and repeating the process till converged results are reached. Although the direct methods can deliver the exact solution of the problem in the absence of rounding errors, the computational effort of iterative methods is relatively lower. Generally, the discretisation error is much larger than the error of the iterative methods. Therefore, the iterative methods are employed in all CFD codes due to their high efficiency and their ability to solve the non-linear system of algebraic equations. Some basic iterative algorithms are Jacobi method, Gauss-Seidel method, successive over-relaxation SOR, incomplete LU decomposition and conjugate gradient method (Ferziger and Perić 2002, Schäfer 2006, Epple et al. 2012).

### 6.2.8 Extended balance equations

In the previous sections, the numerical methods for modelling the single-fluid flow are described. The simulation of the fluid phase in the gas-solid flow, by contrast, is more complicated due to the fluid-solid interaction. The control volumes in the computational domain are not completely occupied with fluid, but rather both fluid and solid phases share the grid cells. In this context, the parameter void fraction is defined, which is a measure of the solid content in the gas-solid flow. Various definitions are used for specifying the void fraction, namely local, chordal, cross-section and volumetric void fractions. Here, the volumetric void fraction is the most parameter used to characterize the gas-solid flow. It is given as:

$$\varepsilon_f^V = \frac{V_f}{V^{CV}} = \frac{V_f}{V_f + V_p}, \quad (6.47)$$

where  $V_f$  and  $V_p$  are the volume of the grid cell occupied by fluid and solid, respectively. The volumetric void fraction can also be expressed to the solid volume, which is called the solid volumetric void fraction:

$$\varepsilon_p^V = \frac{V_p}{V^{CV}} = \frac{V_p}{V_p + V_f} = 1 - \varepsilon_f^V \quad (6.48)$$

The volumetric void fraction consists of inner and outer void fractions, also known as inner and outer porosities (see **Figure 6.6**):

$$\varepsilon_f^V = \varepsilon_f^{V,out} + \varepsilon_f^{V,in} - \varepsilon_f^{V,out} \varepsilon_f^{V,in}. \quad (6.49)$$

The inner porosity is formed by the cavities in the disperse phase itself. The cavities between the particles form the outer porosity, also known as bulk porosity. Generally, it is assumed that the fluid can flow between particles, but cannot flow through the particles. In this case, the volumetric void fraction is equal to the outer porosity.

Similar to the volumetric void fraction, the cross-section void fraction is defined as:

$$\varepsilon_f^S = \frac{S_f}{S^{CV}} = \frac{S_f}{S_f + S_p} = 1 - \varepsilon_p^S. \quad (6.50)$$

(Stiess 1994) proved that the summation of the cross-section void fractions for  $n$  surfaces when  $n \rightarrow \infty$  is equal to the volumetric void fraction.

$$\overline{\varepsilon_f^S} = \lim_{n \rightarrow \infty} \frac{1}{n} \sum_{i=1}^n \varepsilon_{f,i}^S = \varepsilon_f^V = \varepsilon_f. \quad (6.51)$$

The volumetric void fraction is independent of grain size for regular spheres packing with same particle diameter (monodisperse) and the adhesive forces that act between the particles are smaller than the volume forces. If the adhesive forces exceed the volume forces, the cavities within the particles in packing bed will be decreased, resulting in increasing the solid volumetric void fraction. In this context, the empirical parameter packing limit can be introduced, which defines the maximum solid volumetric void fraction of solid when the particles are packed randomly. The packing limit of monodisperse, fine-grained and cohesive particles is significantly larger than the packing limit of monodisperse, coarse-grained and non-cohesive particles of same material. The packing limit depends on the particle size distribution and the particle shape in addition to the particle diameter (see **Table 6.1**).

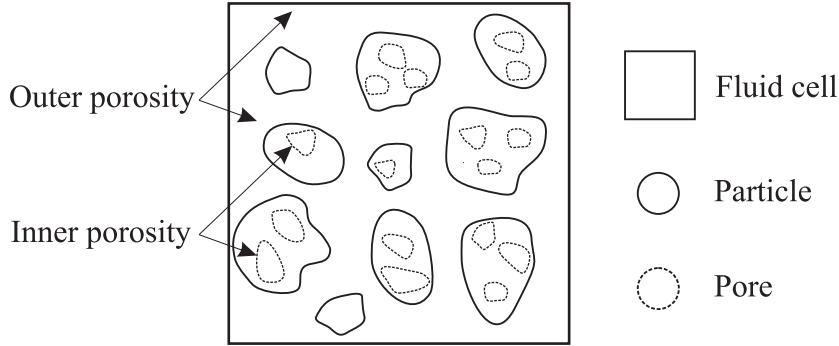


**Figure 6.6:** Void fraction

For a control volume in the computational domain, the volumetric void fraction can be expressed as:

$$\varepsilon_f = \frac{dV_f}{dV_{CV}}. \quad (6.52)$$

**Table 6.1:** Packing limit values of different systems (Stiess 1994)

Systems	Packing limit [-]
Dense regular packing (monodisperse)	0.26
Different materials for fluidized bed	0.40–0.95
Quartz sand packing	0.40

Inserting the volumetric void fraction  $\varepsilon_f$  in the conservation equations for the single-phase flow (see section 6.2), the extended conservation equations for the fluid phase in the gas–solid flow are then obtained. The extended Navier–Stokes equation is given in an integral form as follows:

$$\begin{aligned} \frac{\partial}{\partial t_f} \iiint_V \varepsilon_f \rho_f u_f dV + \iint_S \varepsilon_f \rho_f u_f \vec{u}_f \cdot \vec{n} dS = \\ \iint_S \varepsilon_f \mu_f \nabla u_f \cdot \vec{n} dS - \iint_S \varepsilon_f p \cdot \vec{n} dS + \iiint_V \varepsilon_f \rho_f \vec{g} dV + \iiint_V S_{P \rightarrow f}^{u,P} dV. \end{aligned} \quad (6.53)$$

The extended continuity equation can be expressed by:

$$\frac{\partial}{\partial t_f} \iiint_V \varepsilon_f \rho_f dV + \iint_S \varepsilon_f \rho_f \vec{u}_f \cdot \vec{n} dS = \iiint_V S_{P \rightarrow f}^{m,P} dV, \quad (6.54)$$

where  $\rho_f$  is the gas density,  $\vec{u}_f$  represents the fluid velocity,  $\mu_f$  is the dynamic viscosity,  $p$  and  $\vec{g}$  are the pressure and the standard gravity, respectively. The additional source terms  $S_{P \rightarrow f}^{u,P}$  and  $S_{P \rightarrow f}^{m,P}$  on the right side of both momentum and continuity equations consider the momentum and the mass exchange with the solid phase i.e. interaction between solid and fluid phases.

For each chemical component  $i$ , a gaseous substance transport equation is solved:

$$\frac{\partial}{\partial t_f} \iiint_V \varepsilon_f \rho_f c_i dV + \iint_S \varepsilon_f \rho_f \vec{u}_f c_i \cdot \vec{n} dS = \iint_S \frac{\varepsilon_f \mu_f}{Sc} \nabla c_i \cdot \vec{n} dS + \iiint_V S_f^{c,i} dV. \quad (6.55)$$

To balance the energy in the fluid phase, a transport equation for the specific enthalpy  $h$  is solved:

$$\frac{\partial}{\partial t_f} \iiint_V \varepsilon_f \rho_f h dV + \iint_S \varepsilon_f \rho_f \vec{u}_f h \cdot \vec{n} dS = \iint_S \frac{\varepsilon_f \mu_f}{\text{Pr}} \nabla h \cdot \vec{n} dS + \iiint_V \underbrace{(S_{P \rightarrow f}^{h,P} + S_f^h)}_{S_{P \rightarrow f,f}^h} dV. \quad (6.56)$$

Here,  $\text{Sc}$  and  $\text{Pr}$  are Schmidt and Prandtl numbers. The source term  $S_f^{c,i}$  takes into account the formation/reduction of gaseous components by the reason of chemical reactions. The heat source term  $S_{P \rightarrow f,f}^h$  consists of three parts: the heat released by the homogeneous gas phase reactions, the radiation source term of the fluid phase and the heat transfer between the two phases by convection, radiation and mass transfer due to the phase transformation from solid to fluid phase. The fluid temperature is then calculated from the specific enthalpy and the mean specific heat capacity.

The discretisation of these non-linear, coupled and partial differential equations can be carried out with the aid of the discretisation schemes, explained previously. However, to enable the modelling of the fluid phase in the gas-solid flow, the volumetric void fraction, the momentum and heat transfers from solid to fluid phase should be known (see section 7).

### 6.3 Conclusion

Basically, there are two approaches to describe the fluid motion, namely the mesh-free particle methods and the grid-based methods. In both approaches, the calculating of the fluid physical values involves three main steps: pre-processing, solving and post-processing. In the pre-processing stage, the problem is specified including the geometry, the mesh generation, the discretisation schemes and the initial boundary conditions. In the second step, the partial differential equations are approximated into algebraic equations. The obtained system of non-linear algebraic equations is numerically solved using iterative techniques. Finally, the simulation results are analysed in the post-processing phase.

In the mesh-free particle methods, the continuum is decomposed into a finite number of particles. The fluid quantities are determined without the need of numerical grids. The most of the particle methods are based on the Lagrangian representation, but there are some works based on the Eulerian formulation or the arbitrary Lagrangian Eulerian representation. To obtain the solution using the mesh-free particle methods, the following steps are required: 1) The fluid is discretised into a set of particles. 2) For each particle, the derivatives and the integrals are estimated by mean of all adjacent particles to the investigated particle. 3) The time-depending ordinary differential equations are solved using numerical methods. The absence of the numerical grid offers several advantages for the particle methods such as the exact representation of the geometry, the flexible dealing with large deformations, the easy parallelisation and the possible use of higher-order continuous shape functions. On the other hand, the high computational effort represents the major drawback. The well-known particle methods are the smoothed particle hydrodynamic and the mesh-free Galerkin methods.

The smoothed particle hydrodynamic method is the earliest particle method used to approximate the continuum values using discrete particles. The basic idea behind the SPH is that the partial differential equations are converted into time-dependent ordinary differential equations. The obtained system of ordinary differential equations can be solved using standard time integration methods. Compared to other particle methods, the SPH method shows lower accuracy at the same computational time. The mesh-free Galerkin methods are based on Galerkin weak formulations of the partial differential equations. Here, an inverse distance weighted method is used to formulate the approximations. Based on this concept, different

mesh-free Galerkin methods are developed such as the element free Galerkin method, the reproducing kernel particle method, the partition of unity methods and many others.

By contrast to the mesh-free particle methods, where the fluid phase is decomposed into discrete mass packets, the computational domain in the grid-based methods is divided into a finite number of grid cells. The governing partial differential equations can only be solved analytically under extreme simplifications. Therefore, numerical methods are employed to approximate the solution. This means, the exact solution is estimated by several values through solving a finite number of the algebraic equations instead of the partial differential equations. Here, the fluid motion can be described in the Eulerian or Lagrangian representation. The following steps are necessary to obtain the solution: 1) The computational domain should be discretised into a finite number of control volumes. 2) The partial differential equations are approximated into a system of algebraic equations using one of the discretisation approaches. 3) The algebraic equations system is solved employing iterative techniques. The solution of the discretised algebraic equations is an approximation of the exact solutions. The accuracy of the grid-based methods is highly related to the numerical grid including size, shape etc. Compared to the mesh-free particle methods, the grid-based methods are widely employed due to the calculation efficiency and better description of the fluid properties such as mass density and pressure field. On the other hand, the major disadvantage is the numerical grid, i.e. an additional effort for the grid generation is required. Furthermore, the geometry cannot be exactly represented.

The first step to obtain the solution in the grid-based methods is to divide the geometry of the problem into a finite number of control volumes, also known the numerical grid. The numerical grid can be classified as structured and unstructured grids. In the structured grids, the arrangement of the grid cells is regular, while is irregular in the unstructured grids.

In the next step, the conservation equations are solved numerically based on different discretisation schemes such as the finite difference method, the finite element method and the finite volume method. In this context, the finite difference method represents the oldest discretisation approaches. In the FD method, the conservation equations are in differential forms, where the first and second derivatives of the generic conservation equations are estimated at each grid point using Taylor series. The FD method can be applied to any grid type, but it can produce on the structured girds an accurate result due to the possible using of higher-order approximations. The main drawbacks of the FD method is the limitation to simple geometries and the conservation is not guaranteed unless the consideration of special assumptions (Ferziger and Perić 2002). In the finite element method, the computational domain is divided into finite elements. The solution of the partial differential equations is approximated by a linear combination of parameters that are at the beginning unknown and shape functions that can be derived from its values at the grid points. The possibility to apply to complex geometries is an important advantage of the FE method. The finite volume method approximates the partial differential equations at discrete volumes. The FV method starts from the integral form of the conservation equations that are applied to each control volume. The volume integrals in the partial differential equations are converted to surface integrals with aid of the divergence theorem. The variable at the control volume surface can be determined using the nodal values of neighbour cells. Various interpolations with different orders are available such as the upwind differencing scheme, the central differencing scheme and the quadratic upwind interpolation for convective kinematics. The surface and volume integrals can be then approximate in the centre of each grid cell. The result is an algebraic equation for each control volume. Considering the entire computational domain, a system of algebraic equations is obtained, where the number of the unknowns is equals the number of these equations. The FV method can be applied to the structured and unstructured grids and thus can be used for

complex geometries. Compared to the FD, the using of higher-order interpolations is more difficult especially for 3D cases.

If the investigated problems are unsteady, the time should also be discretised. The most well-known approximations are the forward Euler method, the backward Euler method and the trapezoid rule.

The partial differential equations for the steady-state problems and the time-dependent partial differential equations for the unsteady problems can only be solved when the boundary conditions are defined. The boundary conditions consider the flow interaction with the environment. There are three different boundary conditions: Dirichlet, Neumann and Cauchy boundary conditions.

The direct solution of Navier–Stokes equations is not possible due to the unknown pressure. However, the pressure can be indirectly determined through the continuity equation. Therefore, a pressure–velocity coupling must be introduced. For the incompressible flow, the mass conservation is a kinematic constraint on the velocity field. This means that the pressure field is constructed to satisfy the continuity equation. For this problem, there are several approaches such as SIMPLE, SIMPLEC and SIMPLER algorithms. In the compressible ideal flow, the density is appeared as second variable, where the use of the state equation is required.

The modelling of the turbulent flow needs a special treatment. In the literature, the numerical approaches for modelling the turbulent flow are the direct numerical simulation, the large eddy simulation and the Reynolds averaged Navier–Stokes simulation.

In the last step to obtain the solution in the grid-based methods, the non-linear system of the algebraic equations is solved employing iterative methods. Here, a solution is first guessed and then the equation is used to improve the solution.

Similar to the fluid phase, the solid phase can be treated as a continuum or a discrete phase (see section 3). If the continuum hypothesis is satisfied, the solid phase can be described as a continuum using the conservation equations of the single-phase flow. The solid phase can also be modeled as disperse by solving Newton's equations of motion for each particle. In this context, the numerical simulation of the fluid–solid flow can be carried out with different possibilities (see **Figure 6.7**). 1) The fluid and particle phases are modeled as a continuum (Euler–Euler approach). Here, the fluid and solid phases are calculated implying the grid-based methods. 2) The fluid is modeled as a continuum using the grid-based methods, while the particles are described as a discrete phase (Euler–Lagrange approach). 3) The particle phase is treated as a continuum using the grid-based methods, while the fluid phase is modeled as a discrete phase using the mesh-free particle methods (Euler–Lagrange approach). 4) The fluid and particle phases are considered as a discrete phase (Lagrange–Lagrange approach). Here, the fluid phase is treated as a discrete phase using the mesh-free particle methods.

In this context, the coupling of the grid-based methods (direct numerical simulation) for describing the fluid phase with the discrete element method presents an adequate possibility for the simulation of the gas–solid flows. However, the computational effort is extremely high, making this coupling only applicable for the gas–solid flows with low Reynolds numbers.

The aim of this work is to develop a numerical simulation program for the simulation of reactive, dense gas–solid flow in a fluidized bed. The single-particle method is applied to calculate the solid phase. For each particle, a set of transport equations is solved. The soft sphere model (discrete element method) is applied to the collision treatment between the particle–particle/wall. In principle, the discrete element method can be coupled either with the grid-based methods or the mesh-free particle methods. The grid-based methods allow detailed description of the fluid phase at the same computational effort compared to the mesh-free

particle methods. Furthermore, there are no studies up to date in the literature dealing with the recitative flow using the mesh-free particle methods. As a rule, the mesh-free particle methods are mainly applied to flows with high density such as water. In the DEMEST program the grid-based methods are, therefore, used to model the fluid phase in the gas-solid flow. However, the conservation equations of the single-phase flow should be further extended through additional source terms. Besides the mass and momentum equations, the species transport and energy equations are implemented in the DEMEST program. The constitutive equations, the material properties data and the models for heat and mass transfers are also considered. Here, different parameters such as the volumetric void fraction, the momentum, mass and energy transfers from solid phase to fluid phase must be known (see section 7).

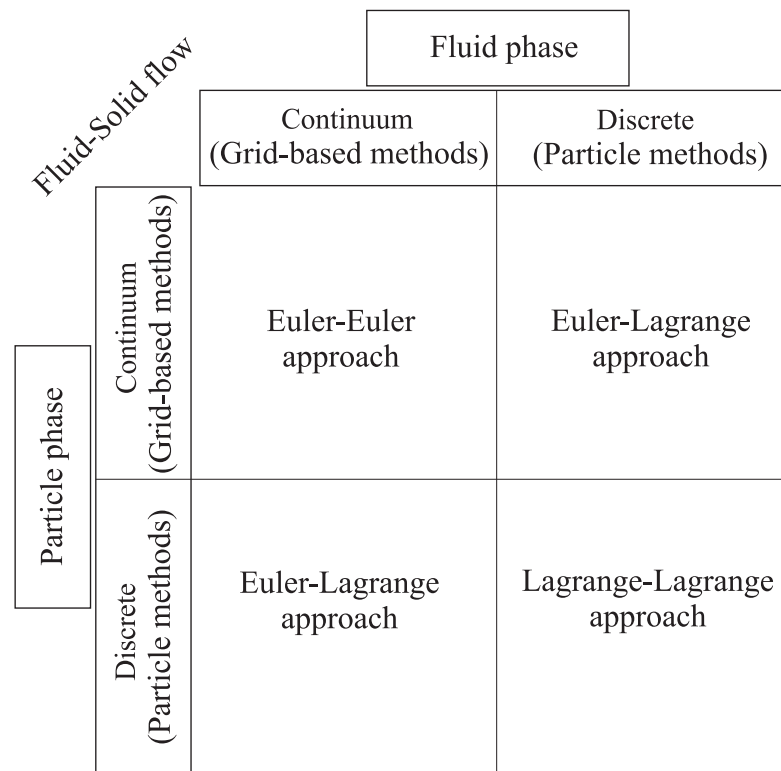


**Figure 6.7:** Different possibilities for the numerical simulation of gas-solid flow

The discretisation of the non-linear, coupled and partial differential equations is carried out in this work with the finite volume method. It is particularly suited for solving the conservation equations in complex geometries. For this reason, it is often used in many computational fluid dynamics packages such as ANSYS-FLUENT®.

In the DEMEST program, the colocated grids and the block-structured grids can be generated. The grid cells consist of hexahedron elements. The surface and the volume integrals of partial differential equations are approximated in this work using a blending method, which combines the upwind differencing scheme with the central differencing scheme.

For the time discretisation, the Crank-Nicolson method is employed. Besides the Dirichlet and Neumann boundary conditions, the periodic boundary condition can be used in the DEMES program. Here, all values of the flow variables at the inlet periodic surface of the computational domain are equated to their values at the outlet periodic surface. Numeric operators such as the gradient are applied to consider this periodicity (Götz 2006).

For the pressure-velocity coupling, the SIMPLE and SIMPLEC algorithms are available. According to (Ferziger and Perić 2002), the solution of the pressure-correction equation is independent of the grid for two neighbouring cells. This decoupling-problem is known in the

literature and it can lead to high oscillations in the pressure–velocity field. There are several approaches to solve this problem. One possibility is to damp the oscillations with appropriate filters. The complexity of the pressure–correction equation increases strongly on non-orthogonal grids and, resulting in lower rates of convergence. Another solution is to use a special interpolation method to determine the velocity at the middle of the control volumes surfaces for the formation of the pressure–correction equation. In this way, the pressure–correction equation remains compact and the rate of convergence stays uninfluenced even on complex grids (Götz 2006).

In the earlier Euler–Lagrange/DEM works, the modelling of the turbulent flow is neglected. The reason of this is that on the one hand the effect of the turbulence on the velocity field in gas–solid flows with solid content higher than 0.001 has low priority (Elghobashi 1994, Elgobashi 2006) and on the other hand low Reynolds numbers were considered. For the fluidized bed, a strong influence of intensive turbulence on particle motions is detected, especially at the region above the nozzle (Zhong et al. 2006). Accordingly, the statistical two-equation turbulent model  $k-\varepsilon$  is used to model the motion of the fluid phase. Complex turbulence models such as Reynolds stress model or large eddy simulation are not necessary due to the fact that these models result in an additional computing time. In the DEM literature, there are, however, some works that combined the DEM model with LES simulation (Zhou, Flamant and Gauthier 2004a, Gui, Fan and Luo 2008).

The generated system of the non-linear equations is solved using iterative methods. As almost all iterative solution methods converge on finer grids with a higher accuracy, but require considerably more computing time. It is useful first to start the calculation on a coarse grid to produce an initial solution for the fine grid. This can reduce the computational effort and maintain the higher accuracy. Therefore, the multi-grid method is implemented in the DEMEST program in combination with following available multi-grid solvers: the Gauss, the Jacobi and the red–black–successive–over–relaxation.

# 7 Fluid–particle interaction

The modelling of the fluid phase in the gas–solid flow requires the extension of the conservation equations for the single–phase flow. This is due to the fact that the control volumes of the computational domain consist of different fluid and solid volume fractions. In order to solve the extended conservation equations, the impact of solid on fluid phase in each grid cell, so-called the interaction coupling values such as volumetric void fraction, momentum and heat transfers ( $\varepsilon_f, S_{P \rightarrow f}^{u,P}, S_{P \rightarrow f}^{h,P}$ ) should first be determined. This can be achieved by averaging process for existing particles in each control volume, their velocities and their temperatures. The averaging process is of great significance for the simulation of the gas–solid flow and thus should be carried out with high accuracy. The exact calculation of the mean values requires considering all particles that are completely located inside the control volume and other particles that are partly located in this CV. This is a complex task, so that numerical approximations should be introduced. Here, the particle centre method represents the simplest approach, since it assumes that the entire volume of the particle is allocated to the fluid cell, where the centre of this particle is found.

In addition to the interaction values, the calculation of the gas–solid flow using the Euler–Lagrange/DEM model requires different time steps (particle and fluid time steps). The fluid time step is constant and can be arbitrarily selected. In the DEM model, the particle time step is assumed to be constant as well. However, the particle time step should be sufficiently small selected to prevent unphysical penetration between the particles. Smaller particle time steps results in higher accuracy, but on the other hand the computational effort increases sharply. The parallelisation of the Euler–Lagrange/DEM model is here of great important.

In the following sections, the numerical methods for determination the interaction values, the calculation of the particle time step and the parallelisation of the Euler–Lagrange/DEM model will be explained in detail.

## 7.1 Inter–phase coupling

The numerical simulation of the gas–solid flow using the Euler–Lagrange approach employs the Lagrangian description for the solid phase and the Eulerian formulation for the continuum phase. In Eulerian coordinates, the determination of fluid physical values requires information from the dispersed phase. In this context, the volumetric void fraction, the momentum and heat transfers should be known as volume average values in each control volume. These average values are functions of geometrical and physical properties of each particle (position, temperature and velocity) that is located in the investigated control volume:

$$\psi_{P \rightarrow f} = f \left( \sum_{\forall i \in CV} f_{P,i}^{CV} \Phi_{P,i} \right). \quad (7.1)$$

The symbol  $\psi_{P \rightarrow f}$  represents one of the interaction values, i.e. the volumetric void fraction, the momentum transfer or the heat transfer. The parameter  $\Phi_{P,i}$  is either the particle volume, the particle velocity or the particle temperature. The spherical section  $f_{P,i}^{CV}$  indicates

the fraction of the particle volume, which exists in the control volume (see **Figure 7.1–(a)**). The most accurate but also the most complex method to determine the interaction values in a grid cell is to consider all particles that are completely and partly located inside the control volume. This can only be achieved with extreme computational time and therefore numerical approximations should be introduced. If the particle centre method is applied to approximate the interaction values, then the complex spherical section  $f_{P,i}^{CV}$  to be determined in equation (7.1) is omitted (see **Figure 7.1–(b)**). The efficiency gained in this method is associated with high uncertainty for the determination of the interaction values. By applying the so-called offset method, which results in several numbers of the spatial displacements of the grid cells (see **Figure 7.1–(c)**), the determination of the interaction values can be significantly improved (Götz 2006, Allobaid and Epple 2013). The interaction values in a grid cell are determined then by averaging all calculated values with regard to the number of displacements (in 2D cases: 9 values with 8 displacements in all directions with  $\Delta x, \Delta y \in [-r_p, 0, +r_p]$  and in 3D cases: 27 values with 26 displacements in all directions with  $\Delta x, \Delta y, \Delta z \in [-r_p, 0, +r_p]$ ). The accuracy and efficiency of using the offset method are investigated in detail in section (8.1.2).

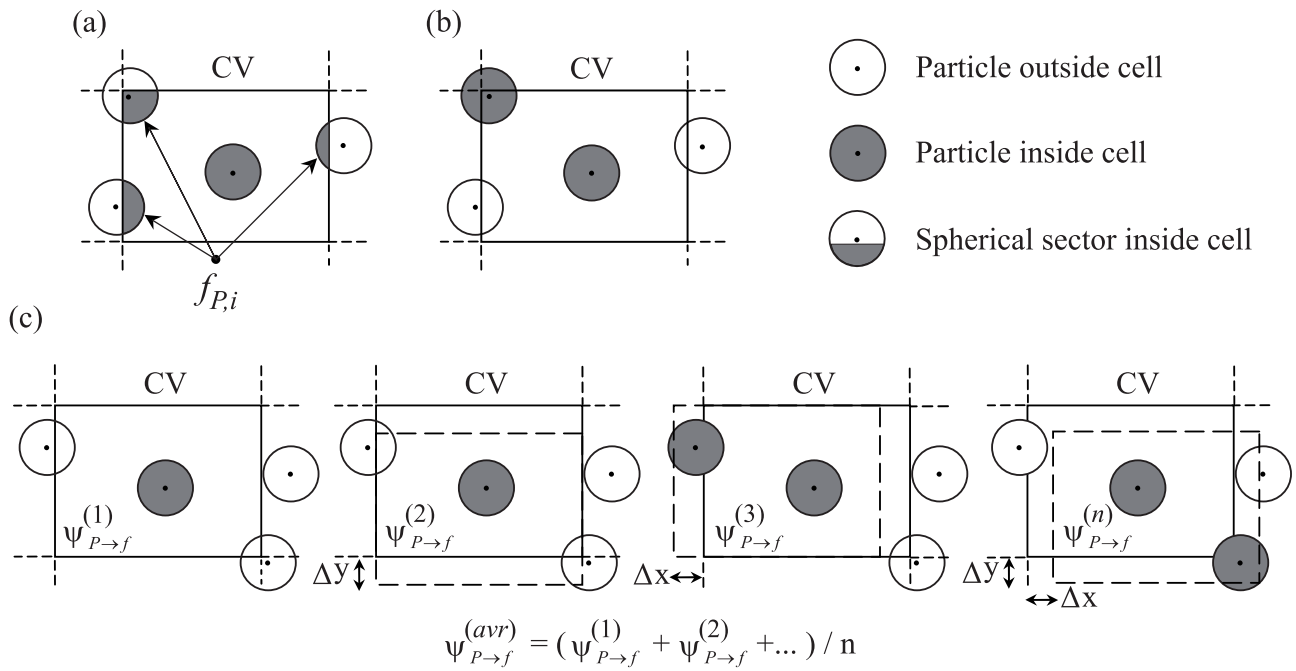


**Figure 7.1:** Determination of interaction values: (a) exact method, (b) particle centre method and (c) particle centre method in combination with offset method

The averaging accuracy depends strongly on the local inhomogeneities, i.e. the particle distribution in the computational domain and thus on the grid resolution. A grid refinement allows the spatial resolution of the local inhomogeneities, but on the other hand leads to an inaccuracy in the averaging process. By improving the grid resolution, the number of particles that belong to different control volumes is significantly increased (see **Figure 7.2–(a)**, (b) and –(c)).

If the particle diameter is equal or greater than the grid size, the local averaging is not possible. In the literature, this problem is known and can be solved using two different approaches. In the first method, the particles are represented as porous cubes with a certain size (Link 2006). In the second method, a new grid so-called particle grid is introduced (Allobaid et al. 2013b). Here, a geometric allocation between the fluid and particle grids is necessary to enable the data exchange from fluid to particle and vice versa (see section 8.1.3).

In both approaches, the grid resolution can be further refined independent of the particle size and the local averaging is still possible.

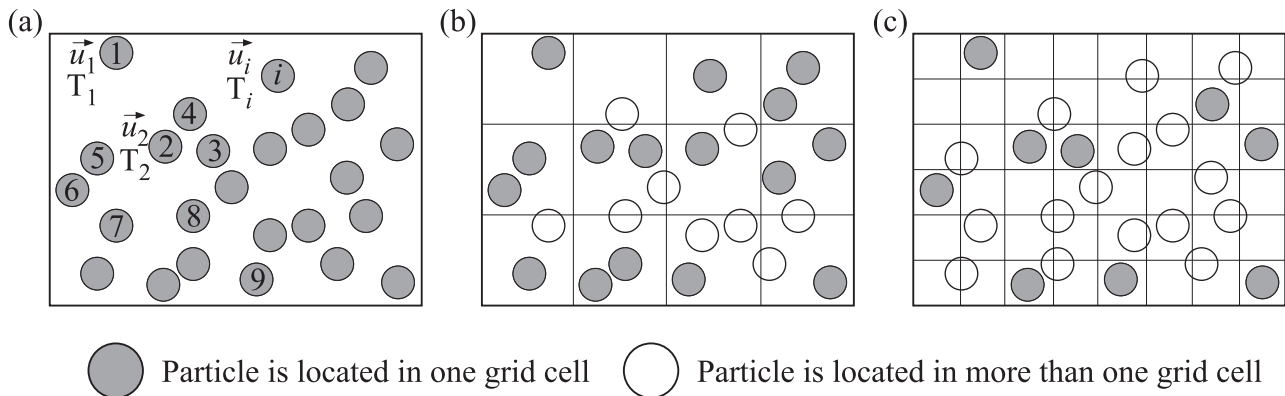


**Figure 7.2:** Spatial resolution of local inhomogeneities and averaging accuracy in dependence on grid resolution

### 7.1.1 Volumetric void fraction

In the gas–solid flow, the volumetric void fraction is a measure of the solid content in each control volume. The most accurate method to calculate the volumetric void fraction in a grid cell  $\varepsilon_f^{CV}$  can be carried out using the equation of (Hoomans et al. 1996) as follows:

$$\varepsilon_f^{CV} = 1 - \varepsilon_p^{CV} = 1 - \frac{1}{V^{CV}} \sum_{\forall i \in CV} f_{P,i}^{CV} V_{P,i}, \quad (7.2)$$

where  $V^{CV}$  is the volume of the grid cell,  $V_{P,i}$  denotes the volume of the particle  $i$  and  $f_{P,i}^{CV}$  is the spherical section.

### 7.1.2 Momentum transfer

The influence of particles motions on the fluid phase is known as momentum transfer. It is calculated for each control volume by determining the change in the particles velocities along their trajectories based on all particles crossing this CV during the time interval between two consecutive fluid time steps. The momentum transfer can be expressed as:

$$S_{P \rightarrow f}^{u,P} = \frac{|\vec{F}_{P \rightarrow f}|}{V^{CV}}. \quad (7.3)$$

According to the third Newtonian axiom, the exerted force from the dispersed phase on the fluid phase  $\vec{F}_{P \rightarrow f}$  must be equal to the force acting from the fluid on the particles  $\vec{F}_{f \rightarrow P}$ , but in the opposite direction. For determination the momentum transfer, the use of completely explicit method may result in convergence problems, while solving the conservation equations of the fluid phase. The reason for this is that the Navier–Stokes equations are stiffly deflected by large velocity differences (Götz 2006). Therefore, a semi-implicit method is generally applied to define the momentum transfer. According to (Feng and Yu 2004), the momentum interaction between the fluid and dispersed phases can be performed in three different approaches. In the first scheme, the transferred force from fluid to solid phase is separately calculated for each particle depending on the particle velocity:

$$\vec{F}_{f \rightarrow P,i} = \left( \vec{F}_{dra} + \vec{F}_{vir} + \vec{F}_{bas} + \vec{F}_{pre} + \vec{F}_{saf} + \vec{F}_{rad} + \vec{F}_{mag} \right)_i, \quad (7.4)$$

while the transferred force from particles to fluid phase is determined using the local arithmetic averaging as follows:

$$\vec{F}_{P \rightarrow f} = \beta \left( \bar{\vec{u}}_P - \vec{u}_f \right) V^{CV} = \beta \left[ \left( \frac{1}{N^{CV}} \sum_{i=1}^{k=N^{CV}} \vec{u}_{P,k} \right) - \vec{u}_f \right] V^{CV}. \quad (7.5)$$

Here, the variables  $N^{CV}$  and  $\bar{\vec{u}}_P$  represent the number of particles and the mean particle velocity in the investigated grid cell, respectively. The symbol  $\beta$  denotes the interaction momentum transfer coefficient (resistance coefficient). This scheme was mainly used in the early development stage of interaction coupling since the compliance of third Newtonian axiom is not guaranteed. In the second scheme, the transferred force from particles to fluid phase  $\vec{F}_{P \rightarrow f}$  is performed by a local averaging method such as in the first scheme. Then, the resultant force is distributed on the particles located in the control volume (uniformly in case of monodisperse systems and non-uniformly in case of polydisperse systems):

$$\vec{F}_{f \rightarrow P,i} = \begin{cases} \frac{\vec{F}_{P \rightarrow f} V^{CV}}{N^{CV}} & \text{For monodisperse system} \\ w(r) \frac{\vec{F}_{P \rightarrow f} V^{CV}}{N^{CV}} & \text{For polydisperse system} \end{cases}, \quad (7.6)$$

where  $\vec{F}_{f \rightarrow P,i}$  corresponds to the fluid force acting on each particle. The weight function  $w(r)$  allows big particles to have more influence than other smaller ones. The scheme 2, although it guarantees the third Newtonian axiom, is inaccurate from a physical perspective. In the third scheme, the fluid force acting on individual particle is calculated according to equation (7.4), while the particle force acting on the fluid phase is determined through the sum of all particles forces:

$$\vec{F}_{P \rightarrow f} = \sum_{i=1}^{N^{CV}} \vec{F}_{f \rightarrow P,i} = \beta \left[ \sum_{i=1}^{k=N^{CV}} \left( \vec{u}_{P,k} - \vec{u}_f \right) \right] V^{CV}. \quad (7.7)$$

Here,  $\vec{u}_f$  represents the fluid velocity in the considered control volume and  $\vec{u}_{P,k}$  is the velocity of the particle  $k$  in CV.

The resistance coefficient  $\beta$  can be modeled using different approaches. However, the selection of a model requires the knowing of the porosity and the particle Reynolds number in the control volume. Since the resistance coefficient must be explicitly predefined, the method for determining the momentum transfer cannot be considered as fully implicit. The semi-implicit treatment of the momentum transfer has the advantage that the resistance coefficient can be treated as constant during each fluid time step (Götz 2006). In the literature, there are a lot of models for calculation the resistance coefficient, where they differ from each other in their application validity. In this context, the Ergun and Wen model is the most frequently model used. It consists of Ergun equation for the high loading sub-areas and the correlation of Wen for low loading sub-areas (Ergun 1952, Wen and Yu 1966):

$$\begin{aligned} \beta_{Ergun} &= \frac{\mu_f}{d_p^2} \frac{1 - \varepsilon_f}{\varepsilon_f} \left[ 150 \left( 1 - \varepsilon_f \right) + 1.75 \text{Re}_P \right] & \text{case } \varepsilon_f < 0.8, \\ \beta_{Wen \& Yu} &= \frac{3}{4} C_{dra} \left( 1 - \varepsilon_f \right) \varepsilon_f^{-2.65} \text{Re}_P & \text{case } \varepsilon_f > 0.8, \end{aligned} \quad (7.8)$$

The drag coefficient  $C_{dra}$  can be calculated for an isolated spherical particle as follows:

$$C_{dra} = \begin{cases} \frac{24}{\text{Re}_P} (1 + 0.15 \text{Re}_P^{0.687}) & \text{case } \text{Re}_P < 10^3 \\ 0.44 & \text{case } \text{Re}_P \geq 10^3 \end{cases}, \quad (7.9)$$

with the particle Reynolds number:

$$\text{Re}_P = \frac{\varepsilon_f \rho_f |\vec{u}_f - \vec{\bar{u}}_P| d_p}{\mu_f}, \quad (7.10)$$

where  $\mu_f$  is the fluid dynamic viscosity,  $\vec{\bar{u}}_P$  and  $d_p$  represent the average particle velocity and the particle diameter (monodisperse) or the equivalent particle diameter (polydisperse) in the control volume, respectively.

Based on the lattice Boltzmann method, (Hill, Koch and Ladd 2001) delivered from the simulation results the following relationship for the resistance coefficient:

$$\beta_{Hill} = \frac{\mu_f}{d_p^2} \left( A \frac{(1 - \varepsilon_f)^2}{\varepsilon_f} + B (1 - \varepsilon_f) \text{Re}_P \right) \quad \text{case } \text{Re}_P > 40, \quad (7.11)$$

with the coefficients  $A$  and  $B$ :

$$A = \begin{cases} 180, & \text{case } \varepsilon_f < 0.6 \\ \frac{18\varepsilon_f^3}{(1-\varepsilon_f)} \frac{1 + \frac{3}{\sqrt{2}}(1-\varepsilon_f)^{\frac{1}{2}} + \frac{135}{64}(1-\varepsilon_f)\ln(1-\varepsilon_f) + 16.14(1-\varepsilon_f)}{1 + 0.681(1-\varepsilon_f) - 8.48(1-\varepsilon_f)^2 + 8.16(1-\varepsilon_f)^3} & \text{case } \varepsilon_f \geq 0.6 \end{cases}, \quad (7.12)$$

$$B = 0.6057(1 - \varepsilon_f)^2 + 1.908(1 - \varepsilon_f)\varepsilon_f^2 + 0.209\varepsilon_f^{-3},$$

Additional models to calculate the resistance coefficient can be found for example in (Deen et al. 2007, Epple et al. 2012). (Goldschmidt et al. 2004) compared the influence of different models on the properties of a gas-solid fluidized bed. The results show that the minimum fluidization velocity and the average bed height can highly depend on the resistance model used. According to Goldschmidt, none of these models can be universally applied.

### 7.1.3 Heat transfer

The heat transfer from solid to fluid phase due to the temperature difference between both phases consists of three parts: the heat transfer through convection, the heat transfer through radiation and the heat transfer due to phase transformation from solid to fluid phase:

$$S_{P \rightarrow f}^{h,P} = \underbrace{S_{P \rightarrow f}^{con}}_{\substack{\text{Heat transfer} \\ \text{through convection}}} + \underbrace{S_{P \rightarrow f}^{rad}}_{\substack{\text{Heat transfer} \\ \text{through radiation}}} + \underbrace{S_{P \rightarrow f}^{het}}_{\substack{\text{Heat transfer} \\ \text{through mass transfer}}}. \quad (7.13)$$

The convection heat transfer from particles to fluid phase between two consecutive time steps can be determined by considering the temperature change of all particles that are located in the control volume:

$$S_{P \rightarrow f}^{con} = \sum_{i=1}^{k=N^{CV}} \alpha_P A_{P,k} (T_{P,k} - T_f), \quad (7.14)$$

where  $\alpha_p$  denotes the heat transfer coefficient,  $A_{p,k}$  is the particle surface,  $T_{p,k}$  is the temperature of the particle  $k$ ,  $N^{CV}$  and  $T_f$  represent the number of particles in the control volume and the fluid temperature in the grid cell, respectively. By contrast to the convection heat transfer, the heat transfer through radiation cannot be easily obtained. The following simplified equation can, however, be used:

$$S_{P \rightarrow f}^{rad} = \sum_{i=1}^{k=N^{CV}} \varepsilon_p A_{p,i} \sigma (T_{p,i}^4 - T_f^4). \quad (7.15)$$

Here,  $\varepsilon_p$  and  $\sigma$  are the particle emissivity and the Stefan–Boltzmann constant. In equation (7.15), the particles that are located in the investigated grid cell are only taken into account. Complex models that can also consider the remaining particles are actual state of research and further theoretical investigations are required.

The heat transfer due to phase transformation from solid to fluid phase occurs by the reason of heterogeneous reactions such as char–oxidation, Boudouard–reaction and hydrogenating gasification.

On the other hand, the heat transfer from fluid to solid phase via convection and radiation is calculated for each particle depending on its temperature as:

$$\begin{aligned} S_{f \rightarrow P,i}^{con} &= \alpha_p A_{p,i} (T_f - T_{p,i}), \\ S_{f \rightarrow P}^{rad} &= \varepsilon_p A_{p,i} \sigma (T_f^4 - T_{p,i}^4). \end{aligned} \quad (7.16)$$

## 7.2 Particle time step

In order to calculate the time-dependent motion of the particle and fluid phases, different time steps are used in the Euler–Lagrange/DEM model, namely the fluid and the particle time steps. The size of the fluid time step can be arbitrarily selected and remains constant during the calculation. The particle time step is assumed to be constant as well in the DEM model. Generally, the fluid time step is chosen large and thus is divided into several constant particle time steps. However, the size of the particle time step must be selected so that each collision is registered in time. Regardless of the relative velocity of particles, the collision partners should not penetrate far away into each other before the collision is detected and the corresponding contact forces counteract the particles' movements. Large particle time steps cause great penetration depths that lead to unrealistic contact forces and consequently an erroneous in the energy balance. To detect the collision at the right time, a path length is defined, which both collision partners should not overtravel it's within the particle time step. The normal particle time step that covers the penetration depth  $\delta^n$  is given by the expression after (Götz 2006):

$$\Delta t_{P,\delta}^n = \frac{1}{\sqrt{(\lambda^n)^2 + (D^n)^2}} \exp \left[ - \left( \frac{D^n}{\lambda^n} \right) \arctan \left( \frac{\lambda^n}{D^n} \right) \right], \quad (7.17)$$

with the normal time constant  $\lambda^n$ :

$$\lambda^n = \sqrt{\frac{k^n}{m_{ij}}} - (D^n)^2, \quad D^n = \frac{\eta^n}{2m_{ij}}, \quad (7.18)$$

where  $k^n$  is the normal stiffness coefficient,  $\eta^n$  is the normal coefficient of damping,  $m_{ij}$  is the reduced mass. Similarly, the tangential particle time step can be determined via the

tangential penetration depth  $\delta^t$ . To ensure the conservation of energy, the tangential and normal particle time steps should be identical (Link 2006). This results with the aid of equations ((5.38) and (5.43)) in the following correlation between  $k^n$  and  $k^t$ :

$$\frac{k^t}{k^n} = \frac{7}{2} \frac{\left(4 - \alpha_{Dam}^2(e^n)\right)}{\left(4 - \alpha_{Dam}^2(\beta^t)\right)}. \quad (7.19)$$

While the normal stiffness coefficient  $k^n$  is defined by equation (5.35), the calculation of the tangential stiffness coefficient is carried out by equation (7.19). The previously described approach for calculating the normal and tangential stiffness coefficients is based on the material properties and provides values of high magnitude ( $10^5$ – $10^9$  N/m). Stiffness coefficients with high-order of magnitude require very small particle time steps, which can hardly be performed by the currently available computers. By selecting smaller stiffness coefficients, the particle time step can be increased and consequently the computing effort is reduced. On the other hand, there is a risk at sufficiently high relative velocity to raise unrealistic penetrations between the collision partners. In order to obtain the minimal stiffness coefficient that prevents the unphysical penetration between the particle–particle/wall, an extra condition must be formulated. By definition, a penetration is unrealistic if the maximum penetration depth is greater than the smallest particle radius. Using this condition ( $\delta_{max}^n \leq r_{p,min}$ ), a minimal normal stiffness coefficient is derived:

$$k_{min}^n = \frac{4}{3} \frac{\pi r_p^3}{\left(\delta_{max}^n\right)^2} \rho_p \left| \vec{u}_{ij,max}^n \right|^2 \exp \left[ \frac{-2\alpha_{Dam}}{\sqrt{4 - \alpha_{Dam}^2}} \arctan \left( \frac{\sqrt{4 - \alpha_{Dam}^2}}{\alpha_{Dam}} \right) \right], \quad (7.20)$$

where the maximum relative velocity  $\vec{u}_{ij,max}^n$  and the maximum penetration depth  $\delta_{max}^n \leq r_{p,min}$  must be predefined before the simulation.

While the size of the particle time step is assumed to be constant in the DEM model, the size of the particle time step is variable in the hard sphere model. Further information regarding the calculation of the adaptive particle time step in the hard sphere model can be found (Epple et al. 2012).

### 7.3 Conclusions

The particle–fluid interaction describes the impact of the solid phase on the fluid phase and vice versa. In order to enable the numerical simulation of the fluid phase in the gas–solid flow using the Euler–Lagrange/DEM model, the volumetric void fraction, the momentum and heat transfers should first be calculated. This can be achieved by averaging process for all particles that exist in the control volume, their velocities and their temperatures. The exact calculation of the interaction values requires the knowing of all spherical sections for the particles that are partly located in a control volume. This can only be performed for simple cases, where the number of particles is relatively low. By increasing the number of particles and/or improving the grid resolution, the number of particles that are allocated to different control volumes is sharply increased. The computational effort for the averaging process increases accordingly and numerical approximations should therefore be introduced.

In the particle centre method, the spherical sections for the particles are not considered. Here, the entire volume of the particle is allocated to the fluid cell, where the centre of this particle is found. The efficiency gained is related to high inaccuracy in the determination of the interaction values. The averaging accuracy can be significantly improved employing the so-

called offset method that results in several numbers of the spatial displacements of the grid cells, (Götz 2006, Albaid and Epple 2013).

The measure of the solid loading in each control volume is described through the volumetric void fraction. It is calculated as the ratio of the fluid volume to the entire volume of the grid cell. The momentum transfer that describes the influence of particles motions on the fluid phase can be calculated by determining the change in the particle velocities along their trajectories. The momentum transfer between the solid and fluid phases can be carried out in three different approaches. In scheme (1), the transferred force from fluid to disperse phase is determined for each particle individually depending on the particle velocity. The transferred force from particles to fluid phase is then calculated with the aid of an arithmetic averaging. In scheme (2), the transferred force from particles to fluid phase is performed by a local averaging method like scheme (1), while the resultant force is distributed to the particles that are located in the control volume. In scheme (3), the fluid force acting on each particle is calculated according to scheme (1), while the particle force acting on the fluid phase is determined through the sum of all forces of particles that are existent in the control volume. Besides the particles velocities, the resistance coefficient should be defined to enable the calculation of the momentum transfer. The resistance coefficient can be modeled using different approaches such as Ergun/Wen, Foscolo, Beetstra, and Koch/Hill models (summarised by (Deen et al. 2007, Epple et al. 2012)). The use of a model needs, however, the knowing of the volumetric void fraction and the particle Reynolds number in the grid cell. The heat transfer from solid to fluid phase can be calculated based on the heat transfer through convection, the heat transfer through radiation and the heat transfer due to phase transformation from solid to fluid phase.

The numerical simulation of the gas–solid flow using Euler–Lagrange/DEM model requires the definition of the particle and fluid time steps. Generally, the fluid time step is constant and can be arbitrarily selected. The particle time step is assumed to be constant in the DEM model. The size of the particle time step should be defined to prevent the unphysical penetration between the collision partners. Larger particle time steps lead to unphysical penetration depths and thus unrealistic contact forces. Smaller particle steps, although they improve the simulation accuracy, result in high computational effort. In this context, the parallelisation of the Euler–Lagrange/DEM model is of great important.

The aim of this work is to develop a numerical simulation program for the simulation of reactive, dense gas–solid flow in a fluidized bed. In this work, the number of investigated particles is more than  $N_p > 10^4$ , so that the exact calculation of the interaction values in the fluid cell is related to additional computational effort. The particle centre method in combination with the offset method is implemented in the DEMEST code for the calculation of the volumetric void fraction, the momentum and heat transfers. Furthermore, the momentum transfer from particles to fluid phase is calculated with the aid of scheme 3. This due to the fact that the scheme (1) cannot guarantee the compliance of third Newtonian axiom and the scheme 2 is an inaccurate from the physical perspective. In the DEM literature, the scheme (3) is frequently applied (among others: (Hoomans et al. 2000, Link 2006)). In this study, the Koch/Hill model is used to determine the resistance coefficient. An important point to be considered in the DEMEST program is the parallelisation due to the intensive computation time of reactive, dense gas–solid flow simulation. Here, the efficiency gain can be achieved by a suitable decomposition of the computational domain in several static blocks, in which the solutions of Navier–Stokes equations, pressure–correction equation, particle trajectories and collision forces are determined. The solution of the discretised fluid equations is performed by every processor in its previously defined sub–region. For the solid phase, each processor manages the particles that are located in its assigned sub–region. At the boundaries, there is the possibility that a particle leaves the sub–region and enters the adjacent sub–region or collides

with particles from other adjacent sub-domains at the border. In the ideal case, each processor is occupied with the same computation effort. While this criterion is possible for the calculation of the fluid phase, different computing time is required by each single processor to compute the dispersed phase. This is due to the continuous variation of solid distribution between successive time steps. To enable the data exchange between the grid blocks, linking cells that are located at the sub-blocks' borders are used. The communication between the linking cells and accordingly the individual processors (grid blocks) is carried out by the message passing interface (MPI). A key advantage of MPI is that the parallel calculation can be performed by special computer clusters as well as by commercial computers with multi-core processors.

Different types of grids are generated for efficient and accurate simulations of gas-solid flow with the aid of the DEMEST code as:

- 1) Fine fluid grid: This grid is used to calculate the physical quantities of the fluid phase.
- 2) Fluid multi-grid: The computing of the physical values of the continuum phase in each fluid cell is achieved by applying iterative methods to the discretised conservation equations. Almost all iterative solution methods converge on finer grids with a higher accuracy, but require considerably more computing time. Therefore, it is advisable first to use a coarse grid to produce a starting solution for the fine grid in order to reduce the computational cost and to maintain the higher accuracy of the fine grid (Schäfer 2006).
- 3) Particle grid: In the DEM literature, the calculation of the solid and fluid phases is always achieved in a common grid (the fluid grid). If the particle volume is, however, bigger than the fluid cell volume, then the calculated porosity is set equal to zero (porosity is negative, see equation (7.2)). Fluid cells with zero porosities result in numerical instabilities during the simulation (Link 2006). To avoid this, the dimensions of the largest particle must be smaller than the smallest grid cell. Relative big particles require fluid grid with rough resolution that causes inaccuracy in the calculation. The introduction of an additional grid, so-called particle grid allows the variation of the fluid grid resolution independently of the particle size (Alobaid et al. 2013b). It should be mentioned here that the particle grid method is also used to determine the momentum and heat transfers.
- 4) Particle search grid: The collision probabilities between particles are indirectly given by the corresponding particle spacing. The algorithm computes the collision probabilities between the tested particle and all other particles regardless of their relative positions. This means distant particles, even their contact probabilities are clearly impossible, are examined for possible contact with the tested particle. The application of the particle search grid improves the collision detection efficiency whereas a particle can only come in contact with particles or walls from its direct neighbourhood. The particle search grid is a virtual grid and thus a geometric allocation with the fluid or particle grid is not required.

Finally, the flow diagram of the DEMEST code for the numerical simulations of reactive, dense gas-solid flows is presented in **Figure 7.3**. The applied program combines the classical computational fluid dynamics to calculate the fluid phase in the Eulerian coordinates with the discrete-particle method to describe the solid phase in the Lagrange coordinate. To determine the fluid phase, the continuity, Navier-Stokes, energy and species transport equations should be first discretised. The generated linear equations are solved using an iterative method. The obtained velocity, pressure and temperature are stored for each cell in the fluid field. By transferring the fluid physical variables from the fluid grid to the particle grid and accordingly to the particle phase, the aerodynamic surface forces can be determined. Employing the DEM model, the short-range forces between the particles and the volume forces are calculated. The translational and angular velocities of particles can be solved by integrating the Newton's equations of motion and the angular momentum, respectively. The particle temperature is obtained by solving the energy equation for each particle. Subsequently, the particle-fluid interaction namely the volumetric void fraction and the momentum and heat transfers are determined in the particle grid and transferred to the fluid cells.

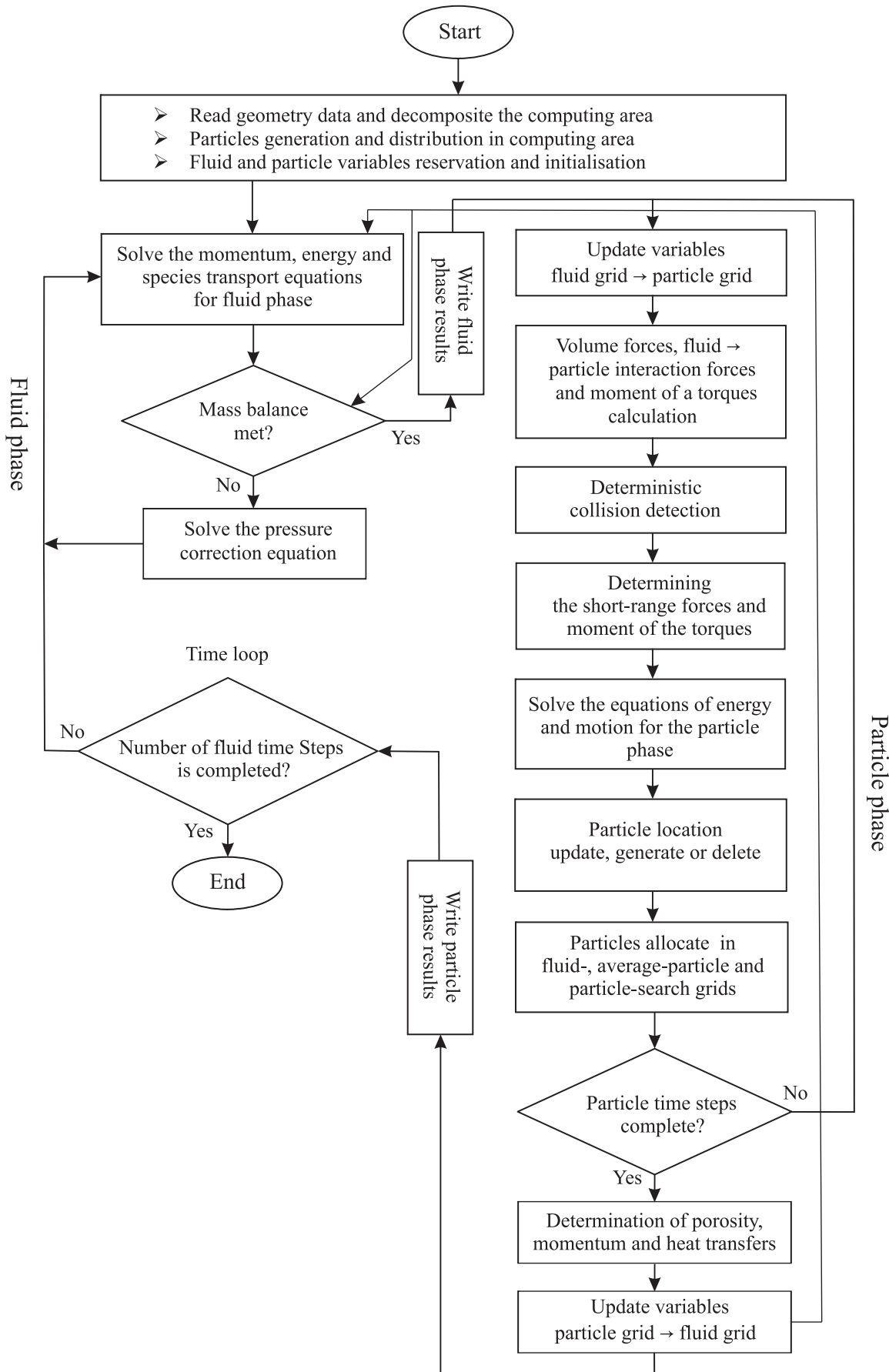


**Figure 7.3:** Flow chart for the computation of gas-solid flow using Euler-Lagrange/DEM model (DEMEST code)

# 8 Results

The developed program DEMEST employs the Lagrangian description for the dispersed phase and the Eulerian formulation for the fluid phase under the consideration of the thermochemical reaction mechanism. In following sections, the hydrodynamic behaviour of reactive and non-reactive gas–solid in fluidized beds is presented. The spouted flow regime (particle of group D) is used for the cold fluidized bed simulations, while the bubbling flow regime (particle of group B) is selected for the warm fluidized bed simulations. For the visualisation of the unsteady physical parameters of two phases such as velocity, temperature, pressure and volumetric volume fraction, several MATLAB® codes are applied.

## 8.1 Non-reactive gas–solid flow

The developed Euler–Lagrange/DEM model offers the possibility to calculate the trajectories of particles and the gas flow in a fluidized bed. Here, the finite volume method for the discretisation of non-linear, coupled and partial differential equations of the fluid phase is coupled with the discrete element method. The particle–particle/wall and gas–solid interactions are considered by tracking all particles. Main attention is given to the determination of the interaction values and the introduction of the particle grid. A validation study is carried out in order to assess the numerical results using the extended Euler–Lagrange/DEM model against 500–millisecond operation of a Plexiglas spouted fluidized bed, showing good qualitative correlation of solid distribution in the bed and acceptable quantitative agreement. The validation of the developed code is achieved with the aid of the visual observation of solid distribution, the absolute bed height and the equivalent bubble diameter. Furthermore, the obtained results are compared with the Euler–Euler and stochastic Euler–Lagrange approaches. The efficiency and accuracy of the extended Euler–Lagrange/DEM model are investigated in detail. Parameter studies, in which the stiffness coefficient, the fluid time step and the processor number are varied for different particle numbers and diameters, are performed.

### 8.1.1 Validation

To validate the simulation results, experiments are carried out on a cold spouted quasi-2D fluidized bed of Plexiglas. The numerical results obtained from the DEMEST program is then compared with the measurements. Furthermore, a comparison study among the deterministic Euler–Lagrange approach using the DEMEST code, the Euler–Euler approach employing the ANSYS–FLUENT® software and the stochastic Euler–Lagrange approach employing the CFD–BARRACUDA® program is achieved.

#### 8.1.1.1 Test rig and numerical models

The Plexiglas model has a height of 100 cm, a width of 15 cm, and a depth of 2 cm (see **Figure 8.1**). While at the inlet the air is supplied through a centrally placed nine holes with 2 mm inner diameter ( $9 \times d = 2$  mm), the outlet is completely opened (15 cm (W)  $\times$  2 cm (D)). Since the experimental work is performed on a flat quasi-2D model, the particle flow and the bubble behaviour of a fluidized bed can be followed by a high temporal resolution camera. Using pressure sensors (at heights of  $p_1$  2 cm,  $p_2$  12 cm,  $p_3$  22 cm,  $p_4$  40 cm), the pressure change in the bed is measured. The air flows upward through the holes in the bed, causing the glass beads particles to be suspended. It should be noted that the mass flow rate

used cannot lead to solid discharge from the Plexiglas model. For safety, a fine-grid net is attached at the outlet of the Plexiglas model, however it causes a negligible pressure drop.

The dispersed phase consists of 36500 spherical particles with an average diameter of 2.5 mm and a density of  $2500 \text{ kg/m}^3$ . The particles have the properties of glass and the fluidization medium is air at room temperature with mass flow rates of 0.006 kg/s (for case 1) and 0.005 kg/s (for case 2) (see **Table 10.1**).

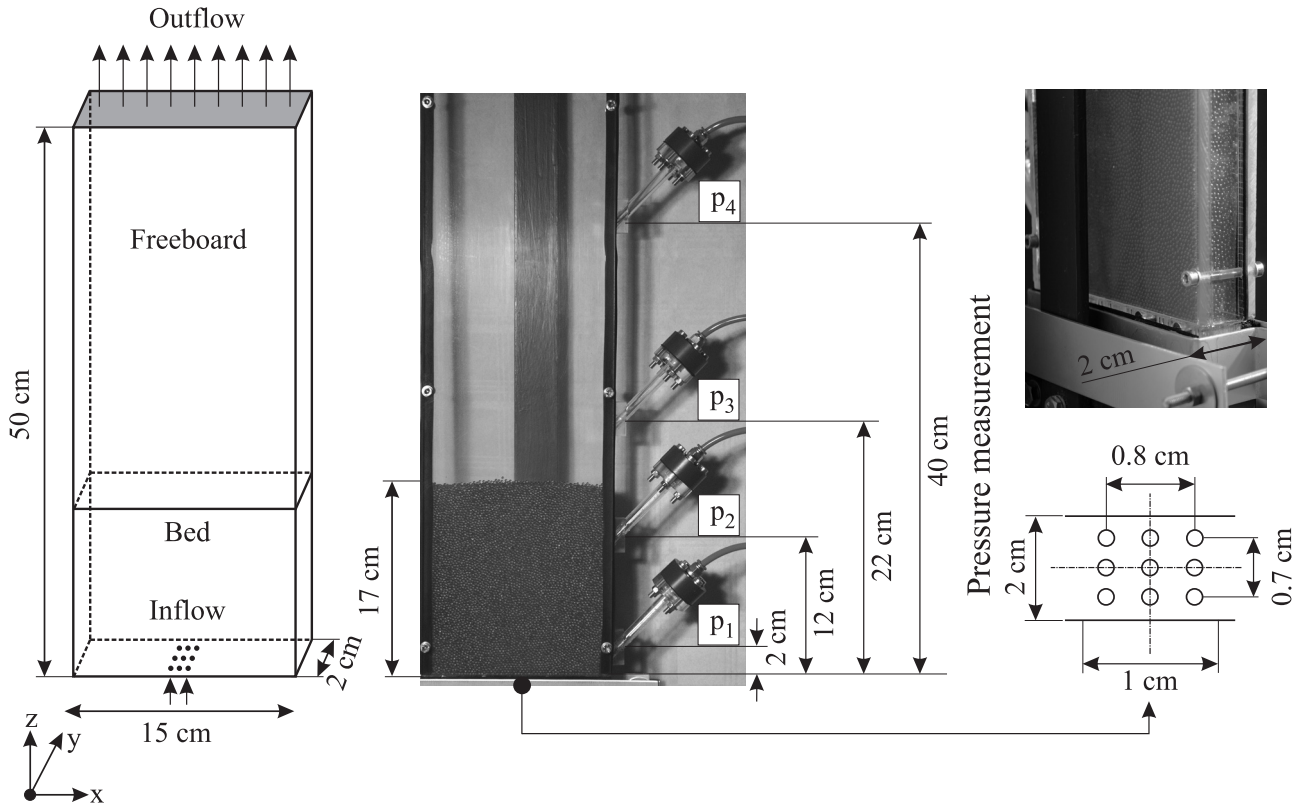
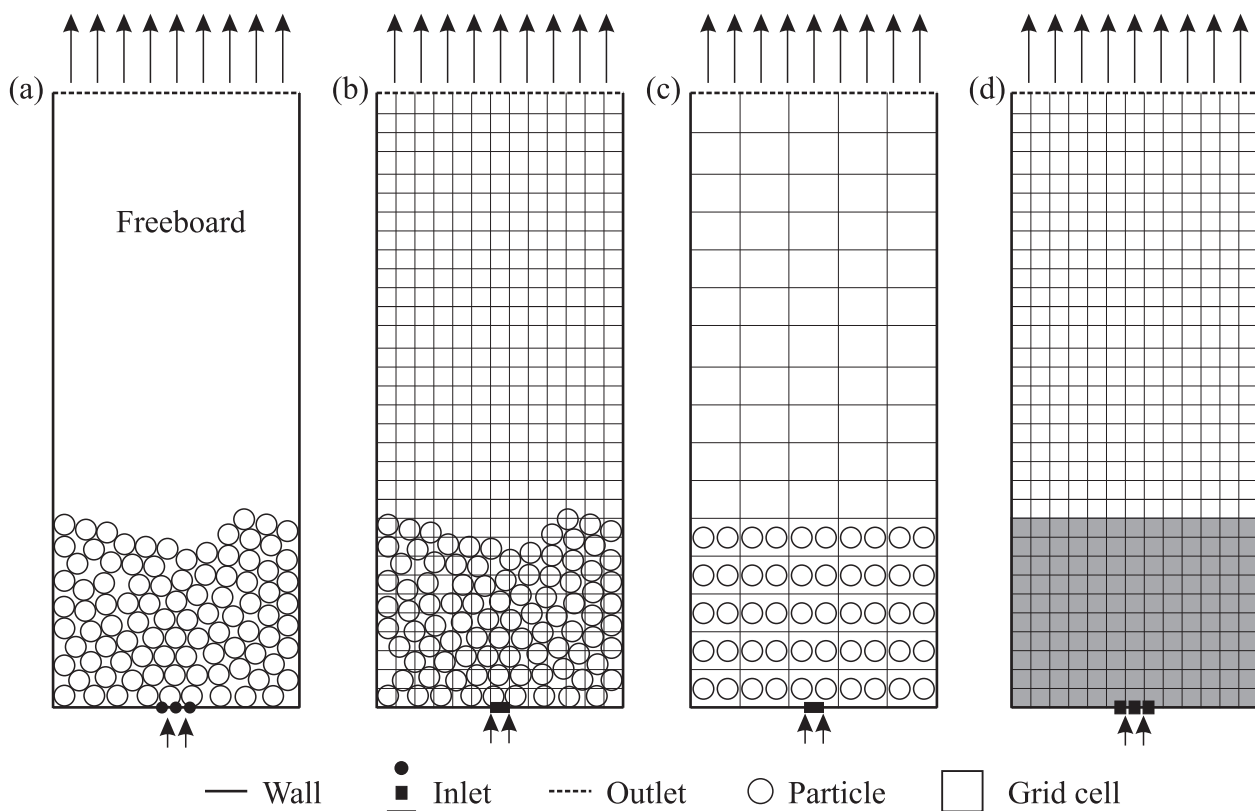


**Figure 8.1:** The test rig model of fluidized bed used for the experiments (only 50 cm of the apparatus height is presented)

For the numerical calculation, the quasi-2D fluidized bed model is simulated using the developed Euler–Lagrange/DEM model employing the DEMEST program. The forces acting on the particles are the gravitational, buoyancy, drag, pressure, Saffman, Magnus, and the contact forces. In **Table 10.2**, the simulation parameters for fluid and solid phases are presented. As mentioned above, at the mass flow rates used (0.006 and 0.005 kg/s), the vertical position of particles should not be higher than 50 cm. If this occurs, however, these particles are removed from the subsequent time steps. Besides the block-structured fine fluid grid with number of nodes:  $72 (\text{W}) \times 12 (\text{D}) \times 440 (\text{H})$ , a total of 380160, three increasingly coarser multi-grids are generated in order to accelerate the fluid calculation. With the first level coarse grid, the number of cells is reduced from 380160 to 47520 (number of nodes:  $36 (\text{W}) \times 6 (\text{D}) \times 220 (\text{H})$ ). For the second and third level coarse grids, the numbers of cells are further decreased to 11880 with number of nodes:  $18 (\text{W}) \times 6 (\text{D}) \times 110 (\text{H})$  and 2970 with number of nodes:  $18 (\text{W}) \times 3 (\text{D}) \times 55 (\text{H})$ , respectively. The computation of the solid phase is performed on the particle grid with a resolution of 47520 cells (number of nodes:  $36 (\text{W}) \times 6 (\text{D}) \times 220 (\text{H})$ ). The deterministic detection of particle–particle/wall collisions is performed on the particle search grid (number of nodes:  $40 (\text{W}) \times 4 (\text{D}) \times 160 (\text{H})$ , a total of 25600 cells). To accelerate the calculations, the entire computational domain is divided into 9 sub-regions, where each region is allocated to one processor. The numerical calculations are carried out with commercial computers with multi-core processors.

Furthermore, the model geometry and the computational mesh have been generated in ANSYS-FLUENT® and CFD-BARRACUDA® platforms. The simulation parameters used for fluid and solid phases in ANSYS-FLUENT® and CFD-BARRACUDA® can be found in **Table 10.3** and **Table 10.4**. In both programs, the block-structured grid is applied. While the number of grid cells in the DEMEST and the ANSYS-FLUENT® programs is the same ca. 380000 cells, the number of grid cells in the CFD-BARRACUDA® program is 25000 cells. The reason of this discrepancy is that the grid cell volume should be much bigger than the particle size in CFD-BARRACUDA®, which results in rough grid resolution. This problem is already solved in the DEMEST code thought the implementation of the particle grid method (see section 8.1.3). In ANSYS-FLUENT®, this problem cannot appear by the reason of the continuum description of the solid phase.

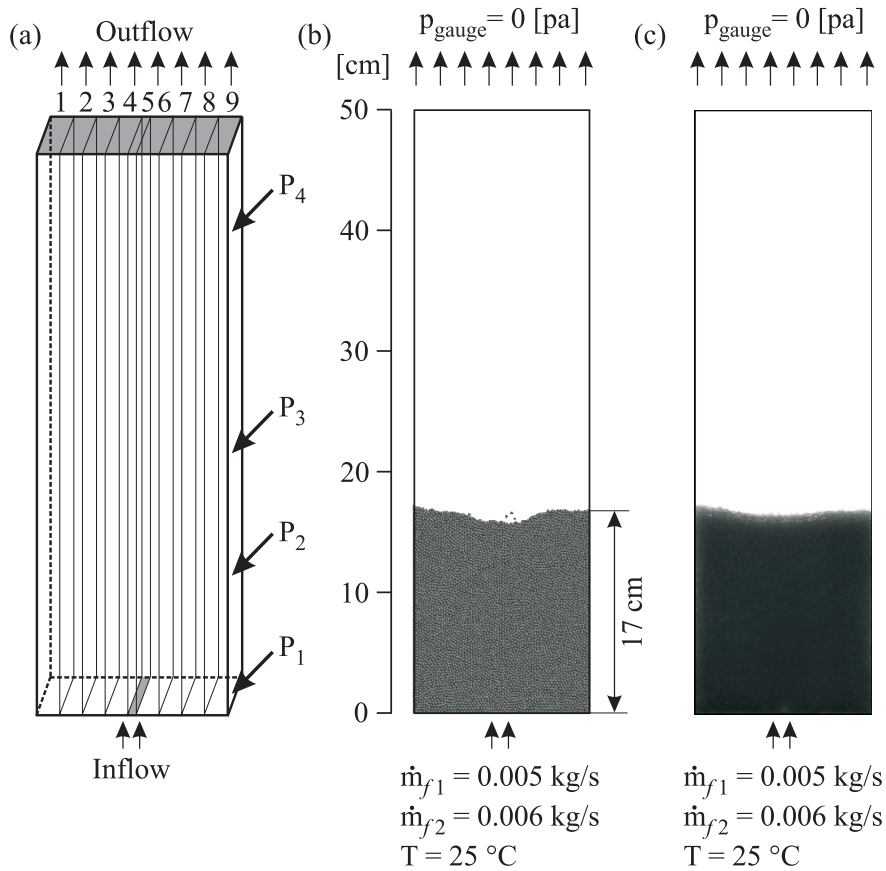
Unlike the experiment, the inlet in the DEMEST program is modeled as a centrally placed nozzle with the same area of nine holes. The reason of this assumption is that each inlet requires a separated sub-block to be generated. In principle, there is no limitation for number of decompositions. However, the inner diameter of inlet holes is 2 mm, which leads to generate sub-blocks with smaller dimension in x direction than the particle diameter (2.5 mm). The dimensions of a sub-block in all directions (x, y and z) should be bigger than the particle size in order to avoid numerical errors during the data exchange among the sub-blocks. Similar to the DEMEST code, the inlet in the CFD-BARRACUDA® program is also modeled as a centrally placed nozzle by the reason of the cell volume restriction (the cell volume should be much bigger than particle size). For the simplification, the inlet in ANSYS-FLUENT® is modeled as a set of nine squares instead of cycles. In this case, a block-structured mesh can be generated, since the modelling of inlet with 9 circular holes results in an unstructured grid. In **Figure 8.2**, the schematic boundary and initial conditions as well as the models assumptions for different approaches are displayed.



**Figure 8.2:** Boundary and initial conditions: (a) test rig, (b) deterministic Euler–Lagrange method, (c) stochastic Euler–Lagrange method and (d) Euler–Euler model (two–fluid model)

### 8.1.1.2 DEM model / experiment

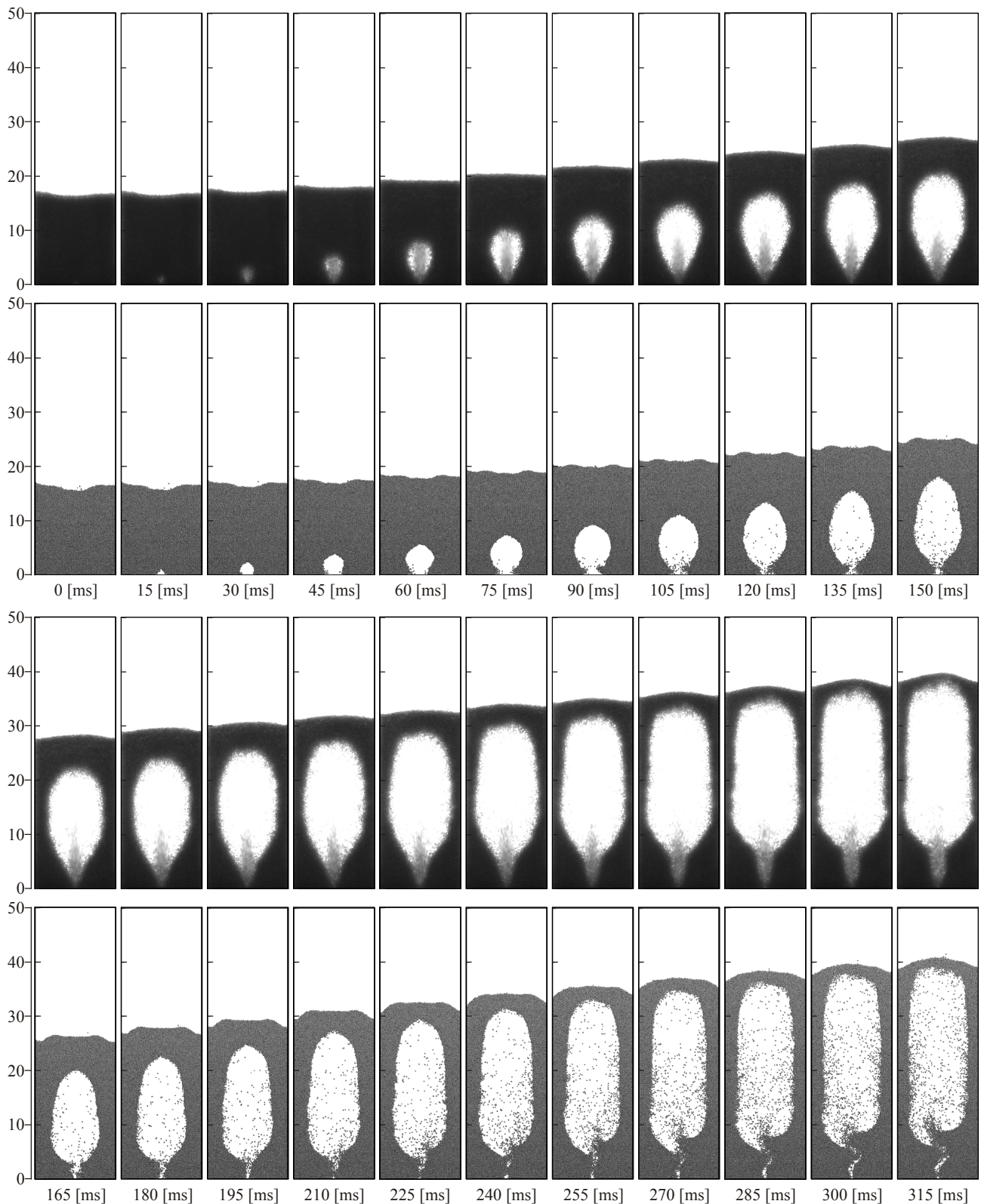
To validate the extended Euler–Lagrange/DEM model, the numerical results of a quasi-2D fluidized bed are compared with the visual observations and measurements obtained from the cold test rig. In **Figure 8.3**, the domain decomposition of the numerical model in 9 sub-blocks and the initial solid distribution are illustrated. In the DEMEST program, particles with 2.5 mm diameter are generated and distributed uniformly in the entire computational domain. The initially positioned particles have zero initial kinetic energies. The particles are then left to drop freely into the test rig. The particles experience the iterative processes of move and drop under gravity. During this phase, the mass flow rate is set equal to zero. In other words, the particles undergo only to volume and short-rang forces including the contact force. The aerodynamic forces that result from the interaction with the fluid phase are not considered in this stage. The final static bed height is 17 cm and the bulk solid fraction is ca. 0.6.



**Figure 8.3:** (a) numeric model with 9 sub-blocks, (b) solid distribution at start point in simulation and (c) in test rig

In **Figure 8.4**, the simulated and measured snapshots for the spatial distribution of solid are displayed in the period of time 0–480 ms for mass flow rate 0.006 kg/s. The initial bed height of test rig and numerical model is 17 cm at the start point. Due to the aerodynamic forces, a bubble is slowly formed near the central nozzle and thus the particle bed starts accelerating. As the bubble moves up and grows further, the bed above the bubble becomes thinner and faster. While the bed height and the bed acceleration have identical characteristics at  $t = 30$  ms and  $t = 75$  ms, the bubble has an explicit ellipsoid form in the experiment and a circular one in the simulation. From the time point 75 ms till 150 ms, the bubble expansion has similar properties in the simulation and the measurement. At time point  $t = 165$  ms, the numerical model still shows high correlation towards the measurement. In both models, the bed height is equal to 27 cm and the bubble form is almost the same. In the period of time between  $t = 165$  ms and  $t = 315$  ms, the top layer of moving particles loses more and more of its

mass and a backflow on the side walls of the bed can be observed. While the simulated bed height indicates exact behaviour to the measurement (at  $t = 225$  ms  $h = 32$  cm, at  $t = 240$  ms  $h = 34$  cm, at  $t = 255$  ms  $h = 35$  cm, at  $t = 270$  ms  $h = 37$  cm, at  $t = 285$  ms  $h = 38$  cm), the solid distribution in the nozzle area differs between both models. In the experiment, the particle backflow streams directly to the nozzle and builds a semi-triangular. This distribution cannot be detected in the Euler-Lagrange/DEM model, where the particles flow to the nozzle as an arc of a circle.



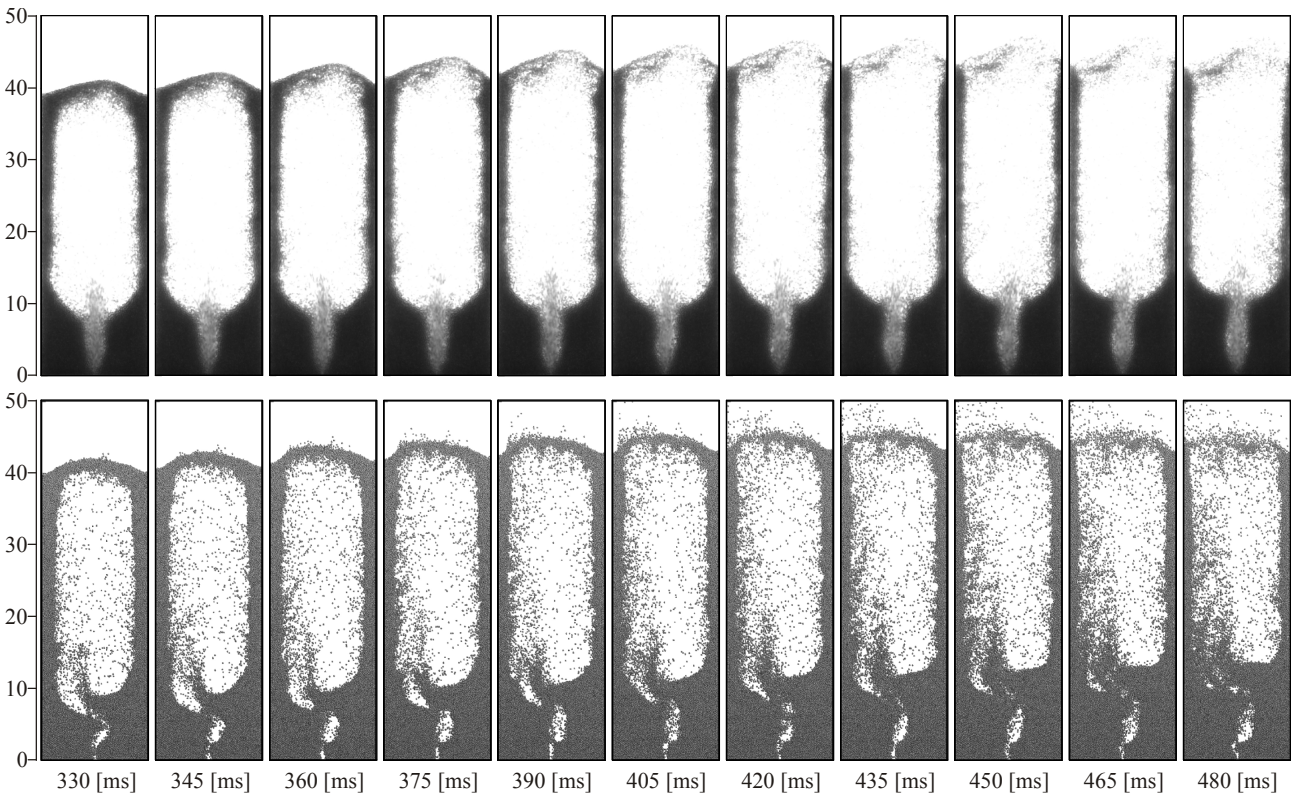


**Figure 8.4:** Snapshots for the spatial distribution of solid: (upper row) experiment and (lower row) simulated result (mass flow rate 0.006 kg/s)

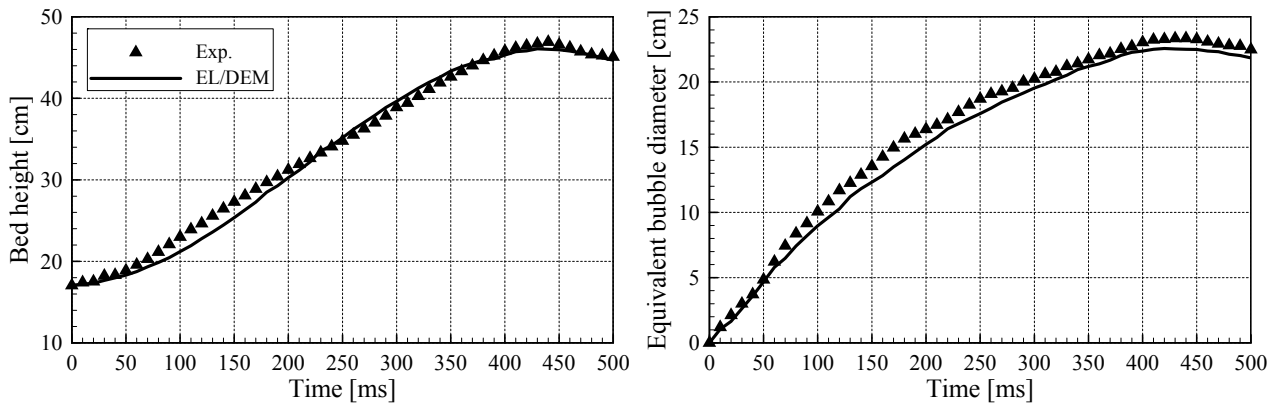
Further comparison between the numerical and test rig models in the range of 330–480 ms is also presented in **Figure 8.4**. While the bubble continues growing, the top layer of particles loses more of its kinetic energy and eventually reaches the standstill after 420 ms with maximum expansion of the bed about 47 cm. From time point 440 ms, both models start to lose their gas bubbles and the particles flow back on the side walls into the bed. The bed height and thus the bubble size decreases then over time. It is obvious that the simulated bed characteristic including the bed height, the bed expansion and the bubble form agrees very well with the experiment. However, a slight deviation in the solid distribution in the nozzle area is noticed. This discrepancy in the numerical model is due to the strong interaction between gas and solid in the nozzle region, where velocity differences between the phases reach a maximum value.

The bed expansion behaviour as a function of time is depicted in **Figure 8.5**. The bed height and the bubble area are measured from the experimental snapshots and the numerically computed contours of the bed for every 10 ms. The equivalent bubble diameter is then calculated from the measured bubble area according to equation (2.6). A good agreement between the numerical prediction and the experimental data can be shown. The simulated bubble height and size is almost identical to the experiment. However, a small deviation can be observed in the period of time between  $t = 50$  ms and  $t = 200$  ms. The maximum relative errors in the bed height and the equivalent bubble diameter amount to 5% and 11%, respectively.

In this work, the measurement errors for the bed height and the bubble area are assumed to be  $\Delta h_{bub} = \pm 0.2$  cm and  $\Delta A_{bub} = \pm 2$  cm<sup>2</sup>, respectively. The uncertainties by measuring the equivalent bubble diameter can then be calculated using the equation (2.6) as:

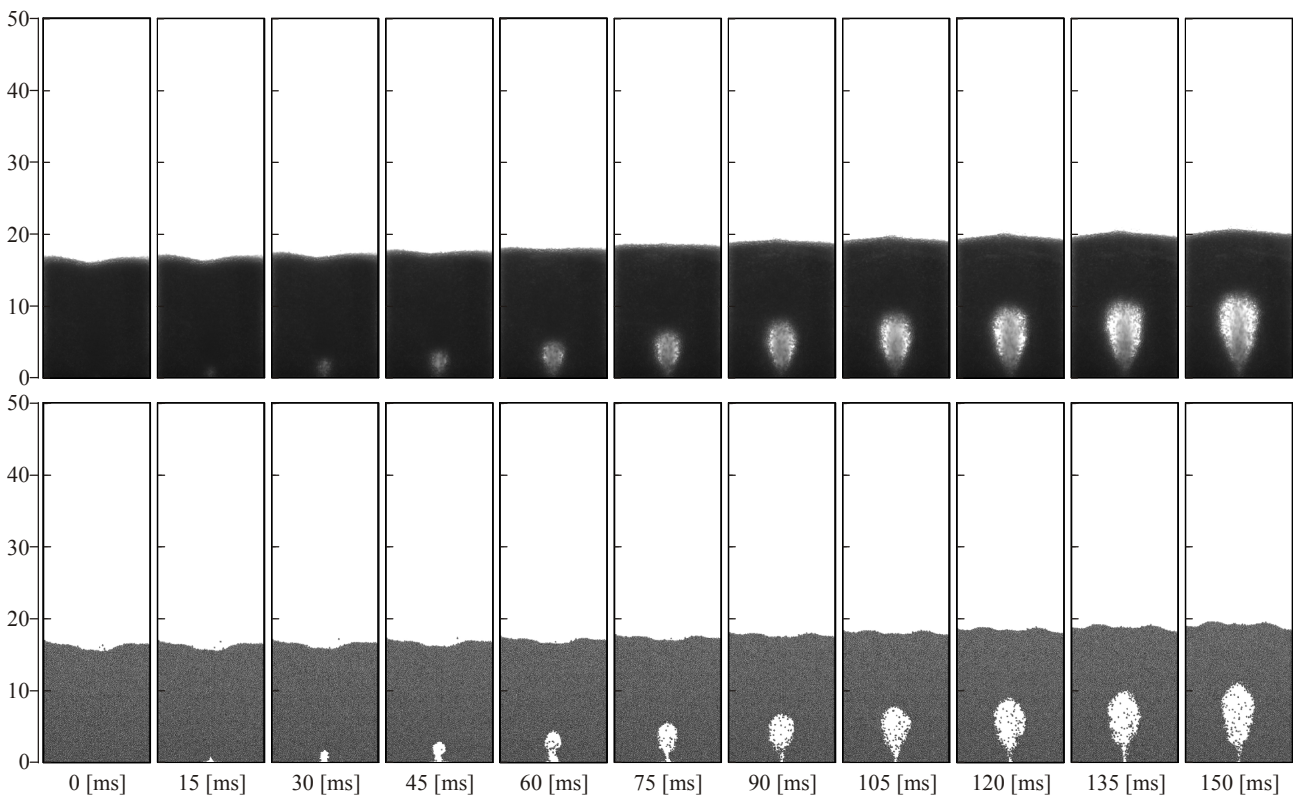
$$\Delta d_{bub}^{equ} = \frac{\Delta A_{bub}}{\sqrt{\pi A_{bub}}}. \quad (8.1)$$

Here, it should be mentioned that the uncertainties will not be included in the plotting graphs in order to simplify the results evaluations.



**Figure 8.5:** Bed expansion behaviour at gas mass flow rate 0.006 kg/s, (left) bed height and (right) equivalent bubble diameter

It can be seen from the comparison between the numerical result and the experimental data that the extended Euler–Lagrange/DEM model can predicate the spatial distribution of solid and the bed behaviour with high accuracy. In order to generalize the model validity, the entire procedure is repeated with smaller mass flow rates. **Figure 8.6** shows the numerical and experimental results for the spatial distribution of solid in the time period between  $t = 0$  and  $t = 480$  ms for mass flow rate 0.005 kg/s. At  $t = 0$ , the numerical model and the test rig have the same initial bed height of ca. 17 cm similar to the first case. From the time point  $t = 15$  ms till  $t = 150$  ms, a small bubble is formed near the central nozzle. The bed expansion behaviour has almost identical characteristic in experiment and simulation. Furthermore, the bubble has an apparent ellipsoid form in both models. The gas bubble moves up and grows further. From  $t = 165$  to 255 ms, the bubble expansion shows the same pattern in the simulation and experiment. The simulated bed height agrees very well with the measured data (at  $t = 165$  ms  $h = 20$  cm; at  $t = 195$  ms  $h = 20.5$  cm; at  $t = 225$  ms  $h = 21$  cm; at  $t = 255$  ms  $h = 21.5$  cm).



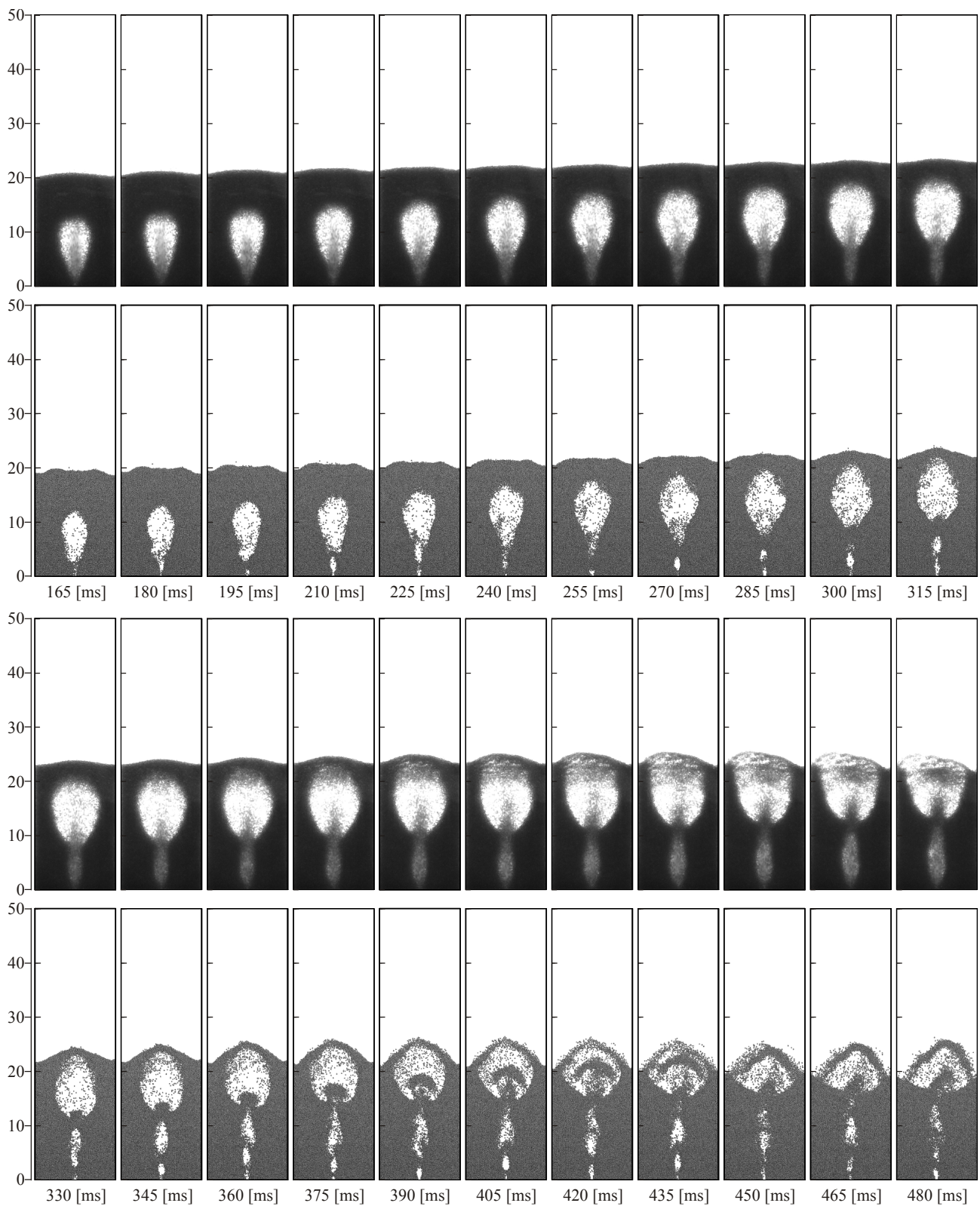


**Figure 8.6:** Snapshots for the spatial distribution of solid: (upper row) experiment and (lower row) simulated result (mass flow rate 0.005 kg/s)

At  $t = 270$  ms, the particle layer above the bubble becomes thinner in the simulation compared to the measurement. In addition, the solid distribution in the nozzle region differs between both models. In the time period between  $t = 330$  ms and 480 ms, the numerical model is still in good agreement with the measurement. However, a deviation in the solid distribution and the bubble area can be observed, especially from the time point  $t = 405$  ms till  $t = 480$  ms

(after the bubble burst). The numerical model indicates a relatively small disagreement of bubble size occurs during the entire time and increases at final stage of the bubble formation. At the time, where the gas bubble collapses, the simulated bubble area deviates from the experiment. The bubble properties (shape and area) obtained numerically shows different forms, though the bed height is close to the measured data. The reasons behind these deviations over the entire simulation time will be discussed later.

Besides the visual observation of solid distribution, the bed behaviour is evaluated during the fluidization quantitatively by plotting the bed height and the bubble size as a function of time (see **Figure 8.7**). The simulated and measured bed heights have the same value (17 cm) at the start point. From  $t = 0$  to  $t = 30$  ms, the simulated bed height shows identical developing as the measured data. The simulated bed height goes below the experiment in the period of time between  $t = 50$  ms and  $t = 300$  ms, while it passes over the experiment in the remaining time. The simulated bed height shows a maximum relative error about 5%. On the other hand, the equivalent bubble diameter, which is a measure of the bubble area, falls short over the experiment during the entire simulation time. The relative error of equivalent bubble diameter increases from 12% at  $t = 50$  ms to 18% at  $t = 250$  ms. After the bubble burst, this error increases further to 22% at  $t = 480$  ms. The difference in the measured and computed bubble area is clear in **Figure 8.6**.

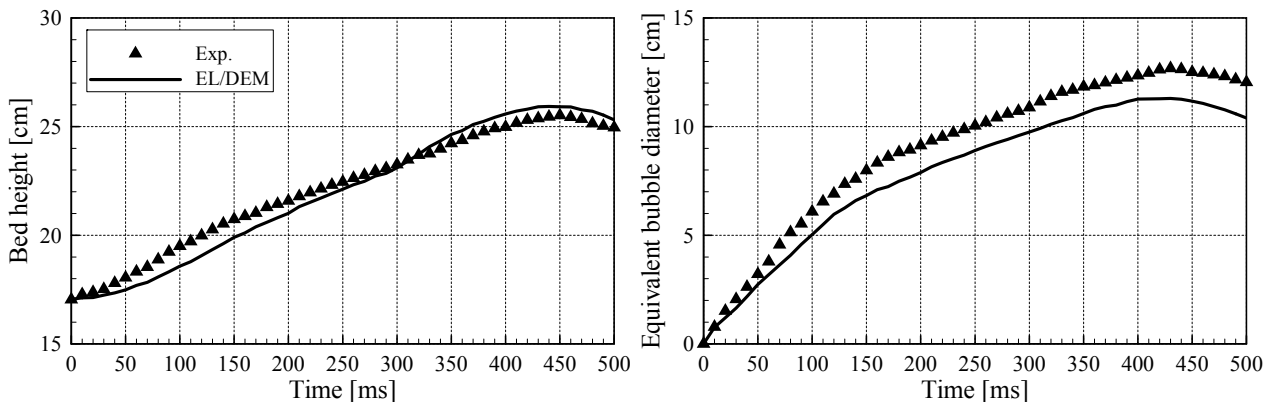


**Figure 8.7:** Bed expansion behaviour at gas mass flow rate 0.005 kg/s, (left) bed height and (right) equivalent bubble diameter

The pressure drops are measured at different heights for case 1 and case 2. After a sudden supply of the air mass flow rate, the measured pressure drops increase steadily and reach maximum values for case 1 ( $p_1 = 7$ ,  $p_2 = 5.1$  mbar,  $p_3 = 2$  mbar and  $p_4 = 0.6$  mbar) and for case 2 ( $p_1 = 7.7$ ,  $p_2 = 5.2$  mbar,  $p_3 = 0.3$  mbar and  $p_4 = 0.1$  mbar). This is caused by the continued expansion of the bed in the time period between  $t = 0$  and  $t = 300$  ms (see **Figure 8.4** and **Figure 8.6**). The pressure drops then decrease from  $t = 300$  to  $= 500$  ms due to the gas bubble collapse and reach quasi-stable values for case 1 ( $p_1 = 2.1$  mbar,  $p_2 = 1.6$  mbar,  $p_3 = 1.2$  mbar and  $p_4 = 0.5$  mbar) and for case 2 ( $p_1 = 6.1$  mbar,  $p_2 = 4.4$  mbar,  $p_3 = 0.2$  mbar and  $p_4 = 0.1$  mbar). Compared to the measured pressure drops, the simulated pressure drops match qualitative with the experiments (Alobaid and Epple 2013).

As previously demonstrated, the simulated results including the spatial distribution of solid, the bed height and the equivalent bubble diameter is analysed for different mass flow rates within 500 milliseconds. It is clear that the numerical results show a good agreement with the measurements. However, deviations of simulated solid distribution and bed expansion from the experiments, especially in the nozzle region, may be caused by several reasons. The inlet assumption of the centrally placed nozzle instead of the nine holes represents the most significant measure for these deviations (see **Figure 8.2**). One important factor is the long-range adhesive force, such as the electrostatic force. For different material pairings, the

electrostatic force that occurs between the oppositely charged surfaces plays an important role in fluidization. While the particles with opposite charges attract each other, the particles with identical polarity are repulsive. During the fluidization, the particle–particle/wall collisions lead to generation of electric charges that result in particle accumulation on the walls (Sowinski, Miller and Mehrani 2010). An examination of the test rig model after the fluidization experiment with material paring of glass–Plexiglas indicates that considerable electrostatic charges on the particles are induced (Alobaid and Epple 2013). Due to the continued particle–particle/wall collisions, the electrostatic charges of particles are increased gradually. The model is not able to simulate the cluster build-up when the adhesive forces, particularly the electrostatic force, are neglected. Therefore, the particles are distributed more evenly in the computation domain. Finally, it can be concluded that for the material combination of glass and Plexiglas, the electrostatic force is a crucial parameter. As a result, the traction forces become effective and lead to significant damping of particles collisions and disturbances. This stabilizing effect causes an early achievement of a quasi-steady flow state. Further reason regarding the deviations between simulation and experiment is related to the inaccurate solid parameters that are used in the calculation. The simulation of the solid phase with the aid of the DEM model requires a lot of material and geometry properties of particle–wall pairing that are not completely available. The stiffness coefficient, the damping coefficient and the friction coefficient of the particle–wall are estimated from the particle–particle coefficients (see **Table 10.2**). The reason of this assumption is that experimental data for the heterogeneous material pairing of glass–Plexiglas is presently not existent in the literature.

The calculation of the fluid phase with the aid of finite volume method involves several errors such as the modeling, the discretisation and the iteration errors (Ferziger and Perić 2002). As a result of fluid–solid interaction, these numerical errors of the fluid phase are forwarded to the particle phase. Apart from the calculation error of the fluid phase, the particle calculation itself with the DEM model is associated with numerical errors such as the penetration depth between the collision partners, especially if the stiffness coefficient is underestimated (Di Renzo and Di Maio 2004). The required stiffness coefficient is in the range of  $10^4$ – $10^9$  N/m depending to a large extent on the material properties. A stiffness coefficient of higher-order of magnitude is hardly applicable with the available computing capability. For this reason, the stiffness coefficient is set two to three orders of magnitude smaller than the proposed values by Di Renzo. The stiffness coefficient in this work is set to be  $5 \cdot 10^5$  N/m (see **Table 10.2**). This recommended value offers a good compromise between efficiency and accuracy (see section 8.1.5.1). Further indication for the deviations between simulation and experiment is related to the impact of solid on fluid phase. The exact calculation of the volumetric void fraction and the momentum transfer in the fluid cell is not possible due to the intensive computational cost. Therefore, an approximation is introduced (see section 7.1). In addition, the empirical models that are used to calculate the resistance coefficient produce an extra error in particular when high velocity differences exist between the phases (Bokkers, van Sint Annaland and Kuipers 2004).

### 8.1.1.3 DEM / Euler–Euler / stochastic Euler–Lagrange models

In the previous section, the extended Euler–Lagrange/DEM model is validated. The numerical results obtained from the DEMEST program show a good agreement with the measurements. In this section, the Euler–Lagrange/DEM results are compared with the numerical results of the Euler–Euler and stochastic Euler–Lagrange approaches.

The commercial CFD package ANSYS–FLUENT®, based on the Euler–Euler formulation, is employed to model the complex gas–solid flow in the previously explained quasi–2D fluidized bed test rig (see **Figure 8.1**). Here, the two–phase flow is treated as interpenetrating continua with the aid of the volume fraction, which denotes to the space occupied by each

phase. The volume fraction is a function of space and time and its sum in each grid cell is equal to unity. The mass and momentum conservation laws are applied to each phase individually. However, additional constitutive relations are required in order to close the governing conservation equations. This can be achieved with the aid of the kinetic theory of granular flows that describes the viscous forces and the pressure of the solid phase as a function of granular temperature (Ding and Gidaspow 1990). The commercial program CPFD-BARRACUDA®, based on the stochastic Euler–Lagrange formulation, is employed to predict the hydrodynamics behaviour of dense gas–solid flow in a cold flow pseudo-2D spouted fluidized bed. In this approach, the Eulerian description of the fluid phase and the Lagrangian representation of the solid phase are combined. The occurrence probability of a collision between two collision partners can be met by means of random numbers (see section 4.1.1). In both programs, the same boundary conditions are applied (see **Figure 8.8**). The gas phase is air at a room temperature. The solid phase consists of monodisperse spherical particles with an average diameter of 2.5 mm. The static bed height is 17 cm and the bulk solid fraction is ca. 0.6. The numerical parameters used in these simulations can be found in **Table 10.3** and **Table 10.4**. The ability of the Euler–Euler and stochastic Euler–Lagrange models to adequately describe the hydrodynamic behaviour of the gas–solid flow in a spouted fluidised bed is investigated at two different operating mass flow rates (0.006 kg/s and 0.005 kg/s). Here, the spatial distribution of solid, the bed height, the equivalent bubble diameter as well as the particle velocity at different position of the bed are analysed.

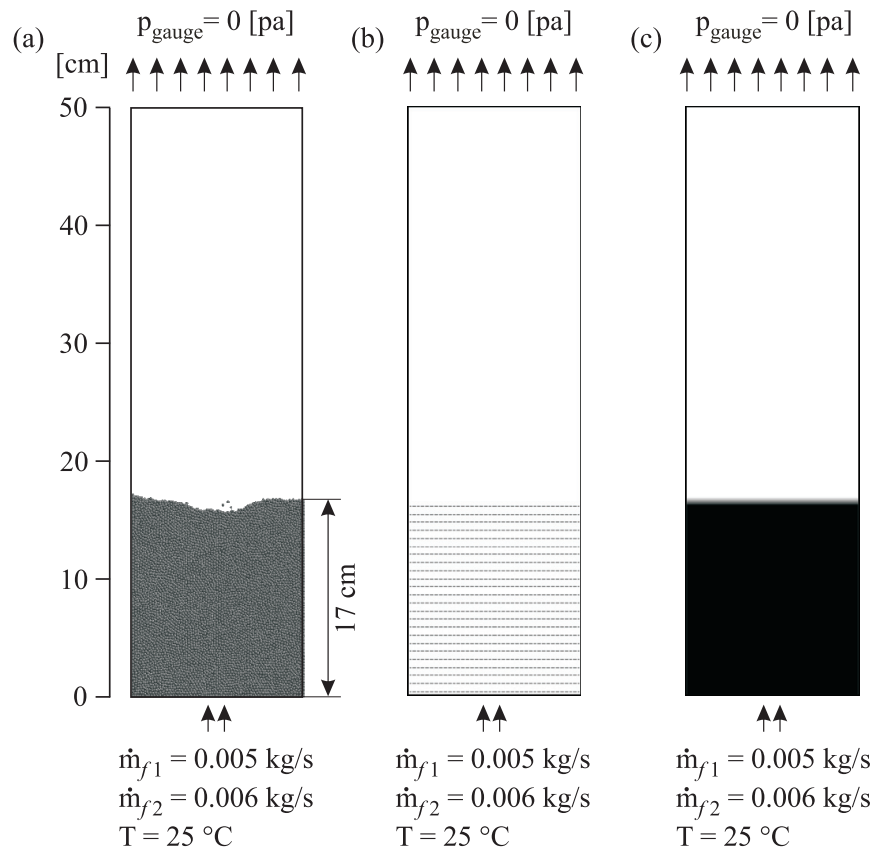


**Figure 8.8:** Solid distribution at start point: (a) Euler–Lagrange/DEM model, (b) stochastic Euler–Lagrange model and (c) Euler–Euler model

In **Figure 8.9**, snapshots for the spatial distribution of solid in the Euler–Lagrange/DEM and stochastic Euler–Lagrange approaches as well as the contours of particle volume fraction in the Euler–Euler model are presented in the period of time 0–150 ms for mass flow rate 0.006 kg/s. At the start point  $t = 0$ , the static bed height of three models is 17 cm. In contrast to the Euler–Lagrange/DEM model, the Euler–Euler and stochastic Euler–Lagrange approaches

are not able to build the bed surface profile (see **Figure 8.3** and **Figure 8.8**). This is due to the fact that the solid phase is assumed to be like a fluid in the Euler–Euler model. In the stochastic Euler–Lagrange approach, the particles are generated in each grid cell with the assumption that no contacts occur between the particles by the reason of the stochastic nature of collision detections. In the period of time between  $t = 15$  ms and  $t = 60$  ms, a bubble is slowly formed near the gas inlet and accordingly the particles in the bed start accelerating. The bubble area and the bed height are almost the same in all models. From time point  $t = 75$  ms, the good agreement decreases. The bubble expands very fast in the stochastic Euler–Lagrange model and thus the bed height increases to 33 cm at  $t = 150$  ms with a relative error of 25%. On the other hand, the Euler–Euler model shows an opposite effect. Here, the bubble grows slowly and the bed height reaches about 23 cm at  $t = 150$  ms with a relative error of 8%.

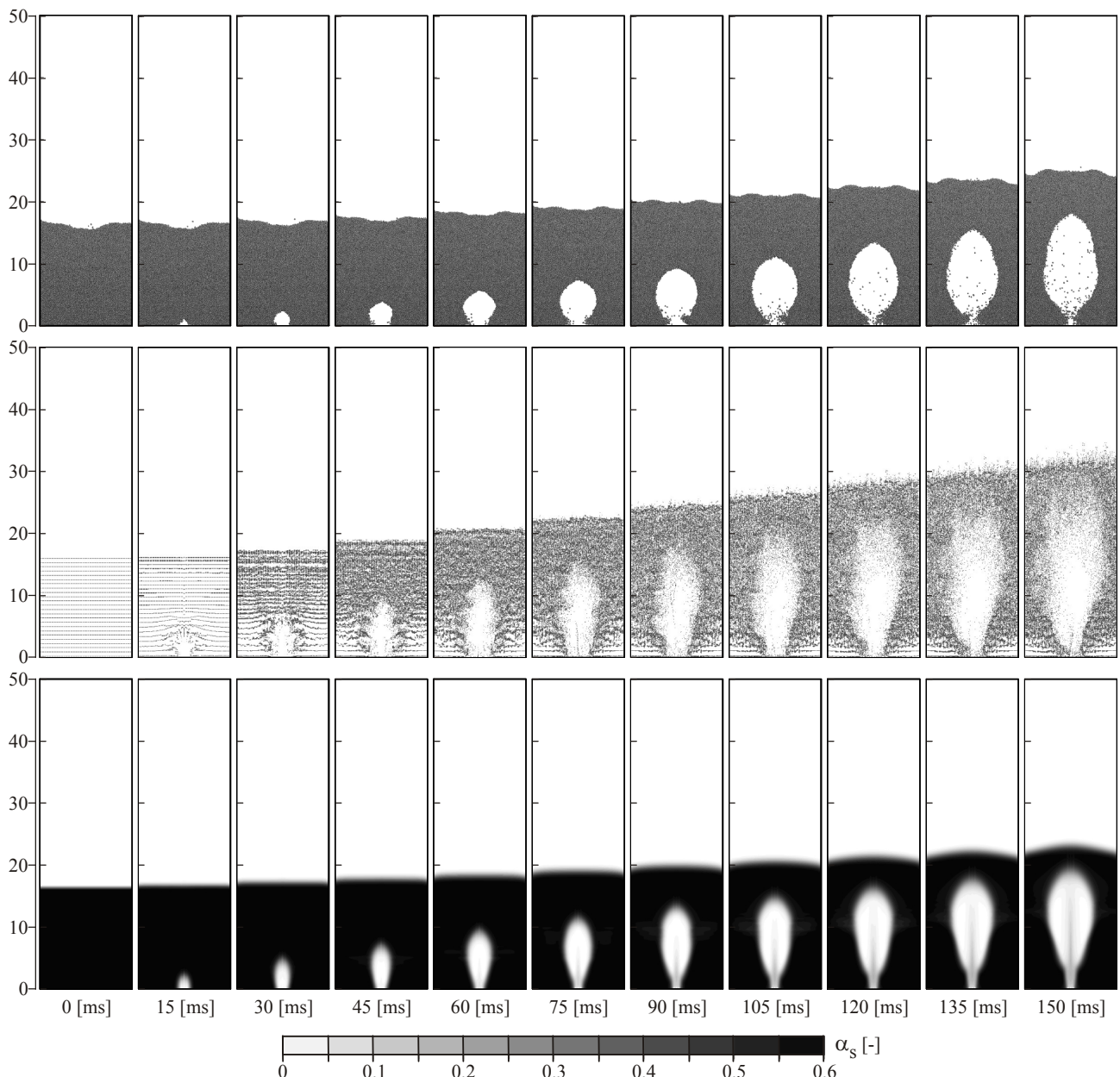


**Figure 8.9:** Snapshots for the spatial distribution of solid (mass flow rate 0.006 kg/s; time range between 0 ms and 150 ms): (upper row) Euler–Lagrange/DEM model, (middle row) stochastic Euler–Lagrange model and (lower row with particle volume fraction legend) Euler–Euler model

One important point should be emphasised here that the Euler–Euler model shows an exact symmetrical contour of particle volume fraction with respect to the y–z midplane. This behaviour can also be detected in the experiment in the time period between  $t = 15$  ms and  $t = 150$  ms. The bubble shape in the Euler–Euler model, although it is slightly smaller than the experiment, has almost an identical form. In contrast, the bubble shape in the stochastic Euler–Lagrange model differs from the measurement. Furthermore, the asymmetry in the solid distributions and the irregular bubble form can be observed.

**Figure 8.10** displays a qualitative comparison between the numerically computed solid distribution in the Euler–Lagrange/DEM and stochastic Euler–Lagrange approaches as well as the contours of particle volume fraction in the Euler–Euler in the period of time between  $t = 165$  ms and  $t = 315$  ms. for mass flow rate 0.006 kg/s.

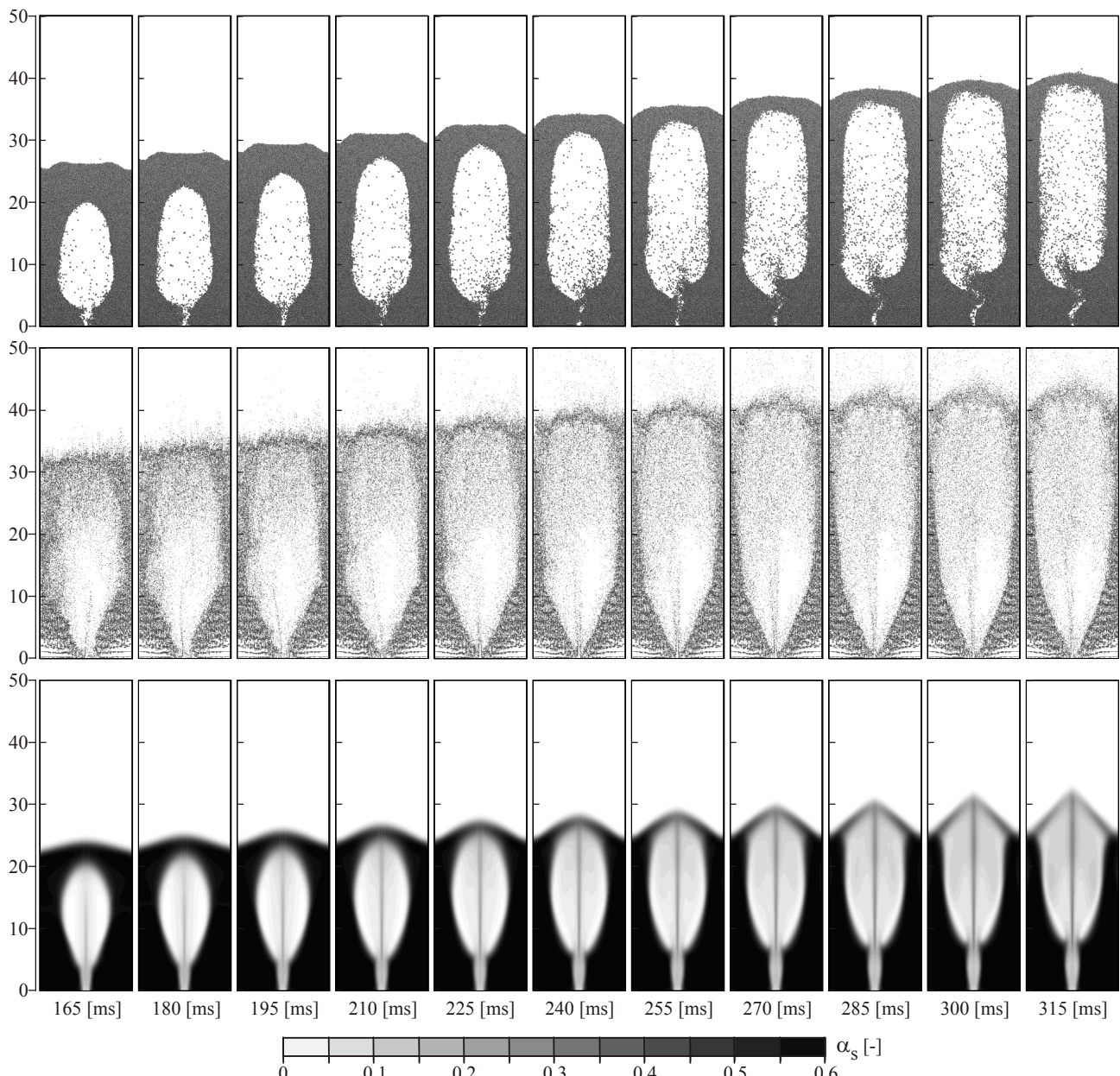
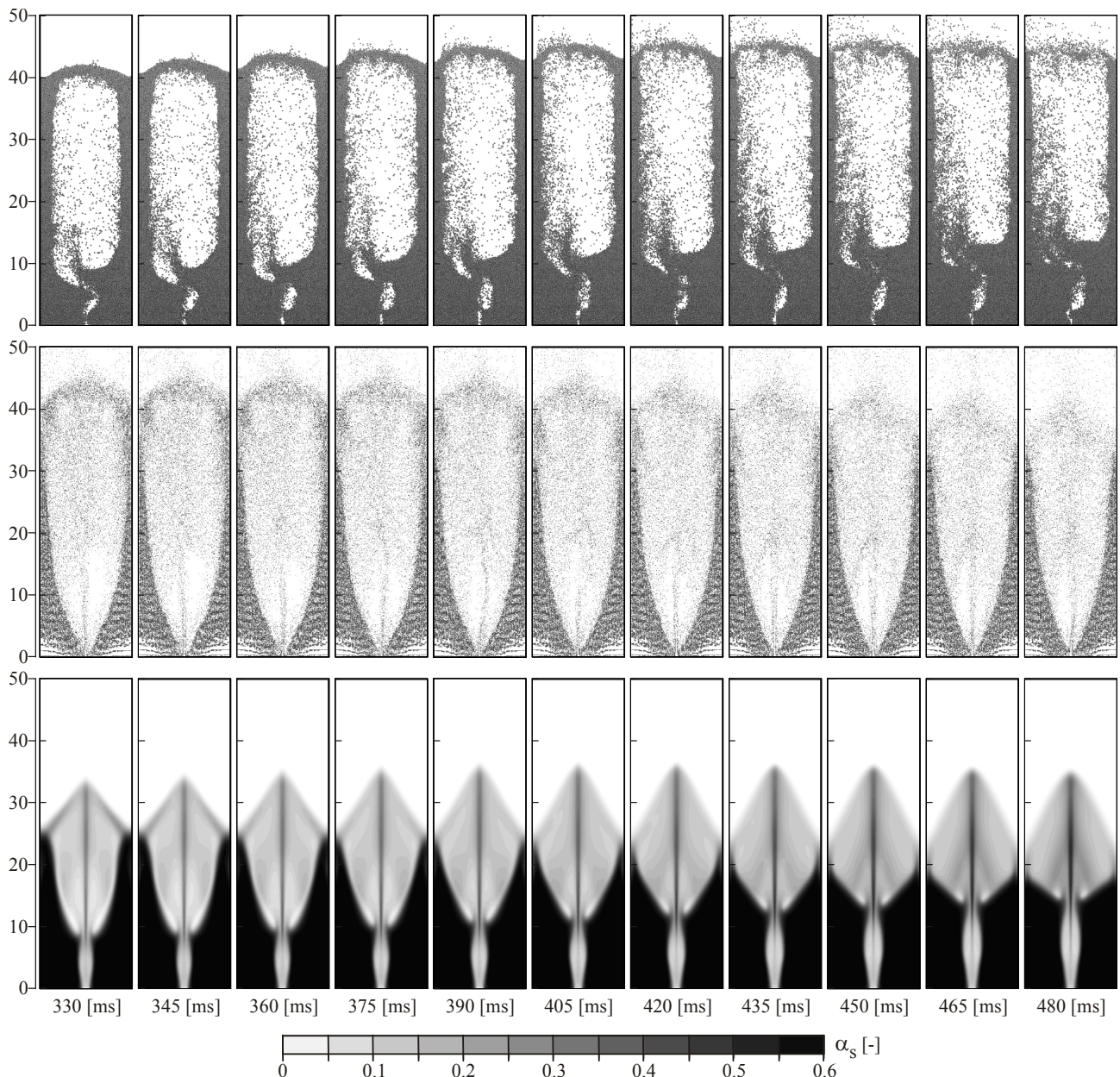


**Figure 8.10:** Snapshots for the spatial distribution of solid (mass flow rate 0.006 kg/s; time range between 165 ms and 315 ms): (upper row) Euler–Lagrange/DEM model, (middle row) stochastic Euler–Lagrange model and (lower row with particle volume fraction legend) Euler–Euler model

The numerical predictions of the stochastic Euler–Lagrange and Euler–Euler approaches agree well with the DEM model and accordingly with the experiment. The bubble shape in both models is similar to the measured data. However, there is a small deviation in the bubble size and the bed height. It can be noticed that the bubble area increases sharply in the stochastic Euler–Lagrange, while the Euler–Euler model underestimates the measured data. At time point  $t = 315$  ms, the bed height reaches a maximum value about 46 cm in the stochastic Euler–Lagrange with a relative error of about 13%. On the other hand, the Euler–Euler model seems to be clearly below the average measured bed height with a relative error of 20%. The asymmetry in the solid distribution can be seen in the Euler–Lagrange/DEM model, especially in the nozzle region. In the stochastic Euler–Lagrange and Euler–Euler approaches, the spatial distribution of solid and the contours of particle volume fraction are axially symmetrical relating to the y–z midplane. Furthermore, the gas bubble has a regular form in the stochastic Euler–Lagrange model compared to the Euler–Lagrange/DEM model.

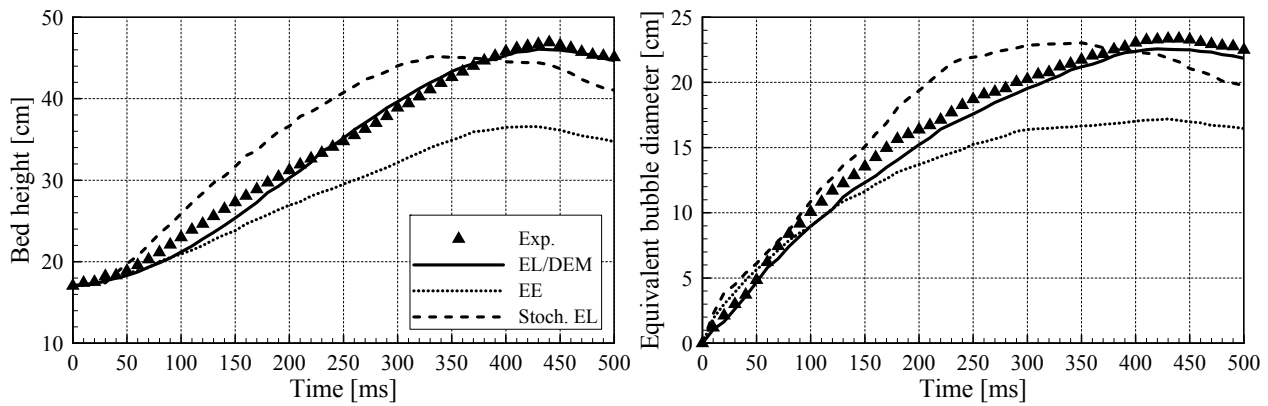
**Figure 8.11** shows the comparison between the Euler–Lagrange/DEM, stochastic Euler–Lagrange and Euler–Euler models in the period of time between  $t = 330$  ms and  $t = 480$  ms for mass flow rate 0.006 kg/s. Here, the typical flow regime of a spouted bed can be clearly observed. The gas penetrates the entire bed, dividing the bed into three regions, namely the spout in the centre, the fountain above the initial bed surface and the annulus between the spout and the walls. In the inlet region, a dilute flow is existent and the particles move upward, while in the annular flow region the particles move downward to the core again. The bed height and the bubble area in the stochastic Euler–Lagrange model decrease until the bubble collapses completely. In general, the bubble area is relatively larger than the Euler–Lagrange/DEM model. A considerable discrepancy between the calculated contours of particle volume fraction and the DEM model is clearly noticed, but the predicted annular flow region is still reasonable and agrees with the experiment. At  $t = 480$  ms, the bed height in the stochastic Euler–Lagrange model reaches ca. 40 cm with a relative error of about 11%, while the bed height in Euler–Euler model is about 34 cm with a relative error of 30%.

**Figure 8.12** displays a quantitative comparison of the experimentally observed and simulated bed expansions including the bed height and equivalent bubble diameter as a function of time for the Euler–Lagrange/DEM, stochastic Euler–Lagrange and Euler–Euler models. During the first stage of the bubble formation ( $t = 0$  and  $t = 100$  ms), a good agreement between the Euler–Euler model prediction and the experimental data can be shown. The stochastic Euler–Lagrange model, by the contrast, exceeds the measured bed height and the bubble size. In the period of time between  $t = 100$  ms and  $t = 300$  ms, the predicted bed height and bubble area in the Euler–Euler model fall below the experimentally observed ones, while it overestimates the measured data in the stochastic Euler–Lagrange approach. The maximum bed height of about 46 cm is achieved after 440 ms in the experiment as well as in the Euler–Lagrange/DEM model. The stochastic Euler–Lagrange reaches the maximum bed height (46 cm) and the maximum bubble size faster than the measured data (at  $t = 325$  ms). From  $t = 350$  ms, the bubble collapses and thus the bed height and the bubble size decrease accordingly. On the other hand, the Euler–Euler model reaches the maximum bed height without delayed in time similar to the experiment. However, this model predicts smaller expansion with a maximum relative error of about 22%. In the final stage of the bubble formation, this error becomes larger and reaches approximately 25%. The deviation in the bubble size increases gradually from 3% at  $t = 150$  ms and reaches a maximum value of ca. 30% at  $t = 480$  ms.



**Figure 8.11:** Snapshots for the spatial distribution of solid (mass flow rate 0.006 kg/s; time range between 330 ms and 480 ms): (upper row) Euler–Lagrange/DEM model, (middle row) stochastic Euler–Lagrange model and (lower row with particle volume fraction legend) Euler–Euler model

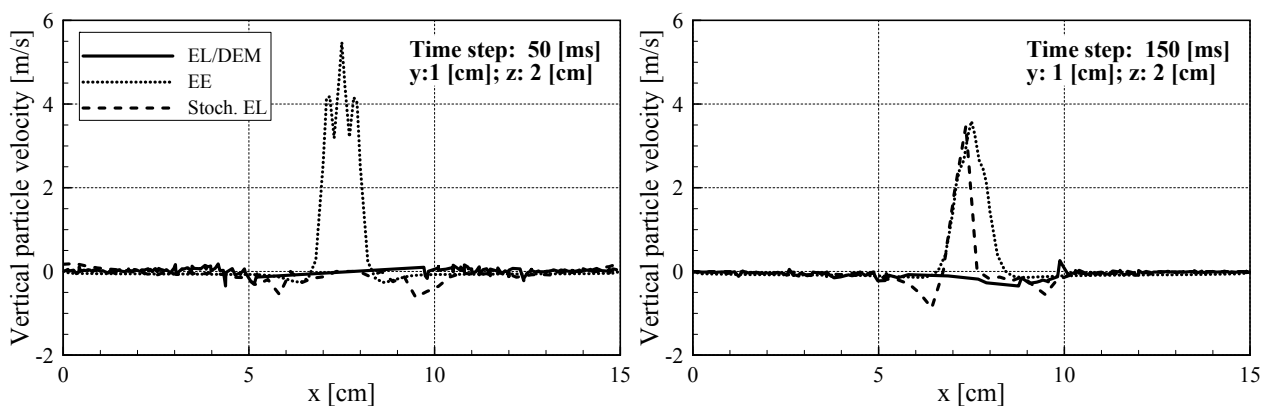
According to the previous evaluation together with the qualitative comparison of the solid volume fraction as well as the quantitative comparison of the bed height and the equivalent bubble diameter, it can be conducted that the Euler–Euler model tends at higher mass flow rates to predict smaller bubble area and bed expansion than the experimentally observed, especially during the final stage of the bubble formation. Furthermore, the Euler–Euler model shows symmetry in the particles distribution compared to the Euler–Lagrange/DEM and stochastic Euler–Lagrange approaches. On the other hand, the stochastic Euler–Lagrange model, although it reaches earlier the maximum bed expansion than the measured data, is able to predict accurately the measured bubble size and the measured bed height.

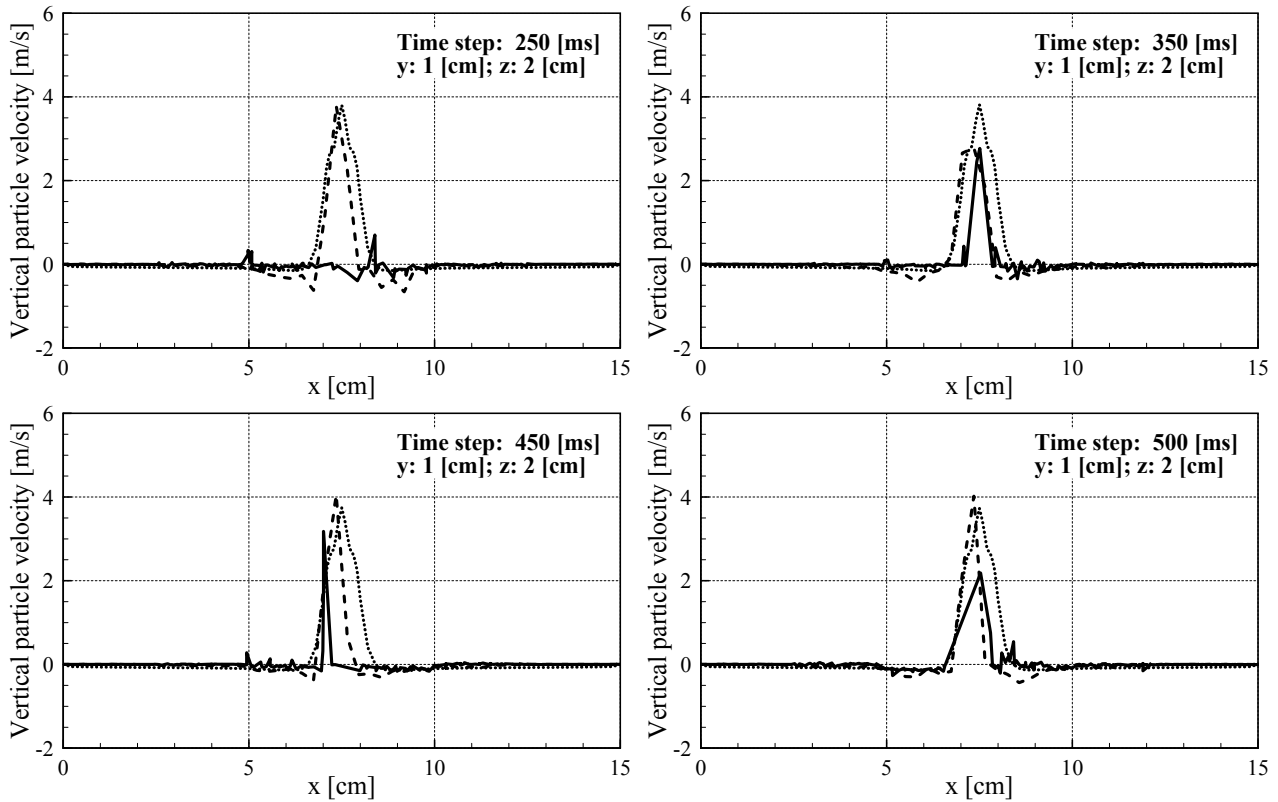


**Figure 8.12:** Bed expansion behaviour for Euler–Lagrange/DEM, stochastic Euler–Lagrange and Euler–Euler models at gas mass flow rate 0.006 kg/s, (left) bed height and (right) equivalent bubble diameter

The vertical particle velocity profiles on the midline at different locations of the bed height ( $z = 2$  cm,  $z = 15$  cm and  $z = 25$  cm) are presented in **Figure 8.13**, **Figure 8.14** and **Figure 8.15**. The height of the observation lines are selected, so that the flow regime of the spouted bed including the main three regions (i.e. spout, annulus and fountain) can be covered during the fluidization. The quantitative comparisons of the vertical particle velocity profiles (at  $z = 2$  cm) for the Euler–Lagrange/DEM, stochastic Euler–Lagrange and Euler–Euler models at gas mass flow rate 0.006 (kg/s) are plotted in **Figure 8.13** for different time steps (50 ms, 150 ms, 250 ms, 350 ms, 450 ms and 500 ms). It is clear in the spout region (between  $x = 6$  cm and  $x = 9$  cm) that the particles move upward at high velocities (ca. 4 m/s). In contrast, the annular region is not detected. The particles, which are located in the dead zone, have no velocity. At  $t = 50$  ms,  $t = 150$  ms and  $t = 250$  ms, the particle velocity peaks cannot be noticed in the Euler–Lagrange/DEM model. This is due to the fact that no particles are existent in the inlet area (see **Figure 8.9** and **Figure 8.10**).

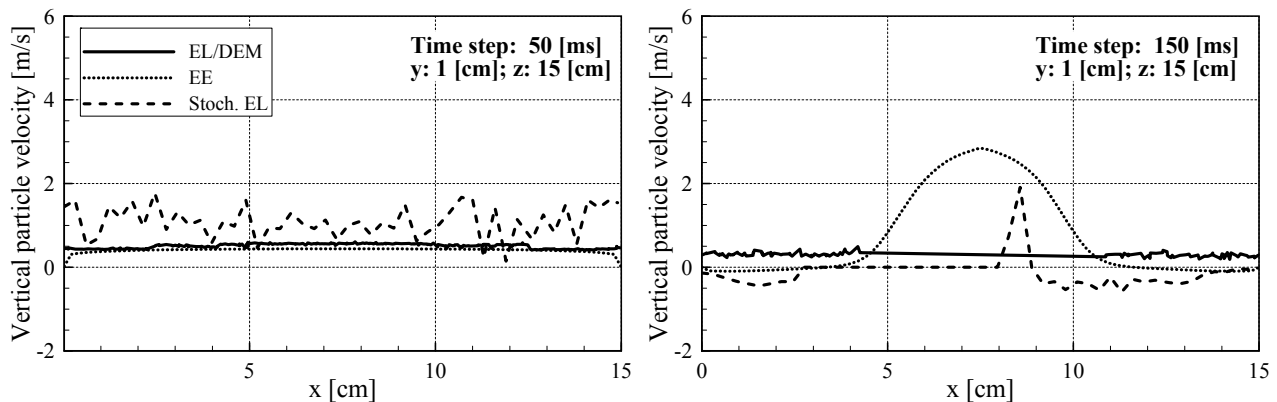
Compared to the DEM model, the Euler–Lagrange and Euler–Euler approaches are able to estimate the vertical particle velocity profiles with a good accuracy. In the dead zone (between  $x = 0$  to  $x = 5$  cm and  $x = 10$  cm to  $x = 15$  cm), all models indicate zero particles velocities. Higher particles velocities, on the other hand, can be detected in the jet zone, where the superficial fluidization velocity has a maximum value. The small peaks in Euler–Lagrange/DEM model at positions  $x = 5$  cm and/or  $x = 10$  cm at different time steps are caused by a few particles that rise upward into the fountain region.





**Figure 8.13:** The vertical particle velocity profiles ( $z = 2 \text{ cm}$ ) for Euler–Lagrange/DEM, stochastic Euler–Lagrange and Euler–Euler models at gas mass flow rate  $0.006 \text{ kg/s}$

**Figure 8.14** displays the vertical particle velocity profiles (at  $z = 15 \text{ cm}$ ) for the Euler–Lagrange/DEM, stochastic Euler–Lagrange and Euler–Euler models at gas mass flow rate  $0.006 \text{ (kg/s)}$  at different time steps (50 ms, 150 ms, 250 ms, 350 ms, 450 ms and 500 ms). Here, the spout and annular regions can be clearly detected. Compared to the position  $z = 2 \text{ cm}$ , the particles velocities in the spout region have a lower values (ca. 3 m/s). Furthermore, negative particles velocities can be noticed in the annulus. This indicates that the particles move downwards in the annular region in the direction of the inlet. At  $t = 50 \text{ ms}$ , the particles velocities (ca. 0.5 m/s) in the Euler–Euler model agree with the Euler–Lagrange/DEM result, while the stochastic Euler–Lagrange approach overestimates the particles velocities obtained from the DEM model. In the spout region, the computed vertical particles velocities in the stochastic Euler–Lagrange and Euler–Euler models show a good agreement with the Euler–Lagrange/DEM model. However, the simulated vertical particles velocities both approaches deviate from the DEM model in the annulus.



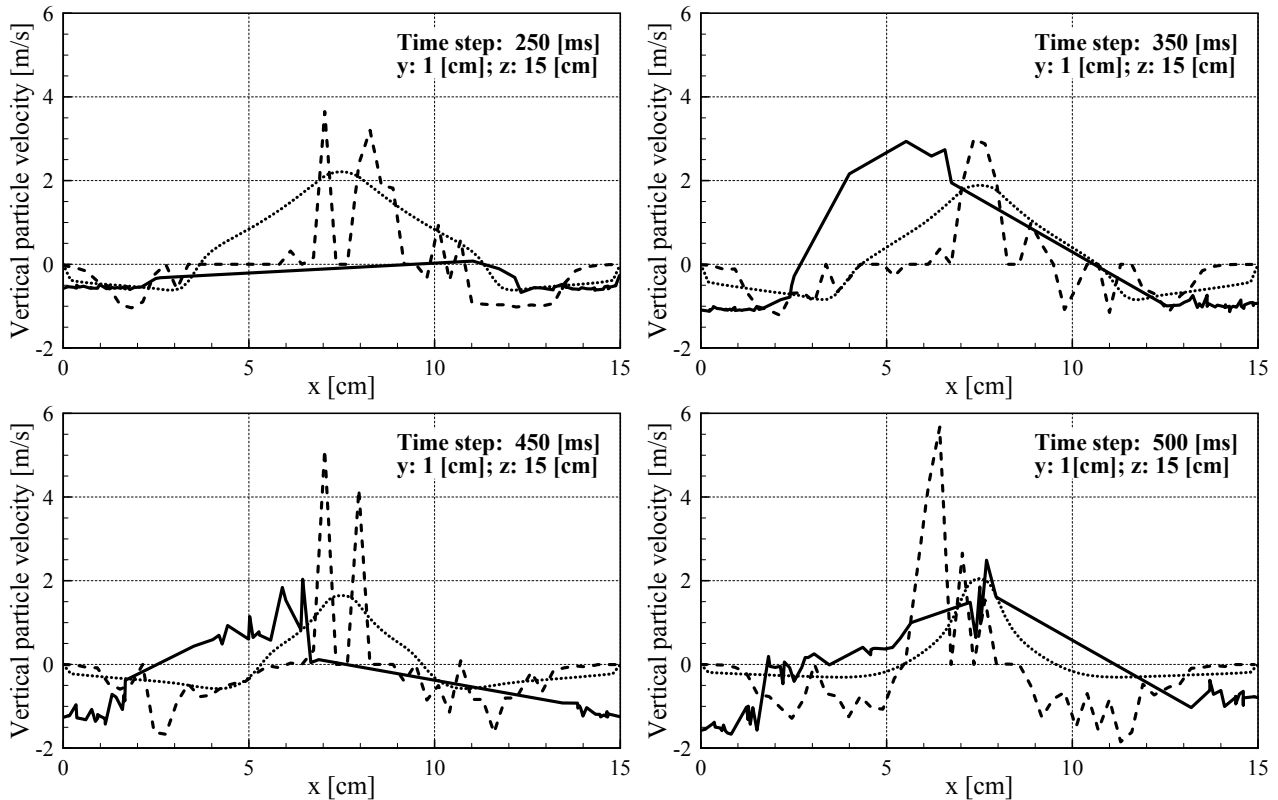


**Figure 8.14:** The vertical particle velocity profiles ( $z = 15 \text{ cm}$ ) for Euler–Lagrange/DEM, stochastic Euler–Lagrange and Euler–Euler models at gas mass flow rate  $0.006 \text{ kg/s}$

In the period of time between  $t = 250 \text{ ms}$  and  $t = 500 \text{ ms}$ , a backflow can be observed in the Euler–Lagrange/DEM model. The Euler–Euler model underestimates the magnitude of the particles velocities in this backflow. On the other hand, the stochastic Euler–Lagrange model can correctly predicate the magnitude of the particles velocities in the annular region. However, the backflow is not directly found on the walls, but rather it is shifted from the wall with about  $1 \text{ cm}$ .

In **Figure 8.15**, the quantitative comparison of vertical particle velocity profiles (at  $z = 25 \text{ cm}$ ) for the Euler–Lagrange/DEM, stochastic Euler–Lagrange and Euler–Euler models at gas mass flow rate  $0.006 \text{ kg/s}$  is shown at different time steps (50 ms, 150 ms, 250 ms, 350 ms, 450 ms and 500 ms). At  $t = 50 \text{ ms}$ , the particle velocities in all models are zero. The reason of this is clear that the plot position is higher than the vertical position of particles. After 150 ms from the start, the simulated particle velocities using the stochastic Euler–Lagrange approach agree very well with the DEM model. The simulated particle velocities in the Euler–Euler model, by contrast, fall short of the DEM results with a relative error of about 65%. At 350 ms, the negative values of the vertical particle velocities refer to a strong downward movement of the particles in the direction of the jet region, i.e. circulation in the annulus. The particles in the fountain region move slowly upwards, leading to positive particle velocities in the positions between  $x = 4 \text{ cm}$  and  $x = 11 \text{ cm}$ . In the period of time between  $t = 350 \text{ ms}$  and  $t = 500 \text{ ms}$ , the particles in the fountain region are separated towards the bed wall, moving back to the jet zone by the reason of the gravity force. Here, it can be seen that the stochastic Euler–Lagrange and Euler–Euler models show good agreement with the Euler–Lagrange/DEM model. The spout and annular regions can be clearly observed in both models. One important point is the particle velocities at the wall. While the Euler–Euler model assumes that the particle velocities at wall have a zero value, the Euler–Lagrange/DEM and stochastic Euler–Lagrange models allow the particles to roll or slide along the walls, resulting in different velocities values.

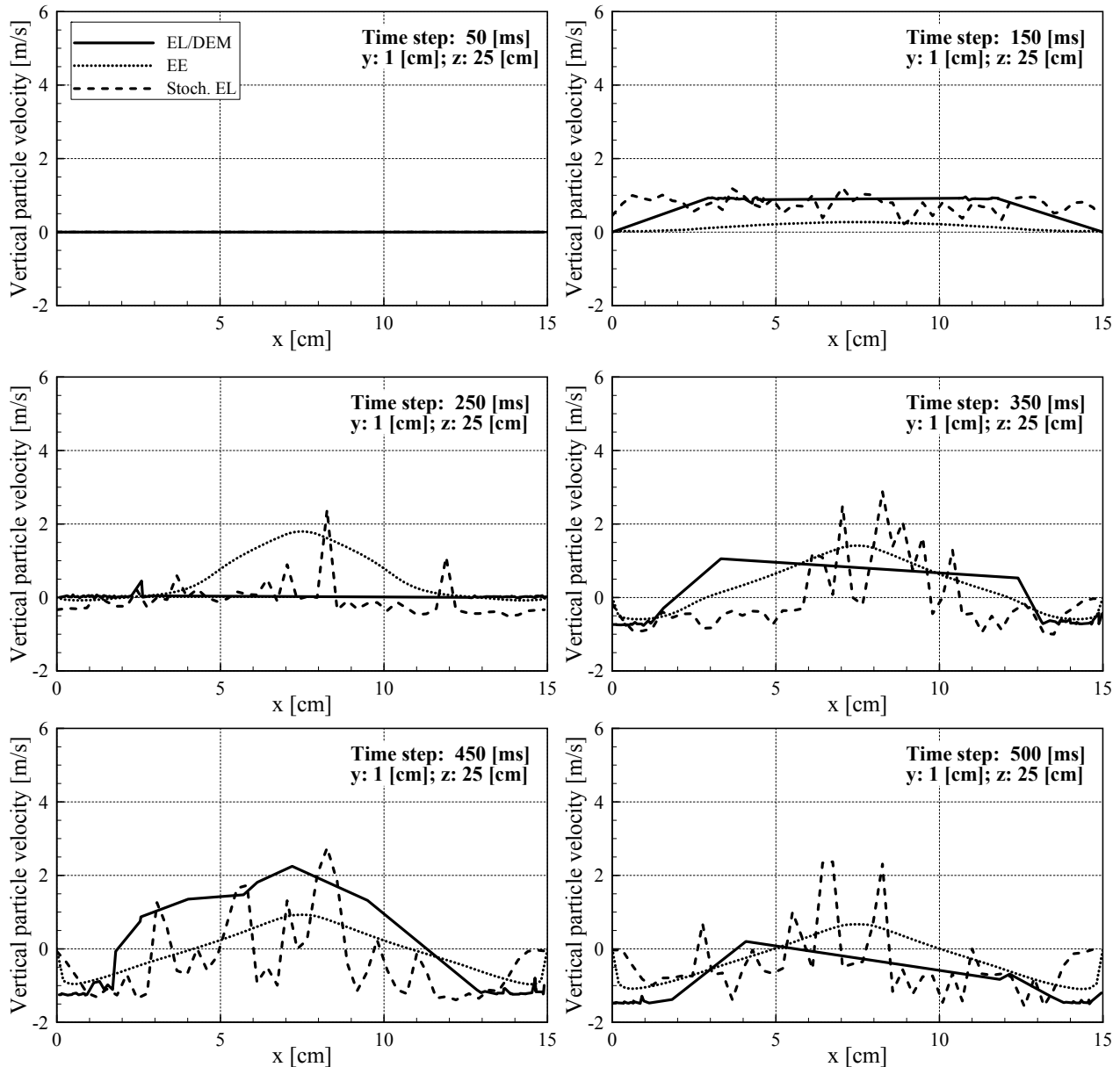


**Figure 8.15:** The vertical particle velocity profiles ( $z = 25 \text{ cm}$ ) for Euler–Lagrange/DEM, stochastic Euler–Lagrange and Euler–Euler models at gas mass flow rate  $0.006 \text{ kg/s}$

Further comparison between the stochastic Euler–Lagrange and Euler–Euler approaches with the DEM model is also carried out for the mass flow rate  $0.005 \text{ kg/s}$ . In **Figure 8.16**, the simulated spatial distribution of solid and the computed contours of particle volume fraction are illustrated. The bed height at the start point is equal to  $17 \text{ cm}$  in the Euler–Euler and stochastic Euler–Lagrange approaches. However, the initial profile of the bed surface cannot be built in both approaches compared to the Euler–Lagrange/DEM model. Due to the aerodynamic forces, a small gas bubble is formed in the jet region. The bubble expands further and the particles in the spout region rise upwards. In the period of time between  $t = 60 \text{ ms}$  and  $t = 150 \text{ ms}$ , the bed height and the bubble area in the Euler–Euler model show a good agreement with the DEM model. In contrast, the stochastic Euler–Lagrange model produces a large bubble size and bed height. Similar behaviour has also observed at the mass flow rates ( $0.006 \text{ kg/s}$ ). In general, the particle volume fraction in the Euler–Euler model has an exact symmetrical contour with respect to  $y$ - $z$  midplane and the bubble form is uniform. This effect cannot be seen in the spatial distribution of solid in the stochastic Euler–Lagrange and Euler–Lagrange/DEM models.

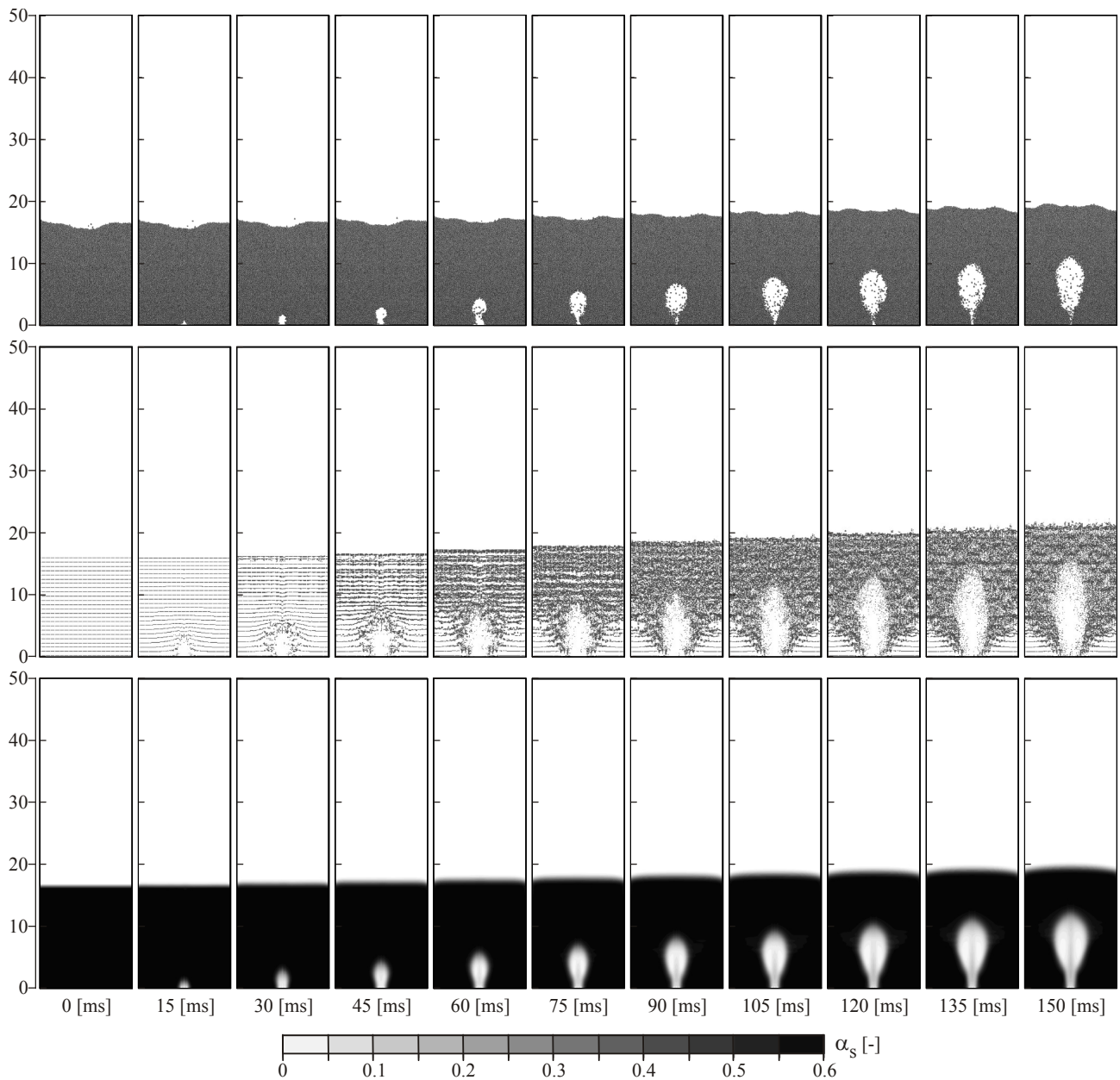


**Figure 8.16:** Snapshots for the spatial distribution of solid (mass flow rate 0.005 kg/s; time range between 0 and 150 ms): (upper row) Euler–Lagrange/DEM model, (middle row) stochastic Euler–Lagrange model and (lower row with particle volume fraction legend) Euler–Euler model

**Figure 8.17** displays a qualitative comparison between simulated particles distribution in the Euler–Lagrange/DEM and stochastic Euler–Lagrange approaches as well as the contours of particle volume fraction in the Euler–Euler model in the period of time between  $t = 165$  ms and  $t = 315$  ms for mass flow rate 0.005 kg/s. The numerical predictions of the stochastic Euler–Lagrange and Euler–Euler approaches agree well with the DEM model. The bed height in all models is close to the experiment. However, a divagation in the bubble form in the stochastic Euler–Lagrange model is recognized. At  $t = 165$  ms, the bed height in the Euler–Euler and DEM models has almost identical value ca. 20 cm. The bed height in the stochastic Euler–Lagrange shows a relative error of about 10%. In the period of time between  $t = 180$  ms and  $t = 270$  ms, the particle layer over the gas bubble accelerates and becomes thinner. From time point  $t = 285$  ms, a new small bubble is built in the jet region besides to the main bubble in the Euler–Lagrange/DEM and Euler–Euler models. While both gas bubbles are completely

separated with the solid phase in the DEM model, they are connected to each other through a narrow neck in the Euler–Euler model. On the contrary, the stochastic Euler–Lagrange model cannot form the second bubble. The single bubble has a semi-triangular shape in opposition to the DEM model that shows an elliptical bubble form. The asymmetry in the solid distribution and the irregular bubble shape can be observed in the DEM model. In the Euler–Lagrange approach as well as the Euler–Euler model, the bubble has a regular form and the solid is symmetrical distributed relating to y–z midplane.

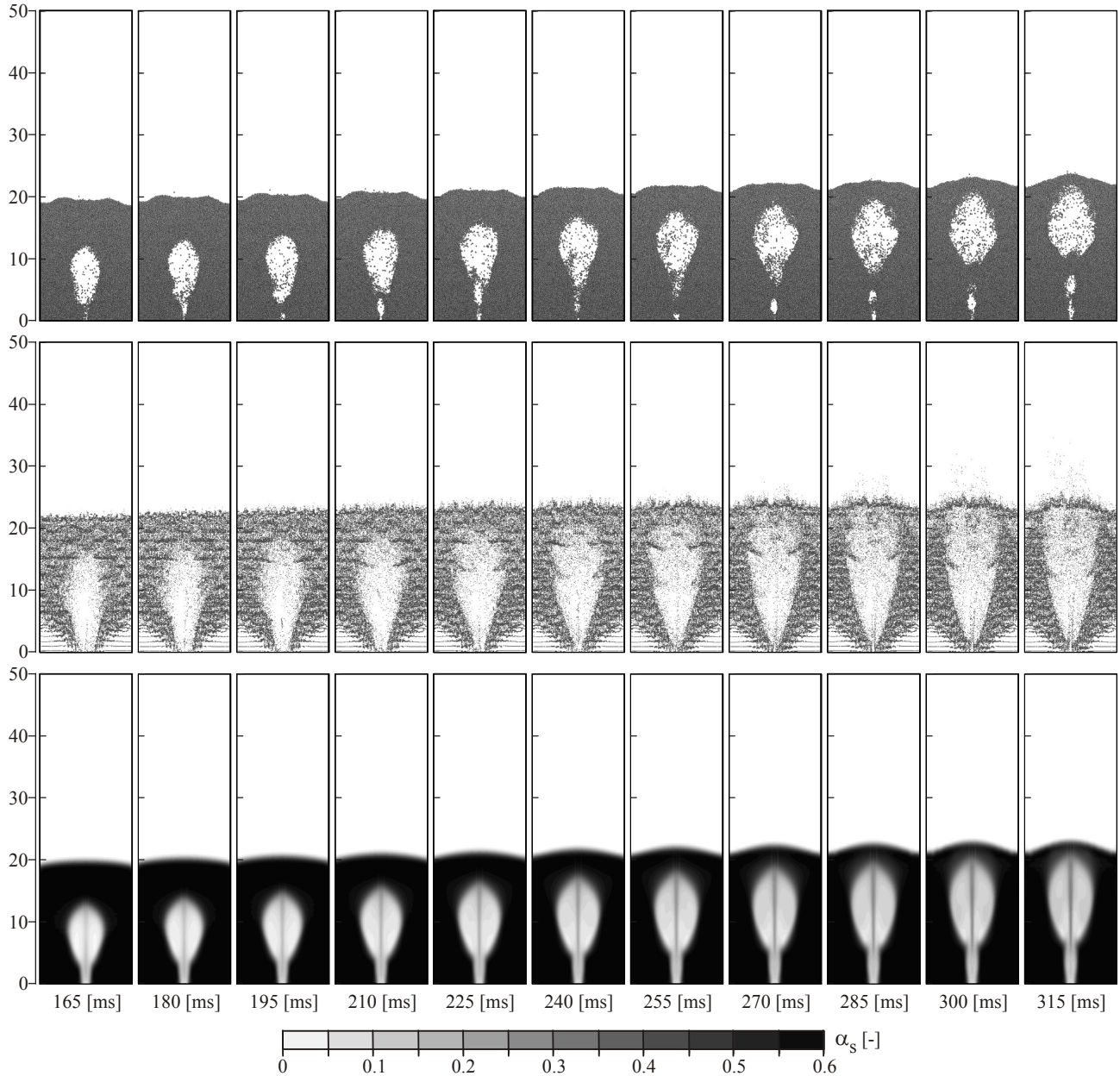


**Figure 8.17:** Snapshots for the spatial distribution of solid (mass flow rate 0.005 kg/s; time range between 165 ms and 315 ms): (upper row) Euler–Lagrange/DEM model, (middle row) stochastic Euler–Lagrange model and (lower row with particle volume fraction legend) Euler–Euler model

**Figure 8.18** shows the comparison between the Euler–Lagrange/DEM, stochastic Euler–Lagrange and Euler–Euler models in the period of time between  $t = 330$  ms and  $t = 480$  ms at mass flow rate 0.005 kg/s. Here, the three different regions of the spouted bed including spout, annulus and fountain can be clearly seen. Each region has its own specific flow behaviour and the solid loading varies from almost zero in the spout to nearly the maximum in the annulus

(solid content of about 0.6). At  $t = 330$  ms, the bed height in all models has similar value about 23 cm. The stochastic Euler–Lagrange model reaches the maximum bed height at  $t = 345$  ms, while the Euler–Lagrange/DEM and Euler–Euler models need additional time of 50 ms to achieve their maximum bed heights. From time point  $t = 345$  ms, the kinetic energy of the particles in the upper region of the bubble is almost dissipated, so that the particles fall back into the side walls. A considerable deviation is noticed between the numerically predicted bubble shape and the experiment, especially during the bubble burst. In time period between  $t = 435$  ms and  $t = 480$  ms, no gas bubble is observed in the stochastic Euler–Lagrange model. The bubble form seems to be similar to an inverted triangle without its basic side. In the DEM model, the bubble has different irregular shapes, while it has an uniform and symmetrical shape in the Euler–Euler model.

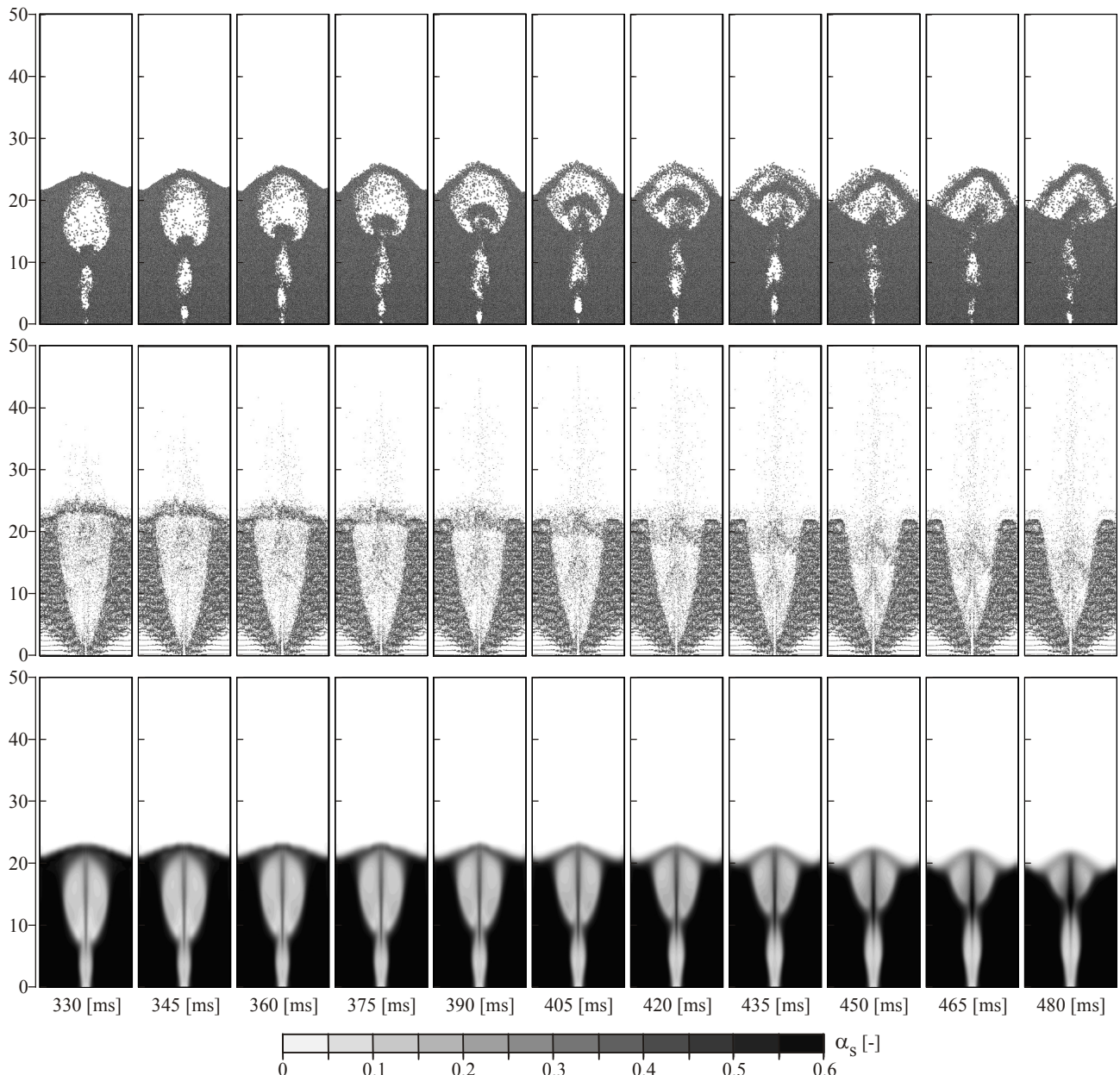


**Figure 8.18:** Snapshots for the spatial distribution of particles (mass flow rate 0.005 kg/s; time range between 330 ms and 480 ms): (upper row) Euler–Lagrange/DEM model, (middle row) stochastic Euler–Lagrange model and (lower row with particle volume fraction legend) Euler–Euler model

A quantitative comparison between the measured and computed bed height as well as the equivalent bubble diameter as a function of time for the Euler–Lagrange/DEM, stochastic Euler–Lagrange and Euler–Euler models is shown in **Figure 8.19** at mass flow rate 0.005 kg/s. At the start point, all models have the same static bed height of 17 cm. During the first stage of the bubble formation, the numerically calculated bed heights show a very good agreement with the measurement. From point of time  $t = 100$  ms, the stochastic Euler–Lagrange model overestimates the measured bed height, while the Euler–Lagrange/DEM and Euler–Euler models fall short the experimentally observed bed height. In the period of time between  $t = 150$  ms and  $t = 300$  ms, the bed height increases sharply in the stochastic Euler–Lagrange model. The bed height in the Euler–Lagrange/DEM and Euler–Euler models, by contrast, are close to the experiment. The bubble continues slowly growing and the top layer of the particles loses more of its kinetic energy till it reaches a standstill with a maximum measured bed height of about 25 cm. Decreasing the air mass flow rate from 0.006 kg/s to 0.005 kg/s results in reduction of the maximum bed height of about 50%. In the stochastic Euler–Lagrange model, the bed height reaches its maximum value 100 ms earlier than the measurement. Similar to experiment, the DEM model reaches its maximum bed height at  $t = 430$  ms. The Euler–Euler model underestimates the measured bed height with a relative error of about 8%. After the bubble collapses at  $t = 500$  ms, the DEM model exceeds the experimentally observed bed height with relative error of 3%. On the other hand, the bed heights obtained from the stochastic Euler–Lagrange and Euler–Euler models seem to be clearly below the average measured bed height with a relative error of 12 %.

The computed bubble growth curves as a function of time are also depicted in the **Figure 8.19**. In the period of time between  $t = 0$  and  $t = 300$  ms, the Euler–Euler model predicts the same experimental equivalent bubble diameter. The stochastic Euler–Lagrange model passes the measurement with maximum relative error about 22%, while the Euler–Lagrange/DEM underestimates the experiment with maximum relative error of 18%. In the remaining time, the Euler–Lagrange/DEM and Euler–Euler models underpredict the experimental bubble diameters. The stochastic Euler–Lagrange model, although the bubble shape is completely different from the measurement (see **Figure 8.18**), shows a good agreement.

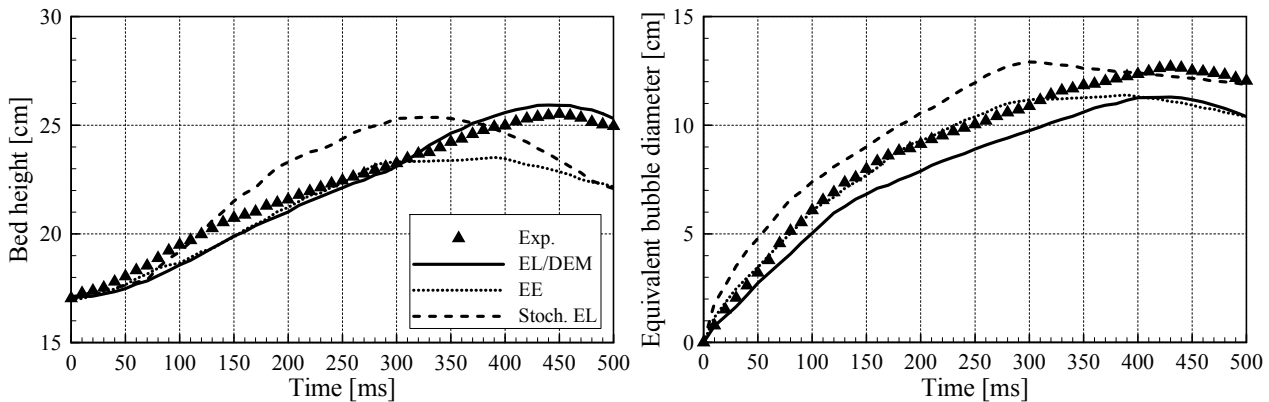
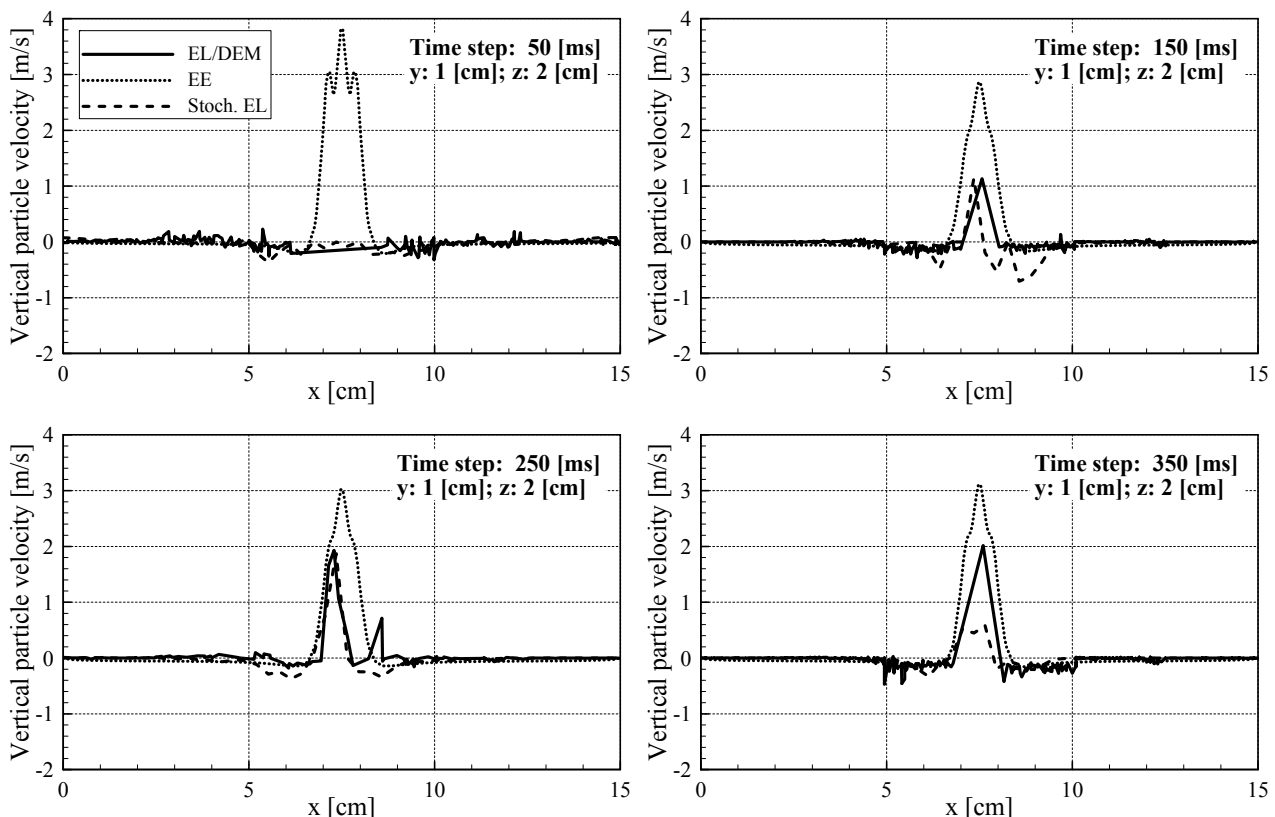


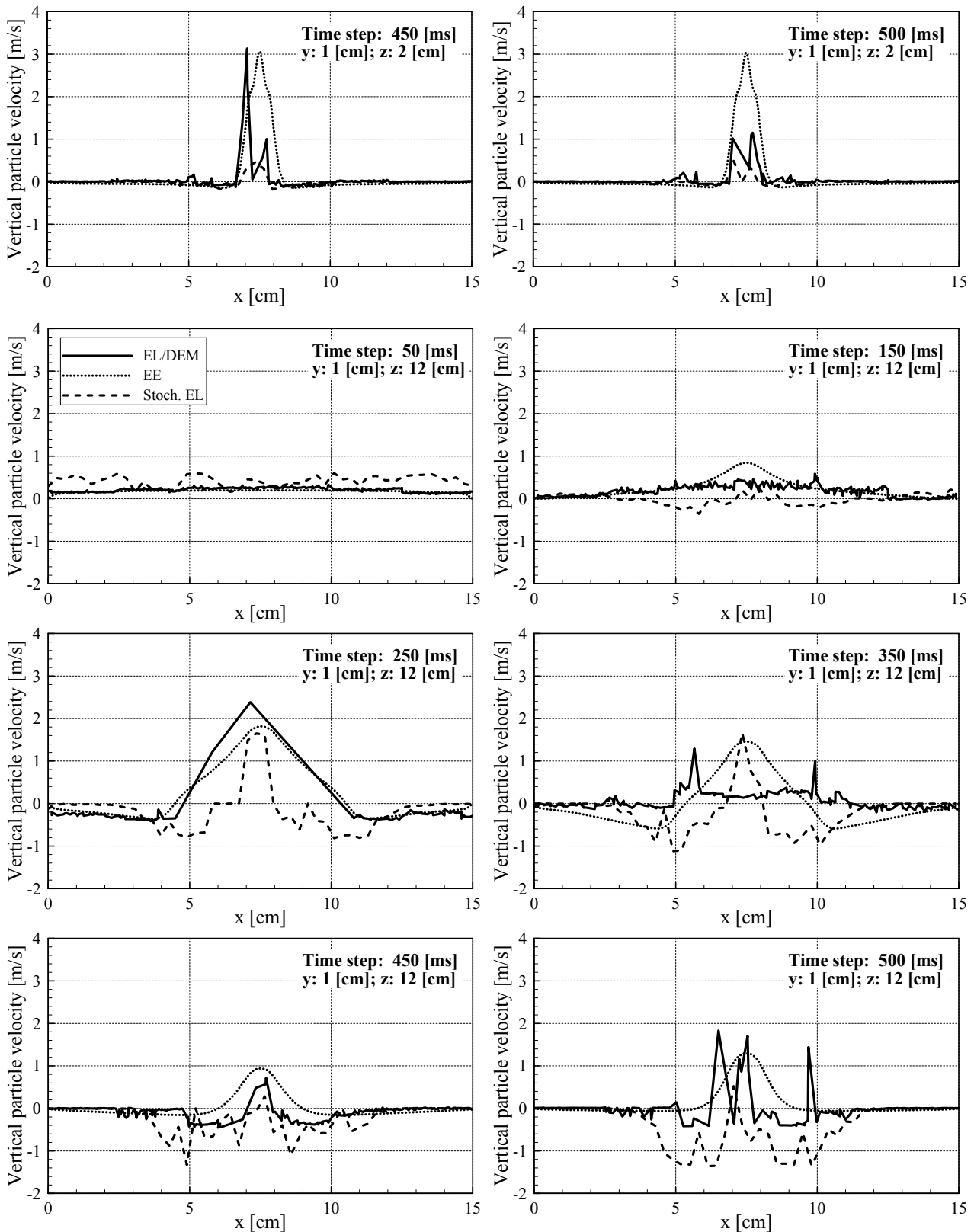
**Figure 8.19:** Bed expansion behaviour for Euler–Lagrange/DEM, stochastic Euler–Lagrange and Euler–Euler models at gas mass flow rate 0.005 kg/s, (left) bed height and (right) equivalent bubble diameter

In accordance with the above discussed assessment together with the qualitative comparison of the spatial solid distribution and the quantitative comparison of the bed height as well as the equivalent bubble diameter, it can be conducted the following points. The bed shows similar behaviour at different mass flows. However, the bubble properties (size, shape and height) at lower mass flow rates have explicitly smaller values. The Euler–Euler model can

predict the bubble size and the bed expansion with a good accuracy. During the bubble collapse stage, this model is, however, still unable to describe the bed behaviour and tends to simulate smaller bed expansion than the experimentally observed one. The stochastic Euler–Lagrange model, although it can qualitatively describe the bed behaviour, shows again faster bed expansion than the measurement. As opposed to the Euler–Lagrange/DEM and stochastic Euler–Lagrange approaches, the Euler–Euler model shows symmetry in the solid distribution with respect to the y–z midplane.

In **Figure 8.20**, the vertical particle velocity profiles on the midline at different locations of the bed heights ( $z = 2 \text{ cm}$ ,  $z = 12 \text{ cm}$  and  $z = 20 \text{ cm}$ ) at different time steps ( $t = 50 \text{ ms}$ ,  $t = 150 \text{ ms}$ ,  $t = 250 \text{ ms}$ ,  $t = 350 \text{ ms}$  and  $t = 500 \text{ ms}$ ) are illustrated at mass flow rate  $0.005 \text{ kg/s}$ . The height of the observation plans are selected according to the mass flow rate, so that the typical flow pattern of a spouted bed including the three main regions can be observed. The vertical particle velocity profiles obtained from the Euler–Lagrange and Euler–Euler approaches show a good agreement towards the DEM model. At  $z = 2 \text{ cm}$ , the spout in the centre of the bed (between  $x = 6 \text{ cm}$  and  $x = 9 \text{ cm}$ ) can be clearly seen. The particles accelerates in this region and move upwards with a moderate velocity (ca.  $3 \text{ m/s}$ ) into the fountain. All models indicate zero particles velocities in the dead zone (between  $x = 0$  to  $x = 6 \text{ cm}$  and  $x = 9 \text{ cm}$  to  $x = 15 \text{ cm}$ ). At  $z = 12 \text{ cm}$ , the typical regions of the spouted bed are recognized, namely the spout in the bed centre, the fountain above the bed surface and the annular region. The dead zone width is decreased at this height (between  $x = 0$  to  $x = 3 \text{ cm}$  and  $x = 12 \text{ cm}$  to  $x = 15 \text{ cm}$ ). In the stochastic Euler–Lagrange and Euler–Euler models, the backflow is  $4 \text{ cm}$  far from the side walls. The DEM model, by contrast, doesn't indicate any backflow at this position. At  $z = 20 \text{ cm}$ , the backflow in the annular region can be clearly observed in the Euler–Lagrange/DEM and Euler–Euler models, while the stochastic Euler–Lagrange shows zero particle velocities.





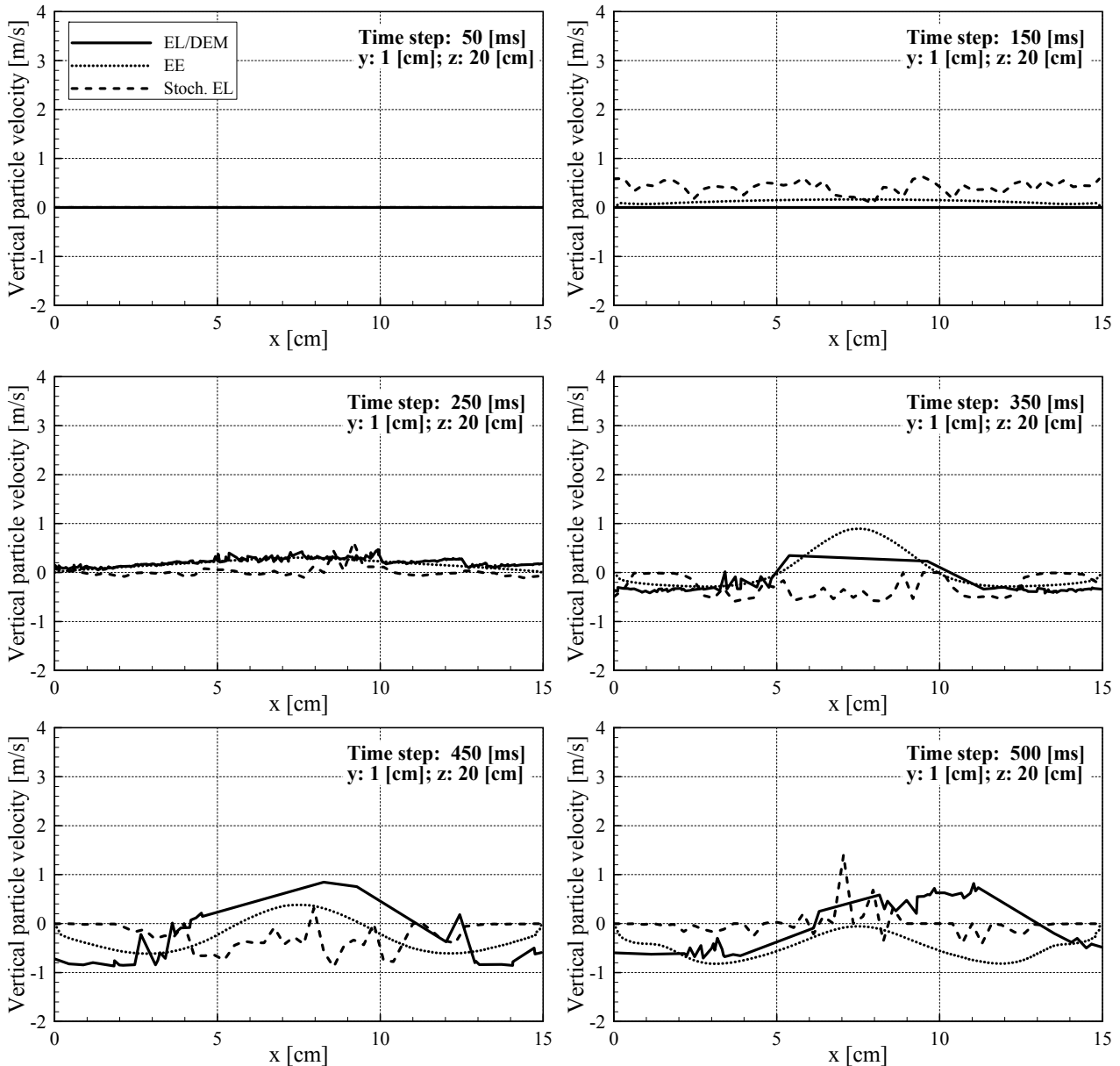


**Figure 8.20:** The vertical particle velocity profiles for Euler–Lagrange/DEM, stochastic Euler–Lagrange and Euler–Euler models at gas mass flow rate 0.005 kg/s at different time steps ( $t = 50$  ms,  $t = 150$  ms,  $t = 250$  ms,  $t = 350$  ms,  $t = 450$  ms and  $t = 500$  ms) and different positions ( $z = 2$  cm,  $z = 12$  cm and  $z = 20$  cm)

### 8.1.2 Offset method

In each control volume, the volumetric void fraction should be known as a volume average value. The most accurate but also the most complex method to determine the average volumetric void fraction in a grid cell is to consider all particles that are completely and partly located inside the control volume. Due to the extreme computational time, this can only be achieved in simple cases, where the number of particles is relatively low. Therefore, numerical approximations should be introduced. The particle centre method assumes that a particle is allocated to one control volume when its centre of mass is located inside this CV. This means particles that are partly located in a grid cell, but their centre of mass are found outside the grid cell, are not considered by the determination of the average volumetric void fraction. The efficiency gained in this approach is, however, related to a high uncertainty by the calculation of the volumetric void fraction. In this work, the volumetric void fraction is determined using a

new procedure, known as the offset method, which results in several numbers of spatial displacements of the fluid grid (see section 7.1).

In order to investigate the accuracy of the particle centre method with and without the offset method,  $k$  sample cells with known porosity  $\bar{\varepsilon}_f^{cv}$  are generated. While the particles are uniformly distributed over the entire computational domain, the particles are randomly distributed in each sample cell. It is assumed that every sample cell consists of  $n$  fluid cells (see Figure 8.21–(a)). The porosity is then calculated in each fluid cell with the aid of both approaches. By determining the average porosity for the  $n$  fluid cells, the porosity of the corresponding sample cell  $\varepsilon_{f,i}$  is calculated. To evaluate the accuracy, the standard deviation for the entire computational domain is applied:

$$\sigma_{\varepsilon_f} = \sqrt{\frac{1}{k} \sum_{i=1}^k \left( \varepsilon_{f,i} - \bar{\varepsilon}_f \right)^2}. \quad (8.2)$$

Furthermore, the ratio of the fluid cell length  $l$  to the particle diameter  $d_p$  is varied and the corresponding standard deviation is then determined. From Figure 8.21–(b), it can be seen that the mean errors of the particle centre method with and without the offset method increase with decreasing the ratio of the fluid cell length to the particle diameter. The application of the offset method improves the calculation accuracy up to an order of magnitude. The accuracy of averaging using the offset method depends highly on the grid resolution. Here, an optimal ratio between the grid size and the particle diameter  $l/d_p \approx [2-3]$  is derived. The solid loading has almost no influence on the accuracy of the calculation, whereas the accuracy of the approximation without the offset method deteriorates with increasing solid loading.

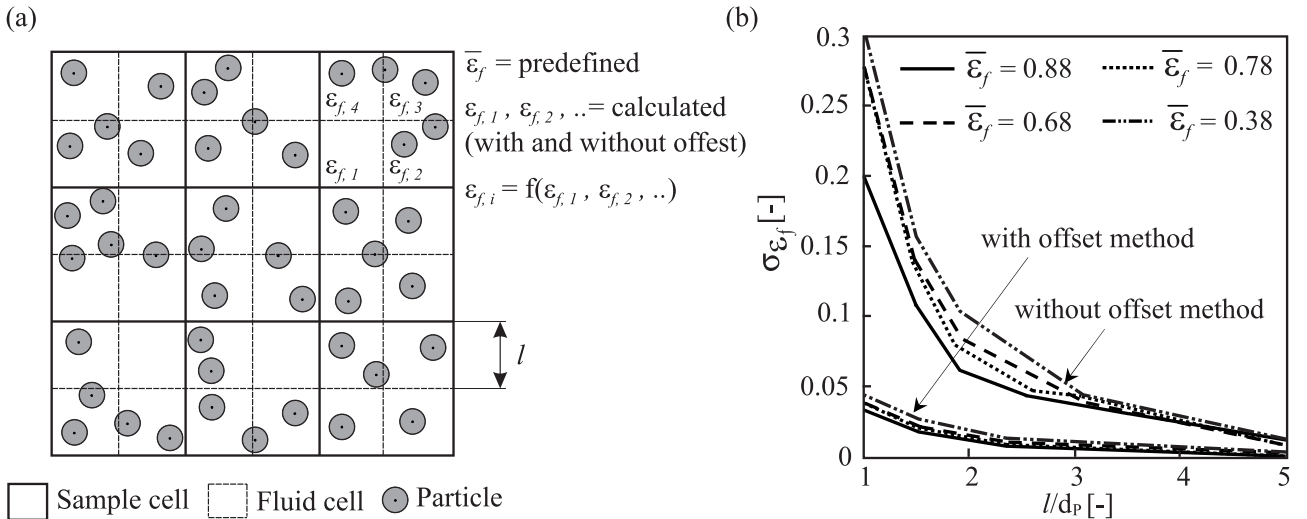


**Figure 8.21:** Sample volumes with equal porosity (predefined) and their fluid cells with different porosities (calculated by the particle centre approach with and without the offset method)

It should be mentioned here that the calculation of the momentum and heat transfers in each control volume can be carried out by the same procedure as the volumetric void fraction, i.e. using the offset method.

In order to illustrate the benefits of the offset method, a complete simulation of the quasi-2D fluidized bed is performed with the aid of the Euler–Lagrange/DEM model using the DEMEST program, but without the application of the offset method. The simulation parameters and the boundary conditions are identical with the validation cases (see section 8.1.1.1). Here,

two different operation conditions, namely air mass flow rates 0.006 kg/s and 0.005 kg/s, are investigated. In **Figure 8.22**, the simulated bed height and the equivalent bubble diameter (with and without the offset method) are compared with the measurements. At the mass flow rate 0.006 kg/s and in the period of time between  $t = 0$  and  $t = 350$  ms, the bed height in both models agrees very well with the experiment. A relative small discrepancy can be detected in the model without the offset method. From the time  $t = 350$ , a large deviation in the simulated bed height occurs. At  $t = 500$  ms, the numerically obtained bed height from the DEM model without the offset method has a relative error of 40%. The error by calculation the equivalent bubble diameter increases over time till it reaches a maximum value of 32% during the gas bubble burst. At the mass flow rate 0.005 kg/s, the simulated bed height using the DEM model without the offset method agrees well with the experimentally observed one. During the last stage of the bubble formation, a small deviation can be observed. It seems that the DEM model without the offset method can predict the correct behaviour of the bed at lower mass flow rates. The calculated equivalent bubble diameter reveals, on the other hand, the weakness of this model. From the  $t = 300$  ms, the DEM model without the offset method underestimates the bubble size with a large discrepancy (60%). According to the result obtained and the quantitative comparisons, the DEM model with the offset method matches very well with the measurements, while the DEM model without the offset method deviates obviously. The discrepancy is attributed to the inaccurate determination of the gas–solid interactions (see section 7.1).

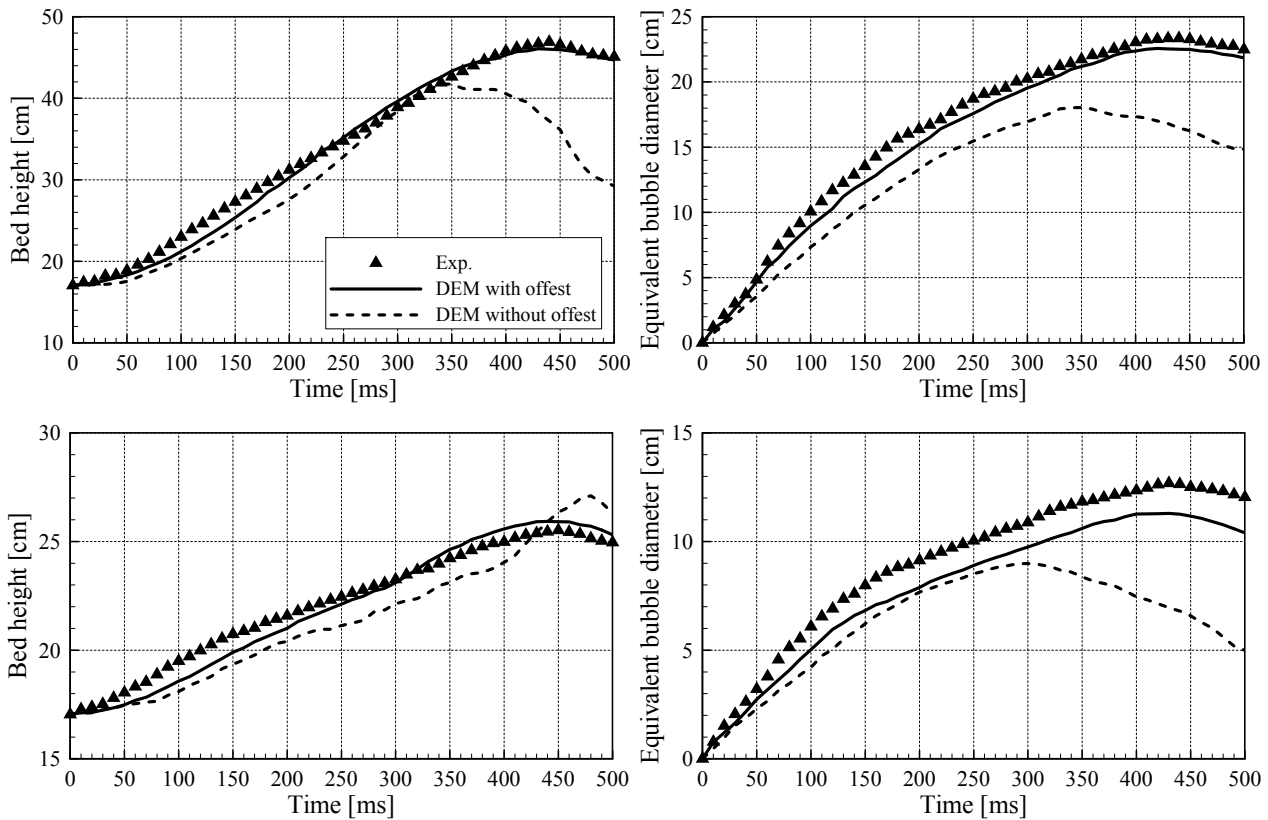


**Figure 8.22:** Comparison of bed expansion with and without the offset method: (upper row) mass flow rate 0.006 kg/s and (lower row) mass flow rate 0.005 kg/s

One important point is the computational time that should always be discussed when the Euler–Lagrange/DEM model is applied to simulate the hydrodynamic behaviour of dense granular flow. In this context, the additional computational effort that results from the using of the offset method is calculated at different particle numbers and various particle diameters. In **Figure 8.23**, the average computing time per time step is plotted against the particle number.

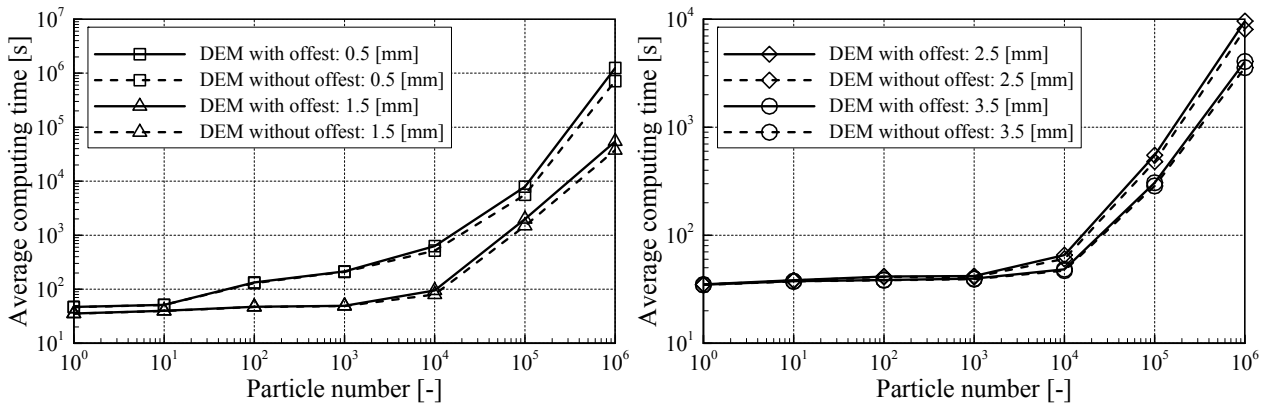


**Figure 8.23:** Comparison of computational effort with and without the offset method at different solid loadings and particle diameters

The geometry of the model and the numerical parameters used for the efficiency study are explained in the section 8.1.5. The additional computational time rises with increasing the solid loading. The particle diameter has a considerable influence on the computational effort. The decrease in the particle diameter leads to an increase in the average computing time per time step if the offset method is employed.

### 8.1.3 Particle grid method

The averaging accuracy by determination the volumetric void fraction, the momentum and heat transfers depends strongly on the solid distribution in the computational domain, i.e. the averaging accuracy is related indirectly with the grid resolution. An optimal ratio between the grid size and the particle diameter  $\Delta_f/d_p \approx [2-3]$  is already suggested. A grid refinement beyond this ratio leads to an inaccuracy in the averaging process (see Figure 8.21-(b)). If the particle diameter is equal or falls short of the grid size, the local averaging is not possible (for example: the volumetric void fraction has a negative value, see equation (7.2)). By the reason of numerical simplifications in the previous Euler–Lagrange/DEM works, the physical values of the fluid and solid phases are calculated in a common grid, namely the fluid grid. This assumes, however, that the dimensions of the largest particle must be smaller than the smallest fluid grid cell. Relative big particles or polydisperse systems with a broad range of particle sizes result in a rough fluid grid resolution and thus an inaccuracy in the fluid calculation. In this study, an additional grid, so-called particle grid, in which the physical values of the solid phase is computed, is introduced. A geometric allocation between the fluid and particle grids is necessary to enable the data transfer from fluid to solid and vice versa. The refinement of the fluid grid resolution beyond the particle scale will not result in local extremes in the gas-fraction around the centre particle mass (Link, 2006). Therefore, the proposed method is consistent with the basis of using the extended Navier–Stokes equations.

The physical values of the fluid and solid phases are determined in separated grids, namely the fluid and particle grids. The proposed procedure maintains the averaging accuracy during the determination of the interaction values, i.e. volumetric void fraction, momentum and heat transfers by selecting the optimal ratio between the particle grid size and the particle diameter  $\Delta_p/d_p \approx [2-3]$ . Furthermore, it allows the variation of the fluid grid resolution  $\Delta_f$  independent of the particle size and consequently improves the calculation accuracy of the fluid phase. Here, the conservation equations of the gas phase are solved in a fine fluid grid using an iterative method. The obtained fluid physical variables are transferred from the fine fluid cells (FC) to the coarse particle cells (PC) using an arithmetic average as:

$$\phi_{PC} = \sum_{i=1}^n \phi_{FC,i} = \frac{\phi_{FC,1} + \phi_{FC,2} + \phi_{FC,3} + \dots + \phi_{FC,n}}{n}, \quad (8.3)$$

where the parameter  $\phi$  is either fluid velocity or fluid pressure and the symbol  $n$  denotes the number of fluid cells that are allocated in one particle cell (see **Figure 8.24**). In the particle cells, the velocity and pressure gradients of the fluid phase are built and accordingly transferred to the particle phase with the aid of a linear interpolation as follows:

$$\phi_P = \phi_{PC,i} + \frac{\phi_{PC,j} - \phi_{PC,i}}{x_{PC,j} - x_{PC,i}} (x_P - x_{PC,i}). \quad (8.4)$$

The parameter  $\phi_P$  represents the fluid gradient values on the particle at the position  $x_P$ . The same procedures are repeated to the other axes (y and z). By transferring the fluid physical variables to the particles, the aerodynamic surface forces can be determined. The particle volume forces as well as the short-range forces between particles (e.g. contact force) are defined employing the DEM model. The translational and angular velocities of particles are then determined with integrating Newton's equations of motion. Finally, the volumetric void fraction, the momentum transfer and the heat transfer are calculated in the particle cells using the averaging procedures (see section 8.1.2) and subsequently are forwarded to the allocated fluid cells using the following equation:

$$\Phi_{FC,i} = \frac{\Phi_{PC}}{n}, \quad (8.5)$$

where the parameter  $\Phi$  denotes to one of the interaction values (e.g. volumetric void fraction). It should be mentioned here that each fluid cell will participate in the fluid calculation even when it is fully occupied with a particle (see **Figure 8.24**; fluid cell FC8). In this cell, the volumetric void fraction is not equal to zero. This is due to the fact that the volumetric void fraction will be calculated in the coarse particle cell (PC2). Obviously, the volumetric void fraction in the PC2 has a value bigger than zero. The obtained volumetric void fraction in the PC2 is then transferred to FC3, FC4, FC7 and FC8 avoiding the zero porosity.

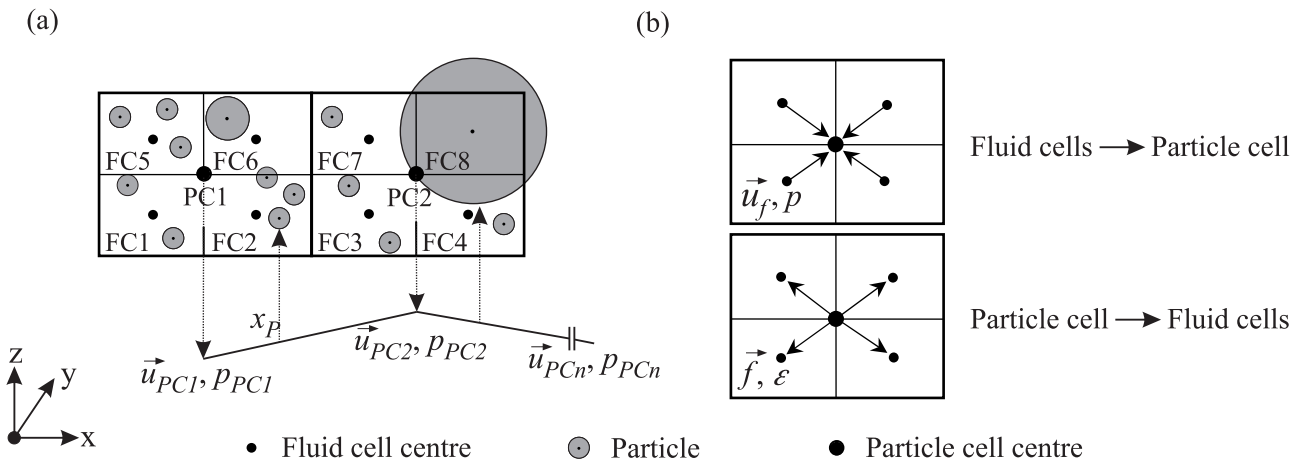


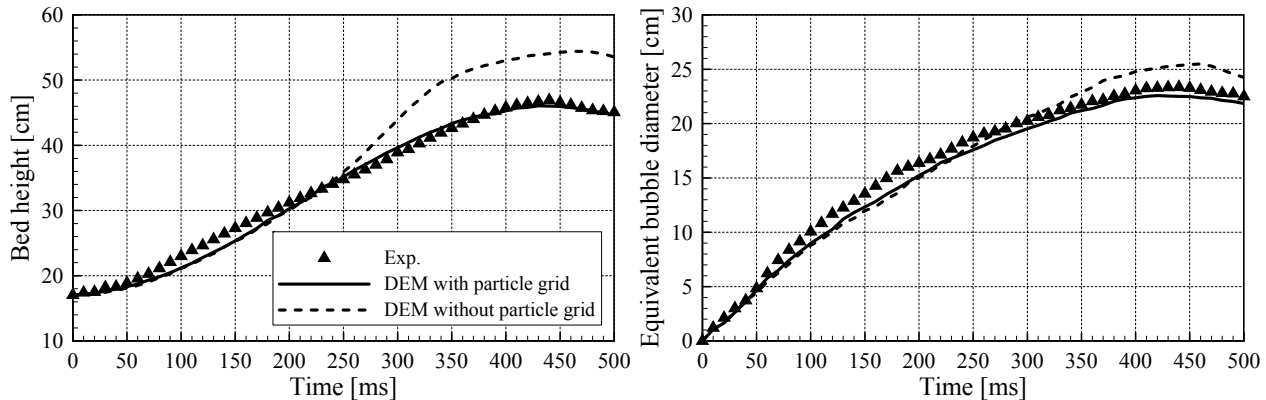
**Figure 8.24:** Fluid and particle grids: (a) particle bigger than the fluid cell but smaller than the particle cell, and (b) data exchange between fluid and particle cells

It should be mentioned here that the particle grid method can be used to determine all interaction values, namely the volumetric void fraction, the momentum and heat transfers.

The ratio between the fluid and particle grids has an influence on the computational time as well as on accuracy of the calculation. However, the selection of the particle grid size depends on the largest particle diameter in the system. To maintain the accuracy of the

averaging procedure, the particle grid size is selected around  $\Delta_p \approx 2d_p^{\max}$  (see **Figure 8.21–(b)**). For polydisperse flow with a wide range of particle size distributions, the particle grid size should be chosen very coarse. In this case, not only the computational effort of the particle grid method decreases, but also the accuracy of the calculation declines. The recommended ratio that shows a very good compromise between an efficient computing time and an acceptable accuracy is between 4 and 10.

To investigate the influence of the particle grid application on the simulation accuracy, two different numerical models of a quasi-2D fluidized bed are generated and then compared with the measurements. In both cases, the simulation parameters and the applied boundary conditions are identical. While in the first case the solid and the fluid phases are calculated by the same fluid grid, each phase is computed on its grid in the second case. For the first case as mentioned previously, the dimension of the smallest fluid grid cell must be much coarser than the largest particle in the system, but smaller than the characteristic scales in a fluidized bed (such as bubbles) (Anderson et al. 1967). Subsequently, the number of grid nodes in x direction, y direction and z direction must be less than (bed width/particle diameter:  $15/0.25 = 60$  nodes), (bed width/ particle diameter:  $2/0.25 = 8$  nodes) and (bed height/ particle diameter:  $100/0.25 = 400$  nodes), respectively, i.e. the finest grid resolution is ( $60 \times 8 \times 400 = 192000$  cells). As a result, the fluid grid resolution for the first case is selected equal to ( $56 \times 6 \times 380 = 127680$  cells). The fluid grid in the second case has the resolution of  $72 \times 12 \times 440 = 380160$  cells, while the particle phase is computed on a particle grid with a resolution of  $36 \times 6 \times 220 = 47520$  cells (see section 8.1.1.1). Two different operation conditions, namely air mass flow rates  $0.006 \text{ kg/s}$  and  $0.005 \text{ kg/s}$ , are analysed for the case 1 and the case 2. In **Figure 8.25**, the simulated bed heights are compared with the experiments over time. For the high mass flow rate ( $0.006 \text{ kg/s}$ ), both models indicate a good behaviour to the measurement in the period of time between  $t = 0$  and  $t = 100 \text{ ms}$ . From time point  $t = 150 \text{ ms}$ , the simulated bed height in the case 1 starts deviating from the test rig. In contrast to the case 1, the case 2 still shows a very good agreement. After  $420 \text{ ms}$ , the bed height in the test rig and in the case 2 reaches a maximum value about  $45 \text{ cm}$ . On the other hand, the simulated bed height for the case 1 differs from the experiment with a relative error of about 30%. The numerically observed bubble size agrees very well with measurement. From time point  $300 \text{ ms}$ , the simulated equivalent bubble diameter in the case 1 deviates from the case 2 as well as from experiment. Here, the bubble size exceeds the measured data with a relative error of 13%. At the mass flow rate  $0.005 \text{ kg/s}$ , a considerable discrepancy in the simulated bed height can be seen in the period of time between  $150 \text{ ms}$  and  $350 \text{ ms}$ . During the bubble burst, a large deviation between the numerically observed bed height and the experiment occurs, suggesting that the first model is not able to predict the bed expansion. At  $t = 500 \text{ ms}$ , a relative error of 32% in the bed height for the case 1 is registered. The error in the simulated bubble size regarding the case 1 increases slightly between  $t = 50 \text{ ms}$  and  $t = 300 \text{ ms}$  and then increases sharply in the remaining time.



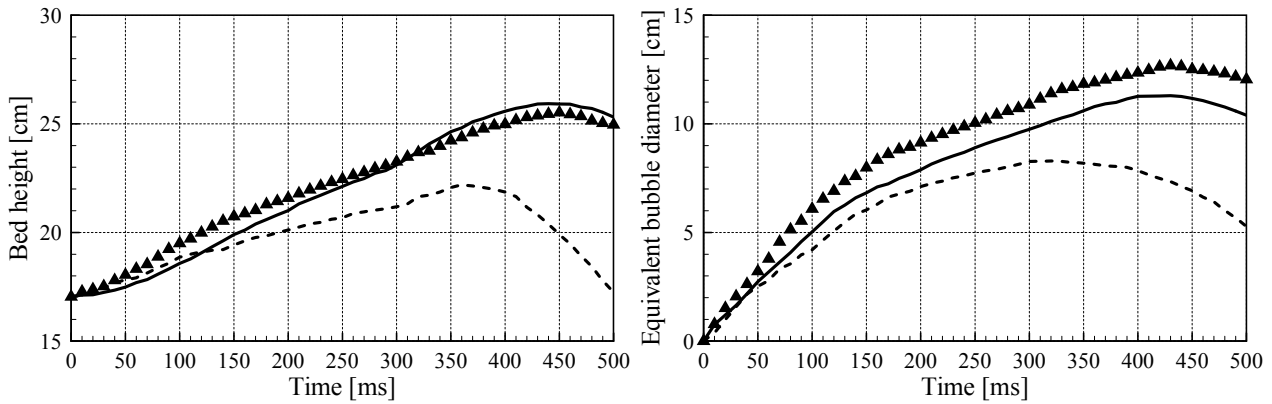


**Figure 8.25:** Comparison of bed expansion with and without the particle grid method: (upper row) mass flow rate 0.006 kg/s and (lower row) mass flow rate 0.005 kg/s

A grid dependence study shows that a further refinement of the fluid grid more than 380160 cells improves the simulation accuracy very slightly. However, the average computing time increases extremely.

The computational efficiency of the DEM model with and without the particle grid method is investigated. Further information regarding the fluidized bed model and the numerical parameters used for this study can be found in the section 8.1.5. In **Figure 8.26**, the average computing time per time step is plotted against the particle number at different particle diameters. The additional computational time, which it results from the different numbers of the fluid grid cells used in both cases, is considered in this comparison. By increasing the solid loadings, a considerable increase in the computing time per time step is observed. The particle diameter has also an influence on the computational effort if the particle grid method is employed. The average computing time per time step increases when the particle diameter decreases.

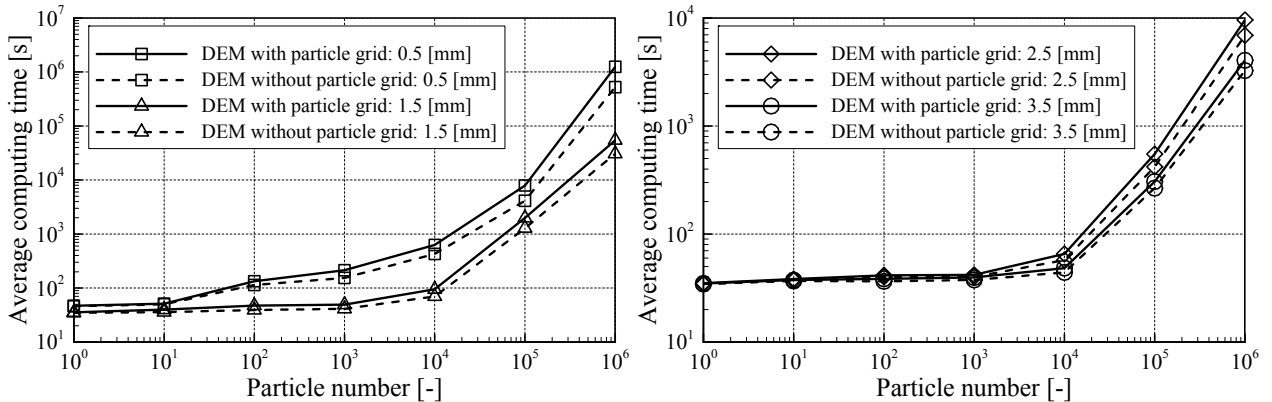


**Figure 8.26:** Comparison of computational effort with and without the particle grid method at different solid loadings and particle diameters

#### 8.1.4 Particle search grid method

The collision detection between particles is based on the assumption of the DEM model and carried out with the aid of the particle search grid method (see section 4.1.2.2). This method requires an additional grid, known as the particle search grid, which is independent of the fluid and particle grids. The size of the particle search grid depends highly on the particle diameter. If the size of the search grid is selected equal to the particle diameter for monodisperse system, the computational effort behaves almost proportional to the number of particles. A further reduction in the search grid size beyond the particle diameter is undesired. Although the computing time is reasonably reduced, it cannot be sure that all particles contacts

are detected. In **Figure 8.27**, the particles  $i$  and  $j$  are in contact. However, the contact cannot be registered in the particle search grid method. The centre of mass of the particle  $i$  is located in the search grid cell 7, so that the particle  $i$  can only collide with particles that their centre of masses are in the search grid cells 2, 3, 4, 6, 8, 10, 11 and 12.

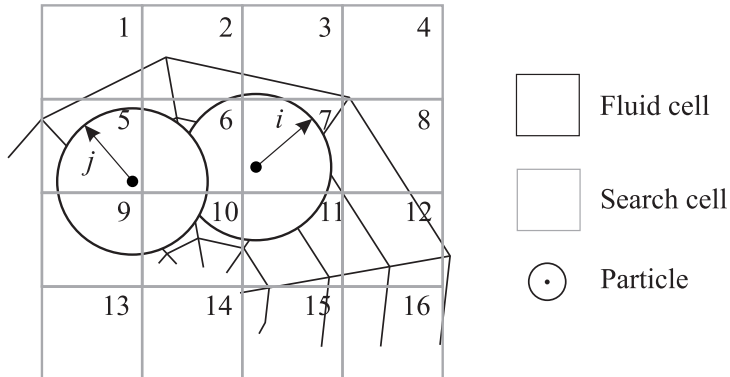


**Figure 8.27:** Search grid size smaller than the particle diameter

The effect of using a search grid with a smaller size than the particle diameter on the simulation accuracy is investigated. A simulation case of the quasi-2D fluidized bed is carried out using a search grid with a high resolution ( $\Delta_{SG} = 0.5d_p$ ). The deterministic detection of particle-particle/wall collisions is then performed on the particle search grid with a number of nodes: 120 (W)  $\times$  16 (D)  $\times$  800 (H). The simulation parameters and the boundary conditions are same as the validation cases (see section 8.1.1.1). It is clearly that the DEM model with a fine search grid deviates from the measurements (see **Figure 8.28**). The kinetic energy conservation is not guaranteed and thus the simulated bed height and the equivalent bubble diameter are underestimated.

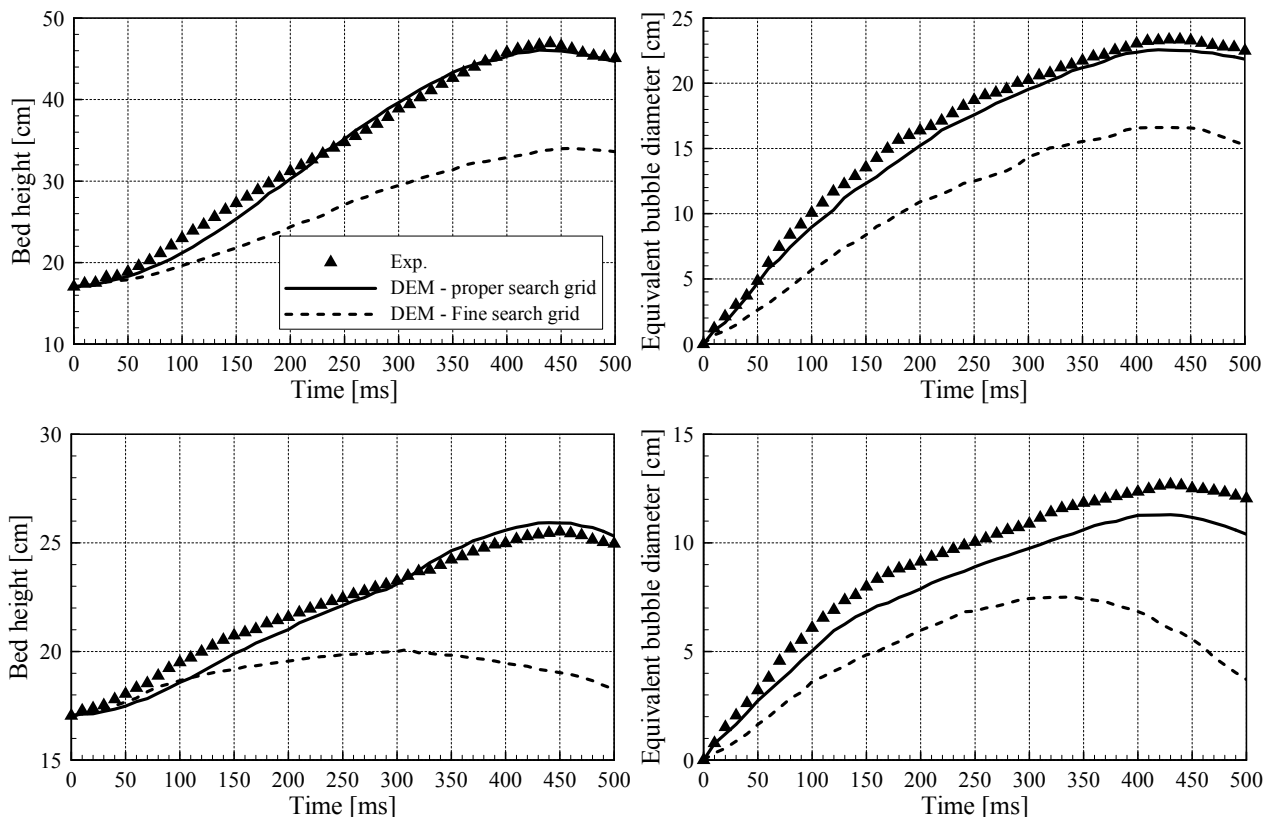


**Figure 8.28:** Comparison of bed expansion using proper search grid and fine search grid: (upper row) mass flow rate 0.006 kg/s and (lower row) mass flow rate 0.005 kg/s

The efficiency gain, resulting from using a fin search grid, is not discussed. This is due to the fact that the DEM model with a search grid size smaller than the particle diameter is incorrect from a physical point of view.

### 8.1.5 Parameter study

In the following sections, the efficiency and accuracy of the extended Euler–Lagrange/DEM model are analysed employing the DEMEST program. Different important parameters, namely stiffness coefficient, fluid time step and processor number are varied under the consideration of various solid loadings and particle diameters. For the validation study, the previously explained quasi-2D fluidized bed model is used (see section 8.1.1.1). Two different mass flow rates ( $0.006 \text{ kg/s}$  and  $0.005 \text{ kg/s}$ ) are investigated. For the efficiency study, a 3D fluidized bed model is constructed (Figure 8.29). The model has a height of 150 cm, a width of 15 cm, and a depth of 20 cm. The air is supplied through a centrally placed nozzle ( $1 \text{ cm (W)} \times 15 \text{ cm (D)}$ ), while the outlet is completely opened ( $15 \text{ cm (W)} \times 20 \text{ cm (D)}$ ). A block-structured fluid grid with number of nodes:  $64 \text{ (W)} \times 80 \text{ (D)} \times 640 \text{ (H)}$  is generated. Besides the fine fluid grid, three increasingly coarser multi-grids are built. In the first level coarse grid, the number of cells is reduced to 409600 (number of nodes:  $32 \text{ (W)} \times 40 \text{ (D)} \times 320 \text{ (H)}$ ). For the second and third level coarse grids, the numbers of cells are further decreased to 51200 with number of nodes:  $16 \text{ (W)} \times 20 \text{ (D)} \times 160 \text{ (H)}$  and 6400 with number of nodes:  $8 \text{ (W)} \times 10 \text{ (D)} \times 80 \text{ (H)}$ , respectively. The calculation of the particle phase is carried out on the particle grid with a resolution of 409600 cells (number of nodes:  $32 \text{ (W)} \times 40 \text{ (D)} \times 320 \text{ (H)}$ ). The deterministic detection of the particles collisions is performed on the particle search grid (number of nodes:  $40 \text{ (W)} \times 40 \text{ (D)} \times 200 \text{ (H)}$ , a total of 256000 cells. The monodisperse particles have the glass properties. The particle number is varied between  $10^0$ ,  $10^1$ ,  $10^2$ ,  $10^3$ ,  $10^4$ ,  $10^5$  and  $10^6$ . Furthermore, the particle diameter is changed between 3.5 mm, 2.5 mm, 1.5 mm and 0.5 mm. Depending on the solid loading, the mass flow used in the efficiency study varies in the range between  $0.01 \text{ kg/s}$  and  $0.5 \text{ kg/s}$ , so that the bubble flow regime is observed.

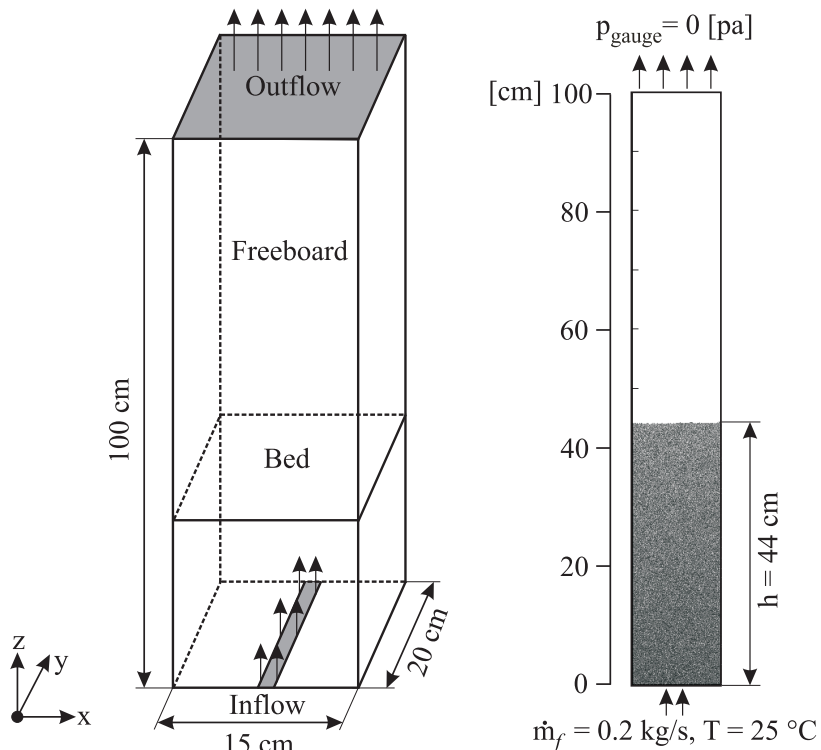


**Figure 8.29:** Numeric model used for efficiency study: (a) schematic diagram (only 100 cm presented), and (b) boundary and initial conditions, e.g. particle diameter (2.5 mm) and particle number ( $10^6$ )

### 8.1.5.1 Variation of stiffness coefficient

In **Table 8.1**, the normal and tangential stiffness coefficients are calculated for identical spherical particles with different diameters (0.5, 1.5, 2.5 and 3.5 mm) under the consideration of glass material properties. The determined stiffness coefficients exhibit high-orders of magnitude and vary in the range between  $10^8$  and  $10^9$  N/m depending on the diameter of collision partners.

**Table 8.1:** Calculation of realistic normal and tangential stiffness coefficients

Stiffness coefficients [N/m]	Particle diameters [mm]			
	0.5	1.5	2.5	3.5
$k^n$ (equation (5.35))	$5.5 \cdot 10^8$	$9.6 \cdot 10^8$	$1.2 \cdot 10^9$	$1.47 \cdot 10^9$
$k^t$ (equation (7.19))	$2.1 \cdot 10^9$	$3.7 \cdot 10^9$	$4.9 \cdot 10^9$	$5.8 \cdot 10^9$

If the stiffness coefficients are defined according to **Table 8.1** and the particle time step is calculated according to equation (7.17), the contact forces are then calculated with high accuracy (equations (5.33) and (5.41)). This means, the unphysical penetrations between the particles and the particles/walls are avoided. The application of realistic stiffness coefficients produces, however, a very small particle time step that is hardly applicable due to the extremely computational effort and the limited computer performance at present. Therefore, a reduction in the selected stiffness coefficient should be introduced. With decreasing the stiffness coefficient and hence increasing the particle time step, larger penetration depths can occur between the collision partners. At high relative velocity of collided particles, there is a risk to arise unrealistic penetrations. A complete penetration for the particle–wall collisions represents the worst case, since the particles leave the computational domain and accordingly are no longer available for the subsequent time steps. This leads to a continuous decline in the number of particles during the Euler–Lagrange/DEM simulations. In **Table 8.2**, the penetration depth is calculated depending on the stiffness coefficients for different diameters of collision partner and a maximum relative velocity of 10 m/s.

**Table 8.2:** Calculation of penetration depths for glass collision partners with different particle diameters (0.5, 1.5, 2.5 and 3.5 mm) and relative velocity of 10 m/s

Stiffness coefficients [N/m]	Penetration depths [mm]			
	$d_p = 0.5$ [mm]	$d_p = 1.5$ [mm]	$d_p = 2.5$ [mm]	$d_p = 3.5$ [mm]
$k^n = 10^2$	14	73	160	260
$k^n = 10^4$	1.4	7.3	16	26
$k^n = 10^6$	0.14	0.73	1.6	2.6
$k^n = 10^8$	0.014	0.07	0.16	0.26

By selecting smaller stiffness coefficients (for example  $10^3$  N/m), the normal penetration depth can reach up to 24 times the particle diameter. Previous numerical studies of the DEM model such as (Tsuji et al. 1992, Tsuji et al. 1993) could show that the variation of stiffness coefficient over several-orders of magnitude has only a minor influence on the results. Therefore, a stiffness coefficient of 800 N/m is recommended by Tsuji, which was used by several other authors. Di (Di Renzo and Di Maio 2004) have found that the proposed value of 800 N/m for the applied material properties and the simulation parameters causes a normal

penetration depth up to 74 times the particle diameter. The underestimating of the stiffness coefficients produces not only unphysical penetrations, but also leads in steady-state case to the shrinkage of the entire bed volume. In **Figure 8.30**, the bed height for 36500 spherical glass particles (monodisperse) with a diameter of 2.5 mm and different stiffness coefficients is presented. Compared to the experiment, a reduction in the stiffness coefficient by four-orders of magnitude (from  $10^2$  to  $10^6$  N/m) results in a dwindling of the entire bed volume with about 10%.

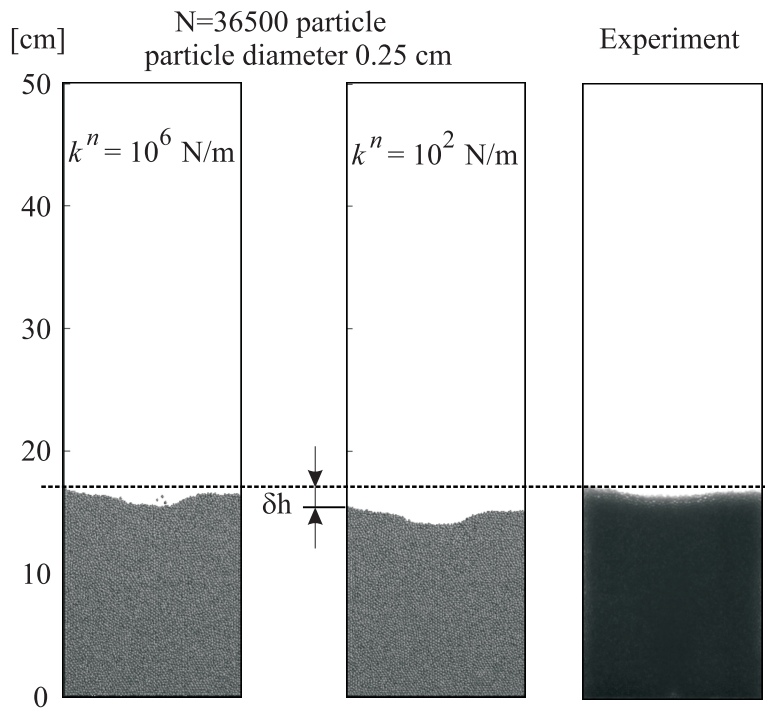


**Figure 8.30:** Comparison of bed heights at different stiffness coefficients towards the measurement (Alobaid, Baraki and Epple 2013a)

In order to obtain the minimal normal stiffness coefficient that prevents the unphysical penetration, an extra condition should be defined. A penetration depth is unrealistic if the maximum penetration depth is greater than the particle radius ( $\delta_{\max}^n > r_p$ ). In **Table 8.3**, the minimal normal stiffness coefficients are calculated at different particle diameters, diverse relative velocity of collision partners and a maximum penetration depth ( $\delta_{\max}^n = r_p$ ). Independent of the particle diameter, the resulted minimal stiffness coefficient values have a range between  $5 \cdot 10^4$  N/m and  $5 \cdot 10^6$  N/m and depend mainly on the relative velocity of collision partners.

**Table 8.3:** Calculation of minimum normal stiffness coefficients at different particle diameters (0.5, 1.5, 2.5 and 3.5 mm), relative velocities (10, 5 and 2 m/s) and maximum penetration depth  $\delta_{\max}^n = r_p$

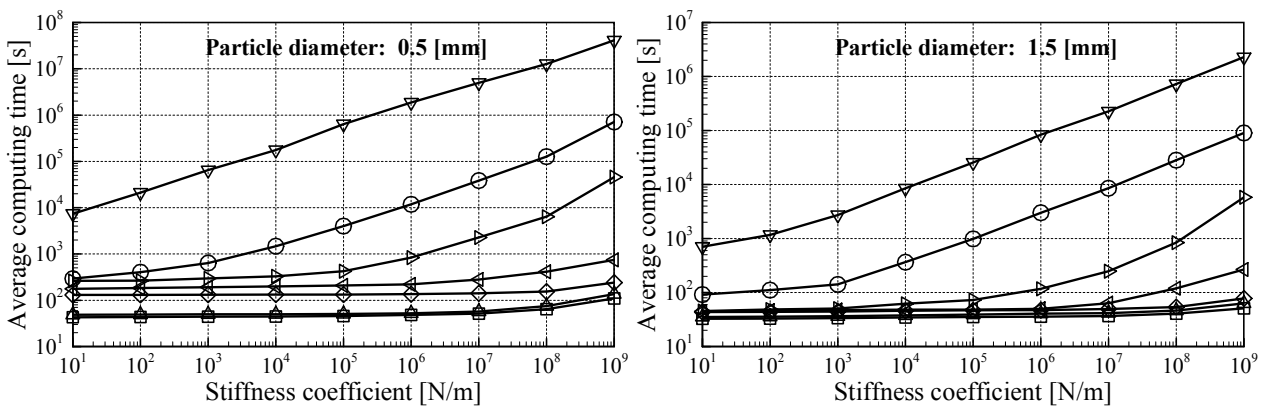
Stiffness coefficients [N/m]	Particle diameters [mm]			
	0.5	1.5	2.5	3.5
$k^n$ (equation (7.20)) ( $u_{\max}^n = 10$ m/s)	$5.1 \cdot 10^6$	$5.1 \cdot 10^6$	$5.1 \cdot 10^6$	$5.1 \cdot 10^6$
$k^n$ (equation (7.20)) ( $u_{\max}^n = 5$ m/s)	$6.3 \cdot 10^5$	$6.3 \cdot 10^5$	$6.3 \cdot 10^5$	$6.3 \cdot 10^5$
$k^n$ (equation (7.20)) ( $u_{\max}^n = 2$ m/s)	$4.1 \cdot 10^4$	$4.1 \cdot 10^4$	$4.1 \cdot 10^4$	$4.1 \cdot 10^4$

In this section, a great attention is paid to the influence of the stiffness coefficient variation on the computation time at different particle numbers and diverse particle diameters (see **Table 8.4**).

**Table 8.4:** Simulation parameters for the stiffness coefficient variation

Variable parameters	stiffness coefficients [N/m]	$10^1, 10^2, 10^3, 10^4, 10^5, 10^6, 10^7, 10^8, 10^9$
	particle numbers	$10^0, 10^1, 10^2, 10^3, 10^4, 10^5, 10^6$
	particle diameters [mm]	0.5, 1.5, 2.5, 3.5
Fixed parameters	fluid time step [ms]	2
	number of calculation steps	10
	number of decompositions	9
Grids	fluid multi-grid	activated
	particle grid	activated

For the first simulation series, the number of particles is set constant equal to  $10^0$  at different particle diameters, while the stiffness coefficient is varied from  $10^1$  to  $10^9$  N/m. The number of particles is changed to  $10^1$  and the entire simulations are repeated again and so on. For each case, ten steps are simulated. The average computing time per time step is then determined through the division of the entire simulation time by the number of calculation steps. Here, it should be mentioned that the multi-grid, particle grid and offset methods are considered in the simulations. In **Figure 8.31**, the effect of the stiffness coefficient variation on the average computing time per time step at different particle numbers ( $10^0, 10^1, 10^2, 10^3, 10^4, 10^5, 10^6$ ) and different particle diameters (0.5, 1.5, 2.5 and 3.5 mm) are illustrated. It can be seen that an increase in the stiffness coefficient values leads to an exponential rise in the average computing time. This is evident from the order of magnitude  $10^3$  N/m, where a jump in the stiffness coefficient by two-orders of magnitude results in an increase in the simulation time by one-order of magnitude. The flattening of the curves at the stiffness coefficient values below  $10^3$  N/m is caused due to the fact that a certain part of the computing time is required for the calculation of the fluid phase. For stiffness coefficients with high-orders of magnitude, this part is not significant in percentage terms; however, it takes at very low stiffness coefficients into account.



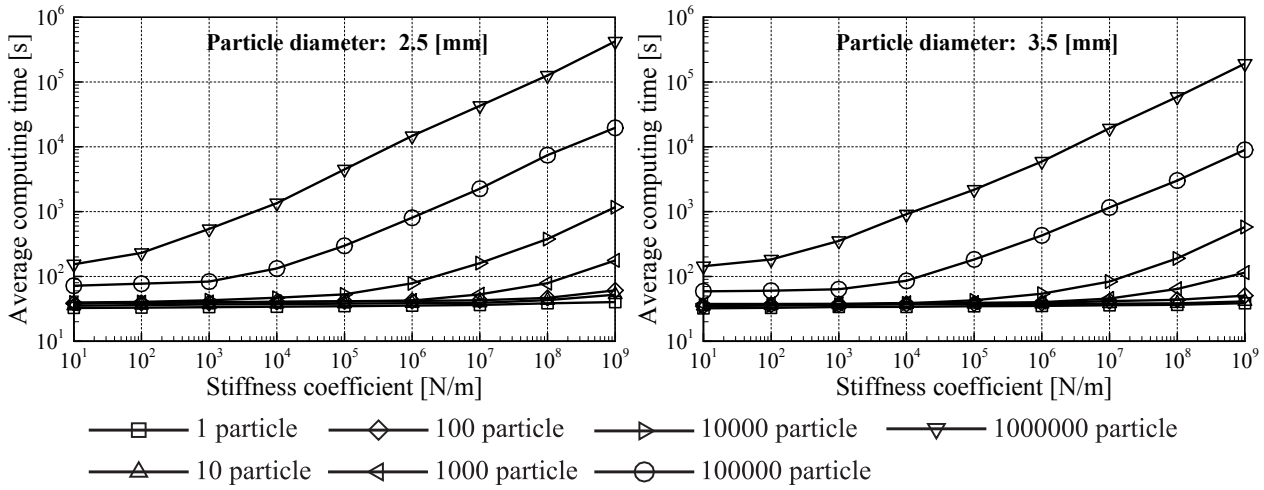


**Figure 8.31:** Influence of stiffness coefficient variation on the average computing time per time step at different particle diameters and various particle numbers (a)

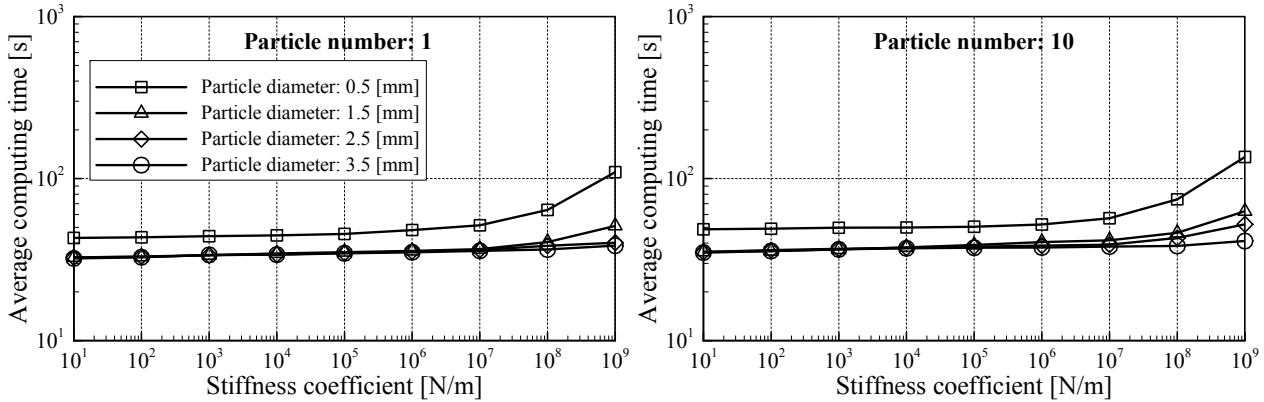
Furthermore, it can be detected that the particle diameter has a relevant influence on the average computation time. The reason of this is that the size of the particle time step is a function of the particle diameter and thus smaller particle diameters lead to finer particle time steps for an identical stiffness coefficient value.

From the logarithmic plots, a power function can be obtained for the average computing time  $T$  and the stiffness coefficient as:

$$T = A\sqrt{k^n} \approx (k^n)^{1/2}, \quad (8.6)$$

where the symbol  $A$  represents the slope of the curve.

In order to understand explicitly the influence of the particle diameter on the average computing time per time step, the previous obtained results are replotted again (see **Figure 8.32**). For various particle numbers, the stiffness coefficient is varied from \$10^1\$ to \$10^9\$ N/m at different particle diameters (0.5, 1.5, 2.5 and 3.5 mm). The obtained curves behave almost the same, whereas the average computation time rises exponentially with increasing the stiffness coefficient. As it is expected, the average computing time escalates considerably for higher solid loadings. This can be explained by the application of the DEM model, where the computational effort depends on the particle number and the particle time step. For an identical stiffness coefficient as well as a constant particle diameter, the particle time step remains unaltered. With increasing the solid loading, the number of equations to be solved is raised and consequently the simulation time increases.



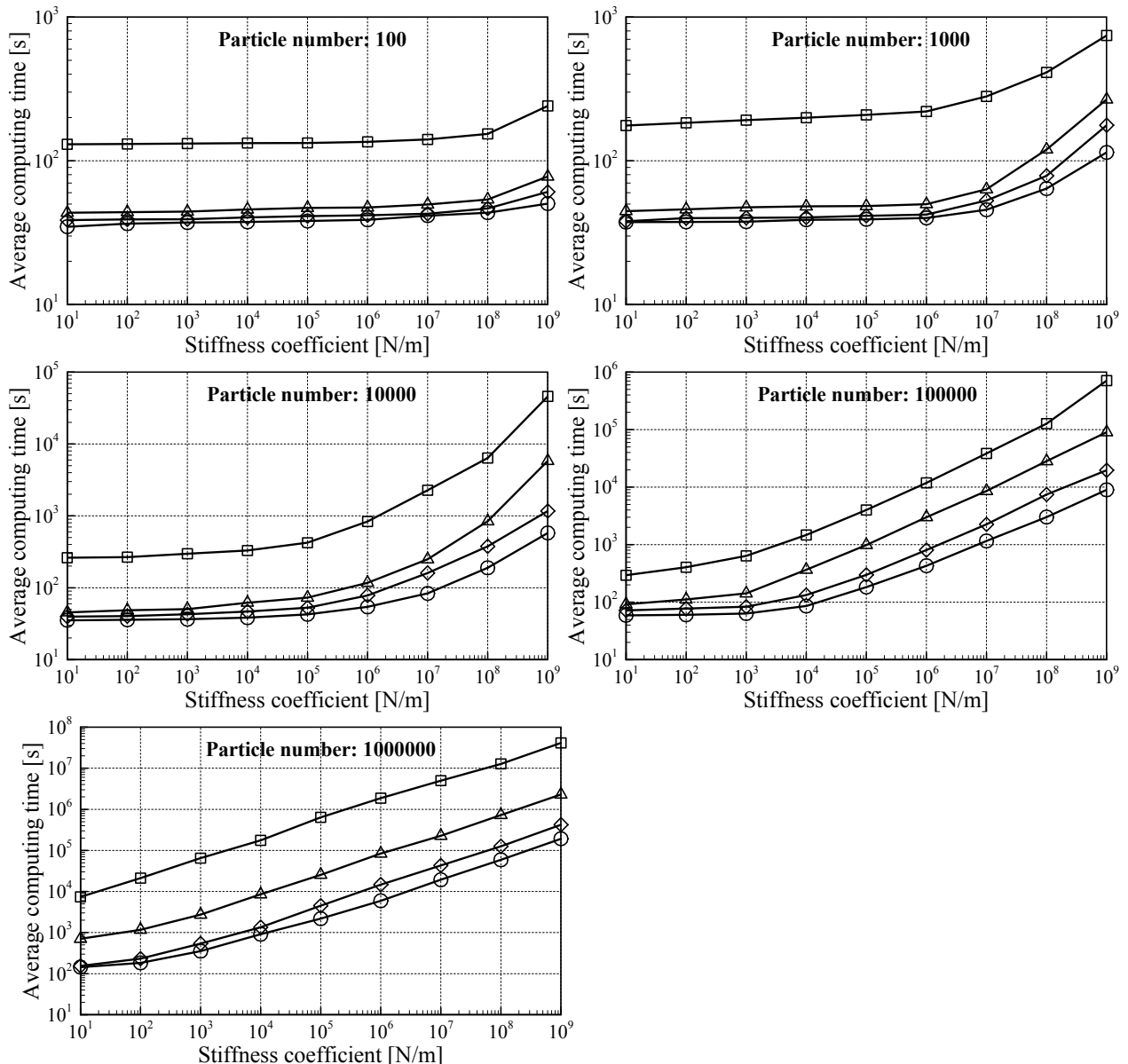


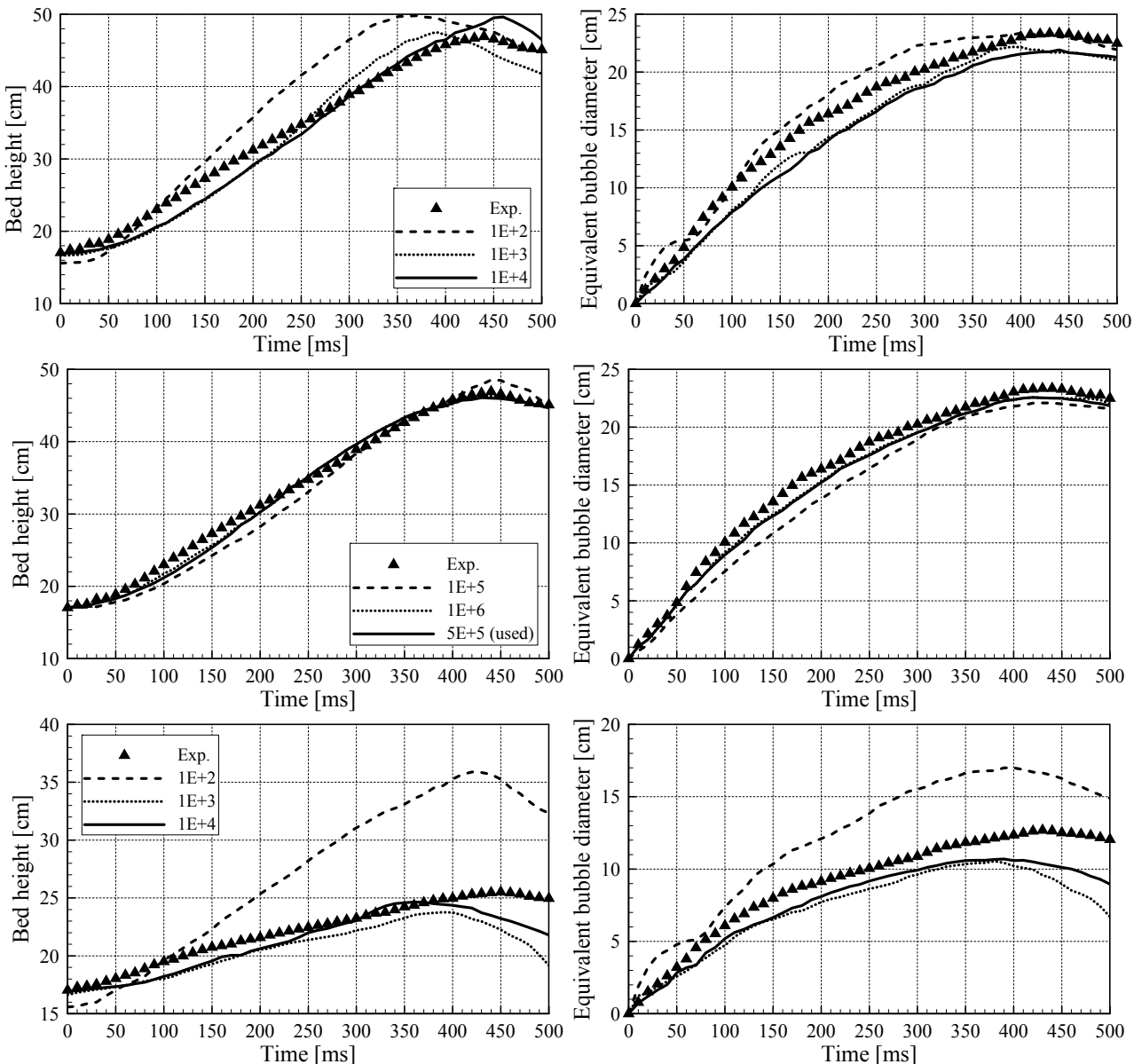
**Figure 8.32:** Influence of stiffness coefficient variation on the average computing time per time step at different particle diameters and various particle numbers (b)

Contrary to expectations, the particle diameter plays a crucially important role concerning the computational effort. The computing time per time step increases sharply with decreasing the particle diameter. At constant particle diameter (for example  $10^6$ ), a reduction in the particle diameter from 3.5 mm to 0.5 mm results in an increase in the simulation time by two-order of magnitude.

To investigate the influence of the stiffness coefficient variation on the simulation accuracy, the numerical model of a quasi-2D fluidized bed is simulated and the obtained results are compared with the measured data. For the simulation, 36500 identical glass particles with a diameter of 2.5 mm are used. The fluid time step is selected equal to 2 ms, while the remained numerical parameters are obtained from **Table 10.2**. The fluid and particle grid resolutions of the numerical model are presented in the section (8.1.1.1). Here it should be mentioned that the simulation parameters, the applied boundary conditions and the grid resolutions are identical for all simulation cases.

In **Figure 8.33**, the simulated bed heights at different stiffness coefficients are compared with the experiments over time (500 ms). The application of stiffness coefficients with low-orders of magnitude has the benefit of a low computational effort; however the accuracy of the Euler–Lagrange/DEM model declines. This can be clearly detected in case of applying stiffness coefficients with values of  $10^2$  and  $10^3$  N/m. Here, the simulated bed heights at mass flow rate 0.006 kg/s and 0.005 kg/s deviate from the measured data with maximum relative errors of 20% and 45%, respectively. On the other hand, stiffness coefficients with high-order of magnitude are related to an extreme computation time, but they result in a high simulation accuracy. Moderate stiffness coefficients in the range between  $5 \cdot 10^4$  and  $5 \cdot 10^6$  N/m show a very good compromise between an acceptable computing time and a good accuracy.

Although the application of stiffness coefficients with moderate values causes normal penetration depths up to the particle radius (see **Table 8.2**), they still show good final results. So they are recommended to apply for the simulation of the fluidized bed especially since the maximum relative velocities of collision partners in this system are smaller than 10 m/s.



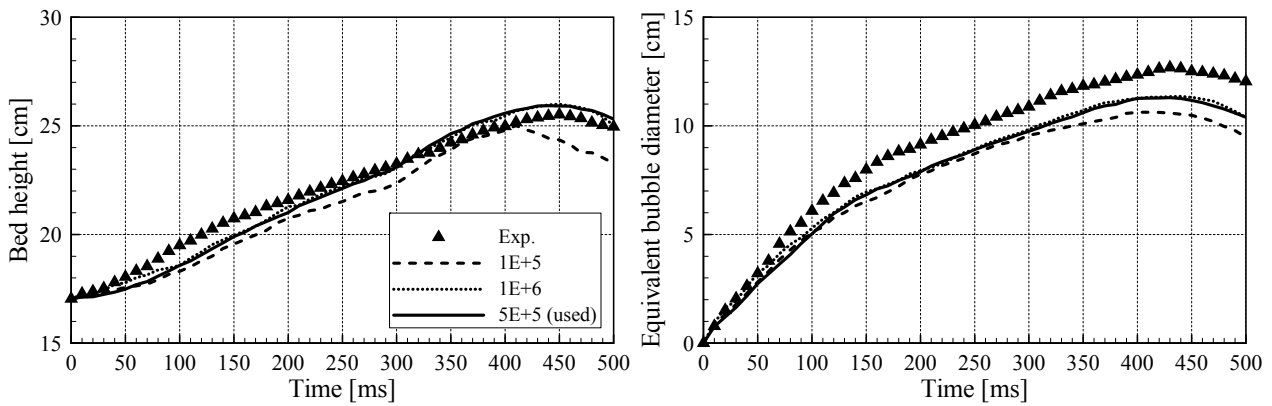


**Figure 8.33:** Influence of stiffness coefficient variation on the simulation accuracy of Euler–Lagrange/DEM model (number of particles is 36500 and the particle diameter is 2.5 mm): (first and second rows) mass flow rate 0.006 kg/s and (third and fourth rows) mass flow rate 0.005 kg/s

### 8.1.5.2 Variation of fluid time step

As previously mentioned in the section 7.2 the fluid time step can be selected arbitrarily and is set constant during the simulation. Generally, the fluid time step is chosen large and accordingly consists of several particle time steps. The size of the particle time step depends directly on the applied stiffness coefficient. In **Table 8.5**, the particle time steps are determined at different stiffness coefficients and particle diameters. It can be seen that the calculated particle time step decreases with increasing the stiffness coefficient and reducing the particle diameter. Independent of the particle diameter, an increase in the stiffness coefficient by four-orders of magnitude leads to a decrease in the particle time step of 100 times. At constant stiffness coefficient, a reduction in the particle diameter from 3.5 mm to 0.5 mm results in a decrease in the particle time step of 26 times.

**Table 8.5:** Calculation of particle time step for glass collision partners at different particle diameters (0.5, 1.5, 2.5 and 3.5 mm)

Stiffness coefficients [N/m]	Particle time steps [s]			
	$d_p = 0.5$ [mm]	$d_p = 1.5$ [mm]	$d_p = 2.5$ [mm]	$d_p = 3.5$ [mm]
$k^n = 10^2$	$0.1 \cdot 10^{-2}$	$0.7 \cdot 10^{-2}$	$1.5 \cdot 10^{-2}$	$2.6 \cdot 10^{-2}$
$k^n = 10^4$	$0.1 \cdot 10^{-3}$	$0.7 \cdot 10^{-3}$	$1.5 \cdot 10^{-3}$	$2.6 \cdot 10^{-3}$
$k^n = 10^6$	$0.1 \cdot 10^{-4}$	$0.7 \cdot 10^{-4}$	$1.5 \cdot 10^{-4}$	$2.6 \cdot 10^{-4}$
$k^n = 10^8$	$0.1 \cdot 10^{-5}$	$0.7 \cdot 10^{-5}$	$1.5 \cdot 10^{-5}$	$2.6 \cdot 10^{-5}$

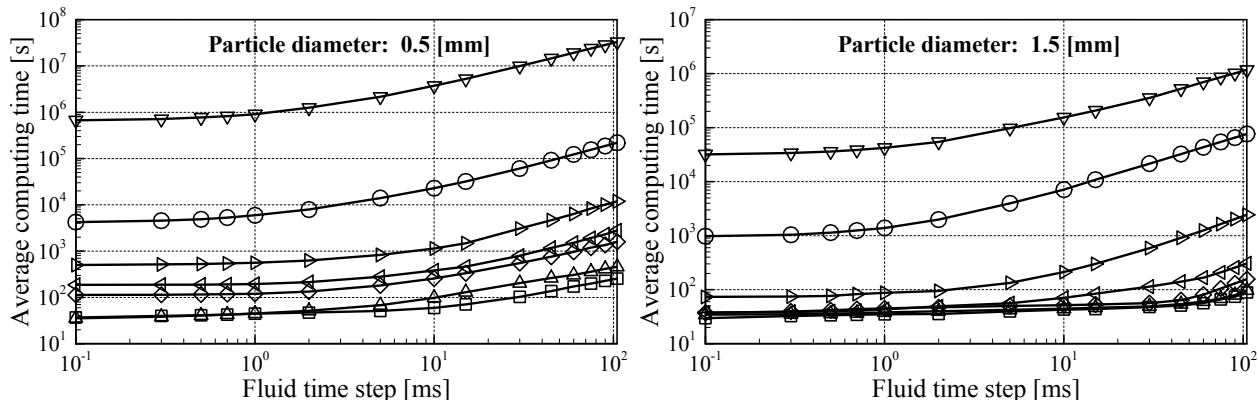
In this section, the influence of the fluid time step variation on the computational time is investigated. Here, the stiffness coefficient is set constant equal to  $5 \cdot 10^5$  N/m, which represents a compromise between a realistic simulation result and an acceptable simulation time. While the resulted particle time step is constant depending on the particle diameter and the stiffness coefficient used, the fluid time step size is varied in the range between 0.1 and 105 ms. The effect of the particle diameter and the particle number variation on the average computing time is also examined. The detailed simulation parameters for the following series of simulations can be found in **Table 8.6**. In these simulations, the calculation of the fluid phase is carried out using the fluid multi-grid method, while the particle phase is computed employing the particle grid method. Furthermore, the determination of the interaction values is based on the offset

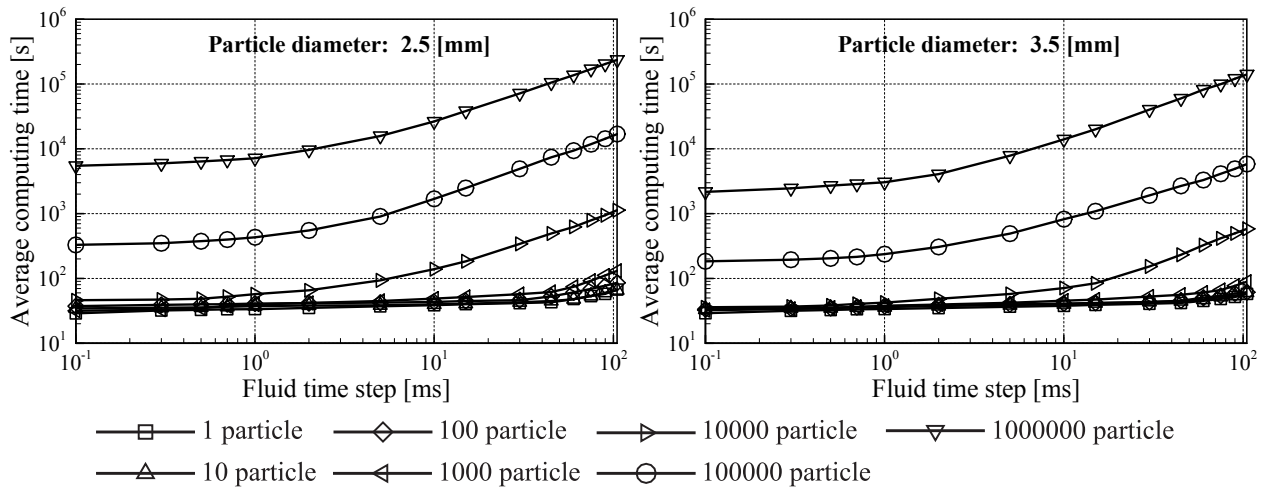
method that is introduced in section 8.1.2. For each fluid time step, ten steps are simulated and the average computing time per time step is then determined through the division of total simulation time by number of calculation steps.

**Table 8.6:** Simulation parameters for the fluid time step variation

Variable parameters	fluid time steps [ms]	0.1, 0.3, 0.5, 1, 2, 5, 10, 15, 30, 45, 60, 75, 90, 105
	particle numbers	$10^0, 10^1, 10^2, 10^3, 10^4, 10^5, 10^6$
	particle diameters [mm]	0.5, 1.5, 2.5, 3.5
Fixed parameters	number of calculation steps	10
	stiffness coefficient [N/m]	$5 \cdot 10^5$
	number of decompositions	9
Grids	fluid multi-grid	activated
	particle grid	activated

In **Figure 8.34**, the effect of the fluid time step variation on the average computing time per time step at different particle numbers ( $10^0, 10^1, 10^2, 10^3, 10^4, 10^5, 10^6$ ) and different particle diameters (0.5, 1.5, 2.5 and 3.5 mm) are displayed. It is assumed that for identical simulation duration, an increase in the size of the fluid time step accelerates the simulation. **Figure 8.34** shows that this relationship is not necessarily correct. An enlargement of the fluid time step in the range between 10 and 105 ms does not accelerate the Euler–Lagrange/DEM calculation, i.e. leads to increase in the average computing time per time step. This is due to the fact that the ratio of the fluid time step to the particle time step is bigger than one. This means, during one fluid time step several particle time steps must be carried out. The number of particle time steps depends on the stiffness coefficient and the particle diameter used as well as on the size of the fluid time step. Subsequently, the computation time to calculate the particle phase has a significantly larger proportion of the total simulation time than the computational effort of the fluid phase. From the curves illustrated in **Figure 8.34**, it can be supposed that fluid time steps smaller than 10 ms could not cause any substantial increase in the computational time. Finer fluid time step sizes produce more accurate simulation results, which is aimed by practical applications. An excessive reduction of the fluid time step leads, however, to a considerable increase in the computational effort. It raises the question, at which ratio of fluid to particle time step, a reduction in the size of fluid time step will not cause a significant increase in computational time. By decreasing the fluid time step till the size of particle time step, the independent correlation between the fluid time step and the computational time is not any more valid.

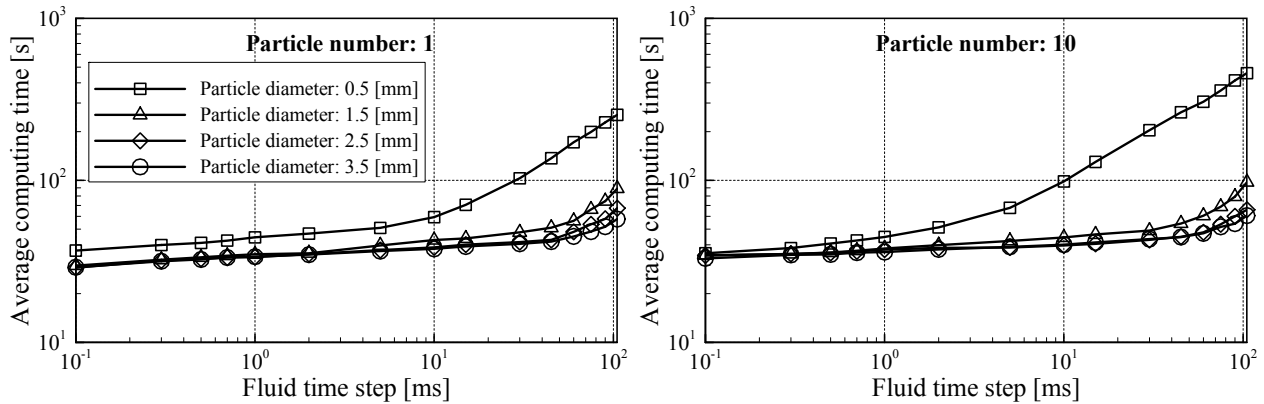


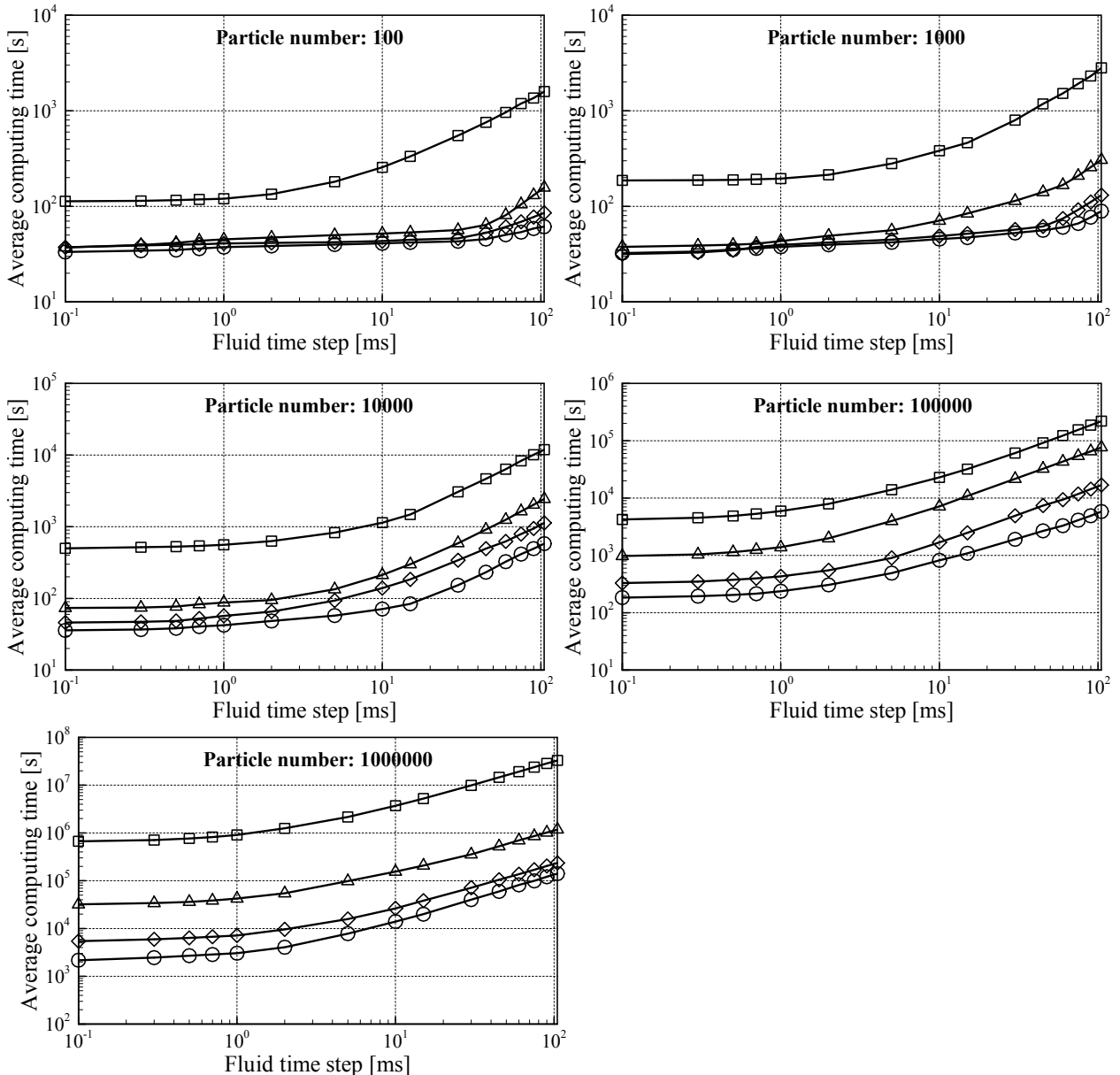


**Figure 8.34:** Influence of fluid time step variation on the average computing time per time step at different particle diameters and various particle numbers (a)

It can be observed in **Figure 8.34** that the particle numbers have a major impact on the computational time. At constant fluid time step, the computational effort is substantially raised by increasing the solid loading. This can easily explained by the reason of the DEM model used. Here, each particle has a set of equations to be solved. Furthermore, the computational effort of collision detection is correlated with the number of investigated particles. At defined particle diameter, an increase in the particle numbers from  $10^5$  to  $10^6$  causes a jump in the simulation time by one-order of magnitude. The obtained results show that the average computing time depends highly on the particle diameter. This is due to the fact that the variation of the particle diameter has a relevant influence on the determined size of the particle time step.

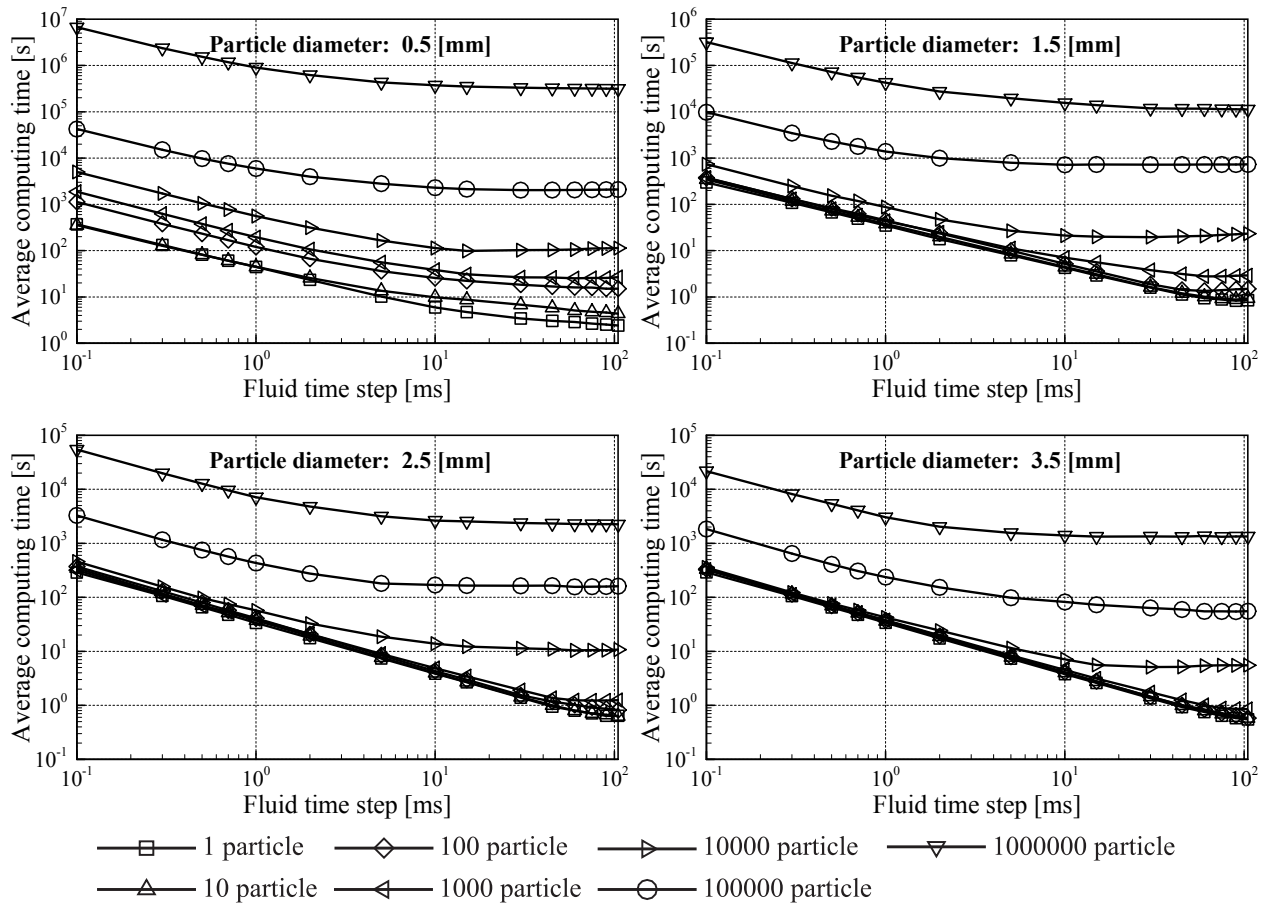
To understand the effect of the particle diameter on the average computing time per time step, the previous obtained results are replotted again (see **Figure 8.35**). For different particle numbers ( $10^0, 10^1, 10^2, 10^3, 10^4, 10^5, 10^6$ ), the fluid time step is varied from 0.1 to 105 ms at various particle diameters (0.5, 1.5, 2.5 and 3.5 mm). At constant particle number, the average computational time rises considerably with decreasing the particle diameter. This significant increase in the computing time results from the decreasing in the particle time step that is a function of the stiffness coefficient and the particle diameter. Since the stiffness coefficient is set constant equal to ( $5 \cdot 10^5$  N/m) in these series of simulations, the particle time step is then related to the particle diameter (see **Table 8.5**). At lower particle numbers ( $10^0, 10^1, 10^2, 10^3$  and  $10^4$ ), the flattening in curves is caused due to the fact that a part of the computing time is required for the calculation of the fluid phase. This part is negligible small for higher numbers of particles ( $10^5$  and  $10^6$ ), but it takes at low particle numbers into account.





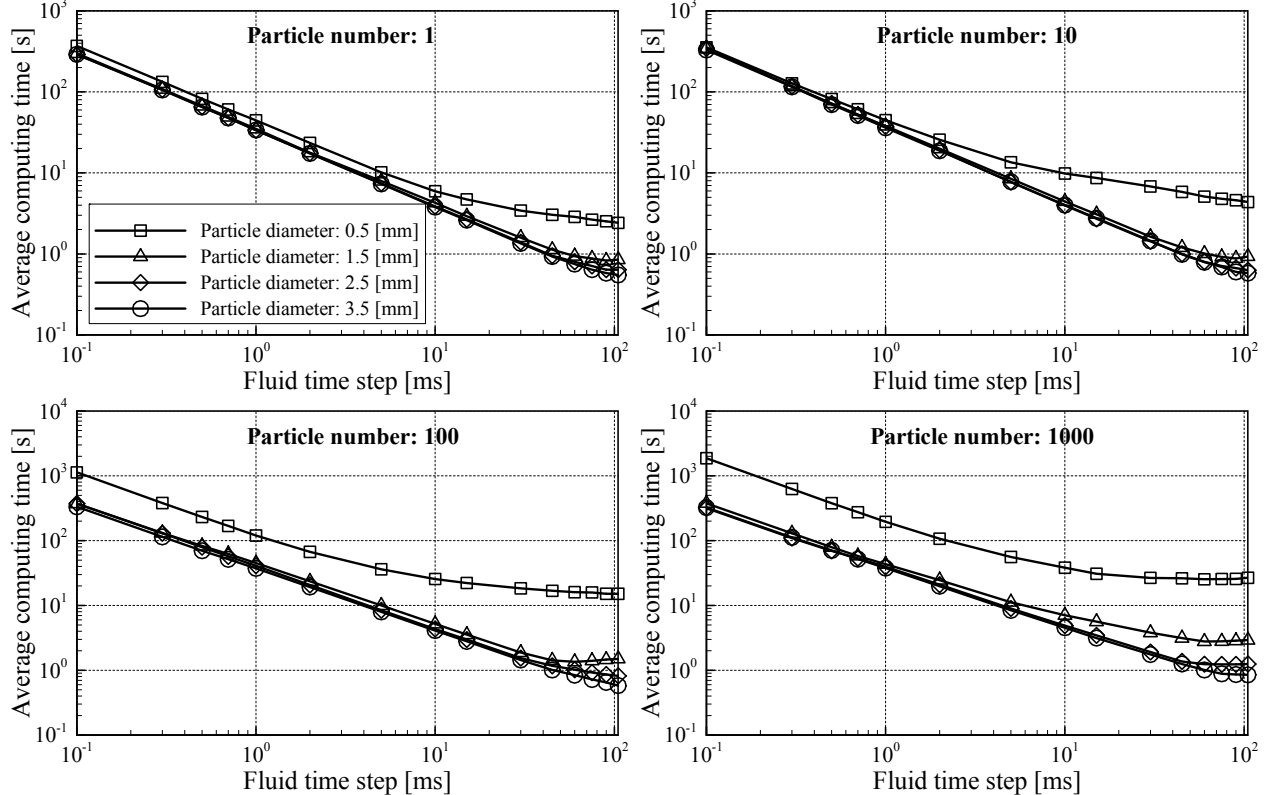
**Figure 8.35:** Influence of fluid time step variation on the average computing time per time step at different particle diameters and various particle numbers (b)

The consideration of the average computing time as a function of the fluid time step is not informative in terms of the efficiency analyse. Therefore, the computation time per simulated millisecond is displayed in **Figure 8.36** at different solid loadings ( $10^0$ ,  $10^1$ ,  $10^2$ ,  $10^3$ ,  $10^4$ ,  $10^5$ ,  $10^6$ ) and various particle diameters (0.5, 1.5, 2.5 and 3.5 mm). For large fluid time steps, the average computing time per one millisecond is remained almost constant depending on the particle number and the particle diameter. At particle diameter 1.5 mm for example, the average computing time per one millisecond is about 1000 and 10000 s for particle numbers  $10^5$  and  $10^6$ , respectively. An exponential increase in the average computing time per simulated millisecond is appeared when finer fluid time steps are applied. From **Figure 8.36**, a fluid time step of about 5 ms ensuring the efficiency of simulations can be extracted. A further increase in the size of the fluid time step more than 5 ms is not correlated with any efficiency gain; but the fluid phase is resolved temporally from bad to worse. A reduction in the fluid time step less than 5 ms in order to achieve higher temporal resolutions leads to a significant loss in the efficiency, since the computing time per simulated millisecond increases exponentially. The variation of particle numbers has almost no influence on the efficient size of the fluid time step.



**Figure 8.36:** Influence of fluid time step variation on the average computing time per one millisecond at different solid loadings and various particle diameters (a)

The previous obtained results are replotted again (see Figure 8.37).



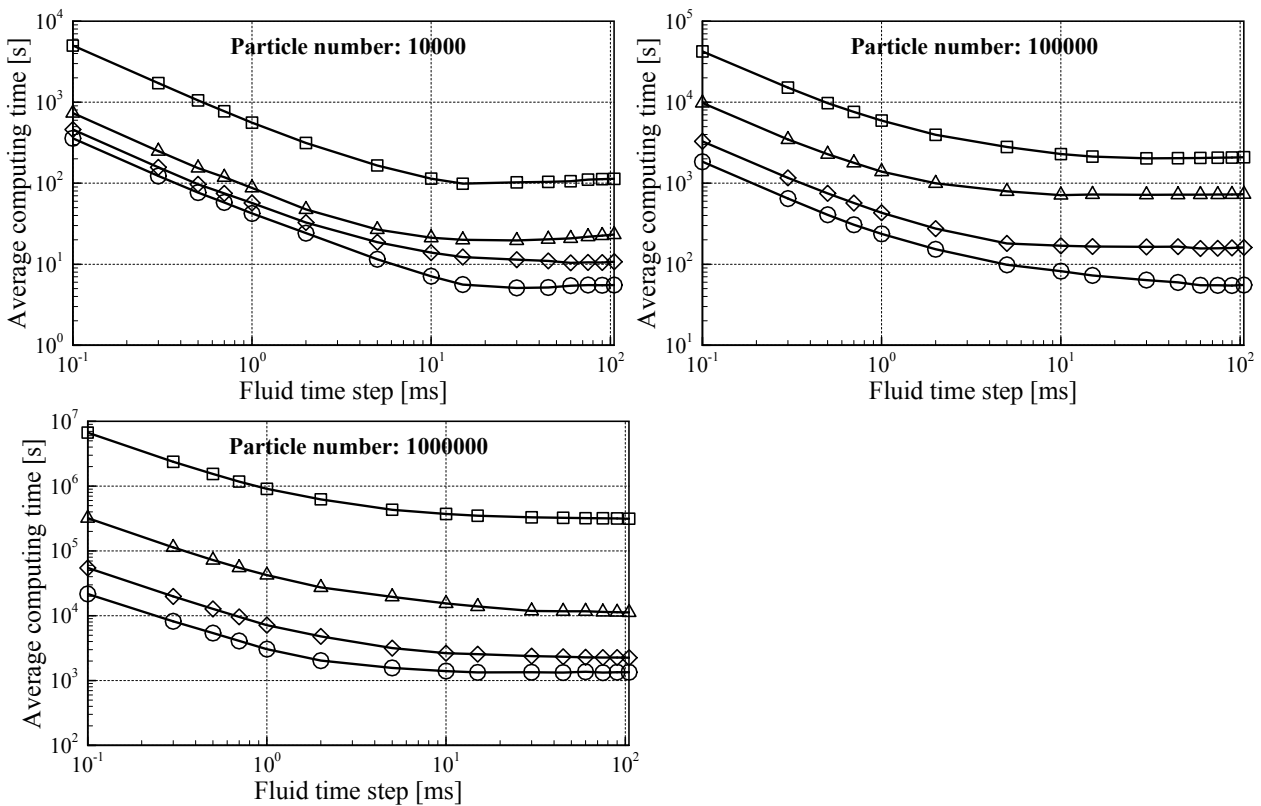


**Figure 8.37:** Influence of fluid time step variation on the average computing time per one millisecond at different solid loadings and various particle diameters (b)

From the received results, an efficient fluid time step in the range between 1 and 5 ms can be selected. In order to estimate the effect of the fluid time step variation on the Euler–Lagrange/DEM model accuracy, a numerical model of a quasi–2D fluidized bed with 36500 identical glass particles (diameter: 2.5 mm) is simulated. While the fluid time step is varied, other simulation parameters remain unaltered (see Table 10.2). The fluid and particle grids resolutions are identical for all simulation cases. In Figure 8.38, the simulated bed height and the bubble size are compared with the experiments over time (500 ms). At finer fluid time steps below 5 ms, a very good agreement between the simulated bed expansion and the experimental observed bed height and area can be detected regarding the mass flow rate 0.006 kg/s. A close comparison between the simulated bed height as well as the equivalent bubble diameter at fluid time step 0.5 ms and 2 ms shows almost exact characteristic. This suggests that a further decrease in the fluid time step below 0.5 ms will not result in an improvement in the Euler–Lagrange/DEM model accuracy. At this point, the discrepancy with measurements is related to other factors (see section 8.1.1.2). At fluid time step 10 ms, the bed starts expanding about 200 ms later compared to the model with 2 ms fluid time step. For coarser fluid time steps, the bed did not move and remains almost unchanged. The bed expansion at the mass flow rate 0.005 kg/s indicates similar behaviour to the mass flow rate 0.006 kg/s. At fluid time step 5 ms, the bed height exceeds the measurement with a relative error of 13%. A large deviation in the bed height and the bubble size can be observed again for fluid time steps bigger than 5 ms.

On the basis of above discussion together with the comparison illustrated in Figure 8.38, it can be concluded that the application of larger fluid time steps (more than 10 ms) displays a negative impact on the Euler–Lagrange/DEM results, although the computational effort remains unaltered. On the other hand, finer fluid time steps (less than 1 ms) lead to a negligible improvement in the Euler–Lagrange/DEM accuracy, but to considerable increase in the computing time. Fluid time steps in range between 1 and 5 ms show a reasonable compromise between the required accuracy and simulation efficiency. So

they are recommended to apply for the simulation of the fluidized bed independent of the solid loading and the particle diameter.

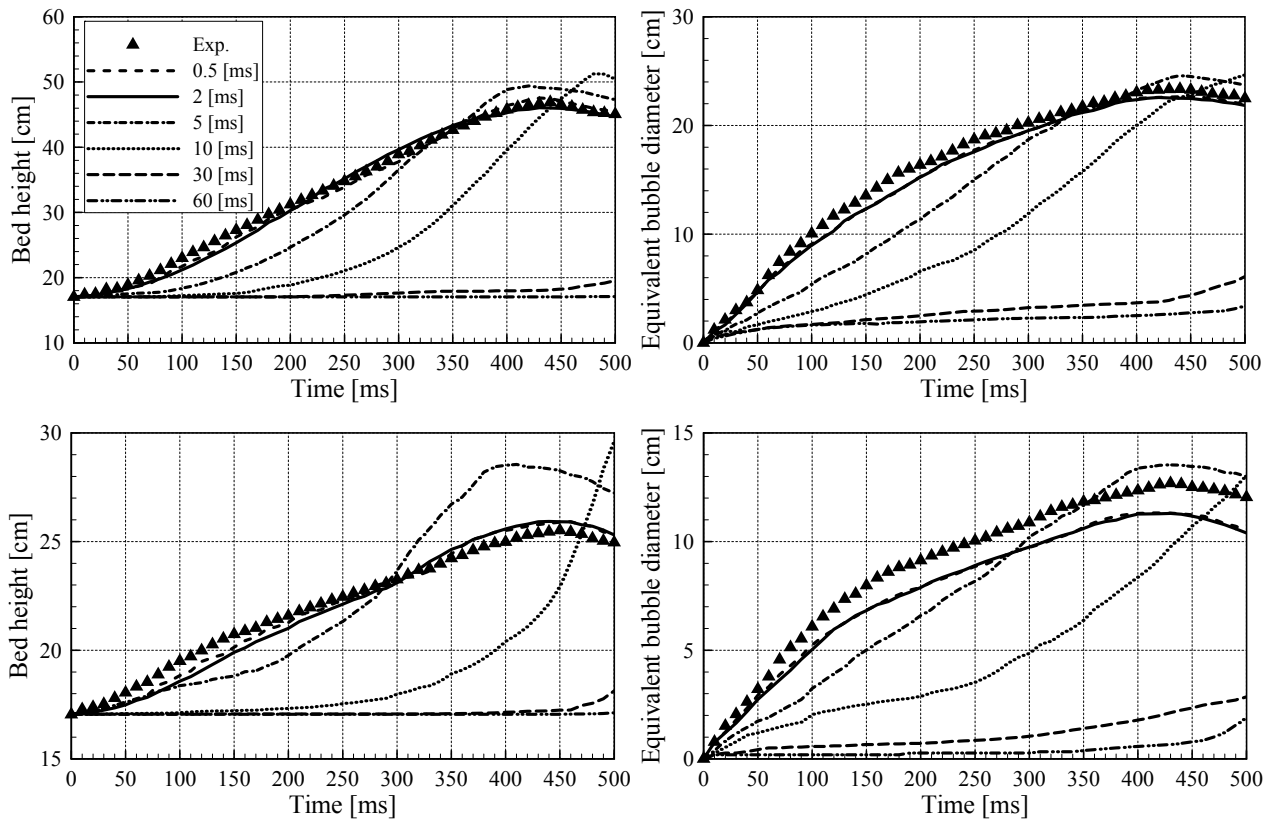


**Figure 8.38:** Influence of fluid time step variation on the simulation accuracy of Euler–Lagrange/DEM model (number of the particles is 36500 and the particle diameter is 2.5 mm): (upper row) mass flow rate 0.006 kg/s and (lower row) mass flow rate 0.005 kg/s

### 8.1.5.3 Variation of processor number

The parallel computation on multi–core processors is of great importance and presents today the most promising way to accelerate the calculation of the Euler–Lagrange/DEM model. Therefore, the influence of parallelisation on the average computing time is investigated. The entire computational domain is divided into several decompositions (1 to 51), where each sub–block is allocated by one processor. As a second variable, the number of particles is modified. Furthermore, the particle diameter is also varied from 0.5 mm to 3.5 mm (see **Table 8.7**).

**Table 8.7:** Simulation parameters for the processor number variation

Variable parameters	number of processor	1, 3, 5, 7, 9, 15, 21, 27, 33, 39, 45, 51
	particle numbers	$10^0, 10^1, 10^2, 10^3, 10^4, 10^5, 10^6$
	particle diameters [mm]	0.5, 1.5, 2.5, 3.5
Fixed parameters	fluid time step	2 ms
	number of calculation steps	10
	stiffness coefficient [N/m]	$5 \cdot 10^5$
Grids	fluid multi–grid	activated
	particle grid	activated

For each simulation case, ten steps are calculated. Through the division of the entire simulation time by the number of calculation steps, the average computing time per time step is then determined. The multi-grid, particle grid and offset methods are considered in the simulations. The stiffness coefficient and the fluid time step are set equal to  $5 \cdot 10^5$  N/m and 2 ms, respectively. Other simulation parameters can be found in **Table 10.2**.

In **Figure 8.39**, the variation of processor number for different solid loadings is plotted against the average computing time. The parallelisation results first in an acceleration of the simulation due to the fact that each processor requires less computing time by the reason of smaller computational sub-domains. By increasing the number of CPUs, the interaction between the processors is raised and thus the performance is not anymore proportional to the number of processors. Besides the additional computational effort for the data exchange, the asynchronism between the processor cores plays an important role why the parallelised calculations run inefficiently. In this context, asynchrony means that the processors utilizations are uneven. This can occur by an undesired distribution of particles in the computational sub-domains. Accordingly, the processors that are subjected to less processing operations finish earlier their calculations and finally have to wait until other processors complete their calculations. The range, in which the average computation time does not further decrease and remains at a nearly constant level, extends over several processors (15 to 33). Further decomposition of the computational domain (more than 33) leads to an increase in the computing time. Hence, the acceleration of the simulation can be achieved by relative lower numbers of processors.

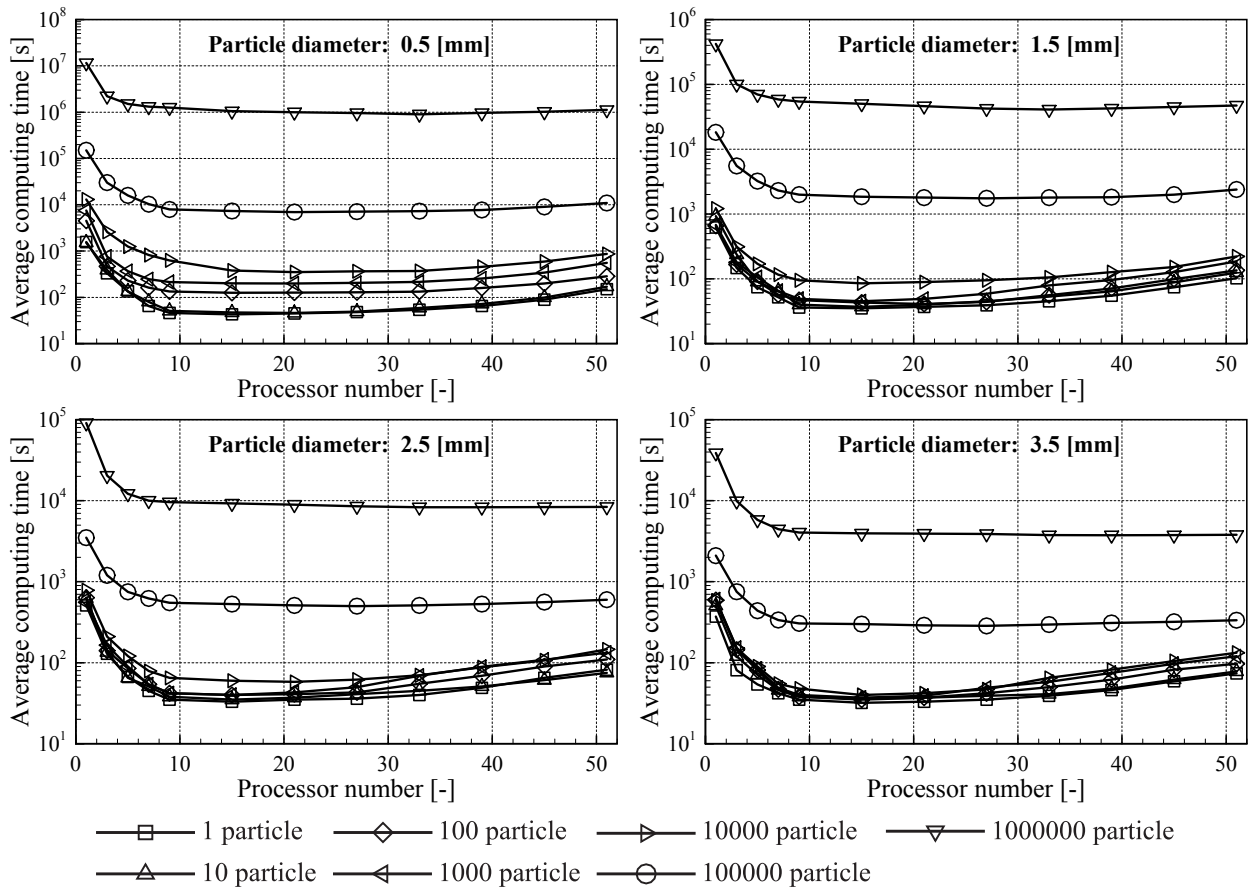
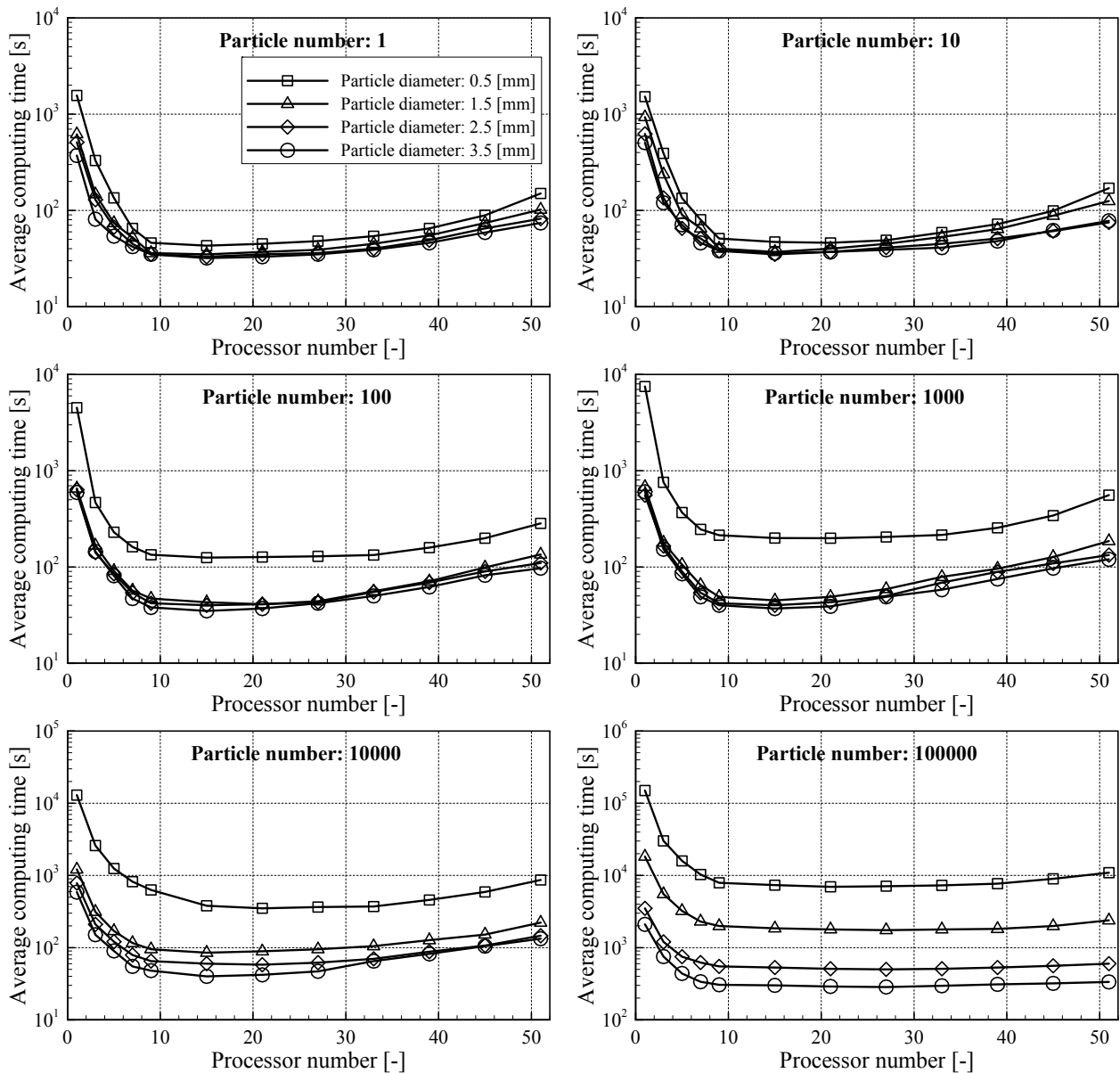


**Figure 8.39:** Influence of processor number variation on the average computing time per time step at different solid loadings and various particle diameters (a)

To investigate the influence of processor number variation on the average computing time per time step, the previous obtained results are replotted again (**Figure 8.40**). For

different particle diameters (0.5, 1.5, 2.5 and 3.5 mm) and various particle numbers ( $10^0, 10^1, 10^2, 10^3, 10^4, 10^5$  and  $10^6$ ), the processor numbers is varied from 1 to 51. It can be clearly detected that higher solid loadings cause an exponential rise in the calculation time. The critical number of the domain decomposition depends on the particle number. An increase in the solid loading from  $10^3$  to  $10^6$  results in a shift of the critical number of the processor from 21 to 39. The particle diameter has a limited effect on the critical number of processor. At constant particle number, a reduction in the particle diameter leads, however, to faster increase in the computing time after reaching the critical number of processor. Furthermore, the critical number of the domain decomposition moves to higher processor numbers when the particle diameter increases.

It is obvious from **Figure 8.39** and **Figure 8.40** that an increase in the processor number from 1 to 9 results in a decrease in the simulation time by one-order of magnitude. Furthermore, an increase in the solid loading improves the number of processors used before reaching the critical number of CPUs.



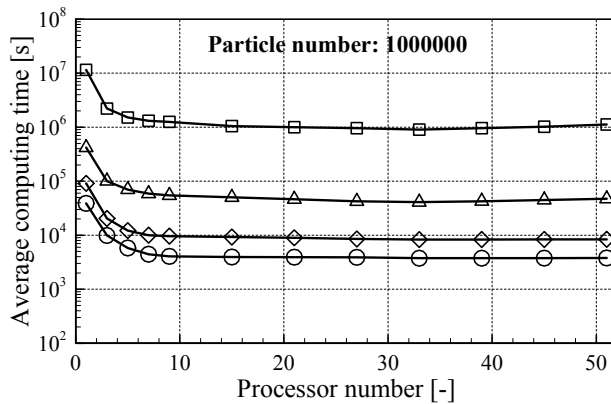


**Figure 8.40:** Influence of processor number variation on the average computing time per time step at different solid loadings and various particle diameters (b)

**Figure 8.41** shows that the absolute gain in the computing time, resulting from the parallelisation rises sharply with increasing the solid loading. For a realistic fluidized bed, where the number of computed particles is enormous, it can be assumed that the parallelisation presents a relevant contribution for realising the Euler–Lagrange/DEM simulations of this facility.

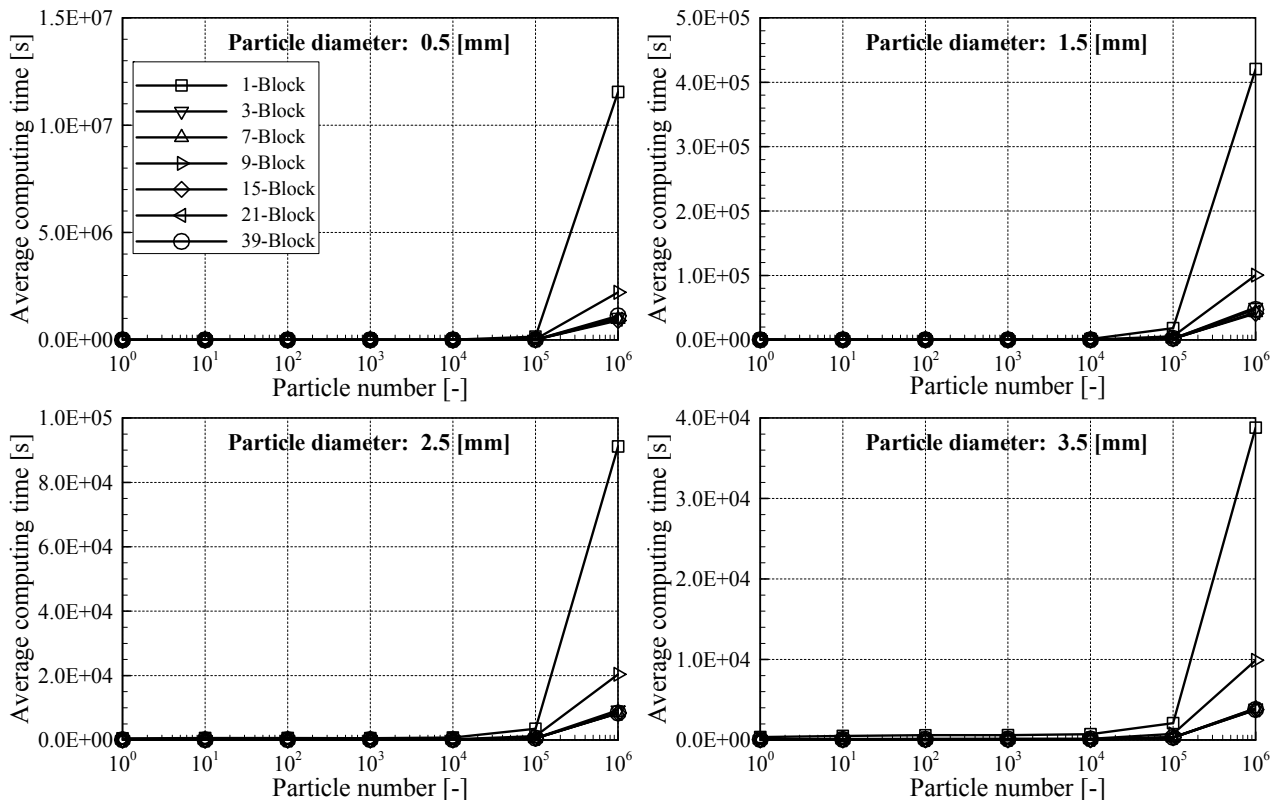


**Figure 8.41:** Influence of processor number variation on the average computing time per time step at different solid loadings and various particle diameters (c)

Finally, it should be noted here that the parallel computation depends critically on the problem geometry. Therefore, the obtained critical number of domain decomposition is related to this case and cannot transfer to other applications with different boundary conditions.

## 8.2 Reactive gas–solid flow

The application of experimental methods to analyse the reactive gas–solid flow in fluidized beds is complex and expensive. The results obtained by the numerical simulation are

cost-effective and give more information regarding the fluid and solid phases inside the reactor, which is very difficult to obtain experimentally.

Besides the calculating of particles trajectories and gas flow streamlines, the extended Euler–Lagrange/DEM model can simulate the behaviour of the reactive gas–solid flow, i.e. biomass conversion in a fluidized bed. This requires the implementation of kinetic models for drying, pyrolysis, char–oxidation and gas phase reactions as well as the associated heat and mass transfer processes in the DEMEST program. Subsequently, the local concentrations of solid and gaseous substances, the local gas and particle temperatures, the local heat release and the heat transfer rates can be calculated. At this point, the coupling of the Euler–Lagrange/DEM model and the chemical reaction mechanism is achieved.

### 8.2.1 Numerical model

For the numerical simulation, the quasi-2D fluidized bed model, explained in the section 8.1.1.1, is used. The supplied air enters, however, through the completely opened bottom ( $15\text{ cm (W)} \times 2\text{ cm (D)}$ ). The dispersed phase consists of 36500 spherical particles with an average diameter of 2.5 mm. The forces on the particles are gravitational, buoyancy, drag, pressure, Saffman, Magnus, and contact forces. The bubbling flow regime (monodisperse particles of group B) is selected. The parallel computation on multi-core processors is not possible for the warm fluidized bed simulations at present. Therefore, the entire numerical model consists of one block. Three series of warm simulations are performed using the developed Euler–Lagrange/DEM model employing the DEMEST program (see **Figure 8.42**).

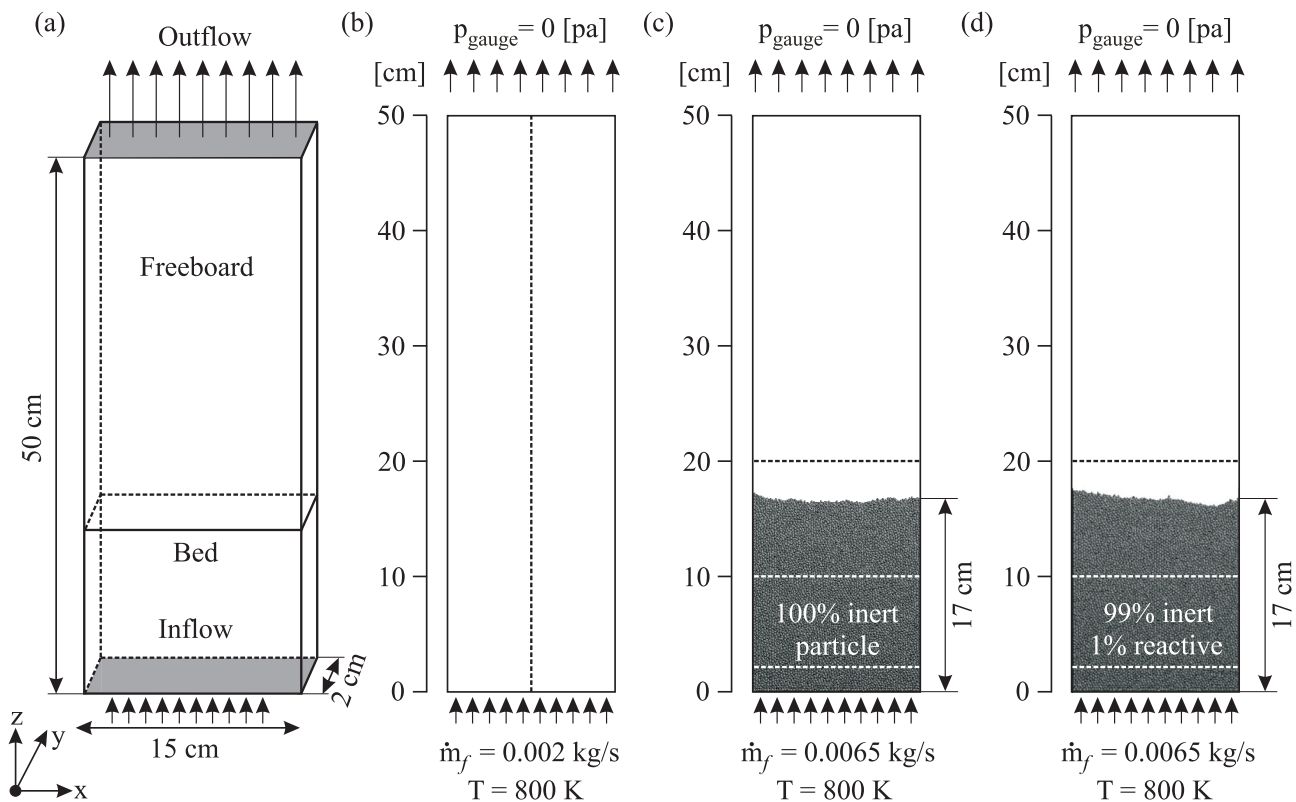


**Figure 8.42:** Numeric model used for the simulation of reactive gas–solid flow: (a) schematic diagram (only 50 cm is presented), (b) combustion with fuel gas (no particle), (c) combustion with fuel gas with sand particles and (d) combustion with solid fuel (99% sand particles + 1% pine wood particle)

For the first case, the model has no particle and a mixture of  $\text{CH}_4$  (0.04 kg/kg<sub>mix</sub>),  $\text{O}_2$  (0.23 kg/kg<sub>mix</sub>) and  $\text{N}_2$  (0.73 kg/kg<sub>mix</sub>) is supplied through the inlet with a mass flow rate of 0.002 kg/s. Second, the reactor is filled with inert particles. The particles have the properties of

sand and the fluidization medium has the same properties as case 1 with a flow rate of 0.0065 kg/s. Finally, the reactor is filled with a mixture of 99% inert sand particles and 1% pine wood particles. The fluidizing medium is air with a mass flow rate of 0.0065 kg/s.

The validity of combustion models in combination with Euler–Lagrange/DEM model is not taken into account due to lack of experimental data at present (see section 9).

### 8.2.2 Combustion with fuel gas

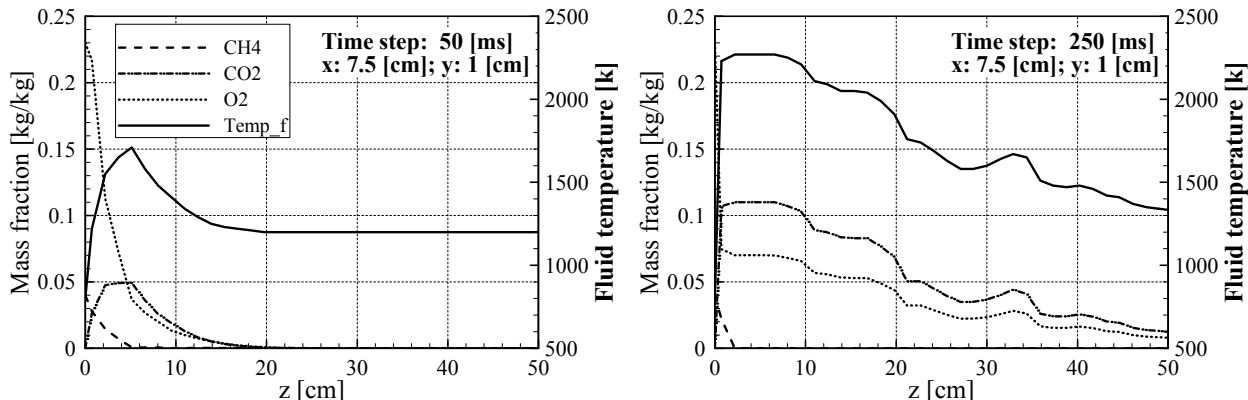
The combustion with the fuel gas is investigated at different operation parameters. While the simulation is performed without the solid phase in the first case, inert particles are added to reactor in the second case. In both simulation cases, a mixture of methane and air is supplied as a fluidization medium.

For the first simulation case, the particle phase is not considered and thus no particles are generated (see **Figure 8.42–(b)**). At the reactor inlet, a mixture of CH<sub>4</sub> (0.04 kg/kg<sub>mix</sub>), O<sub>2</sub> (0.23 kg/kg<sub>mix</sub>) and N<sub>2</sub> (0.73 kg/kg<sub>mix</sub>) is supplied. The mass flow rate amounts to 0.002 kg/s at temperature of 800 K. The temperature of walls is set constant equal to 1000 K. The initial temperature in all grid cells is 1000 K and the initial mass fractions are O<sub>2</sub> (0.23 kg/kg<sub>mix</sub>) and N<sub>2</sub> (0.77 kg/kg<sub>mix</sub>).

At this stage, the reaction mechanism is limited to the homogeneous reactions (methane and carbon monoxide oxidations):



The local mass fraction of each chemical component *i* is calculated based on the gaseous substance transport equation. To balance the energy in the fluid phase, the transport equation for the specific enthalpy is solved in each control volume. The fluid temperature is then determined from the specific enthalpy and the mean specific heat capacity. The source terms in the species transport equations consider the formation/reduction of gaseous components by the reason of chemical reactions (R1 and R2). The heat source term takes into account the heat released by the homogeneous gas phase reactions. The radiation source term is omitted from the calculation. In **Figure 8.43**, the species mass fractions and the fluid temperature profiles along the reactor (see **Figure 8.42–(b)**; dashed line) at different time steps (50 ms, 150 ms, 250 ms, 350 ms, 450 ms and 500 ms) are displayed. At t = 50 ms, the supplied methane reacts with the oxidation agent to CO<sub>2</sub>. The methane is completely consumed about 5 cm far from the inlet. By the reason of methane combustion, the fluid temperature increases gradually and thus the combustion zone becomes closer to the inlet. After 500 ms from the start, the model reaches the steady-state and the fluid temperature is about 2100 K. The mass fractions of CH<sub>4</sub>, O<sub>2</sub> and CO<sub>2</sub> at the reactor outlet are 0, 0.07 and 0.11 kg/kg<sub>mix</sub>, respectively.



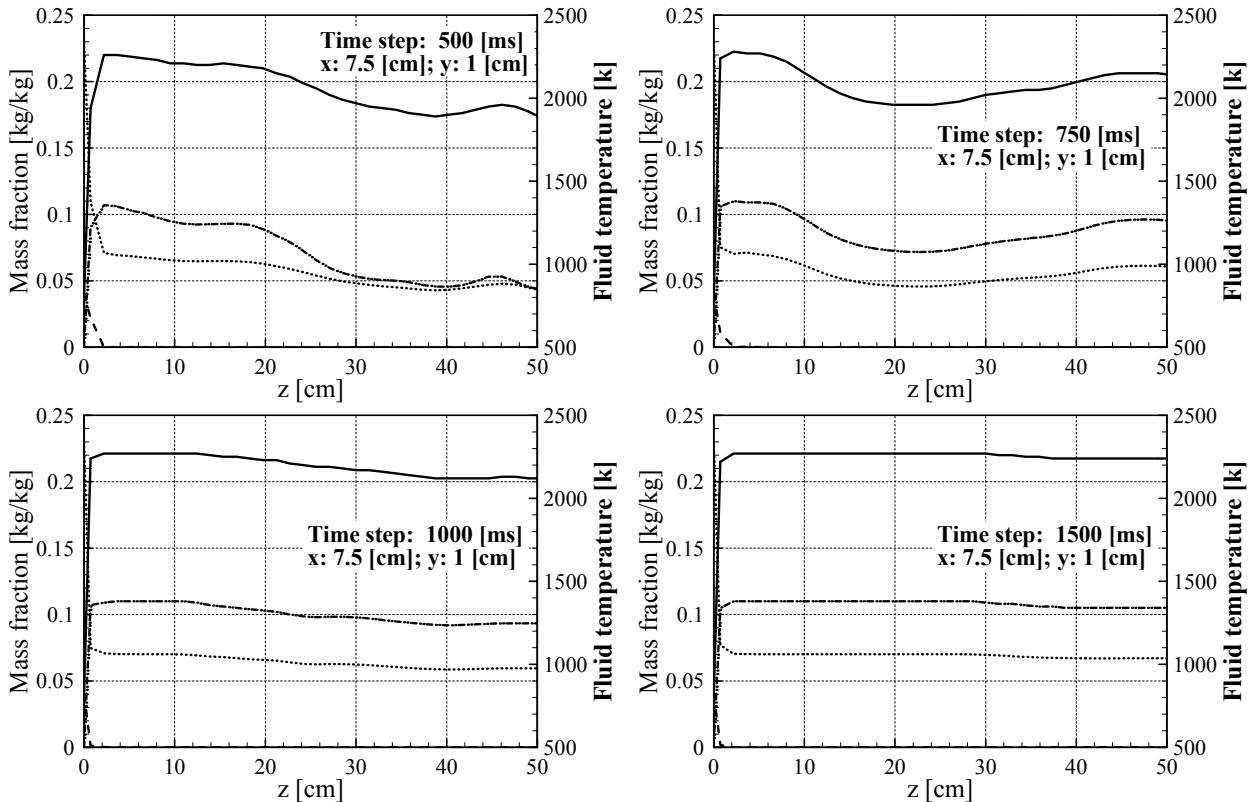


**Figure 8.43:** Species mass fractions (first axis) and fluid temperature profiles (second axis) along z axis of reactor at different time step (combustion with fuel gas)

For the second simulation case, 36500 inert sand particles with 2.5 mm diameter are generated and distributed evenly in the entire computational domain. During this stage, the mass flow rate is set equal to zero. The particles drop freely into the reactor due to the gravity. The static height of sphere particles is 17 cm and the bulk solid fraction is ca. 0.6 (see **Figure 8.42-(c)**). A mixture of CH<sub>4</sub> (0.04 kg/kg<sub>mix</sub>), O<sub>2</sub> (0.23 kg/kg<sub>mix</sub>) and N<sub>2</sub> (0.73 kg/kg<sub>mix</sub>) is supplied at the reactor inlet. The mass flow rate is set equal to 0.0065 kg/s at temperature of 800 K. The mass flow rate is selected, so that the bubbling flow regime is obtained. The initial temperature of particles is 800 K. The temperature of walls and the initial temperature in all fluid grid cells are set equal to 1000 K. The initial mass fractions of species are O<sub>2</sub> (0.23 kg/kg<sub>mix</sub>) and N<sub>2</sub> (0.77 kg/kg<sub>mix</sub>). The simulation parameters for the fluid and solid phases can be found in **Table 10.5**.

Besides the previously explained reaction mechanism, the following energy balance equation for each particle is solved:

$$\underbrace{m_p c_{p,P} \frac{dT_p}{dt_p}}_1 = \underbrace{\alpha_p A_p (T_f - T_p)}_2 + \underbrace{\varepsilon_p A_p \sigma (T_{Rad}^4 - T_p^4)}_3 . \quad (8.8)$$

The equation (8.8) describes the change of the particle temperature  $T_p$  (term 1) as a result of the heat transfer from fluid to particle due to convection (term 2) and radiation (term 3). Here,  $\alpha_p$  is the heat transfer coefficient of particles,  $c_{p,P}$  represents the solid specific heat capacity,  $A_p$  and  $\varepsilon_p$  denote to the particle surface and the emissivity,  $T_{Rad}$  and  $\sigma$  are the surrounding temperature and Stefan–Boltzmann constant, respectively. It should be mentioned here that the radiation term is not considered in the simulation. Similar to the first case, the source terms in the species transport equations take into account the formation/reduction of gaseous components by the reason of chemical reactions (R1 and R2). Besides the heat released

by the homogeneous gas phase reactions, the heat source term in the energy equations of fluid phase consider the heat transfer from solid to fluid by convection.

In **Figure 8.44**, the solid and fluid temperature profiles are presented on the midline at different locations of the bed height ( $z = 2 \text{ cm}$ ,  $z = 10 \text{ cm}$  and  $z = 20 \text{ cm}$ ) at various time steps (0.1 s, 1 s, 5 s, 10 ms, 15 s and 25 s) (see **Figure 8.42-(b)**; dashed lines).

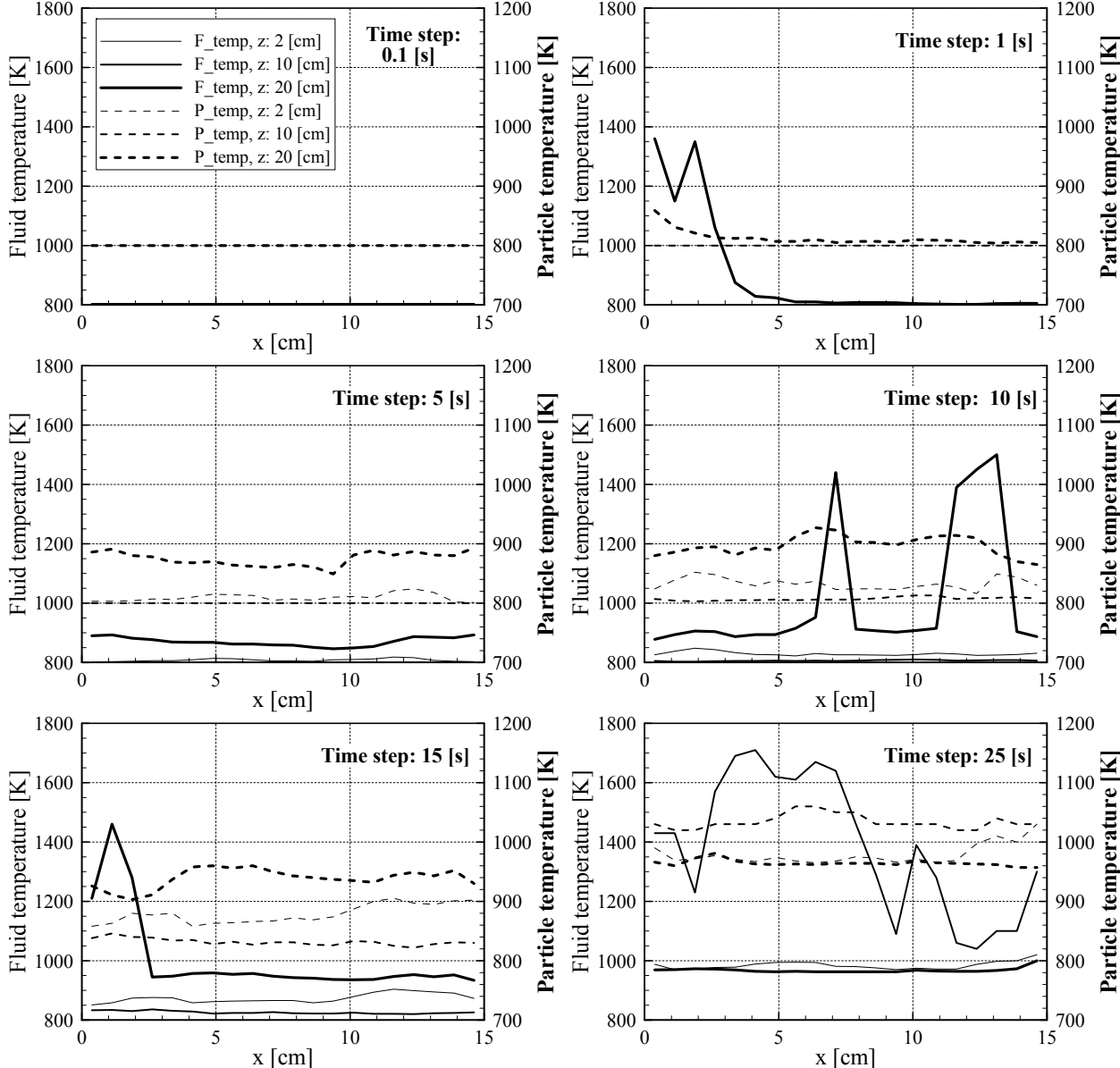


**Figure 8.44:** Fluid temperature (first axis) and particle temperature profiles (second axis) at different bed height of reactor at various time steps

The height of the observation lines are chosen, so that the bubbling flow regime can be covered. In a little while after the start, the particle and fluid temperatures have a value equal to 800 K at all locations. Due to homogeneous reactions (R1 and R2), the fluid temperature increases in the computational domain. The temperature of the particles increases accordingly because of the heat transfer from fluid to solid by convection. At  $t = 10 \text{ s}$ , the temperature of the particles is about 900 K at location  $z = 20 \text{ cm}$ , while it is 850 K and 800 K at positions  $z = 10 \text{ cm}$  and  $z = 2 \text{ cm}$ , respectively. The reason of the solid temperature differences is that the homogeneous reactions occur effectively, where the solid phase is not existent. This means the gaseous species pass through the inert particles and react to each other in the upper region

of the bed, resulting in higher fluid temperatures compared to the lower region. The peaks in the fluid temperature indicate the existence of gas bubbles, where the methane and oxygen can burn. After 25 s, the fluid and solid temperatures reach the values of 1700 K and 1050 K, respectively. The particles are well mixed and the difference in the solid temperature at various locations is gradually decreased. One important point is the heat transfer from solid to fluid, which it can be clearly detected at the location  $z = 2$  cm. Here, the fluid temperature increases to 1000 K, although the  $\text{CH}_4$  as well as CO cannot burn at this region due to dense existence of the solid phase.

### 8.2.3 Combustion with solid fuel

In this section, the combustion with the solid fuel is investigated. The same configurations used for the second simulation case are applied here. However, pure air is entered as a fluidizing medium at the bottom of the reactor. The solid phase consists of a mixture of sand and pine wood particles (36135 + 365). The mechanical properties of the materials used are listed in **Table 10.5**. It is assumed that the parameters of the particle-particle/wall collisions of both solid materials have the same values. Here, the collision parameters of sand are also applied to the pine wood particles. This is due to the fact that on the one hand the bed consists of 99% sand particles and on the other hand the experimental data for the heterogeneous material pairing of sand–pine wood particles are not yet available in the literature. The multi-step reaction mechanism, which it is illustrated in **Figure 8.45**, comprises of drying (R1), pyrolysis (R2), char-oxidation (R3) and combustion of volatile gases, namely methane and carbon monoxide (R4 and R5).

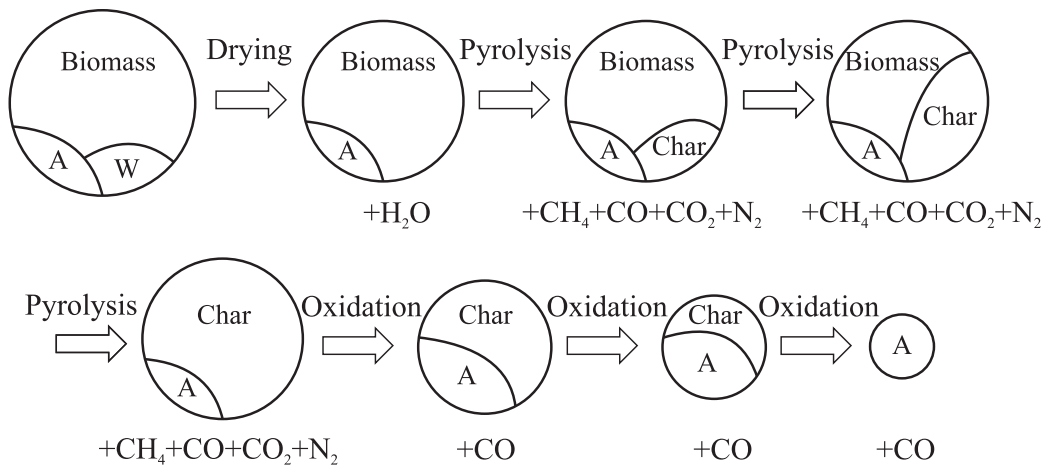
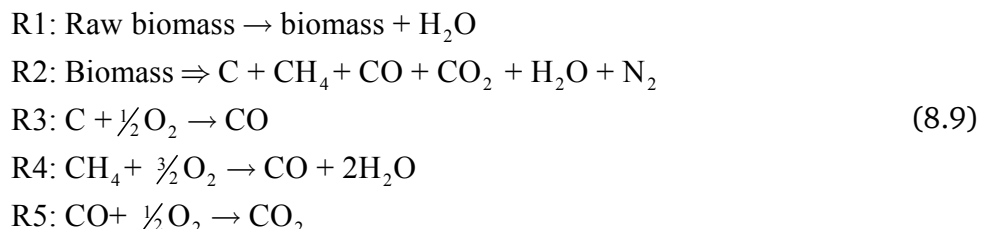


**Figure 8.45:** Representation of multi-step reaction model of a particle (Alobaid et al. 2010b)

The drying process takes place when the temperature of a particle exceeds 100 °C. The kinetics of the pyrolysis is calculated with the aid of the single-step global model (scheme 1) that considers the pyrolysis as one reaction of first-order (see the section 1.1). After (Kutschmitt, Hartmann and Hofbauer 2009), the char-oxidation starts after the complete pyrolysis of biomass particles. For the kinetic of the biochar-conversion, the particle shrinkage model is used. The homogeneous gas reactions are described by CO and  $\text{CH}_4$  oxidations:



The rate of the devolatilisation is calculated according to the following relation:

$$\frac{dm_p^{bio}}{dt} = -k_{pyr} m_p^{bio}, \quad (8.10)$$

where  $k_{pyr}$  is the pyrolysis reaction rate constant. The released gas species during the pyrolysis process can be determined as:

$$\frac{dc_{i,pyr}}{dt} = k_{pyr} v'_{i,pyr} c_{i,pyr}. \quad (8.11)$$

The symbols  $c_{i,pyr}$  and  $v'_{i,pyr}$  are the concentration and the stoichiometric coefficient of a species  $i$  in the pyrolysis reaction (R2). The temporal change in the molar concentration of a chemical component  $i$  due to homogenous gas reactions is determined as:

$$\frac{dc_i}{dt} = \sum_{k=1}^k (v''_{i,k} - v'_{i,k}) r_k^{hom} \quad (i = 1, \dots, N). \quad (8.12)$$

Here,  $k$  is the number of the homogenous gas reactions,  $N$  denotes to total number of the chemical components,  $v'_{i,k}$  and  $v''_{i,k}$  represent the stoichiometric coefficient of the species  $i$  as reactant and product, respectively. The reaction rate  $r_k^{hom}$  of a homogenous gas reaction  $k$  is determined from the reaction rate constant of forward  $k_{for,k}^{hom}$  and backward  $k_{bac,k}^{hom}$  reactions:

$$r_k^{hom} = r_{for,k}^{hom} - r_{bac,k}^{hom} = k_{for,k}^{hom} \prod_{i=1}^N c_i^{v'_{i,k}} - k_{bac,k}^{hom} \prod_{i=1}^N c_i^{v''_{i,k}}. \quad (8.13)$$

The reaction rate constants  $k_{kin}$  in equations (8.10) and (8.13) is defined using Arrhenius expression including a pre-exponential factor  $A$  and the activation energy  $E$ :

$$k_{kin} = A \exp\left(\frac{-E}{RT_j}\right), \quad (8.14)$$

where  $j$  is either a fluid or a solid. The char-combustion (R3) to carbon monoxide is modeled according to the kinetics/diffusion limited reaction model (Epple et al. 2012). The model assumes that reaction rate of the char-combustion combines the kinetic reaction rate constant and the diffusion reaction rate constant of oxygen to particle surface:

$$\frac{dm_p^{cha}}{dt} = -k_{ox}^{cha} A_P^{cha}, \quad (8.15)$$

with:

$$k_{ox}^{cha} = \frac{P_{O_2}}{\left( \frac{1}{k_{kin}^{cha}} + \frac{1}{k_{dif}^{char}} \right)}. \quad (8.16)$$

Here,  $A_P^{cha}$  represents the specific particle surface,  $P_{O_2}$  is the oxygen partial pressure and  $k_{ox}^{cha}$  denotes to the overall reaction rate of the char-combustion. The diffusion rate reaction constant is expressed as:

$$k_{dif}^{cha} = \frac{48D_s}{RT_0^{1.75}} 10^5 \frac{T_P^{0.75}}{d_P^{cha}}. \quad (8.17)$$

The diffusion coefficient  $D_s$  describes the surface diffusion of oxygen in nitrogen and has the value of  $3.49 \cdot 10^{-4} \text{ m}^2/\text{s}$  at reference state temperature  $T_0 = 1600 \text{ k}$ . It should be mentioned here that an additional source term  $S_{P \rightarrow f}^{m,P}$  on the right side of the mass conservation equation (equation (6.54)) should appear as a result of the heterogeneous reactions. This term corresponds to the mass transfer due to the phase transformation from solid to fluid phase.

The source term  $S_f^{c,i}$  in the species transport equation (Equation (6.55)) considers the formation/reduction of the chemical components due to the homogenous and heterogeneous reactions (R3, R4 and R5). The heat source term  $S_{P \rightarrow f,f}^h$  in energy equation of the fluid phase (equation (6.56)) is expressed by the relation:

$$S_{P \rightarrow f,f}^h = \frac{\underbrace{S_f^h}_{S_f^{hom} + S_f^{rad}} + \underbrace{S_{P \rightarrow f}^{h,P}}_{S_{P \rightarrow f}^{conv} + S_{P \rightarrow f}^{rad} + S_{P \rightarrow f}^{het}}}{\dots} . \quad (8.18)$$

It consists of three main parts, namely the heat released by homogeneous gas phase reactions (R4 and R5) as well as the radiation source term of the fluid phase and the heat transfer from solid to fluid by convection, radiation and mass transfer due to the phase transformation. At this stage, the heat released by homogenous and heterogeneous reactions as well as the heat transfer between the two phases by convection are only considered in the DEMEST program. The heat transfer from solid to fluid phase is determined for each control volume taking into account all particles that are located in the control volume during the time interval.

The change of the particle temperature (term 1) is calculated from the energy balance of the particle governed by the heat evaporation (term 2), the heat release due to the char-oxidation (term 3) and the heat transfer from fluid to solid phase associated with convection and radiation (term 4 and term 5):

$$\underbrace{m_p c_{p,p} \frac{dT_p}{dt_p}}_1 = \underbrace{m_{p,wat} k_{wat} \Delta h_{wat}}_2 + \underbrace{m_{p,cha} k_{cha} \Delta h_{cha}^0}_3 + \underbrace{\alpha_p A_p (T_f - T_p)}_4 + \underbrace{\varepsilon_p A_p \sigma (T_{rad}^4 - T_p^4)}_5 . \quad (8.19)$$

Here,  $\Delta h_{wat}$  is the enthalpy of vaporisation of water,  $\Delta h_{cha}^0$  represents the standard enthalpy of char-oxidation,  $k_{wat}$  and  $k_{cha}$  are to evaporation and reaction rates constants, respectively. The quantities  $m_{p,wat}$  and  $m_{p,cha}$  denote to the mass fractions of water and char in the investigated particle. The radiation term (equation (8.19)) can be disregarded. This is due to the fact that the fluidized bed is characterised by a high heat and mass transfer rates between both phases, resulting in uniform temperature distribution. It should be noted here that for all non-reactive particles (99% sand particles), the particle mass remains constant and the reaction terms 2 and 3 are omitted.

**Figure 8.46** shows the particle and fluid temperature profiles on the midline at different height positions (see **Figure 8.42-(d)**; dashed lines) and at various time steps. At  $t = 0.1 \text{ s}$ , the particles have almost a temperature of 800 K. The released volatile components as well as the char are burned, resulting in an increase in solid and fluid temperatures. After 5 s, the solid temperature rises from 800 K to approximately 850 K at  $z = 10 \text{ cm}$  and 950 K at  $z = 20 \text{ cm}$ . The peaks in the fluid temperature profiles occur in areas with large fluid volume fractions. Here, large amounts of oxygen and methane accumulate, whose combustion causes these high temperature peaks. The pine wood particles are completely burned after 25s. Due to the intense mixing, the fluid and solid temperatures at all height positions show nearly constant

temperature gradients of about 1100 K. From time point  $t = 25$  s, the solid starts cooling down since the fluidization medium enters the bed with temperature of 800 k.

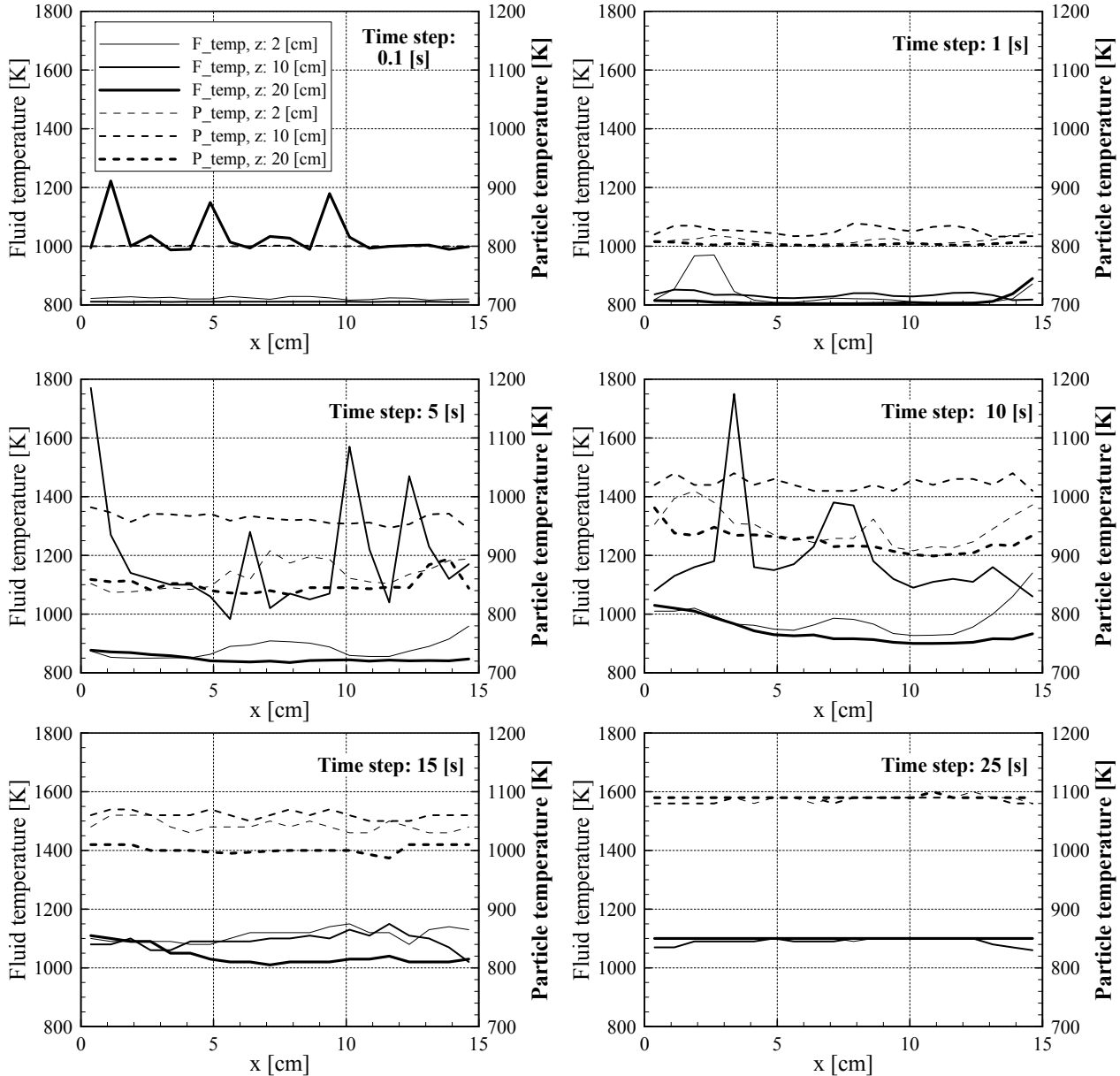


**Figure 8.46:** Fluid temperature (first axis) and particle temperature profiles (second axis) at different bed height of reactor at various time steps (combustion with solid fuel)

### 8.3 Conclusion

The extended DEMEST program, based on the Euler–Lagrange/DEM model, is applied to simulate the hydrodynamic behaviour of reactive and non-reactive gas–solid flow in a fluidized bed. Various numerical procedures, viz. the offset method, the particle grid method and the particle search grid are investigated. The developed Euler–Lagrange/DEM model is compared with the measurements as well as with the stochastic Euler–Lagrange and Euler–Euler models for different mass flow rates. Besides the qualitative comparison regarding the visual observation of solid distribution, the bed behaviour is assessed quantitatively by plotting the bed height and the bubble size as a function of time. The efficiency and accuracy of the developed Euler–Lagrange/DEM model are analysed. Here, the stiffness coefficient, the fluid time step and the processor number are varied at different solid loadings and particle diameters. The coupling of the Euler–Lagrange/DEM model and the chemical reaction

mechanism is achieved. Using the developed DEMEST program, three series of warm simulations are carried out.

The fluid–particle interaction is performed in the DEMEST program using a new procedure so-called the offset method. Here, the fluid grid is shifted in space several times and the interaction values are calculated for each displacement. The interaction values in a grid cell are then determined by averaging all calculated values with regard to the number of displacements. The results show that the application of the offset method improves the calculation accuracy up to an order of magnitude. The accuracy of the procedure depends highly on the resolution of the fluid grid. Accordingly, an optimal ratio between the grid size and the particle diameter in the range of 2 to 3 is obtained. Furthermore, the results show that the offset method can maintain the high accuracy independent of the solid loading. The additional computational effort that results from the using of the offset method is negligibly small for granular flow with a low solid content. At higher solid loadings, the computational effort of the offset method increases. The particle diameter has a remarkable impact on the additional computational effort, where smaller particles cause more additional computing time compared to bigger ones at same number of particles.

The physical values of the fluid and particle phases are determined in the DEMEST program by mean of separated grids. The proposed procedure allows the variation of the fluid grid resolution independent of the particle size. A geometric allocation between the fluid and particle grids is required to enable the data exchange. The results show that the application of the particle grid method improves significantly the calculation accuracy. The ratio between the fluid and particle girds has an influence on the computational time as well as on the quality of the obtained result. A ratio in the range between 4 and 10 is suggested that presents a very good compromise between an acceptable computing time and accuracy. The resolution of the fluid grid should be fine enough to resolve the scales of motion accurately, while the resolution of the particle grid depends on the particle diameter. To maintain the accuracy of the averaging procedure, the particle grid size should be selected around two to three times bigger than the particle diameter. The additional computational effort, resulting from the use of the particle grid method, rises with increasing the solid loading. The particle diameter has a considerable influence on the computing time. When the particle diameter decrease, the computational time increases accordingly.

In the DEMEST program, the collision detection between particle–particle/wall is based on the assumption of the DEM model and carried out with the aid of the particle search grid method. The use of the particle search grid method enhances the efficiency calculation of collision detection. However, it requires an additional grid so-called the particle search grid that is independent of the fluid and particle grids. The size of the particle search grid depends highly on the particle diameter. A decrease in the size of the search grid leads to a gain in the efficiency up to limit of the particle diameter. The results show that the size of the search grid should not fall short of the particle diameter in order to avoid the discrepancy between the Euler–Lagrange/DEM model and the measurements.

A validation studies are performed to assess the results obtained from the extended DEMEST program and the quasi-2D spouted fluidized bed of Plexiglas. Here, the spouted flow regime with particle of group D is investigated. The dispersed phase consists of 36500 spherical particles with an average diameter of 2.5 mm and a density of 2500 kg/m<sup>3</sup>. The particles have the properties of glass and the fluidizing medium is air at room temperature. The spatial distribution of solid, the bed height and the equivalent bubble diameter are analysed for different mass flow rates (0.005 and 0.006 kg/s) within 500 milliseconds. The results suggest that the Euler–Lagrange/DEM can accurately predict the typical flow pattern of a spouted bed including the spout, the fountain and the annulus between the spout and the walls. However, a

relatively small deviation of simulated solid distribution from the experiments, especially in the nozzle region, may be caused by the inlet assumption of the centrally placed nozzle instead of nine holes.

The numerical results obtained from the DEMEST program are also compared with the numerical results of the Euler–Euler model and stochastic Euler–Lagrange approaches. The commercial CFD package ANSYS–FLUENT® and the commercial program CPFD–BARRACUDA® are employed to model the cold test rig of quasi–2D fluidized bed. According to the qualitative and quantitative comparisons, the results show that the Euler–Euler model tends to predict a smaller bubble and bed expansion than the experimentally observed bed behaviour, especially during the final stage of the bubble formation. In addition, the solid distribution in the Euler–Euler model displays symmetry properties. The stochastic Euler–Lagrange model, although it reaches earlier the maximum bed expansion, is able to predict the bed expansion. Considering the deviations in the bed behaviour, the Euler–Euler and stochastic Euler–Lagrange models still show potential to simulate the complex behaviour of dense gas–solid flow in a fluidized bed with an acceptable accuracy.

Parameters studies are performed in order to understand the influence of the stiffness coefficient, the fluid time step and the processor number variations on the efficiency and accuracy of the Euler–Lagrange/DEM model. The obtained results are compared with the measurements in order to derive the optimum parameters for the DEM simulations. The results suggest that the application of higher stiffness coefficients (more than  $10^6$  N/m) improves the simulation accuracy slightly, however, the average computing time increases exponentially. For time intervals larger than five milliseconds, it has been found that the average computation time is independent of the applied fluid time step, while the simulation accuracy decreases extremely by increasing the size of the fluid time step. Fluid time steps smaller than five milliseconds lead to a negligible improvement in the simulation accuracy, but on the other hand to exponential rise in the average computing time. The parallel calculation accelerates the Euler–Lagrange/DEM simulation if the critical number of domain decomposition is not reached. Exceeding this number, the performance is not anymore proportional to the number of processors. The critical number of domain decomposition depends on the solid loading, wherein an increase in the particle number leads to shift in the number of processors that can be used before reaching the critical number of domain decomposition.

In this work, the biomass conversion in the fluidized bed is also investigated. To achieve this, the kinetic models for drying, pyrolysis, char–oxidation, homogenous gas phase reactions and the associated heat and mass transfer processes are implemented in the extended DEMEST program. The bubbling flow regime (particle of group B) is selected for the warm fluidized bed simulations. For the first series of simulations, a mixture of methane and air is delivered at the reactor inlet. While the solid phase in this investigation is disregarded, the reactor is filled with inert sand particles in the second simulation case. The 36500 particles used are spherical with an average diameter of 2.5 mm and a density of  $2200 \text{ kg/m}^3$ . In the last series of warm simulations, the reactor is filled with a mixture of 99% inert sand particles and 1% pine wood particles. Here, pure air is applied as a fluidizing medium. On the basis of these warm simulations, the coupling of the Euler–Lagrange/DEM model and the chemical reaction model is realised. Due to lack of the experimental data at present, the simulation results obtained from the Euler–Lagrange/DEM model in combination with the thermochemical reaction mechanism cannot be validated.

## 9 Conclusion and future work

Several engineering problems involve gas–solid flow, where the particles of a wide range of shapes and sizes undergo time dependent turbulent motion, e.g. fluidized beds, ash deposition on boiler walls, gasification or combustion of biomass and coal as well as CO<sub>2</sub> capture methods. Here, different physical and chemical processes at diverse length and time scales are gathered, including mass, momentum and heat transfers between gas and solid phases. The detailed measurements from real facilities are extremely difficult by the reason of dangerous environment (high temperature and/or high pressure), limited accessibility, measurement costs and related inevitable decline in production. The numerical methods provide on the other hand an effective and alternative way to the direct measurements.

There are two different methods for the representation of the gas–solid flow, namely the Euler–Euler and Euler–Lagrange approaches. In the Euler–Euler model, the gas and solid are treated as coexisting continua, where the particle phase is modeled with the balance equations of single–phase flow. The Euler–Lagrange model combines the continuum descriptions of the fluid phase with the Lagrange representation of the dispersed phase. The single particle–particle/wall collision in the Euler–Euler model is considered with the aid of additional model assumptions. In the Euler–Lagrange approach, the particle–particle/wall collisions can be stochastically modeled or deterministically detected.

The aim of this work is to develop a numerical simulation program (DEMEST), based on the deterministic Euler–Lagrange model, for the biomass conversion in fluidized beds. This requires a coupling of the Euler–Lagrange/DEM model with the chemical reaction mechanism. In the first phase of this study, the DEM model is further extended to the offset method, the particle grid method and the particle search grid. The developed Euler–Lagrange/DEM model is qualitative and quantitative compared with the measurements as well as the stochastic Euler–Lagrange and Euler–Euler models at different mass flow rates. The efficiency and accuracy of the developed Euler–Lagrange/DEM model are also analysed at different particle numbers and particle diameters. In the second phase, kinetic reaction models, heat and mass transfer processes are implemented in the extended DEMEST program. Three series of warm simulations are carried out, realising the coupling of the Euler–Lagrange/DEM model with the thermochemical reaction mechanism.

The gas–solid interaction is performed using a new procedure, known as the offset method, which results in several numbers of spatial displacements of the fluid grid. The proposed method is highly precise in determining the interaction values and thus improving the simulation accuracy. The results show an improvement in the calculation accuracy up to an order of magnitude. The accuracy of the procedure is depending on the fluid grid resolution, but independent of the solid loading. An optimal ratio between the grid size and the particle diameter in the range of 2–3 is suggested. The additional computational effort rises with increasing the number of particles. At same solid loading, smaller particles cause more additional computing time compared to bigger ones.

In this work, an additional grid, so-called the particle grid, in which the physical values of the solid phase are computed, is introduced. The proposed procedure allows the refinement

of the fluid grid resolution beyond the particle size. The results show a significant improvement in the calculation accuracy. The quality of the result and the additional computational time are a function of the fluid grid to the particle grid ratio. A ratio in the range between 4 and 10 is suggested, showing a very good compromise between an acceptable computing time and high simulation accuracy. The particle grid size should be selected around two to three times bigger than the particle diameter in order to maintain the averaging procedure accuracy. At constant grid ratio, the additional computational time rises with increasing the particle numbers. A reduction in particle diameter results in an increase in the computing time.

The collision detection between particle-particle/wall is performed using the particle search grid method. This method requires an additional grid so-called the particle search grid that is independent of the fluid and particle grids. The results show an efficiency dependence on the size of the search grid. A refinement in the search grid size leads to a gain in the calculation efficiency. However, the size of the search grid should not fall short of the particle diameter in order to maintain the kinetic energy conservation and to avoid the decline in the simulation accuracy.

A validation study is carried out to assess the results delivered from the extended Euler–Lagrange/DEM model and the quasi-2D spouted fluidized bed of Plexiglas. Air at different mass flow rates (0.005 and 0.006 kg/s) is supplied from the bottom of the model, i.e. through the centrally placed nozzle. The results show that the Euler–Lagrange/DEM model can accurately predict the hydrodynamic behaviour of the gas-solid flow in the fluidized bed. The simulated spatial distribution of solid, the bed height and the equivalent bubble diameter agree very well with the experiments. A relatively small deviation is noticed, especially in the nozzle region, caused by the inlet assumption of the centrally placed nozzle instead of the nine holes. Furthermore, the numerical results of the Euler–Lagrange/DEM model are compared with the numerical results of the Euler–Euler and stochastic Euler–Lagrange models. The results show that the Euler–Euler model tends to predict smaller bubble sizes and bed expansions than the measurements, while the stochastic Euler–Lagrange model reaches faster the maximum bed expansions. Considering the quantitative deviations in the bed expansion in the Euler–Euler model, it can be suggested that the validation against the experiments should not be waived. According to the qualitative comparisons, on the other hand, the Euler–Euler and stochastic Euler–Lagrange models still show potential to simulate the complex behaviour of dense gas-solid flow in fluidized beds with an acceptable accuracy. For industrial applications, where the number of particles is enormous and thus the use of the Euler–Lagrange/DEM model is associated with a high computational effort, the Euler–Euler and stochastic Euler–Lagrange models can present a relevant contribution to experiments.

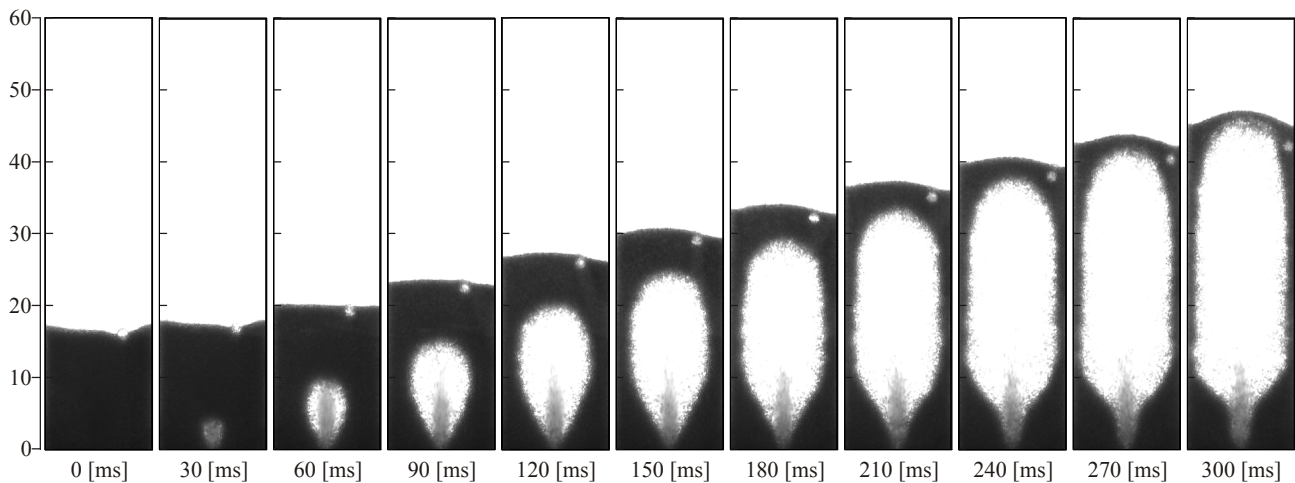
The effect of different numerical parameters used in the Euler–Lagrange/DEM simulations has been studied. Different important parameters, viz. the stiffness coefficient, the fluid time step and the processor number are varied under the consideration of various particle numbers and particle diameters. The results show that the stiffness coefficient, the fluid time step and the number of processors need to be set up very precisely in order to achieve an efficient and accurate DEM calculation. The application of the realistic stiffness coefficients is not possible due to the exponential increase in the computational time. Depending on the relative velocity of collision partners, stiffness coefficient values between  $5 \cdot 10^4$  and  $5 \cdot 10^6$  N/m are recommended, since they offer a good compromise between the efficiency and accuracy. The obtained results show that fluid time steps with interval size larger than five milliseconds cannot accelerate the simulation, but lead to worse temporal resolution of the fluid phase. The reduction of the fluid time step size smaller than five milliseconds in order to achieve higher resolutions causes an efficiency loss together with a negligible improvement in the simulation accuracy. Independent of solid loading and particle diameter, a fluid time step in the range between 1 and 5 ms is suggested according to the simulations and the experiments. The

parallelisation accelerates the Euler–Lagrange/DEM simulation if the critical number of domain decomposition is not exceeded. Further decomposition of computational domain leads to increase in the data exchange between the CPUs and thus to loss in the calculation efficiency. The critical number of domain decomposition depends on solid loading, where an increase in the particle number leads to rise in the number of CPUs that can be used before reaching the critical number of domain decomposition. The absolute gain in computing time resulting from the parallelisation increases sharply at higher solid loadings. It can be assumed that the parallelisation presents a relevant contribution for realising the Euler–Lagrange/DEM simulation for large facilities.

In the second phase of this work, the biomass conversion in a bubbling fluidized bed is investigated. The Euler–Lagrange/DEM model is further extended with the kinetic models for drying, pyrolysis, char–oxidation, homogenous gas phase reactions and the associated heat and mass transfer processes. Three series of reactive gas–solid flow simulations are performed with the developed DEMEST program. A mixture of methane and air is supplied at the reactor inlet. The solid phase in first simulation case is not considered, while the reactor is filled with inert sand particles in the second case. In the third case, the reactor is filled with a mixture of 99% inert sand particles and 1% pine wood particles. Here, a pure air is applied as a fluidization medium. The received results realise the coupling between the Euler–Lagrange/DEM model and the thermochemical reaction mechanism model. The use of other solid fuels such as coal or a mixture of coal and biomass can also be simulated by the same token. Here, it should be mentioned that the simulation results obtained from the Euler–Lagrange/DEM model in combination with the thermochemical reaction mechanism cannot be validated at present due to the lack of experimental data.

All in all, the extended DEMEST program, based on the Euler–Lagrange/DEM model under the consideration of the thermochemical reaction mechanism, is successfully applied to simulate the hydrodynamic behaviour of the reactive and non-reactive gas–solid flow in fluidized beds. However, the following points should be kept in mind for the future works:

- 1) The high-speed camera used in experiments, although it belongs to high performance class, cannot follow the motion of an individual particle even in the quasi-2D test rig due to the relatively small particle diameter (2.5 mm). Generally, the tracking of a single particle trajectory can be accomplished using different measurement techniques such as the positron emission particle tracking. Since these methods are associated with considerable experimental and financial costs, an alternative way, illustrated in **Figure 9.1**, is proposed.



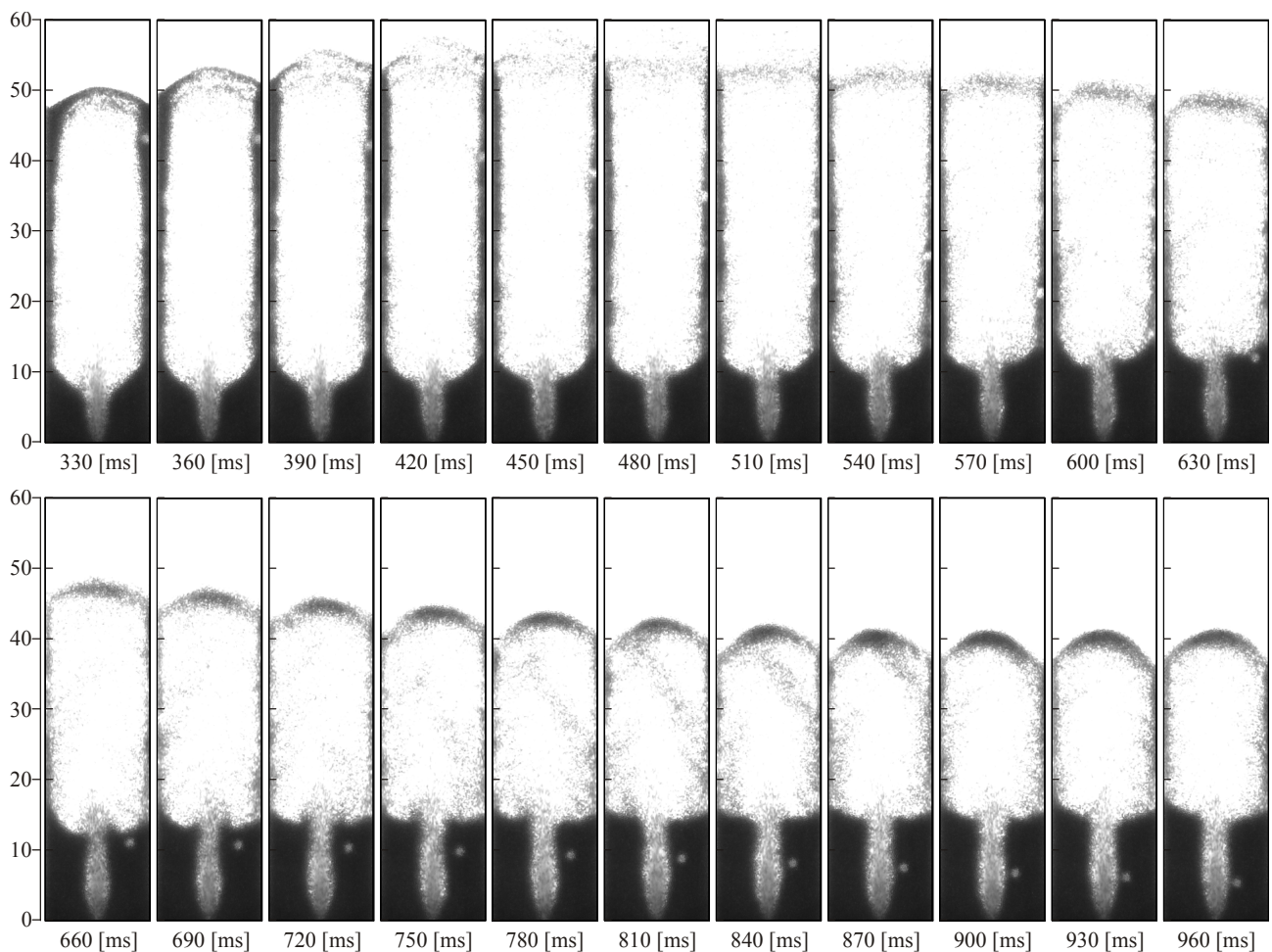


**Figure 9.1:** Snapshots for the spatial distribution of solid (mass flow rate 0.007 kg/s)

A large glass particle with a diameter of 15 mm is added to the bed besides the 36500 glass particles. The mass flow rate is set equal to 0.007 kg/s. The big particle remains visible to the high-speed camera at any point in time. The change in the particle position can be considered as a further quantitative indication for the validation of the DEMEST program in addition to the spatial distribution of solid, the bed height and the bubble size.

2) To extend the validity of the developed DEMEST program, a cold 3D fluidized bed test rig of Plexiglas is built. The dispersed phase consists of  $10^6$  limestone particles with an average diameter of 1 mm and a density of  $1500 \text{ kg/m}^3$ . As fluidization medium, air at room temperature with a flow rate of 0.015 kg/s is supplied uniformly through the nozzle plate (see **Figure 9.2**). The temporal change of pressure is measured by pressure sensors at different positions ( $z = 1 \text{ cm}$ ,  $z = 28 \text{ cm}$  and  $z = 48 \text{ cm}$ ) starting from the nozzle plate. The particle flow and the bubble behaviour are registered by a high-speed camera. In **Figure 10.1**, the measured snapshots for the spatial distribution of solid in the period of time between 0–1120 ms are displayed.

3) The pyrolysis model should be extended to the single-step multi-reaction mechanism (scheme 2) and the secondary kinetic mechanism for the tar-cracking (Scheme 3). For heterogeneous reactions, the following reactions, namely steam gasification, Boudouard-reaction and hydrogenating gasification should be considered during the combustion process:



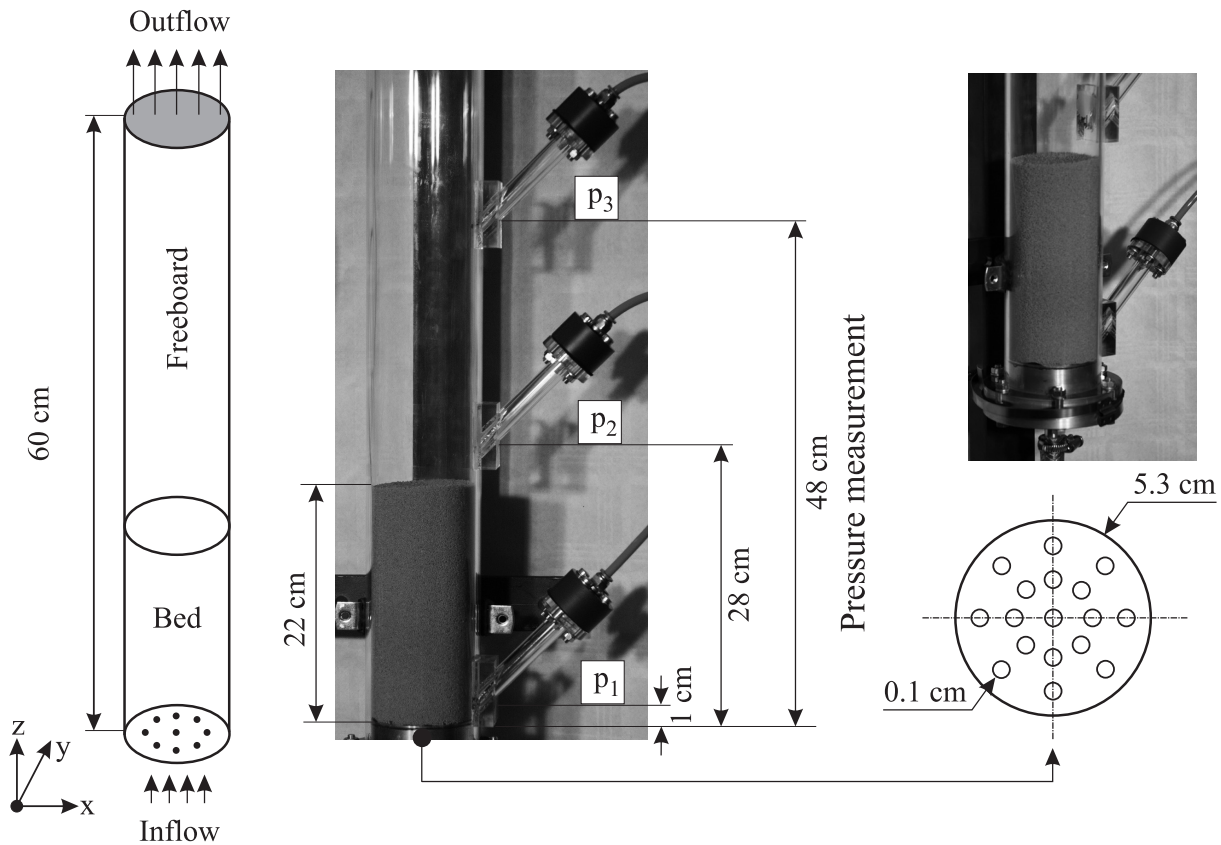
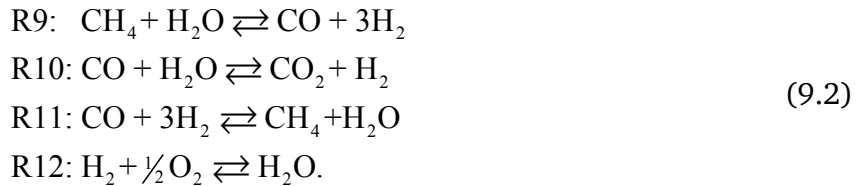


**Figure 9.2:** Cold 3D test rig model of fluidized bed

By the application of complex pyrolysis models and heterogeneous reactions, the homogenous gas phase reaction should also be extended:



Due to the high particle-particle/wall interactions in the fluidized bed, the conduction heat transfer during the particle-particle and particle-wall collisions is of relevance to the simulation accuracy. The transient heat conduction between the collision partners can be determined by a non-steady heat conduction equation (Zhou, Yu and Horio 2008). This procedure results in a considerable additional computational time. For reasons of simplicity, the heat transfer by conduction can explicitly be expressed by term 6 in the particle energy equation as:

$$\begin{aligned}
 m_p c_{p,p} \frac{dT_p}{dt_p} = & \underbrace{m_{p,wat} k_{wat} \Delta h_{wat}}_1 + \underbrace{m_{p,cha} k_{cha} \Delta h_{cha}^0}_2 + \underbrace{\alpha_p A_p (T_f - T_p)}_3 \\
 & + \underbrace{\varepsilon_p A_p \sigma (T_{rad}^4 - T_p^4)}_4 + \underbrace{\alpha_p \sum_{\substack{k=1 \\ k \neq i}}^N A_{ik} (T_{P,i} - T_{P,k})}_5.
 \end{aligned} \tag{9.3}$$

The index  $N$  represents the number of contacts for the particle  $i$ . The area  $A_{ik}$  corresponds to the contact area between the particle and a collision partner (particle or wall) and can be defined from the known tangential penetration depth:

$$A_{ik} = \pi r_{ij}^2 = \frac{\pi (\delta_{ij}^t)^2}{4}.$$

In case of 2D simulations, the contact line between the collision partners is equal to the tangential penetration depth.

To accelerate the calculation of the Euler–Lagrange/DEM model under the consideration of the thermochemical reaction model, the parallel computation on multi-core processors should be extended to include the species transport and energy equations of the fluid phase.

The validity of the combustion models in combination with the Euler–Lagrange/DEM model will be achieved with the aid of the warm 3D fluidized bed test rig at EST department. The reactive fluidized bed facility has the same experimental setup of the cold 3D fluidized bed test rig (see **Figure 9.2**).

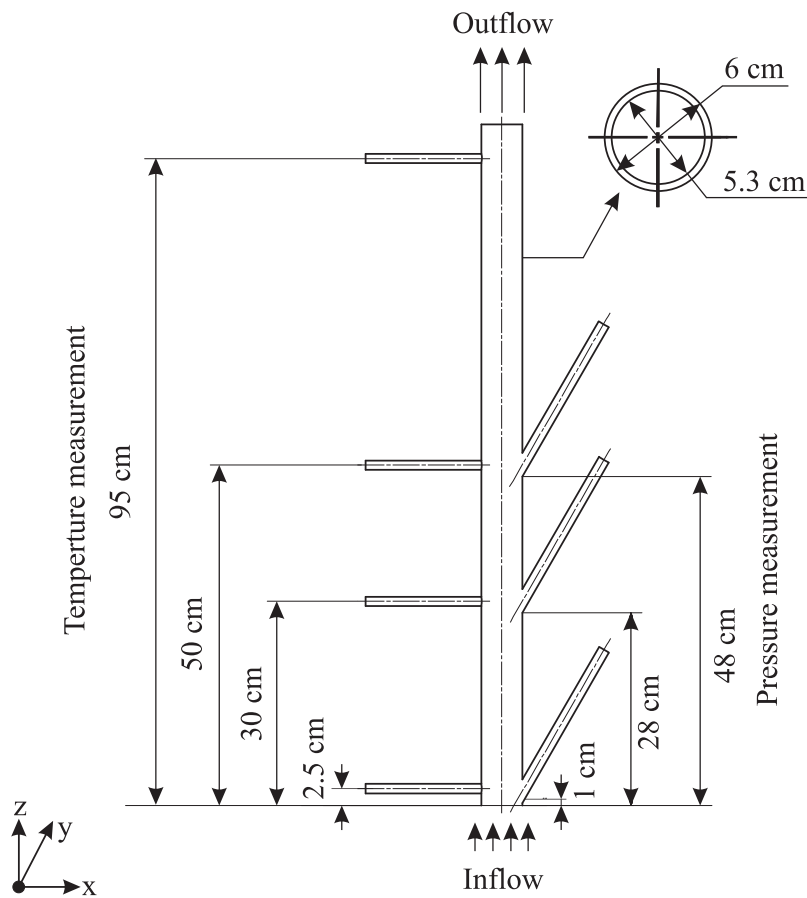


**Figure 9.3:** Warm 3D test rig model of fluidized bed

Besides the pressure measurement at the positions 1, 28 and 48 cm, the temperature is measured at different positions ( $z = 2.5$  cm,  $z = 50$  cm and  $z = 95$  cm; see **Figure 9.3**). At the outlet, the species concentrations can be determined using a gas chromatography gas analyser. The warm 3D fluidized bed test rig can be filled with biomass and/or other solid fuels such as coal. It should be noted that a bubbling flow regime will be investigated.

In case of continuously feeding of the solid fuel, a dynamic particle generator function is required to be implemented in the DEMEST code. This is due to the fact that the actual stand of the program enables only the particles generation before the start of simulation.

# 10 Appendix

## 10.1 Experimental and simulation parameters

**Table 10.1:** Experiment parameters for the cold quasi-2D fluidized bed test rig

Particle phase	particle type	glass sphere (monodisperse)
	density	2500 [kg/m <sup>3</sup> ]
	average diameter	2.5 [mm]
	Geldart's particle classification	group D
	particle number	ca. 36500
	particle weight	0.75 [kg]
Fluid phase	fluidization medium	air
	density	1.2 [kg/m <sup>3</sup> ]
	dynamic viscosity	$18.27 \times 10^{-6}$ [Pa s]
	temperature	25 [°C]
	mass flow rates	0.006 (case 1), 0.005 (case 2) [kg/s]
Experiment	material type	Plexiglas
	demission	$15 \times 2 \times 100$ [cm]
	pressure measuring heights	2, 12, 22 and 40 [cm]
	initial bed height	ca. 17 [cm]
	measuring time	500 [ms] (each case)

**Table 10.2:** Simulation parameters used for the cold Euler–Lagrange/DEM simulations

Fluid parameters (air)	viscosity	$18.27 \cdot 10^{-6}$ [Pa s]
	density	1.2 [kg/m <sup>3</sup> ]
	mass flow rates	0.006 (case 1), 0.005 (case 2) [kg/s]
	fluid time step	2 [ms]
Particle parameters (Glass)	total number	36500 [spherical particle] (glass)
	average diameter	2.5 [mm]
	density	2500 [kg/m <sup>3</sup> ]
	shear modulus	31 [GPa]
	Poisson number	0.17 [-]
	restitution coefficient in normal direction (P–P)	0.97 [-] (Kharaz et al. 1999)
	restitution coefficient in normal direction (P–W)	0.97 [-] (Kharaz et al. 1999)
	restitution coefficient in tangential direction (P–P)	0.33 [-] (Kharaz et al. 1999)
	restitution coefficient in tangential direction (P–W)	0.33 [-] (Kharaz et al. 1999)
	damping parameter (P–P, P–W) in normal direction	calculated [N s/m] with $\alpha_{Dam} = 1$ [-] (equation (5.38))
	damping parameter (P–W, P–W) in tangential direction	calculated [N s/m] with $\alpha_{Dam} = 1$ [-] (equation (5.43))
	stiffness coefficient (P–P)	$5 \cdot 10^5$ [N/m]
	stiffness coefficient (P–W)	$5 \cdot 10^5$ [N/m]
	friction coefficient (P–P)	0.1 [-] (Link 2006)
	friction coefficient (P–W)	0.1 [-] (Link 2006)
	particle sub-time step	calculated [s] (equation (7.17))
Numerical parameters	under relaxation velocity	0.3
	under relaxation pressure	0.2
	number of iterations velocity	100
	number of iterations pressure	10
	turbulence of the fluid phase	deactivated
	pressure–velocity coupling	SIMPLEC
	spatial discretisation	central differencing scheme
	temporal discretisation	second–order implicit Crank–Nicolson method

	solver	multi-grid/red-black-successive-over-relaxation
Calculation	operating system	Windows® 64 bit architecture
	CPU	Intel i7®
	domain decomposition	9 sub-blocks

**Table 10.3:** Simulation parameters used for the cold Euler–Euler simulations

Fluid parameters (air)	viscosity	$18.27 \cdot 10^{-6}$ [Pa s]
	density	1.2 [kg/m <sup>3</sup> ]
	mass flow rates	0.006 (case 1), 0.005 (case 2) [kg/s]
	time step	0.2 [ms]
Particle parameters (Glass)	average diameter	2.5 [mm]
	density	2500 [kg/m <sup>3</sup> ]
	granular viscosity	(Syamlal and O'Brien 1989)
	granular Bulk Viscosity	(Lun et al. 1984)
	granular Temperature	Algebraic, partial differential approach
	solids pressure	(Lun et al. 1984)
	radial distribution	(Lun et al. 1984)
	elasticity modulus	derived
	maximum packing limit	0.63 [-]
	drag model	(Syamlal and O'Brien 1989)
	restitution coefficients	0.5 (case 1), 0.6 (case 2)
	specularity coefficients	0.05 (case 1), 0.5 (case 2)
Numerical parameters	under relaxation momentum	0.3
	under relaxation pressure	0.2
	viscous	laminar
	pressure–velocity coupling	phase coupled SIMPLE
	spatial Discretisation	first–order upwind
	temporal discretisation	first–order implicit
Calculation	operating system	Windows® 64 bit architecture
	PC	Intel i7®
	domain decomposition	4 sub-blocks

A parameter study is carried out to understand the influence of various simulation parameters on the Euler–Euler simulation accuracy. Here, different numerical parameters have been varied such as gas–particle drag models, solid–phase wall boundary conditions (specularity coefficient), restitution coefficient, granular temperature approach and partial differential equation approach. In each simulation case, a comparison study has been conducted. Finally, the best simulation parameters, presented in **Table 10.3**, are obtained. The influence of simulation parameters variations on the numerical results of the Euler–Euler model can be found at EST in the master thesis of (Almohammed 2013).

**Table 10.4:** Simulation parameters used for the cold stochastic Euler–Lagrange simulations

Fluid parameters (air)	viscosity	$18.27 \cdot 10^{-6}$ [Pa s]
	density	1.2 [kg/m <sup>3</sup> ]
	mass flow rates	0.006 (case 1), 0.005 (case 2) [kg/s]
	time step	2 [ms]
Particle parameters (Glass)	average diameter	2.5 [mm]
	density	2500 [kg/m <sup>3</sup> ]
	maximum momentum redirection from collision	40%
	restitution coefficient	0.99 [-]
	normal-to-wall momentum retention	0.3 [-]
	tangent-to-wall momentum retention	0.99 [-]
	diffuse bounce	0
Numerical parameters	under relaxation velocity	0.3
	under relaxation pressure	0.2
	turbulence of the fluid phase	deactivated
	pressure–velocity coupling	SIMPLE
	spatial Discretisation	first–order upwind
	temporal discretisation	first–order implicit
Calculation	operating system	Linux 64 bit architecture
	PC	Intel i7®
	domain decomposition	1 block

The influence of simulation parameters variations on the accuracy of the stochastic Euler–Lagrange simulations can be found at EST in the bachelor-thesis of (Spitz 2013).

**Table 10.5:** Simulation parameters used for the warm Euler–Lagrange/DEM simulations

Fluid parameters (air)	viscosity	$18.27 \cdot 10^{-6}$ [Pa s]
	density	1.2 [kg/m <sup>3</sup> ]
	mass flow rates	0.002 (case 1), 0.0065 (case 2 and case 3) [kg/s]
	fluid time step	2 [ms]
Particle parameters (Glass)	total number	36500 [spherical particle] (100% sand for fuel combustion and 99% sand + 1% wood for solid fuel combustion)
	average diameter	2.5 [mm]
	density	2200 (sand), 520 (pine wood) [kg/m <sup>3</sup> ]
	shear modulus	19 [GPa]
	Poisson number	0.3 [-]
	restitution coefficient in normal direction (P–P/P–W)	0.05 [-]
	restitution coefficient in tangential direction (P–P/P–W)	0.03 [-]
	damping parameter (P–P/P–W) in normal and tangential directions	calculated (equation (5.38) and (5.43))
	stiffness coefficient (P–P/P–W)	$5 \cdot 10^5$ [N/m]
	friction coefficient (P–P/P–W)	0.1 [-]
Numerical parameters	particle sub-time step	calculated [s] (equation (7.17))
	under relaxation velocity	0.3
	under relaxation pressure	0.2
	under relaxation temperature	0.1
	under relaxation concentration	0.1
	number of iterations velocity	100
	number of iterations pressure	10
	number of iterations temperature and concentration	350
	turbulence of the fluid phase	deactivated
	pressure–velocity coupling	SIMPLEC
	spatial discretisation	central differencing scheme
	temporal discretisation	Second-order implicit Crank–Nicolson method

	solver	multi-grid/red-black-successive-over-relaxation
Calculation	operating system	Windows® 64 bit architecture
	CPU	Intel i7®
	domain decomposition	1 block

## 10.2 Spatial distribution of particles in a cold 3D fluidized bed test rig

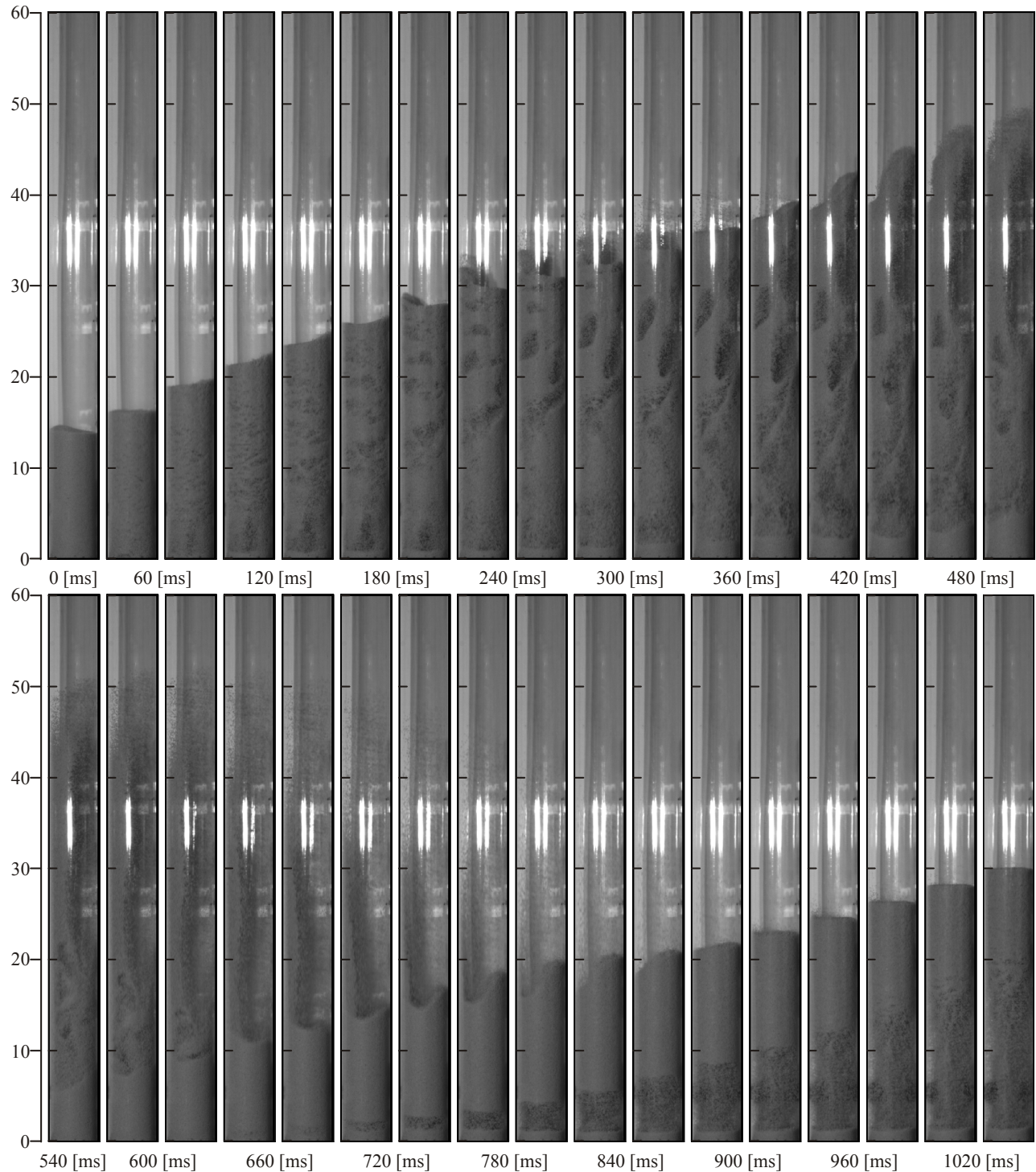


**Figure 10.1:** Snapshots for the spatial distribution of solid in a cold 3D test rig (mass flow rate 0.015 kg/s)

# Bibliography

- Abbas, T., M. Awais & F. Lockwood (2003) An artificial intelligence treatment of devolatilization for pulverized coal and biomass in co-fired flames. *Combustion and flame*, 132, 305-318.
- Allen, M. P. & D. J. Tildesley. 1989. *Computer simulation of liquids*. Oxford university press.
- Almohammed, N. 2013. *Numerical Investigation on the Hydrodynamic Behaviour of Particulate Flows in a Fluidized Bed using Eulerian–Eulerian and Eulerian–Lagrangian Approach*. Master thesis - Eigenverlag des Instituts, Fachgebiet Energiesysteme und Energietechnik.
- Alobaid, F., N. Baraki & B. Epple (2013a) Investigation study for improving the efficiency and accuracy of the CFD/DEM simulations. *Particuology*, Submitted.
- Alobaid, F., J.-P. Busch, J. Ströhle & B. Epple (2012a) Investigations on torrefied biomass for co-combustion in pulverized coal-fired furnaces. *VGB powertech*, 11, 50-55.
- Alobaid, F. & B. Epple (2013) Improvement, validation and application of CFD/DEM model to dense gas–solid flow in a fluidized bed. *Particuology*, 11, 514-526.
- Alobaid, F., A. Galloy, J. Ströhle & B. Epple. 2010a. 3D Simulation of a limestone fluidized bed with the discrete element method. In *Jahrestreffen der ProcessNet-Fachausschüsse Mehrphasenströmungen*. Frankfurt am Main.
- Alobaid, F., S. Pfeiffer, B. Epple, C.-Y. Seon & H.-G. Kim (2012b) Fast start-up analyses for Benson heat recovery steam generator. *Energy*, 46, 295-309.
- Alobaid, F., R. Postler, J. Ströhle, B. Epple & H.-G. Kim (2008) Modeling and investigation start-up procedures of a combined cycle power plant. *Applied Energy*, 85, 1173-1189.
- Alobaid, F., J. Ströhle & B. Epple. 2010b. Numerical simulation of reactive fluidized beds for conversion of the biomass with discrete element method. In *Modellierung von Biomassevergasung und–verbrennung mit Hilfe der numerischen Strömungsmechanik*. Leipzig.
- Alobaid, F., J. Ströhle & B. Epple. 2011. Coupled CFD/DEM for the simulation of dense fluid solid flow. In *2nd International Conference on Computational Engineering*. Darmstadt.
- Alobaid, F., J. Ströhle & B. Epple. (2013b) Extended CFD/DEM model for the simulation of circulating fluidized bed. *Advanced Powder Technology*, 24, 403-415.
- Alobaid, F., J. Ströhle, B. Epple & H.-G. Kim (2009) Dynamic simulation of a supercritical once-through heat recovery steam generator during load changes and start-up procedures. *Applied Energy*, 86, 1274-1282.
- Anand, A., J. S. Curtis, C. R. Wassgren, B. C. Hancock & W. R. Ketterhagen (2009) Predicting discharge dynamics of wet cohesive particles from a rectangular hopper using the discrete element method (DEM). *Chemical Engineering Science*, 64, 5268-5275.
- Asotani, T., T. Yamashita, H. Tominaga, Y. Uesugi, Y. Itaya & S. Mori (2008) Prediction of ignition behavior in a tangentially fired pulverized coal boiler using CFD. *Fuel*, 87, 482-490.
- Babovsky, H. (1989) A convergence proof for Nanbu's Boltzmann simulation scheme. *European journal of mechanics. B, Fluids*, 8, 41-55.

- Babu, B. & A. Chaurasia (2004) Dominant design variables in pyrolysis of biomass particles of different geometries in thermally thick regime. *Chemical Engineering Science*, 59, 611-622.
- Backreedy, R., L. Fletcher, J. Jones, L. Ma, M. Pourkashanian & A. Williams (2005) Co-firing pulverised coal and biomass: a modeling approach. *Proceedings of the Combustion Institute*, 30, 2955-2964.
- Baraff, D. (1995) Interactive simulation of solid rigid bodies. *Computer Graphics and Applications, IEEE*, 15, 63-75.
- Basu, P. & P. Kaushal (2009) Modeling of pyrolysis and gasification of biomass in fluidized beds: a review. *Chemical Product and Process Modeling*, 4, 1-47.
- Beer, F. P. & E. R. Johnston. 1967. *Mechanics for engineers: statics and dynamics*. McGraw-Hill.
- Belosevic, S., M. Sijercic, S. Oka & D. Tucakovic (2006) Three-dimensional modeling of utility boiler pulverized coal tangentially fired furnace. *International journal of heat and mass transfer*, 49, 3371-3378.
- Belytschko, T., Y. Krongauz, D. Organ, M. Fleming & P. Krysl (1996) Meshless methods: an overview and recent developments. *Computer methods in applied mechanics and engineering*, 139, 3-47.
- Bird, G. A. 1976. *Molecular Gas Dynamics*. Clarendon, Oxford.
- Blasi, C. D. (1998) Physico-chemical processes occurring inside a degrading two-dimensional anisotropic porous medium. *International journal of heat and mass transfer*, 41, 4139-4150.
- Bokkers, G. A., M. van Sint Annaland & J. A. M. Kuipers (2004) Mixing and segregation in a bidisperse gas-solid fluidised bed: a numerical and experimental study. *Powder Technology*, 140, 176-186.
- Brilliantov, N. V. & T. Pöschel (1998) Rolling friction of a viscous sphere on a hard plane. *EPL (Europhysics Letters)*, 42, 511-516.
- Campbell, C. S. & C. Brennan (1985) Computer simulation of granular shear flows. *Journal of Fluid Mechanics*, 151, 167-188.
- Chapman, S. & T. G. Cowling. 1970. *The mathematical theory of non-uniform gases*. Cambridge university press.
- Chiesa, M., V. Mathiesen, J. A. Melheim & B. Halvorsen (2005) Numerical simulation of particulate flow by the Eulerian–Lagrangian and the Eulerian–Eulerian approach with application to a fluidized bed. *Computers & chemical engineering*, 29, 291-304.
- Cohen, J. D., M. C. Lin, D. Manocha & M. Ponamgi. 1995. I-COLLIDE: An interactive and exact collision detection system for large-scale environments. In *Proceedings of the 1995 symposium on Interactive 3D graphics*, 189-196. ACM.
- Collazo, J., J. Porteiro, J. Míguez, E. Granada & M. Gómez (2012) Numerical simulation of a small-scale biomass boiler. *Energy Conversion and Management*, 64, 87-96.
- Crowe, C. (1982) Review-numerical models for dilute gas-particle flows. *Journal of Fluids Engineering*, 104, 297-303.
- Cundall, P. A. & O. D. Strack (1979) A discrete numerical model for granular assemblies. *Geotechnique*, 29, 47-65.
- Deen, N., M. Annaland & J. Kuipers (2006) Detailed computational and experimental fluid dynamics of fluidized beds. *Applied mathematical modelling*, 30, 1459-1471.
- Deen, N., M. Van Sint Annaland, M. Van der Hoef & J. Kuipers (2007) Review of discrete particle modeling of fluidized beds. *Chemical Engineering Science*, 62, 28-44.

- Dennis, S., S. Singh & D. Ingham (1980) The steady flow due to a rotating sphere at low and moderate Reynolds numbers. *Journal of Fluid Mechanics*, 101, 257-279.
- Di Renzo, A. & F. P. Di Maio (2004) Comparison of contact-force models for the simulation of collisions in DEM-based granular flow codes. *Chemical Engineering Science*, 59, 525-541.
- Ding, J. & D. Gidaspow (1990) A bubbling fluidization model using kinetic theory of granular flow. *AIChE Journal*, 36, 523-538.
- Elghobashi, S. (1994) On predicting particle-laden turbulent flows. *Applied Scientific Research*, 52, 309-329.
- Elghobashi, S. 2006. An updated classification map of particle-laden turbulent flows. In *IUTAM Symposium on Computational Approaches to Multiphase Flow*, 3-10. Springer.
- Epple, B., R. Leithner, W. Linzer & H. Walter. 2012. *Simulation von Kraftwerken und Feuerungen*. Springer.
- Ergun, S. (1952) Fluid flow through packed columns. *Chemical Engineering and Processing*, 48, 89-94.
- Fan, L.-S. & C. Zhu. 2005. *Principles of gas-solid flows*. Cambridge University Press.
- Feng, Y. & A. Yu (2004) Assessment of model formulations in the discrete particle simulation of gas-solid flow. *Industrial & engineering chemistry research*, 43, 8378-8390.
- Ferziger, J. H. & M. Perić. 2002. *Computational methods for fluid dynamics*. Springer Berlin.
- Fletcher, D., B. Haynes, F. Christo & S. Joseph (2000) A CFD based combustion model of an entrained flow biomass gasifier. *Applied mathematical modelling*, 24, 165-182.
- Flynn, D. 2003. *Thermal power plant simulation and control*. Institution of Engineering and Technology.
- Geldart, D. (1973) Types of gas fluidization. *Powder technology*, 7, 285-292.
- Gera, D., M. Mathur, M. Freeman & A. Robinson (2002) Effect of large aspect ratio of biomass particles on carbon burnout in a utility boiler. *Energy & fuels*, 16, 1523-1532.
- Germano, M., U. Piomelli, P. Moin & W. H. Cabot (1991) A dynamic subgrid-scale eddy viscosity model. *Physics of Fluids A: Fluid Dynamics*, 3, 1760-1765.
- Gerun, L., M. Paraschiv, R. Vijeu, J. Bellettre, M. Tazerout, B. Gøbel & U. Henriksen (2008) Numerical investigation of the partial oxidation in a two-stage downdraft gasifier. *Fuel*, 87, 1383-1393.
- Ghenai, C. & I. Janajreh (2010) CFD analysis of the effects of co-firing biomass with coal. *Energy Conversion and Management*, 51, 1694-1701.
- Gidaspow, D. 1994. *Multiphase flow and fluidization: continuum and kinetic theory descriptions*. Academic press.
- Goldschmidt, M., R. Beetstra & J. Kuipers (2004) Hydrodynamic modelling of dense gas-fluidised beds: comparison and validation of 3D discrete particle and continuum models. *Powder Technology*, 142, 23-47.
- Gómez-Barea, A. & B. Leckner (2010) Modeling of biomass gasification in fluidized bed. *Progress in Energy and Combustion Science*, 36, 444-509.
- Götz, S. 2006. *Gekoppelte CFD-DEM-Simulation blasenbildender Wirbelschichten*. Shaker.
- Grüner, C. 2004. *Kopplung des Einzelpartikel- und des Zwei-Kontinua-Verfahrens für die Simulation von Gas-Feststoff-Strömungen*. Shaker.

- Gryczka, O., S. Heinrich, N. Deen, M. van Sint Annaland, J. Kuipers, M. Jacob & L. Mörl (2009) Characterization and CFD-modeling of the hydrodynamics of a prismatic spouted bed apparatus. *Chemical Engineering Science*, 64, 3352-3375.
- Gui, N., J. R. Fan & K. Luo (2008) DEM-LES study of 3-D bubbling fluidized bed with immersed tubes. *Chemical Engineering Science*, 63, 3654-3663.
- Hartge, E.-U., L. Ratschow, R. Wischnewski & J. Werther (2009) CFD-simulation of a circulating fluidized bed riser. *Particuology*, 7, 283-296.
- Hertz, H. (1882) Über die Berührung fester elastischer Körper. *Journal für die reine und angewandte Mathematik*, 92, 156–171.
- Herzog, N., M. Schreiber, C. Egbers & H. J. Krautz (2012) A comparative study of different CFD-codes for numerical simulation of gas-solid fluidized bed hydrodynamics. *Computers & Chemical Engineering*, 39, 41-46.
- Hill, R. J., D. L. Koch & A. J. Ladd (2001) Moderate-Reynolds-number flows in ordered and random arrays of spheres. *Journal of Fluid Mechanics*, 448, 243-278.
- Hockney, R. W. & J. J. W. Eastwood. 1988. *Computer simulation using particles*. Taylor & Francis Group.
- Hoomans, B., J. Kuipers, W. Briels & W. Van Swaaij (1996) Discrete particle simulation of bubble and slug formation in a two-dimensional gas-fluidised bed: a hard-sphere approach. *Chemical Engineering Science*, 51, 99-118.
- Hoomans, B., J. Kuipers & W. Van Swaaij (2000) Granular dynamics simulation of segregation phenomena in bubbling gas-fluidised beds. *Powder Technology*, 109, 41-48.
- Hußmann, B. 2009. *Modellierung und numerische Simulation der zweiphasigen Strömungs- und Verbrennungsvorgänge in einem Staustrahltriebwerk mit Bor als Festreibstoff*. VDI-Verlag.
- Iwashita, K. & M. Oda (1998) Rolling resistance at contacts in simulation of shear band development by DEM. *Journal of engineering mechanics*, 124, 285-292.
- Iwashita, K. & M. Oda (2000) Micro-deformation mechanism of shear banding process based on modified distinct element method. *Powder Technology*, 109, 192-205.
- Jiménez, P., F. Thomas & C. Torras (2001) 3D collision detection: a survey. *Computers & Graphics*, 25, 269-285.
- Kær, S. K. (2004) Numerical modelling of a straw-fired grate boiler. *Fuel*, 83, 1183-1190.
- Kær, S. K., L. A. Rosendahl & L. Baxter (2006) Towards a CFD-based mechanistic deposit formation model for straw-fired boilers. *Fuel*, 85, 833-848.
- Kaltschmitt, M., H. Hartmann & H. Hofbauer. 2009. *Energie aus Biomasse: Grundlagen, Techniken und Verfahren*. Springer.
- Kanther, W. 2003. *Gas-Feststoff-Strömungen in komplexen Geometrien*. Shaker.
- Kaushal, P., T. Pröll & H. Hofbauer (2008) Model for biomass char combustion in the riser of a dual fluidized bed gasification unit: Part 1—Model development and sensitivity analysis. *Fuel Processing Technology*, 89, 651-659.
- Khan, A. A., W. De Jong, D. R. Gort & H. Spliethoff (2007) A fluidized bed biomass combustion model with discretized population balance. 1. Sensitivity analysis. *Energy & fuels*, 21, 2346-2356.
- Kharaz, A., D. Gorham & A. Salman (1999) Accurate measurement of particle impact parameters. *Measurement Science and Technology*, 10, 31-35.

- Knight, P., J. Seville, H. Kamiya & M. Horio (2000) Modelling of sintering of iron particles in high-temperature gas fluidisation. *Chemical engineering science*, 55, 4783-4787.
- Kosinski, P., A. Kosinska & A. C. Hoffmann (2009) Simulation of solid particles behaviour in a driven cavity flow. *Powder Technology*, 191, 327-339.
- Kruggel-Emden, H., E. Simsek, S. Rickelt, S. Wirtz & V. Scherer (2007) Review and extension of normal force models for the discrete element method. *Powder Technology*, 171, 157-173.
- Kuczynski, G. C. (1949) Self-diffusion in sintering of metallic particles. *AIME TRANS*, 185, 169-178.
- Kuipers, J., W. Prins & W. Van Swaaij (1991) Theoretical and experimental bubble formation at a single orifice in a two-dimensional gas-fluidized bed. *Chemical engineering science*, 46, 2881-2894.
- Kunii, D. & O. Levenspiel. 1991. *Fluidization engineering*. Butterworth-Heinemann Boston.
- Kuwagi, K., T. Mikami & M. Horio (2000) Numerical simulation of metallic solid bridging particles in a fluidized bed at high temperature. *Powder Technology*, 109, 27-40.
- Leva, M. 1959. *Fluidization*. McGraw-Hill.
- Li, S. & W. K. Liu (2002) Meshfree and particle methods and their applications. *Applied Mechanics Reviews*, 55, 1-34.
- Li, S. & W. K. Liu. 2004. *Meshfree particle methods*. Springer Verlag.
- Lian, G., C. Thornton & M. J. Adams (1993) A theoretical study of the liquid bridge forces between two rigid spherical bodies. *Journal of colloid and interface science*, 161, 138-147.
- Link, J., L. Cuypers, N. Deen & J. Kuipers (2005) Flow regimes in a spout-fluid bed: A combined experimental and simulation study. *Chemical Engineering Science*, 60, 3425-3442.
- Link, J. M. 2006. *Development and Validation of a Discrete Particle Model of a Spout-fluid Bed Granulator*. PrintPartners Ipskamp.
- Liu, G. G.-R. & M. Liu. 2003. *Smoothed particle hydrodynamics: a meshfree particle method*. World Scientific Publishing Company.
- Lucy, L. B. (1977) A numerical approach to the testing of the fission hypothesis. *The astronomical journal*, 82, 1013-1024.
- Lumley, J. L. 1990. *Whither turbulence? Turbulence at the crossroads*. Springer.
- Lun, C. K. K., S. B. Savage, D. J. Jeffrey & C. N. (1984) Kinetic theories for granular flow: inelastic particles in Couette flow and slightly inelastic particles in a general flow field. *Journal of Fluid Mechanics*, 140, 223-256.
- Lungfiel, A. 2002. *Ermittlung von Belastungsgrößen mittels der Diskrete-Elemente-Methode für die Auslegung von Sturzmühlen*. Eigenverlag der Technischen Universität Bergakademie Freiberg.
- Ma, L., J. Jones, M. Pourkashanian & A. Williams (2007) Modelling the combustion of pulverized biomass in an industrial combustion test furnace. *Fuel*, 86, 1959-1965.
- Marcus, R. D., Leung LS, Klinzing GE & R. F. 1990. *Pneumatic conveying of solids*. Chapman and Hall.
- Maw, N., J. Barber & J. Fawcett (1976) The oblique impact of elastic spheres. *Wear*, 38, 101-114.
- Mei, R. (1992) An approximate expression for the shear lift force on a spherical particle at finite reynolds number. *International Journal of Multiphase Flow*, 18, 145-147.
- Mikami, T., H. Kamiya & M. Horio (1996) The mechanism of defluidization of iron particles in a fluidized bed. *Powder technology*, 89, 231-238.

- Mikami, T., H. Kamiya & M. Horio (1998) Numerical simulation of cohesive powder behavior in a fluidized bed. *Chemical Engineering Science*, 53, 1927-1940.
- Moghtaderi, B. (2006) The state-of-the-art in pyrolysis modelling of lignocellulosic solid fuels. *Fire and Materials*, 30, 1-34.
- Mohan, D., C. U. Pittman & P. H. Steele (2006) Pyrolysis of wood/biomass for bio-oil: a critical review. *Energy & Fuels*, 20, 848-889.
- Monaghan, J. J. (1992) Smoothed particle hydrodynamics. *Annual review of astronomy and astrophysics*, 30, 543-574.
- Muguruma, Y., T. Tanaka & Y. Tsuji (2000) Numerical simulation of particulate flow with liquid bridge between particles (simulation of centrifugal tumbling granulator). *Powder Technology*, 109, 49-57.
- Nanbu, K. (1980) Direct simulation scheme derived from the Boltzmann equation. I. Monocomponent gases. *Journal of the Physical Society of Japan*, 49, 2042-2049.
- O'Rourke, P. J. 1981. *Collective Drop Effects on Vaporizing Liquid Sprays*. Princeton University.
- Oberlack, M., G. Khujadze, S. Barth, S. Günther, M. Frewer, T. Weller & J. Peinke. 2007. *Progress in Turbulence II: Proceedings of the ITi Conference in Turbulence 2005*. Physica-Verlag.
- Oesterle, B. & A. Petitjean (1993) Simulation of particle-to-particle interactions in gas solid flows. *International journal of multiphase flow*, 19, 199-211.
- Oevermann, M., S. Gerber & F. Behrendt (2009a) Euler–Lagrange/DEM simulation of wood gasification in a bubbling fluidized bed reactor. *Particuology*, 7, 307-316.
- Oevermann, M., S. Gerber & F. Behrendt (2009b) Numerical simulation of wood gasification in a fluidized bed reactor using Euler-Euler modeling. *Proceedings of the European Combustion Meeting*, 1, 1-5.
- Paschedag, A. R. 2004. *CFD in der Verfahrenstechnik: allgemeine Grundlagen und mehrphasige Anwendungen*. Wiley VCH Verlag GmbH.
- Peters, N. 2000. Turbulent combustion (Cambridge monographs on mechanics). Cambridge University Press.
- Pope, S. B. 2000. *Turbulent Flows*. Cambridge University Press.
- Prakash, N. & T. Karunани thi (2008) Kinetic modeling in biomass pyrolysis—a review. *Journal of Applied Sciences Research*, 4, 1627-1636.
- Rubinow, S. & J. B. Keller (1961) The transverse force on a spinning sphere moving in a viscous fluid. *J. Fluid Mech*, 11, 447-459.
- Rukes, B. & R. Taud (2004) Status and perspectives of fossil power generation. *Energy*, 29, 1853-1874.
- Saffman, P. (1965) The lift on a small sphere in a slow shear flow. *Journal of fluid mechanics*, 22, 385-400.
- Schäfer, M. 2006. *Computational Engineering - Introduction to Numerical Methods*. Springer.
- Schiller, L. & A. Z. Naumann (1933) Über die grundlegenden Berechnungen bei der Schwerkraftaufbereitung. *Verein Deutscher Ingenieure*, 77, 318-320.
- Schinner, A. (1999) Fast algorithms for the simulation of polygonal particles. *Granular Matter*, 2, 35-43.
- Schlichting, H. & K. Gersten. 2000. *Boundary-layer theory*. Springer Verlag.
- Schubert, H. (1979) Grundlagen des agglomerierens. *Chemie Ingenieur Technik*, 51, 266-277.

- Sedgewick, R. 1992. *Algorithmen*. Addison-Wesley Longman Verlag.
- Shi, D. & J. J. McCarthy (2008) Numerical simulation of liquid transfer between particles. *Powder Technology*, 184, 64-75.
- Simsek, E., B. Brosch, S. Wirtz, V. Scherer & F. Krüll (2009) Numerical simulation of grate firing systems using a coupled CFD/discrete element method (DEM). *Powder technology*, 193, 266-273.
- Smagorinsky, J. (1963) General circulation experiments with the primitive equations, part I: the basic experiment *Monthly weather review*, 91, 99-164.
- Sommerfeld, M. 1996. *Modellierung und numerische Berechnung von partikelbeladenen turbulenten Strömungen mit Hilfe des Euler,Lagrange-Verfahrens*. Shaker.
- Sommerfeld, M. 2002. Kinetic simulations for analysing the wall collision process of non-spherical particles. ASME.
- Soo, S.-I. & T. Deyan. 1990. *Multiphase fluid dynamics*. Science Press Brookfield.
- Sowinski, A., L. Miller & P. Mehrani (2010) Investigation of electrostatic charge distribution in gas-solid fluidized beds. *Chemical Engineering Science*, 65, 2771-2781.
- Spitz, R. 2013. *Numerical Simulation of gas-solid flows in fluidized bed employing Barracuda software*. Bachelor thesis - Eigenverlag des Instituts, Fachgebiet Energiesysteme und Energietechnik.
- Stiess, M. 1994. *Mechanische Verfahrenstechnik*. Springer.
- Sutkar, V. S., N. G. Deen & J. Kuipers (2012) Spout Fluidized Beds: Recent Advances in Experimental and Numerical Studies. *Chemical Engineering Science*.
- Syamlal, M. & T. O'Brien. 1989. Computer simulation of bubbles in a fluidized bed. In *AIChE Symp. Ser*, 22-31.
- Syred, N., K. Kurniawan, T. Griffiths, T. Gralton & R. Ray (2007) Development of fragmentation models for solid fuel combustion and gasification as subroutines for inclusion in CFD codes. *Fuel*, 86, 2221-2231.
- Tsuji, T., K. Yabumoto & T. Tanaka (2008) Spontaneous structures in three-dimensional bubbling gas-fluidized bed by parallel DEM-CFD coupling simulation. *Powder Technology*, 184, 132-140.
- Tsuji, Y., T. Kawaguchi & T. Tanaka (1993) Discrete particle simulation of two-dimensional fluidized bed. *Powder technology*, 77, 79-87.
- Tsuji, Y., Y. Morikawa & O. Mizuno (1985) Experimental measurement of the Magnus force on a rotating sphere at low Reynolds numbers. *Journal of fluids engineering*, 107, 484-488.
- Tsuji, Y., T. Tanaka & T. Ishida (1992) Lagrangian numerical simulation of plug flow of cohesionless particles in a horizontal pipe. *Powder technology*, 71, 239-250.
- Van Buijtenen, M. S., W.-J. Van Dijk, N. G. Deen, J. Kuipers, T. Leadbeater & D. Parker (2011) Numerical and experimental study on multiple-spout fluidized beds. *Chemical Engineering Science*, 66, 2368-2376.
- Vemuri, B. C., L. Chen, L. Vu-Quoc, X. Zhang & O. Walton (1998) Efficient and Accurate Collision Detection for Granular Flow Simulation. *Graphical Models and Image Processing*, 60, 403-422.
- Wakai, F. & K. Brakke (2011) Mechanics of sintering for coupled grain boundary and surface diffusion. *Acta materialia*, 59, 5379-5387.
- Wang, Y. & L. Yan (2008) CFD studies on biomass thermochemical conversion. *International journal of molecular sciences*, 9, 1108-1130.

- Wen, C. & Y. Yu (1966) Mechanics of fluidization. *AIChE Journal*, 62, 100–111.
- Yuen, R., G. Yeoh, G. de Vahl Davis & E. Leonardi (2007) Modelling the pyrolysis of wet wood—I. Three-dimensional formulation and analysis. *International journal of heat and mass transfer*, 50, 4371-4386.
- Yurong, H., L. Huilin, S. Qiaoqun, Y. Lidan, Z. Yunhua, D. Gidaspow & J. Bouillard (2004) Hydrodynamics of gas–solid flow around immersed tubes in bubbling fluidized beds. *Powder technology*, 145, 88-105.
- Zhong, W., Y. Xiong, Z. Yuan & M. Zhang (2006) DEM simulation of gas–solid flow behaviors in spout-fluid bed. *Chemical engineering science*, 61, 1571-1584.
- Zhou, H., G. Flamant & D. Gauthier (2004a) DEM-LES of coal combustion in a bubbling fluidized bed. Part I: gas-particle turbulent flow structure. *Chemical engineering science*, 59, 4193-4203.
- Zhou, H., G. Flamant & D. Gauthier (2004b) DEM-LES simulation of coal combustion in a bubbling fluidized bed Part II: coal combustion at the particle level. *Chemical Engineering Science*, 59, 4205-4215.
- Zhou, J., A. Yu & M. Horio (2008) Finite element modeling of the transient heat conduction between colliding particles. *Chemical Engineering Journal*, 139, 510-516.
- Zhou, Y., B. Wright, R. Yang, B. Xu & A. Yu (1999) Rolling friction in the dynamic simulation of sandpile formation. *Physica A: Statistical Mechanics and its Applications*, 269, 536-553.
- Zhu, H. & A. Yu (2002) Averaging method of granular materials. *Physical Review E*, 66, 21-32.
- Zhu, H., Z. Zhou, R. Yang & A. Yu (2007) Discrete particle simulation of particulate systems: theoretical developments. *Chemical Engineering Science*, 62, 3378-3396.
- Zienkiewicz, O. C., R. L. Taylor & P. Nithiarasu. 2005. *The Finite Element Method for Fluid Dynamics*. Elsevier Science.
- Zobel, N. 2007. *The Representative Particle Model*. Eigenverlag des Instituts, Fachgebiet Energieverfahrenstechnik und Umwandlungstechniken regenerativer Energien.

# Lebenslauf

Name: Alobaid, Falah

Geburtsdatum: 20.03.1979

Geburtsort: Damaskus

1996: Abitur, Damaskus

1997 – 2002: Bachelor, Maschinenbau – Damaskus Universität

2002 – 2004: Dipl.-Ing. , Maschinenbau – Damaskus Universität

2005 – 2007: M.Sc. , Maschinenbau – Technische Universität Darmstadt

2007 – 2013: Wissenschaftlicher Mitarbeiter am Fachgebiet für Energiesysteme und Energietechnik – Technische Universität Darmstadt

## Publikationen

### Bücher:

[1] *Simulation von Kraftwerken und Feuerungen (810 Seiten)*. 2-Auflage 2012; Springer-verlag, Wien, NewYork (Co-Autor).

[2] *Abbildung und prozesseitige Untersuchung von Anfahrvorgängen eines Kombikraftwerktes mit der Software APROS*. 2007; Master thesis, Eigenverlag des Instituts, Fachgebiet Energiesysteme und Energietechnik.

[3] *Hydrogen hybrid cars*. 2004; Diploma thesis, Eigenverlag der Damaskus Universität.

[4] *Hydrogen fuel as an alternative energy source*. 2002; Bachelor thesis, Eigenverlag der Damaskus Universität.

### Paper:

[1] Alobaid F., Postler R., Ströhle J., Epple B., Hyun-Gee K. (2008) Modeling and investigation start-up procedures of a combined cycle power plant, *Applied Energy*, 85:1173-1189.

[2] Alobaid F., Ströhle J., Epple B., Hyun-Gee K. (2009) Dynamic simulation of a supercritical once-through heat recovery steam generator during load changes and start-up procedures, *Applied Energy*, 86:1172-1182.

[3] Alobaid F., Pfeiffer S., Epple E., Seon C., Kim H. (2012) Fast start-up analyses for Benson heat recovery steam generator, *Energy*, 46:295-309.

[4] Alobaid F., Busch J.P., Ströhle J., Epple B. (2012) Investigations on torrefied biomass for the co-combustion in pulverized fired furnaces, *VGB-Powertech*, 11: 50-55.

[5] Alobaid F., Epple B. (2013) Improvement, validation and application of CFD/DEM model to a dense gas-solid flow in a fluidized bed, *Particuology*, 11:514-526.

[6] Alobaid F., Ströhle J., Epple B. (2013) Extended CFD/DEM model for the simulation of circulating fluidized bed. *Advanced Powder Technology*, 24:403-415.

[7] Alobaid F., Baraki N., Epple B. Investigation study for improving the efficiency and accuracy of the CFD/DEM simulations. *Particuology*, Submitted 2013 (Manuscript Number: PARTIC-D13-00117).

[8] Alobaid F., Karner K., Belz J., Epple B., Hyun-Gee K. Numerical and experimental study of a heat recovery steam generator during start-up procedure. *Energy*, Submitted 2013 (Manuscript Number: EGY-D-13-01637).